

**UCSF**

**UC San Francisco Electronic Theses and Dissertations**

**Title**

The Development and Role of Megavoltage Cone Beam Computed Tomography in Radiation Oncology

**Permalink**

<https://escholarship.org/uc/item/0qn8q535>

**Author**

Morin, Olivier

**Publication Date**

2007-10-15

Peer reviewed|Thesis/dissertation

**The Development and Role of Megavoltage Cone Beam Computerized  
Tomography in Radiation Oncology**

by

Olivier Morin

B.Sc. (Laval University, Québec City, Canada) 2003

A dissertation submitted in partial satisfaction of the  
requirements for the degree of  
Doctor of Philosophy

in

Bioengineering

in the

GRADUATE DIVISIONS  
of the  
UNIVERSITY OF CALIFORNIA, SAN FRANCISCO

UMI Number: 3288953

Copyright 2007 by  
Morin, Olivier

All rights reserved.

UMI<sup>®</sup>

---

UMI Microform 3288953

Copyright 2008 by ProQuest Information and Learning Company.  
All rights reserved. This microform edition is protected against  
unauthorized copying under Title 17, United States Code.

---

ProQuest Information and Learning Company  
300 North Zeeb Road  
P.O. Box 1346  
Ann Arbor, MI 48106-1346

**The Development and Role of Megavoltage Cone Beam Computed  
Tomography in Radiation Oncology**

Copyright 2007

by

Olivier Morin

Pour mon pti-coeur, Samantha.

Que nous vivions une longue vie heureuse et remplie d'aventures.

## Acknowledgments

I want to express my deepest gratitude to all that have made this work possible. Foremost, I would like to thank my research director and dear friend Jean Pouliot for the immense amount of effort and time he has put into this dissertation and into my education and guidance. It is a privilege to have a supervisor who always keeps the door open and is eagerly willing to discuss the work. I will always be grateful for all the opportunities that he has presented to me. Thank you to Lynn Verhey for his thoughtful guidance in the journey of a doctorate degree. Thank you to Bruce Hasegawa and Lijun Ma for the time spent reading this document and providing valuable comments and corrections. I would also like to thank the research lab members from past and present for their numerous enlightening discussions and comments on all the group activities. It is wonderful to be surrounded daily by such good scientists. I would like to acknowledge the contribution of Ali Bani-Hashemi and his team at Siemens Oncology Care Systems who provided support and unique tools for research. Special thanks to the admission committee of the Joint Bioengineering program at UCSF/UC Berkeley for believing in the application of a young French-Canadian. I would like to acknowledge that the text presented in the appendix is a reprint of the material as it appears in *Medical Physics*, *Medical Dosimetry*, the *British Journal of Radiology*, and the *International Journal of Radiation Oncology, Biology and Physics*. Those publications summarize our group's contributions and a significant fraction of the work presented in the dissertation.

I am also very grateful for all those who have invested so much in my education and development through the years. I would like to thank my parents, Monique Roussel and Michel Morin, my brothers, Jean-Nicolas and Frédéric, my parents-in-law Evelyne and Michel Merlin, my friends, all my previous teachers and coaches, and most importantly my wife, Samantha. All of your love and encouragements have been my greatest inspiration.

## Abstract

The Development and Role of Megavoltage Cone Beam Computed Tomography in  
Radiation Oncology

by

Olivier Morin

Doctor of Philosophy in Bioengineering

University of California, San Francisco and Berkeley


Jean Pouliot, Ph.D., Dissertation Research Director

and Bruce Hasegawa, Ph.D., Chair

External beam radiation therapy has now the ability to deliver doses that conform tightly to a tumor volume. The steep dose gradients planned in these treatments make it increasingly important to reproduce the patient position and anatomy at each treatment fraction. For this reason, considerable research now focuses on in-room three-dimensional imaging. This thesis describes the first clinical megavoltage cone beam computed tomography (MVCBCT) system, which utilizes a conventional linear accelerator equipped with an amorphous silicon flat panel detector. The document covers the system development and investigation of its clinical applications over the last 4-5 years. The physical performance of the system was evaluated and optimized

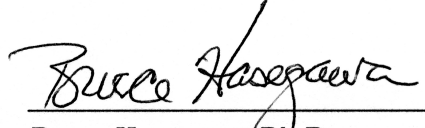


for soft-tissue contrast resolution leading to recommendations of imaging protocols to use for specific clinical applications and body sites. MVCBCT images can resolve differences of 5% in electron density for a mean dose of 9 cGy. Hence, the image quality of this system is sufficient to differentiate some soft-tissue structures. The absolute positioning accuracy with MVCBCT is better than 1 mm. The accuracy of isodose lines calculated using MVCBCT images of head and neck patients is within 3% and 3 mm. The system shows excellent stability in image quality, CT# calibration, radiation exposure and absolute positioning over a period of 8 months. A procedure for MVCBCT quality assurance was developed. In our clinic, MVCBCT has been used to detect nonrigid spinal cord distortions, to position a patient with a paraspinous tumor close to metallic hardware, to position prostate cancer patients using gold markers or soft-tissue landmarks, to monitor head and neck anatomical changes and their dosimetric consequences, and to complement the conventional CT for treatment planning in presence of metallic implants. MVCBCT imaging is changing the clinical practice of our department by increasingly revealing patient specific errors. New verification protocols are being developed to minimize those errors thus moving the practice of radiation therapy one step closer to personalized medicine.



---

Jean Pouillot, Ph.D.  
Dissertation Research Director



---

Bruce Hasegawa, Ph.D.  
Dissertation Committee Chair

# Contents

<b>List of Tables</b>	<b>xi</b>
<b>List of Figures</b>	<b>xiii</b>
<b>1 Background and Motivation</b>	<b>1</b>
1.1 Cancer and Treatment Strategies . . . . .	1
1.2 Basics of Radiation Therapy . . . . .	2
1.3 Clinical Workflow and Treatment Planning . . . . .	5
1.4 Motivation for Image-Guided Radiotherapy . . . . .	6
1.5 Historical Perspective of In-Room CT Imaging . . . . .	8
1.6 Basics of Megavoltage Cone-Beam CT . . . . .	10
1.7 Scope of the Dissertation . . . . .	11
1.7.1 Research Goals . . . . .	11
1.7.2 Thesis Content . . . . .	11
<b>I System Description and Physical Performance</b>	<b>16</b>
<b>2 System Overview and Requirements</b>	<b>17</b>
2.1 Image Reconstruction . . . . .	19
2.1.1 System Geometry . . . . .	20
2.1.2 Reconstruction Algorithm . . . . .	21
2.1.3 Geometric Calibration . . . . .	28
2.2 Treatment Beam Modified for Imaging . . . . .	31
2.3 Flat Panel Detector . . . . .	32
2.3.1 Flat Panel Design and Image Acquisition Mode . . . . .	34
2.3.2 Flat Panel Corrections . . . . .	37
2.4 Major System Components . . . . .	39
2.5 Image Acquisition Procedure . . . . .	41
2.6 Technical Summary of MVCBCT . . . . .	43

<b>3</b>	<b>System Performance</b>	<b>45</b>
3.1	Duration of Acquisition and Reconstruction . . . . .	47
3.2	Field of View and Clearance . . . . .	48
3.3	Geometric Stability and Absolute Positioning . . . . .	51
3.4	Stability of CT Number Calibration Factor . . . . .	53
3.5	Image Quality . . . . .	58
3.5.1	Uniformity and Cupping Artifact . . . . .	61
3.5.2	Spatial Resolution . . . . .	66
3.5.3	Contrast-to-Noise Ratio . . . . .	69
3.6	Electron Density Calibration . . . . .	76
3.7	Dose Delivered to Patients . . . . .	78
3.7.1	Measurements vs. Simulations . . . . .	78
3.7.2	Patient Dose . . . . .	80
3.7.3	Plan Compensation for Routine MVCBCT Imaging . . . . .	84
<b>4</b>	<b>Quality Assurance</b>	<b>93</b>
4.1	Beam output in MVCBCT mode . . . . .	94
4.2	Absolute Positioning . . . . .	95
4.3	Image Quality . . . . .	98
4.4	Practical Artifact Library . . . . .	104
4.5	Recommendations for Quality Assurance . . . . .	111
<b>II</b>	<b>Clinical Applications</b>	<b>114</b>
<b>5</b>	<b>Overview</b>	<b>115</b>
5.1	Examples of Clinical Images . . . . .	117
5.2	Proposed Imaging Protocols . . . . .	119
<b>6</b>	<b>Patient Positioning</b>	<b>121</b>
6.1	Patient Positioning Methods . . . . .	122
6.2	Patient Alignment: 2D vs. 3D . . . . .	124
6.2.1	Absolute Positioning Accuracy . . . . .	126
6.2.2	Phantom Positioning Studies . . . . .	126
6.2.3	Patient Positioning Study . . . . .	127
6.3	Evaluating Complex Spinal Cord Displacement During Setup . . . . .	131
6.4	Performing Setup of a Patient with a Lung Tumor . . . . .	134
6.5	Setup of Patient with Paraspinal Tumor in the Presence of Orthopedic Hardware . . . . .	135
6.6	Alignment of Prostate Patients . . . . .	139

<b>7</b>	<b>Monitoring Patient Anatomy Over Time</b>	<b>142</b>
7.1	Soft-Tissue Variation in the Nasal Cavity . . . . .	142
7.2	Weight Loss for a Head and Neck Patient . . . . .	145
<b>8</b>	<b>Dose Calculation</b>	<b>147</b>
8.1	Effect of Cupping Artifact . . . . .	149
8.2	Validation of MVCBCT . . . . .	152
8.3	Dosimetrical Impact of Anatomical Changes . . . . .	153
8.4	Discussion . . . . .	162
8.4.1	Dose calculation accuracy achieved with MVCBCT . . . . .	162
8.4.2	Expanding dose calculation to more clinical sites . . . . .	163
8.4.3	MVCBCT to monitor the dosimetric impact of weight loss . . . . .	164
<b>9</b>	<b>Other Applications</b>	<b>167</b>
9.1	Organ Delineation in Presence of Metallic Implants . . . . .	167
9.2	Tomosynthesis . . . . .	169
9.3	High-Dose Rate Brachytherapy . . . . .	169
<b>10</b>	<b>Conclusion and Future Directions</b>	<b>172</b>
10.1	Clinical Significance of Thesis . . . . .	172
10.2	Management of New Technology . . . . .	177
10.3	Future Development . . . . .	179
<b>A</b>	<b>Summary of Terms and Abbreviations</b>	<b>183</b>
<b>B</b>	<b>Published Papers</b>	<b>185</b>
	<b>Bibliography</b>	<b>238</b>

# List of Tables

2.1	Technical characteristics of MVCBCT imaging. . . . .	44
3.1	MVCBCT imaging protocol baseline. Abbreviations of protocol components are used throughout the chapter. . . . .	46
3.2	Time required for image acquisition and reconstruction for different imaging protocol. Only the specified protocol component is changed compared to the baseline (Table 3.1). . . . .	48
3.3	Mean $I_{0perframe}$ and beam intensity variations over a period of 8 months at different exposure (MU) for linac 1. . . . .	57
3.4	Mean $I_{0perframe}$ and beam intensity variations over a period of 8 months at different exposure (MU) for linac 2. . . . .	57
3.5	Effect of using different $I_{0,\theta}$ normalization factors on the reconstructed CT#, noise and CNR. . . . .	58
3.6	Uniformity performance for different craniocaudal imaging lengths (CCIL) and gain types. . . . .	62
3.7	Spatial resolution performance for different reconstruction protocols. The full-width at half maximum of the point spread function ( $PSF_{FWHM}$ ) is reported. Only the specified protocol component is changed compared to the baseline specified in Table 3.1. . . . .	70
3.8	Contrast-to-noise ratio (CNR) performance for different reconstruction protocols. Only the specified protocol component is changed compared to the baseline defined in Table 3.1. The CNR performances are reported for three electron density differences relative to water (rED). . . . .	73
3.9	Dose delivered to a prostate patient for daily alignment verification. MVCBCT (9 MU) and portal imaging ( $2 \times 3$ MU = 6 MU). . . . .	83
3.10	Dose delivered to a typical head and neck patient for weekly verification of alignment and anatomy. MVCBCT (5 MU), CR film ( $2 \times 4$ MU = 8 MU) and portal imaging ( $2 \times 2$ MU = 4 MU). . . . .	84

4.1	Contrast-to-noise ratio (CNR) quality assurance performance for inserts of different electron density relative to water (rED). . . . .	102
4.2	Spatial resolution quality assurance performance. The modulation transfer function (MTF in line pairs per mm) is reported at 50% (MTF <sub>50</sub> ) and 10% (MTF <sub>10</sub> ) of the maximum value. . . . .	103
4.3	Uniformity and noise quality assurance performance. . . . .	103
4.4	Recommendations for quality assurance of MVCBCT. Daily, monthly and binannual QA tasks are specified with an approximation of the total time required for the tasks. . . . .	112
5.1	MVCBCT acquisition protocol recommendations for a specific clinical application and body site. The radiation exposure used in our clinic is slightly lower than reported since all reconstructions are processed with diffusion filtering. The right arrow ( $\Rightarrow$ ) signifies that the user should resample or combine transverse slices before analysis. . . . .	120
A.1	Summary of Terms and Abbreviations. . . . .	184

# List of Figures

1.1	Key components of modern medical linear accelerators . . . . .	5
1.2	Basic principle of megavoltage cone-beam CT versus conventional CT	12
2.1	Reconstruction geometry for MVCBCT imaging . . . . .	22
2.2	Diagram describing the steps of MVCBCT image reconstruction . . .	27
2.3	Geometric calibration of the MVCBCT imaging system . . . . .	30
2.4	Beam electron current pulses for different dose delivery modes: treatment versus MVCBCT imaging . . . . .	33
2.5	Diagram describing the flat panel detector designed for MVCBCT . .	36
2.6	Synchronization of the flat panel detector with x-ray beam output . .	37
2.7	Major system components for MVCBCT imaging . . . . .	40
2.8	Key components in the head of the treatment machine . . . . .	42
3.1	Size and shape of the MVCBCT field of view . . . . .	50
3.2	Stability of the system geometry assessed with inspection of the projection matrices in rotation . . . . .	52
3.3	Raw projection intensity variations during MVCBCT image acquisition	55
3.4	Calibration of the CT number normalization factor for linac 1 and 2 .	57
3.5	Uniformity and cupping artifact for a head-size water cylinder . . . .	64
3.6	Uniformity correction method applied to head and neck images . . . .	65
3.7	Summary of the method used to evaluate the spatial resolution of MVCBCT . . . . .	68
3.8	Photo of the phantom specifically designed for CNR measurements on MVCBCT images . . . . .	72
3.9	Snapshots of the CNR performance as a function of exposure for the three best reconstruction protocols . . . . .	74
3.10	CNR performance as a function of exposure for the three best imaging protocols identified . . . . .	75
3.11	Electron density calibration of MVCBCT for different exposures and phantom configurations . . . . .	77

3.12	Dose delivered for MVCBCT imaging: simulation vs measurements . . . . .	80
3.13	Dose distribution for MVCBCT imaging on a typical pelvis patient . . . . .	82
3.14	Plan compensation for routine MVCBCT imaging: dose distributions for a prostate patient treated with a 4-field box with boosts . . . . .	88
3.15	Plan compensation for routine MVCBCT imaging: DVH for a prostate patient treated with a 4-field box with boosts . . . . .	89
3.16	Plan compensation for routine MVCBCT imaging: DVH for prostate patient treated with IMRT . . . . .	89
3.17	Plan compensation for routine MVCBCT imaging: dose distributions for a head and neck treated with IMRT . . . . .	90
3.18	Plan compensation for routine MVCBCT imaging: DVH for head and neck patient treated with IMRT . . . . .	91
4.1	Photos of the geometric calibration and image quality phantom provided with the commercial MVCBCT system . . . . .	96
4.2	Reconstruction position of a gold marker placed at isocenter over time to assess the absolute positioning stability of the MVCBCT system . . . . .	97
4.3	Graphical user interface developed to evaluate the image quality of MVCBCT using EMMA . . . . .	99
4.4	Library of image artifacts possibly occurring with MVCBCT imaging . . . . .	107
4.5	Library of image artifacts possibly occurring with MVCBCT imaging -continued . . . . .	109
5.1	Overview of various image-guided radiation therapy schemes using only a conventional linac and a flat-panel detector . . . . .	117
5.2	Image quality of MVCBCT for typical prostate and head and neck patients . . . . .	118
6.1	Patient setup methods: 2D versus 2D . . . . .	125
6.2	Rando phantom setup methods: 2D versus 3D . . . . .	128
6.3	Alignment of head and neck patients: 2D versus 3D . . . . .	130
6.4	Head and neck patient with cervical vertebrae distortion not visible on portal imaging but appreciated with MVCBCT imaging . . . . .	133
6.5	Alignment of a patient with lung tumor . . . . .	136
6.6	Alignment of a patient with paraspinous tumor in presence of metallic hardware . . . . .	138
6.7	Typical alignment of prostate patients implanted gold seeds using MVCBCT imaging . . . . .	140
7.1	Variations in tumor size observed on MVCBCT images for a patient with parasinus carcinoma . . . . .	144
7.2	Weigth loss assessed with MVCBCT imaging for a head and neck patient treated with IMRT . . . . .	146



8.1	Dosimetric impact of the cupping artifact observed with MVCBCT . . . . .	151
8.2	Dose calculation with MVCBCT for an ideal head and neck patient . . . . .	154
8.3	Dose calculation with MVCBCT for a head and neck patient affected by weight loss and tumor shrinkage . . . . .	157
8.4	Dose calculation comparison between CT and MVCBCT for a head and neck patient affected by weight loss and tumor shrinkage . . . . .	158
8.5	Dosimetrical impact of weight loss for a head and neck patient treated with IMRT . . . . .	160
8.6	Evaluating the capability of contouring anatomical structures using MVCBCT images . . . . .	161
9.1	Image quality of MVCBCT in presence of implanted metallic objects . . . . .	170

# Chapter 1

## Background and Motivation

### 1.1 Cancer and Treatment Strategies

Cancer treatment presents a complex problem that has affected human beings for centuries. A recent survey from the American Cancer Society [1] reports that, after heart disease, cancer is the most frequent cause of mortality in the United States (23% of all deaths in 2003). In 2007, it is estimated that 600,000 Americans will die of cancer. Statistically, half of all men will be diagnosed with cancer in their lifetime with 1 man out of 6 developing prostate cancer disease. For women, the odds of developing a type of cancer is 33%. It is obvious that these are significant health concerns that compel us to invest our scientific and medical resources to develop safe, effective treatments.

Despite the statistics, recent advances in the treatment of cancer have made the

search and development of a cure more promising. It is said that researchers have had more impact on survival rates in the last 20 years than in the rest of cancer treatment history. A multidisciplinary effort, including significant contributions from biology, chemistry, physics and engineering is being made to answer questions about this multifaceted problem. Cancer patients are now being treated with one or a combination of surgery, hormone therapy, radiation therapy, chemotherapy, thermal therapy and biological agents [2]. This dissertation presents advances in radiation therapy (RT).

## 1.2 Basics of Radiation Therapy

The use of radiation to treat cancer started soon after the somewhat fortuitous discovery of x-rays by Roentgen in 1896. Work on radioactivity by Becquerel and the Curie was equally important, and identified both the risk and the potential clinical benefits of radiation on cancer. Early physicians merely applied exposure to radiation to "see what happened" and based their clinical practice on follow-up observations [3]. Today, radiation is administered safely with treatment procedures increasingly designed to provide fully personalized treatment instead of treating patients following a prescribed regimen for a tumor at a general body site. Advances in dose delivery are allowing radiation oncologists to deliver a tumoricidal dose of radiation to a defined tumor volume without causing undue harm to surrounding normal tissues. The obvious question becomes how can radiation be delivered so that it can cure

cancer without causing toxicity to normal organs? Fortunately, radiation can stop replication of cancer cells by inducing DNA cell damage (ionization), which make normal tissues generally less sensitive to radiation. In addition, by using techniques and insights from physics and radiobiology (e.g. dose fractionation), scientists can improve the preferential toxicity of radiation to the tumor without causing a high level of complications in normal tissues.

Depending on the patient diagnosis, treatment can be administered with ionizing radiation (photons, electrons, protons and heavy ions) produced by radionuclides or particle accelerators. This dissertation focuses on the most widely used treatment machine called a medical linear accelerator ("linac") which can deliver photons and electrons of different energies. External-beam radiation therapy (EBRT) refers to the use of equipment to focus radiation on the tumor from outside the patient. Most patients treated with EBRT are treated with a linac. Patients are generally treated daily (Monday through Friday) for a period of 3 to 8 weeks. Such a fractionation of the treatment improves tumor response and allows normal tissue repair (less side effects).

The use of linacs in RT has evolved substantially in the last 20 years. Not too long ago, patients were roughly aligned on a treatment table and large square radiation fields were delivered to the treatment volume. The high dose received by normal organs from such treatment limited the dose that could safely be prescribed to the tumor thus reducing cure rates. Modern linacs now have the capability to deliver much

more conformal dose distributions with methods such as three-dimensional conformal radiation therapy (3DCRT) and intensity-modulated radiation therapy (IMRT). Figure 1.1 shows the main components of a modern linac (Oncor™, Siemens Oncology Care Systems, Concord, CA). Electrons injected by an electron gun (b) are accelerated along the waveguide (c) by stationary microwave produced by the klystron (a). The bending magnet (d) changes the orientation of the electrons and rejects electrons that do not have the energy specified by the delivery mode. A tungsten target (e) is placed in the path of the electrons to create bremsstrahlung x-rays (photons). A flattening filter (f) is placed after the target to preferentially reduce the energy fluence on-axis and obtain a flat dose deposition profile at 10 cm depth in water. Finally, collimators (g) are the key components for 3DCRT and IMRT. They now are designed as multileaf collimators which can achieve nearly any beam shape. To reach tumor at different depth, two energy-modes (6 and 18 MeV) are available for photon treatment. Patients are placed on the treatment table (4) each day (i.e. for each fraction) and aligned with laser positioning at the machine isocenter. The use of multileaf collimators and different x-ray energies allows the radiation oncologist and physicist to tailor the radiation beam to suit the shape, depth, and type of tumor being treated while trying to spare surrounding normal tissue as much as possible.

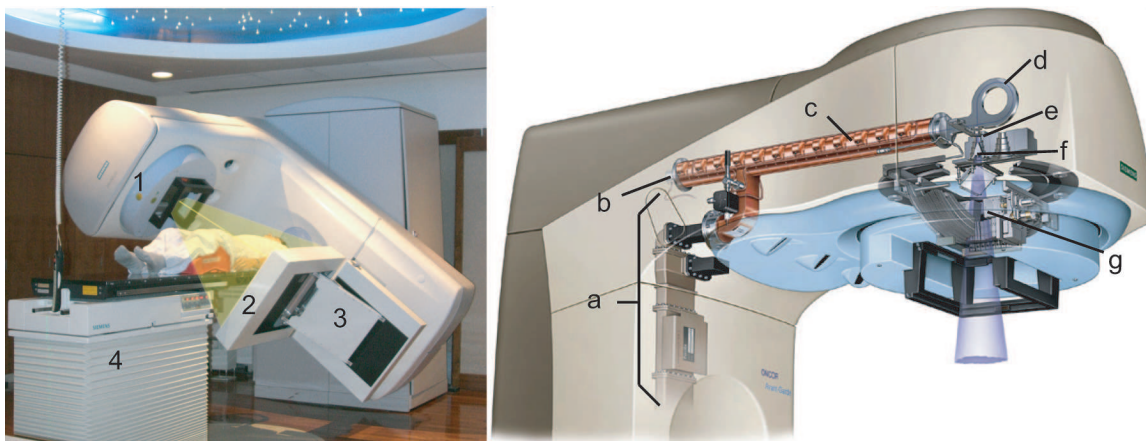


Figure 1.1: (*Left*) a modern medical linear accelerator gantry head (1) with the electronic portal imaging device (2), the detector positioner (3) and the patient table (4) ready for external beam radiation therapy and megavoltage imaging. (*Right*) the key components of the system include the klystron (a), the electron gun (b), the waveguide (c), the bending magnet (d), the target (e), the flattening filter (f) and the primary and secondary collimators (g). Image courtesy of Kevin Hulsey Illustration, Inc.

### 1.3 Clinical Workflow and Treatment Planning

The accurate delivery of radiation in a therapeutic procedure depends heavily on being able to identify the three-dimensional (3D) shape and location of the tumor within the patient. In current practice, this is achieved using a conventional kilovoltage computed tomography (CT) scanner to acquire multiple CT cross-sectional images (a 3D snapshot) of the patients anatomy prior to the beginning of therapeutic procedure. This 3D image data set is imported into a treatment planning computer that has software to define the treatment isocenter, contour anatomical structures (target and organs at risk), and choose a beam arrangement to deliver a dose distribution that conforms to given dose prescriptions and limitations. Other 3D

imaging modalities such as magnetic resonance (MR) and positron emission tomography (PET) increasingly are being used in addition to CT to guide the tumor and soft-tissue organ delineation process. Ideally, the dose delivered upon completion of radiotherapy would be identical to the dose prescribed during the treatment planning procedure. In reality, there are sources of error related to patient positioning, patient motion, and anatomical variations over time. In addition, the dose calculation engine typically relies on assumptions for handling radiation build-up across heterogeneities, while the treatment machine output will have slight (and hopefully negligible) differences between the intended and actual magnitude and shape of dose delivery. Finally, numerous authors have reported that organs may shift in size, shape, and position from day to day and week to week due to normal anatomical variability as well as changes over time, such as tumor shrinkage, edema, or weight loss [4, 5, 6, 7, 8] related to the therapeutic application. These variables potentially may reduce the probability of tumor control and increase the severity of side effects. As a result, such patient specific variables have motivated the development of 3D verification tools of patient anatomy over the course of RT.

## 1.4 Motivation for Image-Guided Radiotherapy

Image-guided radiation therapy (IGRT) refers to the use of patient imaging in the treatment room to increase the conformality of the radiation dose to the tumor, improving tumor control and reducing normal tissue complications. The development

of image-guidance tools and techniques in RT has been greatly motivated by the continual advances in EBRT. Many clinical studies and simulations indicate that the more conformal and higher dose treatments provided by 3DCRT and IMRT can decrease both the spread of disease and normal tissue complications [9, 10, 11, 12, 13]. However, as the planned dose distributions conform more closely to the pre-treatment planning CT, the precision of dose delivery becomes limited by the validity of using the planning CT to represent the patient on the treatment table throughout an extended course of treatment. Therefore, anatomical and positional information that can be obtained immediately before the patient's treatment is extremely valuable.

Imaging has long played a key role in assuring the accuracy of radiation therapy treatment. Traditionally, portal images (i.e. projection images of the patient using a rectangular radiation beam delivered through the treatment aperture) have been used to confirm the patient position based on bony anatomy or gold markers implanted in or near the tumor. The use of radiographic film for portal imaging has limited the frequency of this verification due to the time required to process the films and a relatively high dose to the patient. Recent implementation of highly sensitive and automated on-board electronic portal imaging devices (EPID) (Figure 1.1, #3) now enables daily low-dose portal imaging to visualize and adjust the patient position before each treatment. However, the utility of portal imaging to adjust the patient position is limited by reduced soft-tissue and 3D geometrical visualization caused by projection onto a two-dimensional (2D) plane. This has motivated the development



of 3D imaging of the patient while lying on the treatment table of the linac.

## 1.5 Historical Perspective of In-Room CT Imaging

Since CT is the current standard for localization of soft-tissue organs and target in treatment planning there has been a growing interest in integrating CT directly with the treatment machine in the treatment room. Several in-room 3D CT systems have been studied and developed in the last 10 years including I) a "CT on rails" system [14, 15] requiring an additional diagnostic CT machine in the treatment room, II) a kilovoltage cone-beam CT (kVCBCT) system [16, 17] consisting of an additional kV X-ray source and detector attached to the treatment gantry, III) a mobile C-arm kilovoltage imager [18], IV) a megavoltage cone-beam CT (MVCBCT) system [19, 20] using the pre-existing treatment machine and EPID for imaging, V) a MVCT system [21, 22] using the pre-existing treatment machine with an attached arc of detectors for imaging, and VI) a Tomotherapy (TomoTherapy Inc., Madison, WI) system [23] in which the traditional treatment machine (beam) is replaced with a CT ring for imaging and a MV beam source for both imaging and treatment. The potential clinical applications of these IGRT technologies depend on the physical performance, which continues to improve for many of the systems.

The history of megavoltage imaging using the pre-existing treatment machine is of particular interest for this dissertation. Approximately 20 years ago, researchers first used a linac beam for 3D imaging. These early systems reconstructed 2D slices

using a fan-beam geometry [24, 25]. As the technology of 2D x-ray detectors advanced [26], cone-beam reconstruction systems became increasingly feasible. Subsequently, several researchers acquired MVCBCT images using standard linacs with liquid-filled ionization chamber detectors [27], video-based EPIDs [27, 28] and amorphous silicon (a-Si) flat panel detectors [29, 30]. In much of the early work, signal was maximized by applying high doses (50-200 cGy per 3D image, the dose equivalent to approximately 50 to 200 conventional CT scans). Strategies such as the development of more sensitive detectors [31, 32] and the restriction of the imaging volume to the treatment volume [33, 34] have reduced these doses to clinically acceptable values which are generally higher in radiotherapy than for diagnostic applications given the large amount of radiation already received by the patients for treatment. Depending on the clinical benefits, an imaging dose as high as 20 cGy may be acceptable for IGRT applications. Other developments include the adaptation of MVCBCT for lung tumor visualization by synchronizing image acquisition with respiration [20], and also serve to improve image quality while reducing radiation dose to the patient.

Dr. Jean Pouliot's group at the University of California San Francisco (UCSF) has worked in collaboration with Siemens Oncology Care Systems (OCS) on the clinical implementation of MVCBCT since the summer of 2001. In early 2002, a proof of feasibility [35] was demonstrated. I joined the group in the summer of 2003. Over the last 4 years, our group has made substantial contributions by developing and showing the feasibility of image-guidance techniques based on MVCBCT imaging. In

such a short amount of time, the initial system has evolved from an experimental and clinically cumbersome system to an operationally robust image-guidance system that now is fully approved by the Food and Drug Administration (FDA), and this is being used routinely to image and treat patients at more than 100 RT departments in the world.

## 1.6 Basics of Megavoltage Cone-Beam CT

Figure 1.2 compares the basic image acquisition principles of MVCBCT to conventional CT. A cone-beam CT image is reconstructed from a set of open field 2D projection images acquired at different positions around the patient. The rays form a cone with its base on the detector and its apex on the source. The process is similar to conventional CT which uses the signal from a single row (several rows for modern CT scanners) of detectors to reconstruct a slice. For conventional CT, the 3D image is formed by translating the patient during image acquisition so that multiple slices can be reconstructed from a volumetric region. For CBCT, the data are acquired with a 2D detector array that allows a direct 3D image dataset to be acquired and reconstructed without multiple gantry rotations or table movement. In addition, the linac x-ray source naturally produces a cone of rays, so cone-beam acquisition not only increases the scanning speed, but also makes better use of the emitted rays otherwise removed by collimation. For MVCBCT, projection images are acquired using a linac with photons primarily in the mega-electron volt (MeV) energy range, compared to

conventional CT which uses kilovoltage x-rays for diagnostic imaging.

## **1.7 Scope of the Dissertation**

This dissertation presents the recent developments and the clinical investigation of a novel IGRT system based on MVCBCT imaging. The following section describes the initial goals that were identified at the beginning of this project 4 years ago.

### **1.7.1 Research Goals**

1. Develop MVCBCT for 3D image-guidance techniques in EBRT.
2. Characterize and optimize the physical performance of MVCBCT.
3. Define a quality assurance protocol for MVCBCT.
4. Investigate the clinical applications of MVCBCT.
5. Introduce MVCBCT in the clinical workflow of our department.

### **1.7.2 Thesis Content**

The body of this dissertation is divided in two parts. Part I focuses on the physical description and performance of the imaging system. Based on its physical performance, Part II investigates possible clinical applications of this new technology.

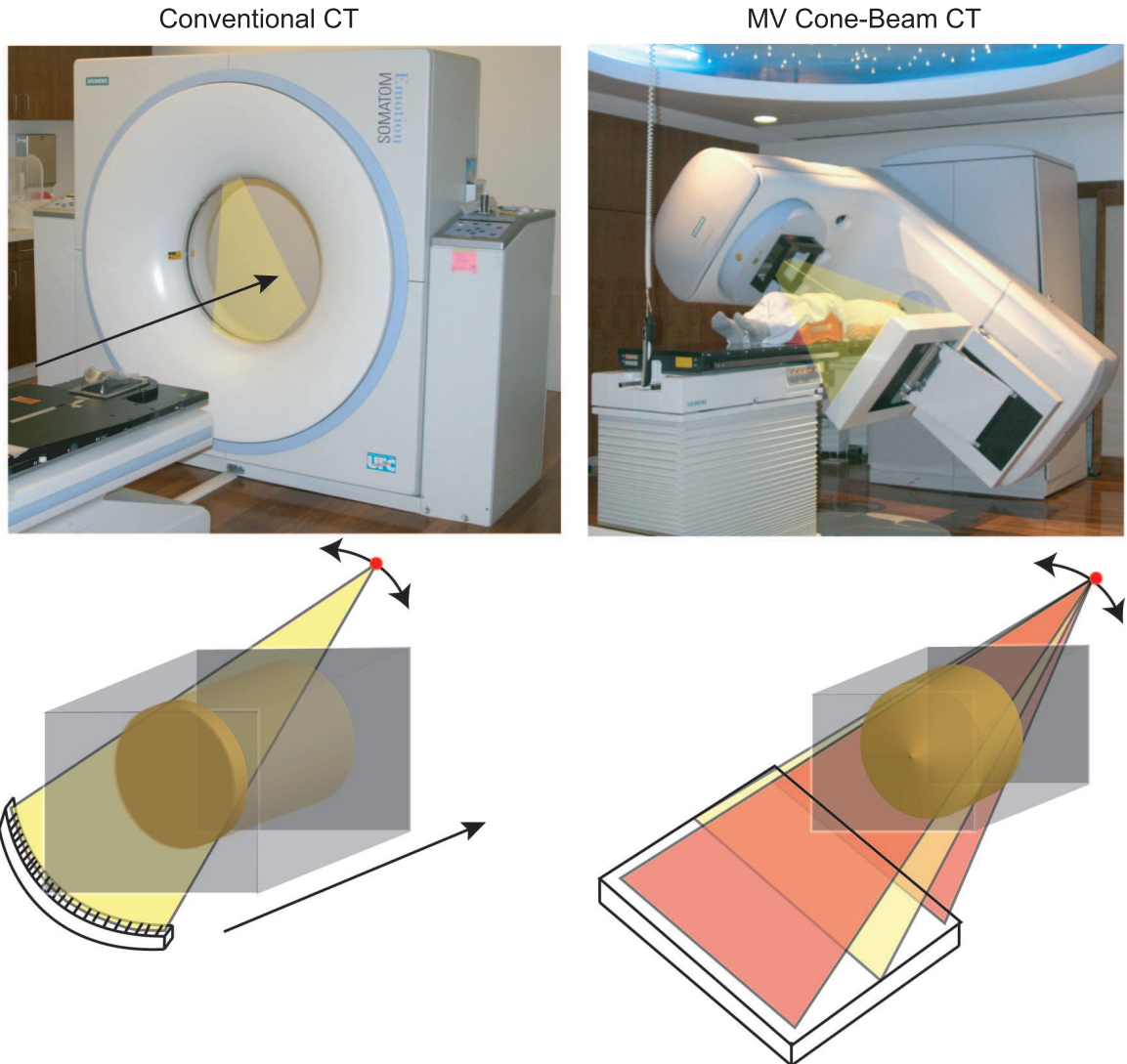


Figure 1.2: Basic principle of image acquisition and reconstruction volume for (*left*) conventional CT and (*right*) megavoltage cone-beam CT (MVCBCT). MVCBCT uses a 2-dimensional detector and a wide open radiation field to obtain an image over an extended region of the patient's anatomy without the need for table movement.

The text is divided into ten chapters that follow a thematic rather than a chronological organization.

The first chapter provides background information on radiation oncology, EBRT, in-room CT imaging and MVCBCT.

Chapter 2 presents the system geometry and the specific reconstruction algorithm used for MVCBCT in details. The treatment beam formation for MVCBCT imaging and the flat panel detector synchronization are described. The system calibrations related to MVCBCT imaging are addressed. We presents the major system components and the image acquisition procedure of the clinical implementation of MVCBCT imaging. Finally, a technical summary of the imaging system is provided. The content of this chapter is required to understand the main personal contributions of this dissertation.

Chapter 3 evaluates the complete physical performance of MVCBCT. During the course of this project, several system components were modified to implement the MVCBCT system. We therefore measured and compared the performance of these components at baseline and then following modification. The chapter also provides details on the duration of acquisition and reconstruction and the size of the imaging volume (field of view). The performance of two MVCBCT systems were followed for a period of 8 months with respect to their geometric stability, the absolute positioning accuracy, the stability of the beam output and detector intensity, the image quality, the electron density calibration and the dose delivered to patient.

Chapter 4 presents quality assurance performed on our two MVCBCT systems. The beam output, the absolute positioning and the image quality were measured with decreasing frequency and followed for a period of 8 months. On each day of quality assurance, images were acquired using the initial system calibrations and compared against newly acquired calibrations to establish the frequency at which calibration of the system is necessary. A graphical user interface was developed with the scientific software package Matlab (The Mathworks, Inc., Natick, MA) to quantify and follow the image quality performance. A practical library of MVCBCT artifacts compiled over the last 4-5 years is provided. The chapter concludes with recommendations for MVCBCT quality assurance.

Chapter 5 is the first chapter of the Part II of the dissertation which explores the clinical applications of MVCBCT imaging. The chapter gives an overview of the applications discussed in the following chapters and provides examples of typical MVCBCT images for patients with cancer in the pelvis, and the head and neck regions. The chapter concludes by tabulating recommendations of imaging protocols recommended for specific clinical applications and body sites.

Chapter 6 addresses patient set-up with MVCBCT. The current 2D standard for alignment is compared with 3D positioning methods using conventional CT and MVCBCT imaging. Examples of clinical cases clearly benefiting from 3D imaging are described. Chapter 7 gives two examples of clinically significant anatomical changes occurring over the course of therapy.

Chapter 8 explores the possibility of using MVCBCT images for dose calculation. The validation of MVCBCT images for dose calculation is done using phantom and patient images. The chapter also evaluates the potential impact of weight loss during a therapeutic regimen on radiation dose calculations.

Chapter 9 describes other possible applications of MVCBCT imaging, including its use in improving image quality of CT in patients with metallic implants.

Chapter 10 discusses my personal journey in the doctoral program with a emphasis on the significance of the work presented and a note on the difficulty of managing new technology. Finally, I give my recommendations for future development and a vision of the possible clinical opportunities with MVCBCT.



## Part I

# System Description and Physical Performance

# Chapter 2

## System Overview and Requirements

The purpose of this chapter is to give a technical description of MVCBCT while explaining the rationale behind the decisions made during the development of the system. The chapter is written as a basic scientific description of the system components and requirements rather than a user guide for the clinical product developed by Siemens (Siemens Oncology Care Systems, Concord, CA). First, the specific reconstruction algorithm developed for MVCBCT is presented. Background information is provided on key aspects (x-ray imaging beam and flat panel detector) of the system design. The major system components and the image acquisition procedure are presented. Finally, a summary of the system design and characteristics is provided in Table 2.1 at the end of the chapter. It is important to mention that the description of

my personal contributions truly starts in Chap. 3, which presents a detailed discussion of the system physical performance for different acquisition and reconstruction settings.

The initial objective of this project was to develop an in-room 3D CT imaging system. At the time when we started this project, MVCBCT was not yet available but became a strong choice for implementation because its simplicity, efficiency and cost makes it appealing for clinical and commercial implementation. In developing this system, several decisions had to be made for the x-ray beam, the geometry, the detector shape and type, the reconstruction algorithm as well as the acquisition and reconstruction settings. While I did personally contribute on several aspects of the system development, several decisions concerning the system geometry and the reconstruction algorithm had already been made before my arrival. In addition, some system parameters were set from the very beginning to reduce the system complexity. Finally, certain aspects of the system were not thoroughly tested in order to accelerate the availability of MVCBCT for clinical use. Often, the gain in operational speed and simplicity outweighed the advantages of having more options and slightly better image quality. The motivations for the decisions made during the development of this first clinical MVCBCT system are described throughout the chapter.

## 2.1 Image Reconstruction

Computed tomography is a technique for imaging and then calculating (or "reconstructing") cross-sections of an object using a series of x-ray measurements taken from different angles around the object. The theory of CT reconstruction of two-dimensional (2D) or three-dimensional (3D) functions from their projections is well-known. Detailed presentations for simple geometries can be found in the book of Kak and Slaney [36] and in the dissertation of Turbell [37] specifically for cone-beam geometries characteristic of point x-ray sources and 2D x-ray detector. This chapter presents the main reconstruction steps of MVCBCT images, which is based on the Feldkamp, Davis and Kress (FDK) algorithm [38] for circular cone-beam tomography. Mathematically, the reconstruction is not exact off the central fan of the cone beam but it provides an excellent approximation for the small cone angle used with MVCBCT. For clinical applications, the gain in speed of the FDK algorithm outweighed the advantage of exactness offered by other algorithms. In the FDK algorithm, each horizontal row of detector values is preprocessed and filtered just as if they were projections of a conventional 2D (i.e., planar) tomographic reconstruction algorithm. The filtered projection data are then backprojected along the original rays to a volume element (voxel) in space, a procedure called 3D backprojection with weighting factors that count for the 3D cone-beam nature of the projection data.

From the theory of CT reconstruction, the CBCT system needs to acquire a sufficient number of 2D projection images around the object for exact reconstruction.

The "exact" reconstruction terminology here strictly assumes noise-free projections and an exact reconstruction algorithm. In the 2D case, it is easy to understand that if parallel projection data are lacking in a certain angular interval, certain frequency components of the object are simply missing and therefore exact reconstruction is impossible. It has been demonstrated that for CBCT imaging, projection images need to be acquired over an angular range of half a rotation plus twice the fan angle (see Fig. 2.1) of the cone beam [37]. The acquisition can start at any angle as long as these requirements for the angular interval and range are satisfied. Image quality will degrade substantially if the angular sampling of 2D projection images is insufficient. Therefore, these sampling requirements indeed were satisfied for the MVCBCT image acquisition presented in Sec. 2.5.

### 2.1.1 System Geometry

The system geometry for MVCBCT reconstruction is illustrated in Fig. 2.1. The source-axis distance ( $S_{AD}$ ) and the source-imager distance ( $S_{ID}$ ) are respectively represented by  $D$  and  $f$  in the reconstruction algorithm described next. The 3D coordinate system (CT image to be reconstructed) represented by  $(X_f, Y_f, Z_f)$  is fixed in space. The detector coordinate system rotates with the gantry and is represented by the coordinate system  $(U, V)$ . The flat panel detector rotates at a projection angle  $\theta$  around the  $Y_f$  axis. An object point in space  $\vec{P}_{3d}:(x_f, y_f, z_f)$  is projected on the flat panel at  $\vec{P}_{2d}:(u, v)$ . The projection position of a point in space  $(x_f, y_f, z_f)$  is also

denoted  $\vec{P}_{2d}:(a_{x_f,y_f,z_f},\theta)$  since it depends on both the point in space  $(x_f, y_f, z_f)$  and the gantry angle  $\theta$ . The argument  $a_{x_f,y_f,z_f,\theta}$  is used to reflect the backprojection process described below. Finally, the angular position of a point away from the central axis is represented by  $\gamma(u)$  which is measured from the x-ray source at the angular vertex and which can take any value between 0 (on-axis) and the maximum fan angle of the cone beam  $\pm\gamma_{max}$ .

## 2.1.2 Reconstruction Algorithm

The attenuation coefficient  $\mu_{X,Y,Z}$  of a voxel in space (i.e. a small volume element of the patient anatomy) can be obtained or "reconstructed" in 3D from a weighted and filtered backprojection of the 2D projection images over all the acquisition angles  $\theta$ . The following steps and Fig. 2.2 are intended to clarify the steps involved in the FDK algorithm implemented for MVCBCT reconstruction.

### Steps for MVCBCT image reconstruction (also illustrated in Fig. 2.2):

1. Two-dimensional projection images  $I(u, v)_\theta$  are acquired at positions  $\theta$  around the patient.
2. Each raw projection is corrected for dark current, gain and dead pixels.
3. A median filter is applied to each projection to remove transient dead pixels not captured in the dead pixel calibration procedure.

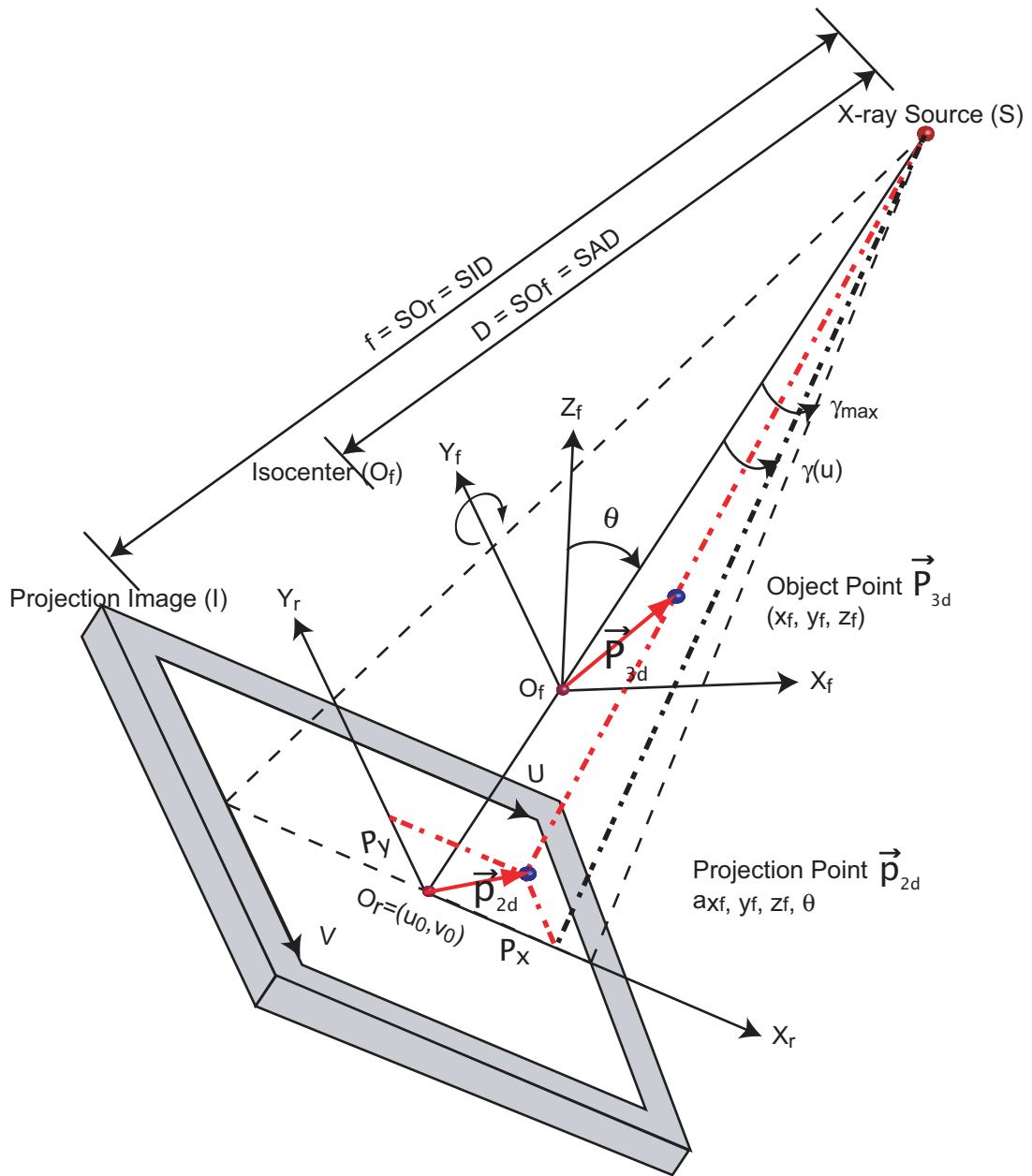


Figure 2.1: Description of the geometry and coordinate systems used for MVCBCT reconstruction. The x-ray source (S) produces a cone beam attenuated by the object and captured as a projection image  $I(u, v)$  by the detector. The central point of the imaging system, called the isocenter, is represented by  $O_f$ . The detector rotates at a projection angle  $\theta$  around the  $Y_f$  axis. A point or voxel in space  $\vec{P}_{3d} : (x_f, y_f, z_f)$  is projected to a point on the detector  $\vec{P}_{2d} : (u, v)$ .

4. Average or diffusion filtering is applied to the projection images to reduce noise. A diffusion filter uses different levels of averaging depending on the local gradient changes in intensity [39].
5. Logarithmic conversion of all projections and intensity normalization.

$$p(a_{x_f, y_f, z_f, \theta}) = \ln \left( \frac{I_{0, \theta}}{I(a_{x_f, y_f, z_f, \theta})} \right) \quad (2.1)$$

with

$$I_{0, \theta} = I_{0perMU} \cdot MU_{\theta} \quad (2.2)$$

$I_{0, \theta}$  is the detector intensity for the nonattenuated x-ray beam at an angle  $\theta$ . It is obtained by multiplying the system calibration factor  $I_{0perMU}$  (the detector sensitivity to 1 MU exposure of the nonattenuated x-ray beam) and by  $MU_{\theta}$  (the fractional x-ray exposure per projection recorded using the dosimetry system (ion chamber) in the head of the gantry (see Fig. 2.8, 1e)). The  $I_{0perMU}$  factor is measured during gain calibration performed in air as explained in Sec. 2.3.2. The argument  $a_{x_f, y_f, z_f, \theta}$  is used later to reflect the concept of backprojection in which a processed value on the detector with position  $(u, v)$  for the projection angle  $\theta$  is added to a voxel  $(x_f, y_f, z_f)$ . This step is done using projection matrices described in the next section. The relationship between  $a_{x_f, y_f, z_f, \theta}$  and  $(u, v)$  and how they are related to one another  $(u, v) \leftrightarrow (a_{x_f, y_f, z_f, \theta})$  using projection matrices will be clarified in the step of backprojection (step 13).

6. Prewighting of each row: Cosine and Parker weighting are applied on  $p(a_{x_f, y_f, z_f, \theta})$ .



The cosine weighting is geometrically interpreted as the cosine of the angle between the ray and the central ray of the projection.

$$\underbrace{\tilde{p}(a_{x_f, y_f, z_f, \theta})}_{\text{pre-weighting}} = \underbrace{\left( \frac{f}{\sqrt{f^2 + x_r^2 + y_r^2}} \right)}_{\text{cosine-weight}} \cdot \mathcal{P}(a_{x_f, y_f, z_f, \theta}) \cdot \underbrace{w(\theta, \gamma(x_r))}_{\text{Parker weight}} \quad (2.3)$$

with

$$w(\theta, \gamma(x_r)) = \begin{cases} \sin^2 \left[ \frac{\pi}{2} \cdot \frac{\theta - \theta_{min}}{\theta_{max} - \pi + 2\gamma - \theta_{min}} \right] , & \theta_{min} \leq \theta \leq \theta_{max} - \pi + 2\gamma \\ 1 & , \quad \theta_{max} - \pi + 2\gamma \leq \theta \leq \pi + \theta_{min} + 2\gamma \\ \sin^2 \left[ \frac{\pi}{2} \cdot \frac{\theta_{max} - \theta}{\theta_{max} - \pi - 2\gamma - \theta_{min}} \right] , & \pi + \theta_{min} + 2\gamma \leq \theta \leq \theta_{max} \end{cases} \quad (2.4)$$

for  $\gamma(x_r) \in [-(\theta_{max} - \theta_{min} - \pi)/2, (\theta_{max} - \theta_{min} - \pi)/2]$

The Parker weighting accounts for redundant angles of the acquisition [36].

7. Zero padding along the U axis (for extrapolation) and binning (2×2) to reduce noise.
8. Extrapolation of truncated signal along the affected rows of the detector. Truncation of the signal occurs when the patient anatomy extends beyond the x-ray beam (shoulders or pelvis) and therefore is not represented on the detector. The extrapolated signal is not illustrated in Fig. 2.2. Extrapolation is currently performed by slowly ramping down the signal along rows beyond the physical borders along which the recorded signal drops sharply at the detector edges.
9. Compute Fourier transform of each row  $\tilde{p}$ .

$$\tilde{P}(\rho) = F \left( \tilde{p}(a_{x_f, y_f, z_f, \theta}) \right) \quad (2.5)$$

where  $\rho$  represents the spatial frequency along the U axis.

10. Apply a filter ( $G(\rho)$ ) to each row in the frequency domain.

$$H(\rho) = \tilde{P}(\rho) \cdot G(\rho) \quad (2.6)$$

Different types of  $G(\rho)$  filters (edge enhancing (ramp), edge preserving and smoothing) have been tested to optimize image quality. For the ramp filter,

$$G_{ramp}(\rho) = \begin{cases} |\rho| & |\rho| \leq \frac{1}{2\tau} \\ 0 & otherwise \end{cases} \quad (2.7)$$

The other filters generally have reduced intensity at high frequency compared to the ramp filter. They are used to reduce noise in the reconstruction.

11. Compute the inverse Fourier transform of  $H(\rho)$ .

$$\tilde{p}^F(a_{x_f, y_f, z_f, \theta}) = F^{-1}(H(\rho)) \quad (2.8)$$

12. Distance weighting (DW) applied in Eq. (2.10). DW accounts for the reduction in intensity of the x-ray beam away from the source. Hence, it is independent of the y-coordinate of the voxel and only depends on the distance between the source and the reconstructed voxel projected onto the central ray as

$$DW = \frac{D^2}{U(x_f, z_f, \theta)^2} \quad (2.9)$$

with  $U(x_f, z_f, \theta) = x_f \sin\theta + z_f \cos\theta - D$

13. Backprojection of  $\tilde{p}^F(a_{x_f, y_f, z_f, \theta})$  to every voxels  $(x_f, y_f, z_f)$  in space for all projection images acquired at angles  $\theta$ .

$$\mu(x_f, y_f, z_f) = \Delta\theta \cdot \sum_{j=\theta_{min}}^{\theta_{max}} \cdot DW \cdot \tilde{p}^F(a_{x_f, y_f, z_f, \theta}) \quad (2.10)$$

where  $\Delta\theta$  represents the angular sampling of projection images.

The projection matrices  $P_{mat}(\theta)$ , obtained from geometric calibration of the system, provide a means to backproject a preprocessed and weighted value on the detector plane  $\tilde{p}^F(a_{x_f, y_f, z_f, \theta})$  to a voxel in space using  $\vec{p}_{2d}(u, v) = P_{mat}(\theta) \cdot \vec{P}_{3d}(x_f, y_f, z_f)$ . The expression  $(u, v) \leftrightarrow (a_{x_f, y_f, z_f, \theta}) \leftrightarrow (x_f, y_f, z_f)$  takes the form of a change of coordinate system (2D to 3D) and represents the backprojection task handled by the projection matrices  $P_{mat}(\theta)$ . The calibration of  $P_{mat}(\theta)$  is discussed in Sec. 2.1.3.

Equation (2.10) summarizes the clinical implementation of the FDK algorithm for MVCBCT reconstruction. The backprojection process is performed for each voxel of the reconstruction (voxel-based reconstruction) at all projection angles  $\theta$  of the acquisition.

Equation (2.11) is a more theoretical form of the FDK algorithm. The voxel-driven algorithm uses projection matrices (obtained from geometric calibration of the linac) to find the filtered, preweighted and preprocessed projection image data  $\tilde{p}(a_{x_f, y_f, z_f, \theta})$ .

$$\mu(x_f, y_f, z_f) = \underbrace{\int_{\theta_{min}}^{\theta_{max}} \frac{D^2}{U(x_f, z_f, \theta)^2} \left[ \underbrace{\tilde{p}(\cdot)}_{\text{Pre-weighting}} * \underbrace{g(\cdot)}_{\text{Filtering}} \right](a_{x_f, y_f, z_f, \theta}) d\theta}_{\text{Weighted filtered-backprojection}} \quad (2.11)$$

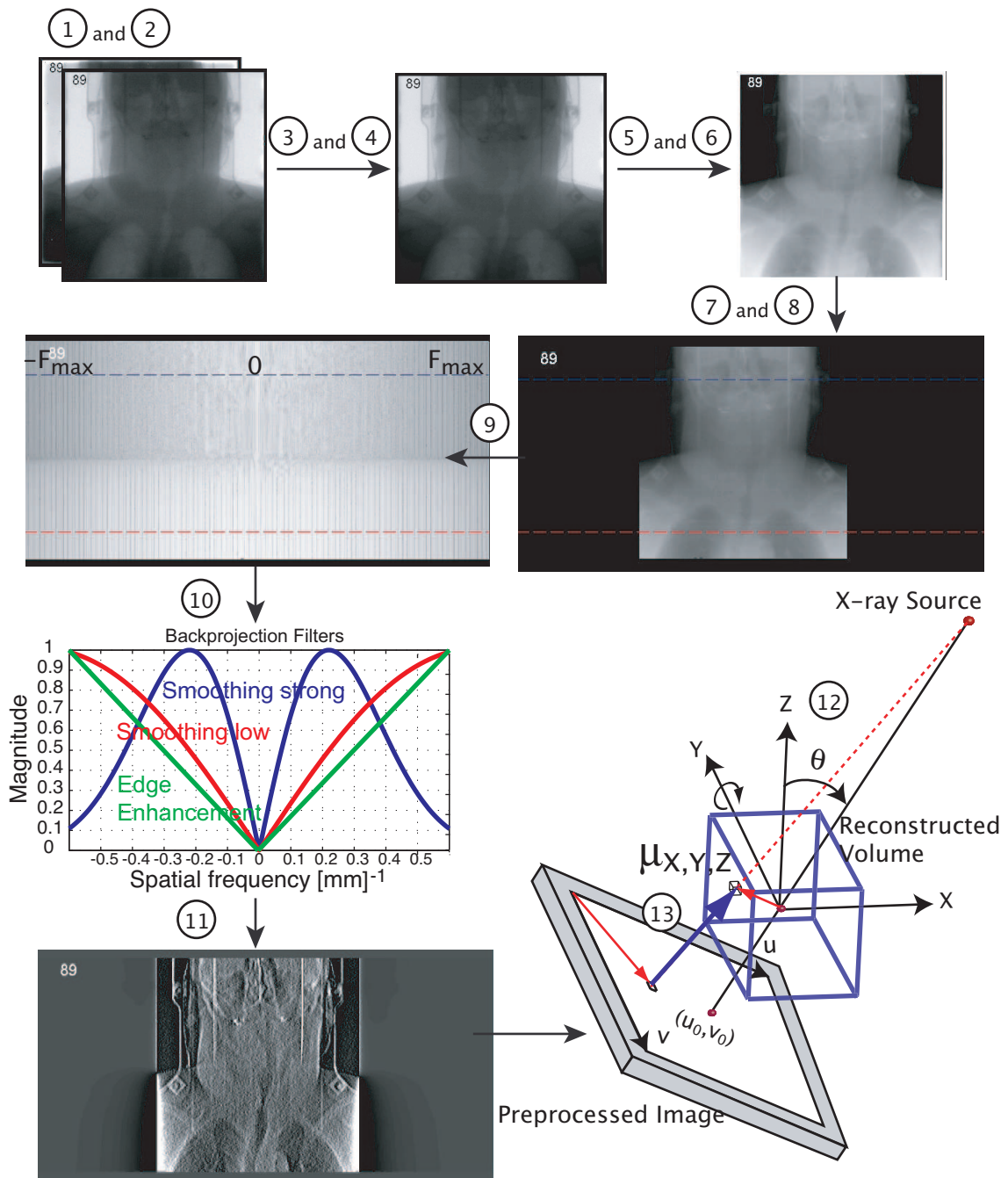


Figure 2.2: Steps for MVCBCT image reconstruction: (1) raw projection image acquisitions, (2) dark current, gain and dead pixel correction, (3) median filter, (4) projection filtering (average or diffusion), (5) log conversion, (6) preweighting, (7) zero-padding and binning, (8) extrapolation, (9) to (11) backprojection filtering, (12) distance weighting and (13) backprojection.

The algorithm produces a reconstruction volume containing a large number of voxels representing the attenuation coefficient  $\mu_{X,Y,Z}$ , a physical attenuation property of object being imaged for a given x-ray beam energy spectrum. The reconstructed intensity of each voxel is therefore proportional to the linear attenuation coefficient of the physical material within that voxel.

### 2.1.3 Geometric Calibration

The backprojection step of the reconstruction algorithm presented requires a complete characterization of the relationship between any point in space and its projected positions on the detector plane at all projection angles  $\theta$ . In conventional CT, the relative source and detector positions are constant during rotation and analytical equations can be used to describe the system geometry (2D-3D relationship). The linac x-ray source and an EPID positioner, however, may lose their ideal isocentric positions as the gantry rotates due to sagging of the mechanical supports. A geometric calibration [40, 19] is performed to correct for this effect and conserve image quality. The position of the EPID must then only be reproducible for the calibration to remain geometrically accurate.

Figure 2.3 describes the principle of the geometric calibration procedure. Mathematically, the backprojection step is represented by  $\vec{P}_{2d} = P_{mat}(\theta) \cdot \vec{P}_{3d}$ . The goal of the geometric calibration is to calculate the projection matrices  $P_{mat}(\theta)$  which define where a point in space  $\vec{P}_{3d}$  is projected on the flat panel detector  $\vec{P}_{2d}$  for all projection

angles  $\theta$  of the acquisition.

The projection matrices  $P_{mat}(\theta)$  are a set 12-element matrices for each angle  $\theta$  of the acquisition and that characterizes the system rotating geometry. The geometric calibration procedure consists of calculating  $P_{mat}(\theta)$  by acquiring 2D projection images of a cylindrical phantom (also displayed in Fig. 4.1, left) containing 108 tungsten beads placed at precise locations in space  $(x_f, y_f, z_f)$ . The position of each bead in space is known by design of the phantom. The beads exact position on the detector plane  $(u, v)$  are then automatically identified (using a bead detection software developed by Siemens OCS) on the projection images of a 60 MU MVCBCT acquisition. This gives for each projection a large number of the following linear equation.

$$\begin{bmatrix} \overbrace{u}^{2D} \\ v \\ 1 \end{bmatrix} = [P_{mat}(\theta)]_{3 \times 4} \begin{bmatrix} \overbrace{x_f}^{3D} \\ y_f \\ z_f \\ 1 \end{bmatrix} \quad (2.12)$$

The geometric calibration problem is therefore over-determined. The 12 elements of  $P_{mat}(\theta)$  are calculated (by minimizing the total error of the linear equations in a least-square sense) for all projection angles  $\theta$ . Additional post-processing is currently performed on the projection matrices to compensate for possible error in positioning the calibration phantom at the treatment isocenter. The projection matrices are unique for a MVCBCT system, they play an important role in assuring the absolute positioning accuracy of the MVCBCT reconstruction volume in the treatment field.

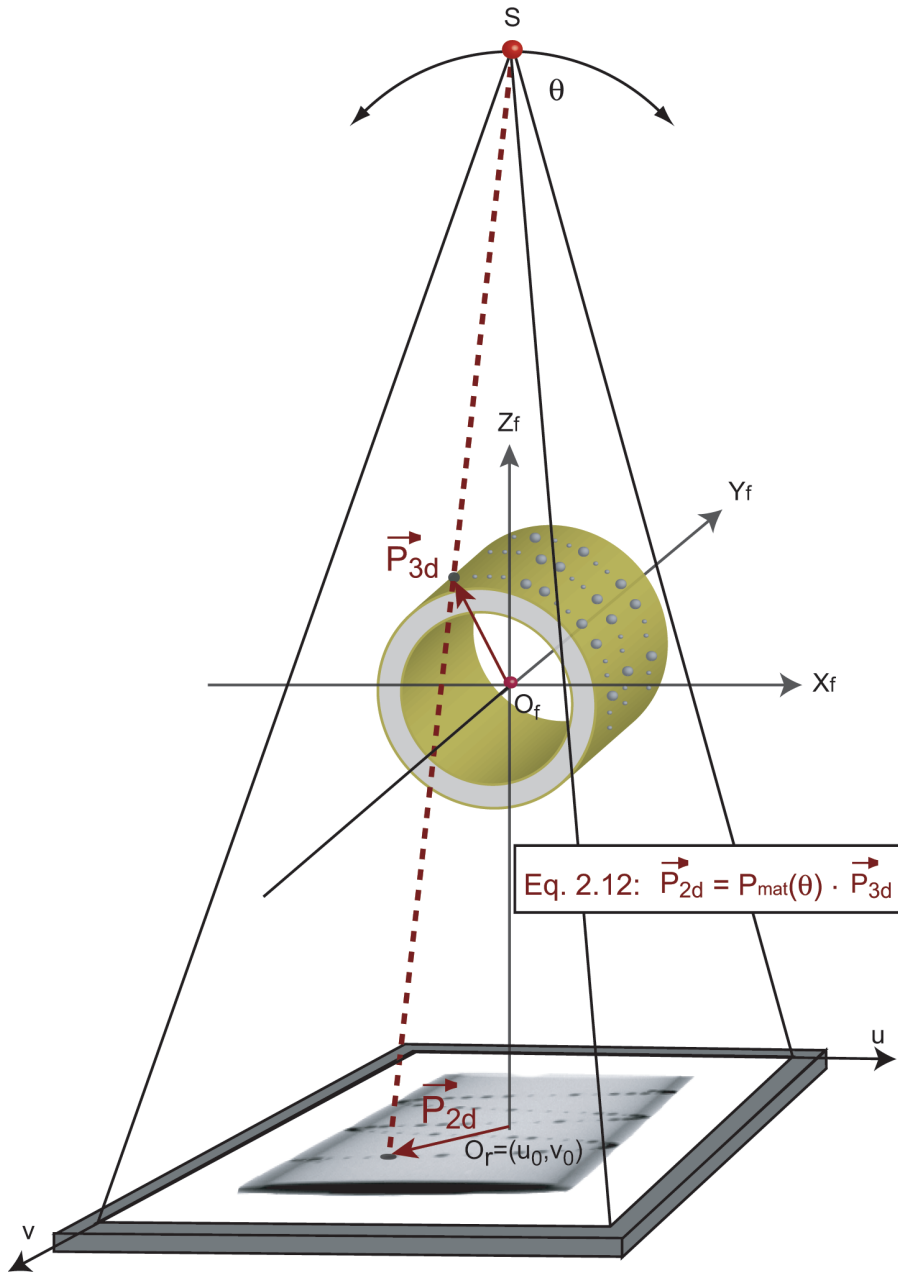


Figure 2.3: The geometric calibration procedure consists of acquiring projection images of a calibration phantom (containing 108 tungsten beads) for each angle of the reconstruction to define where a point in space  $\vec{P}_{3d}$  is projected on the flat panel detector plane  $\vec{P}_{2d}$  using Eq. (2.12). The positions  $\vec{P}_{3d}$  for the beads are known by design of the phantom while  $\vec{P}_{2d}$  are automatically detected on the projection images. The projection matrices  $P_{mat}(\theta)$  are obtained from the calibration procedure. See photo of the calibration phantom in Fig. 4.1.

## 2.2 Treatment Beam Modified for Imaging

A specific MVCBCT dose delivery mode was designed to minimize the patient dose delivered during imaging. Figure 2.4 compares the electron current of the beam before the target for the treatment and MVCBCT imaging dose delivery modes. For normal treatment with photons, dose rates of 50 MU/min and 300 MU/min are available. The electron current (converted to an equivalent voltage) per pulse for the two treatment modes are kept equal. Only the pulse rate frequency (PRF) is increased to obtain the higher dose rate.

For MVCBCT, the electron beam current is reduced by a factor of roughly 7 with respect to the current used to generate the treatment beam in order to deliver a small fraction of MU per degree and to obtain a faster beam formation. The PRF had therefore to be increased (by a factor of roughly 7) in order to conserve a dose rate of 50 MU/min for imaging. It is important to note that the dose rate of 50 MU/min is only maintained for MVCBCT imaging when the beam is on. The alternating beam-on and beam-off in rotation greatly reduces the actual dose rate during MVCBCT imaging. Calibration is then necessary to determinate the number of electron pulses required to obtain a total acquisition dose for MVCBCT imaging. Calibration is performed at several exposure (2, 3, 5, 8, 10, 20, 40 and 60 MU) and the number of pulses is recorded in a dose scale factor (CBCT page in the control console). Interpolation of the dose scale factors is used in the clinic for performing acquisitions at different exposure. In Fig. 2.4, the number of pulses per frame for 3 and 10 MU



MVCBCT acquisitions are roughly 4-5 and 14-16 respectively. Based on the MU per frame and the fixed dose rate of 50 MU/min the system defines the time period for one frame. For 3 and 10 MU MVCBCT, the total time required to complete one projection are roughly 280 and 366 ms. The gantry speed is then adjusted based on the amount of time required for a frame delivery. The angular velocity of the gantry is therefore faster for lower exposure (see Sec. 3.1 for acquisition time performance). The maximum angular velocity of the system during acquisition is limited to 1 rotation per minute for patient safety. Finally, the system uses servo capabilities to adjust slightly the number of electron pulses per frame during the acquisition to assure that both the desired dose and the total acquisition arc are achieved. The following section discusses how flat panel detector read-out is synchronized with the x-ray beam output in MVCBCT dose delivery mode.

## 2.3 Flat Panel Detector

Flat panel detectors as EPID technology have gained popularity in radiation oncology over the past years owing to their light weight, large area, compact size, better image quality compared to old video EPID system, linearity with dose, great stability over time and their tolerance to receive high integrated levels of radiation dose. The purpose of the next section is merely to describe the first detector used clinically for MVCBCT and to review the principle of x-ray detection. A complete description of modern flat panel detectors and internal components is available in the literature [41].

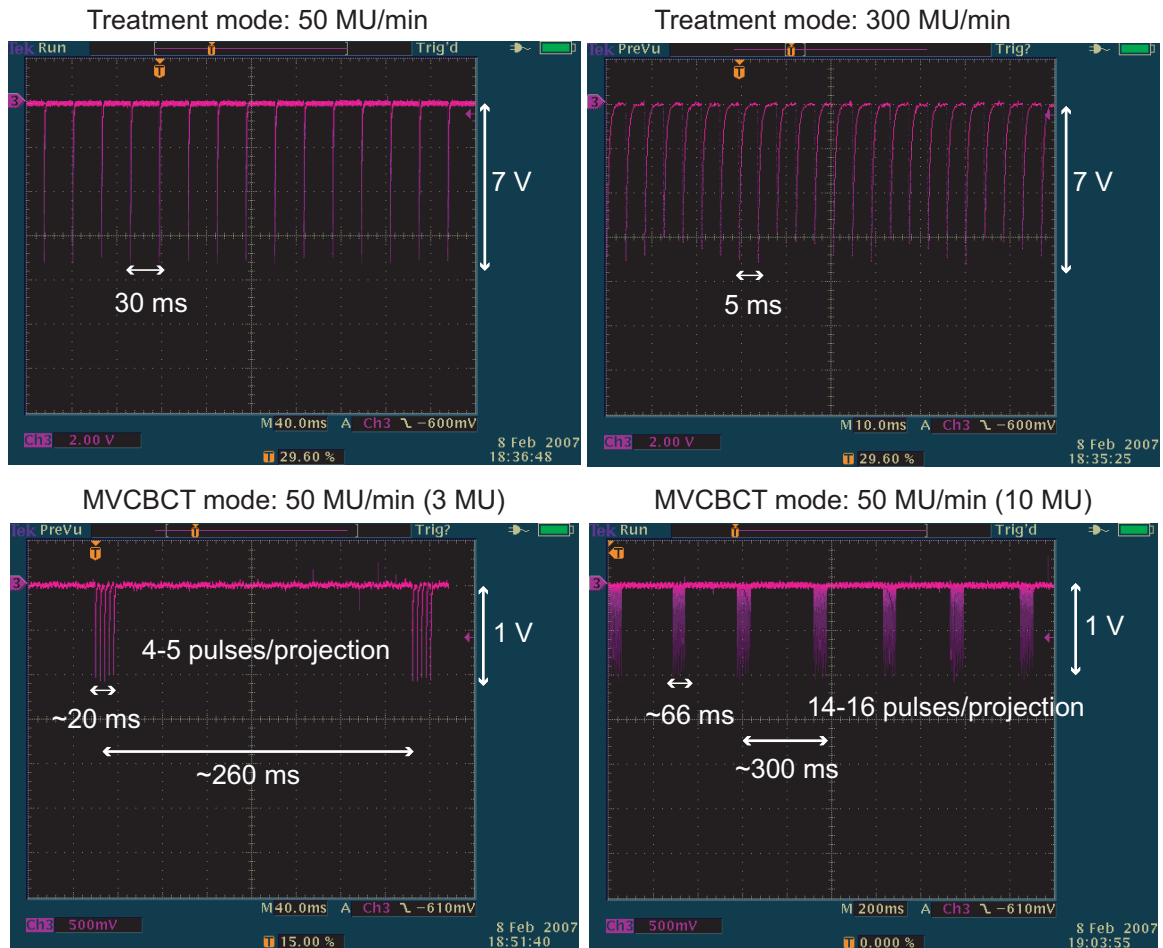


Figure 2.4: Beam electron pulses for treatment and MVCBCT dose delivery modes. A dose rate of 50MU/min is used for MVCBCT only when the beam is on. The gantry speed is adjusted to deliver the required number of electron pulses per projection in order to achieve the total dose specified in the MVCBCT protocol.

### 2.3.1 Flat Panel Design and Image Acquisition Mode

This paragraph simultaneously presents the flat panel design (Fig. 2.5) and describes how high-energy x-rays are converted to a 2D digital signal (a raw projection). The current amorphous silicon flat panel detector used for MVCBCT has four main layers: converter (copper plate), scintillator (phosphor screen), detector (thin-film transistor (TFT) and photodiodes) and a glass substrate. The amorphous silicon appellation refers to the material structure of the detector layer. First, a fraction of the incident x-ray interacts with the converter which generates electrons from Compton and photoelectric interactions. The scintillator absorbs energy from electrons and a small portion of the incident photons to emit visible light (predominantly in the green portion of the electromagnetic spectrum). This visible light is then captured by light sensing and charge integrating photodiode switching TFT. The flat panel detectors chosen for MVCBCT contains a large number ( $1024 \times 1024$ ) of small ( $0.4 \times 0.4 \text{ mm}^2$ ) detector elements (pixels) capable of storing charge in response to x-ray exposure. During exposure, charge is built-up in each detector element. After exposure, the charge is read out using electronics as illustrated in Fig. 2.5b. The readout logic reduces the total number of electrical connection needed. By closing the gate of a given row (illustrated in red), the multiplexer is capable of reading the amplified charge of a detector element (illustrated in dark blue) along the row. The charge is finally converted to digital signal (16 bits) with an analog-to-digital (A/D) converter. Rows are read sequentially following this method. Modern flat panel detector have fast

electronics capable of acquiring more than 7 frames per second. For MV applications, most of the electronics are located at the side of the flat panel so that they are not placed in the path of the radiation beam and the most active area of the detector.

A total of 3 flat panel designs were tested over the past 4-5 years. The main difference between the panels was the scintillator type which provided different levels of light output and different scintillator thicknesses which affects the detector sensitivity. The decision on which detector to use was purely based on availability, cost, and image quality. Other detectors optimized for MV imaging are still being actively studied [42].

Because it is nearly impossible to manufacture an entire panel with identical detector element properties, corrections for flat panel defects need to be applied prior to image display or reconstruction. These corrections or calibrations are discussed in the next section.

Figure 2.6 describes the image acquisition sequence and the synchronization of the detector with the beam-on signal. Prior to any movement of the system, the detector is refreshed (emptied) to remove any unwanted signal. The detector then integrates the charge for the full duration of the beam-on signal (a projection). The image is digitized immediately after the beam-on signal of the linac. The same applies to other projections except that the panel is only refreshed once prior to beam-on. Images are automatically corrected (corrections discussed in the next section) and transferred to the computer workstation for MVCBCT image reconstruction. For time efficiency,

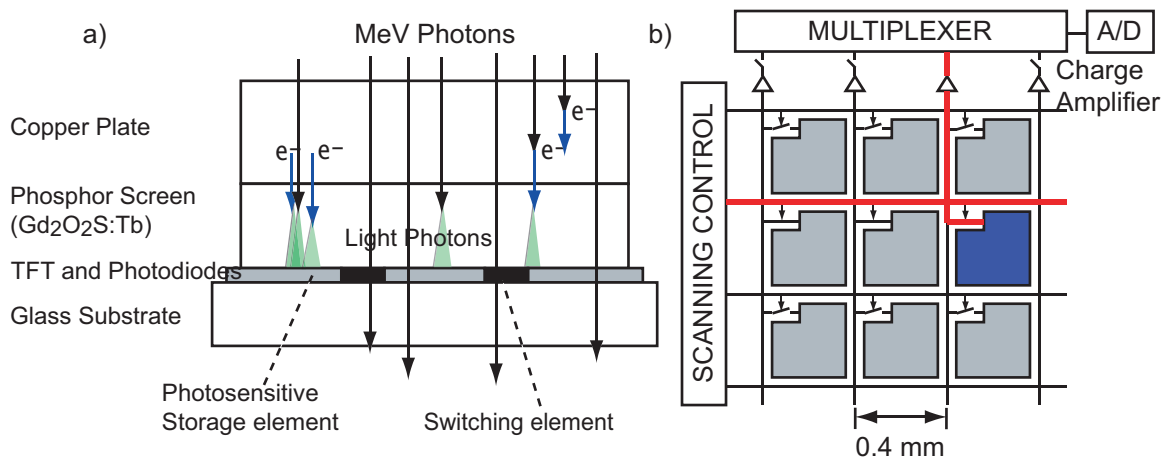


Figure 2.5: Flat panel detector used for MVBCT imaging. a) Describes the detector layers and the process by which MeV photons create a digital projection image. A small fraction of the incident MeV photons are converted to electrons. Some of the incident photons and the newly produce electrons produce visible light which can be capture by TFT and photodiodes as charges on a capacitor. b) Shows how specific electronics (scanning control and multiplexer) can be used to read the charge across each capacitor (pixel). The specific electronic components reduce the number of connections required for complete panel readout and digitization. The dark blue pixel is currently being read by closing the circuit along the appropriate row and column.

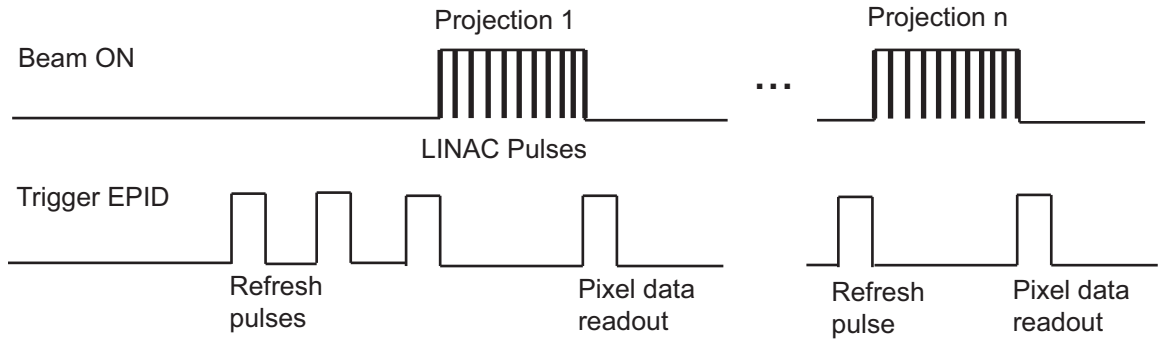


Figure 2.6: Synchronization of the flat panel detector read-out with the x-ray beam output for MVCBCT imaging. After each beam-on signal, and the delivery of all linac pulses, the panel transfers the image pixel data to the computer workstation for image reconstruction.

the voxel-based reconstruction of MVCBCT was designed to start as soon as one projection image is acquired.

### 2.3.2 Flat Panel Corrections

Flat panel images need to be corrected for dark current, gain and dead pixels. Calibration of these panel defects is performed with the computer workstation illustrated in Fig. 2.7.

Dark current primarily is generated by electrical noise that accumulates on the detector elements even in the absence of x-ray exposure. For our system, calibration of dark current is automatically performed for a series of detector integration time. This automatic calibration is performed when the radiation is turned off. The calibrated dark current image is then simply subtracted to the raw flat panel image.

A gain correction is required to account for differences in pixel sensitivities. For

large flat panel detector, pixels are generally manufactured in sections. Differences in section sensitivities are inevitable. This is easily corrected with a flood field image (air image) in which the detector is exposed to an unattenuated beam. For MVCBCT, gain calibration has to be acquired at a dose per projection similar to what is used during image acquisition in order to capture the behavior of the flat panel detector (sensitivities) at low exposure. Therefore, the gain is obtained in MVCBCT dose delivery mode over an arc acquisition (same arc as for MVCBCT imaging) since it is currently the only dose delivery mode allowing exposure of less than 1 MU per projection. Generally, the most typical MVCBCT exposure used in the clinic is also used for gain calibration. Section 3.5.1 discusses the impact of this type of gain calibration on the uniformity of MVCBCT images.

Dead pixels refer to detector elements that are either insensitive or too sensitive for a given x-ray exposure. This defect is the natural result of difficult panel fabrication and imperfection in the materials. To correct for this, an average image is acquired for a large x-ray exposure (200 MU). Pixels with signal outside a statistical range ( $n$  standard deviations from the mean) are automatically classified by the software as dead pixels. An additional manual calibration is generally also required. A portal image of 1 MU is acquired and the user can calibrate/remove pixels or lines of defective pixels. Finally, a median filter of size  $3 \times 3$  is applied to every identified dead pixel. This correction generally works well for portal imaging. For MVCBCT, however, the small dose delivered per projection causes the occurrence of transient dead pixels. An

additional median filter ( $3 \times 3$ ) is currently applied before reconstruction to correct for these unstable pixels.

## 2.4 Major System Components

The major components of the MVCBCT system are displayed in Fig. 2.7. From outside the treatment room, only two computers and one monitor for the video camera are necessary for performing 3D imaging and treatment. The video camera is required to assure the safety of the patient inside the treatment room. The computer workstation (Syngo™, Siemens Oncology Care Solutions, Concord, CA) plays an important role for imaging since it is connected to both the control console of the linac and the EPID, as well as the network of the entire department of radiation oncology. Nearly all the calibrations and clinical tasks related to MVCBCT including image reconstruction and patient set-up are performed with the computer workstation.

In addition to the computer workstation and the control console of the linac, most of the results presented in the dissertation were produced with a research workstation. The system presented in Fig. 2.7 was only used to acquire raw projection images of the MVCBCT acquisition, whereas the research workstation was used to perform image reconstruction using different settings, apply corrections, perform data analysis, and connect to the department network. Image processing scripts and analysis tools were developed using Matlab (The Mathworks Inc., Natick, MA) and MeVisLab (MeVis Research GmbH, Bremen, Germany). Matlab is a powerful tool to quickly inspect



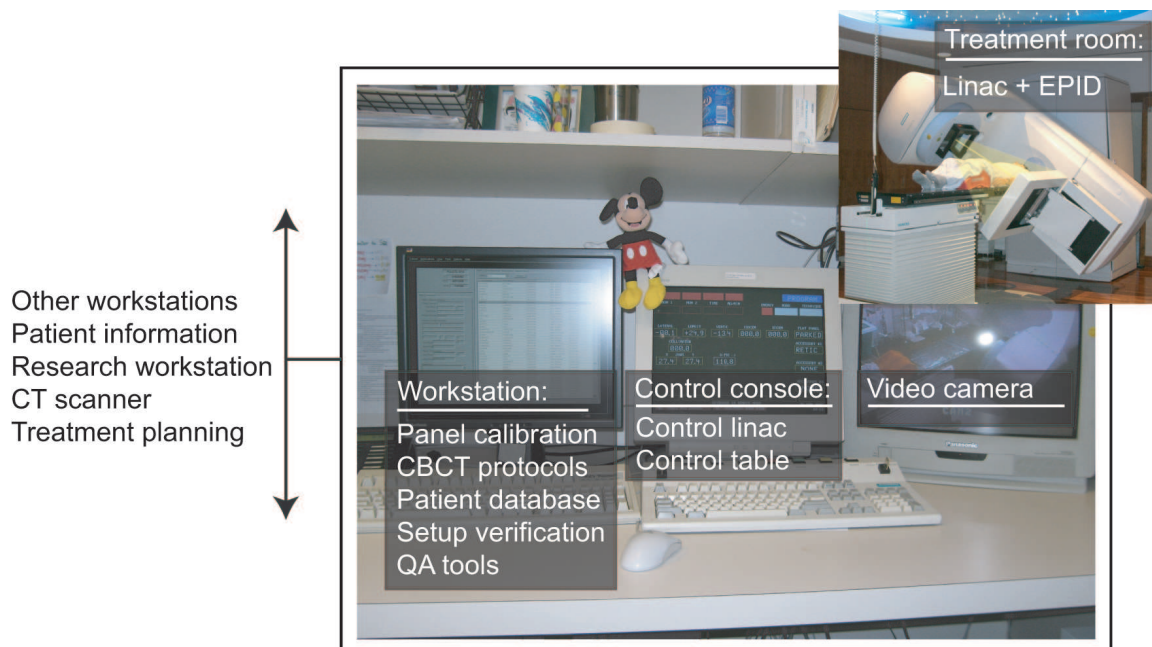


Figure 2.7: Major system components for MVCBCT imaging. Nearly all the calibrations and clinical tasks related to MVCBCT are performed with the computer workstation. A separate research workstation was used to produce most of the results (offline reconstruction, image processing and analysis) presented in the dissertation.

any type of medical images and manipulate file header information. Scripts were written to read MVCBCT images and automatically extract statistics. Scripts were also written to compare dose distributions. MeVisLab is a free software (available online) with robust and efficient scripts to perform specific task on medical images. The software was used to apply advanced filters (e.g. diffusion filtering discussed in the next chapter) on projection images and to resample the MVCBCT reconstruction cube to different slice thickness and pixel size. MeVisLab has also excellent displaying tools which were used to produce snapshots of reconstruction images for meetings and publications.

## 2.5 Image Acquisition Procedure

Figure 2.7 depicts the acquisition of raw projection images and the image reconstruction for the MVCBCT system. A MVCBCT acquisition is similar to an arc treatment in which x-ray exposure is delivered as the treatment unit rotates around the patient. An image acquisition field is created in the computer workstation using one of the predefined MVCBCT protocols, which contain the information needed by the system to perform the acquisition (field size, start and end angle, total exposure, flat panel distance, etc.). As mentioned before, some parameters such as the start ( $270^\circ$ ) and end ( $110^\circ$ ) angle, the number of projections (200) and the flat panel distance (145 cm) are set, while others, such as the total exposure, the field size, the reconstruction size and the image-processing filters can be modified. The start and end angle of the acquisition were chosen to meet the minimum arc required for "exact" CT reconstruction while avoiding a gantry position that would bring the detector above the patient. In theory the acquisition could have started at any angle. The source detector distance was chosen to allow the acquisition to be performed safely on patients while maximizing the reconstructed volume. The maximum field size allowed ( $27.4 \times 27.4 \text{ cm}^2$ ) was chosen to protect sensitive components of the detector. The primary collimator (Y jaws) in the head of the linac (Fig. 2.8, 1g) can be moved independently to reduce the amount of tissue being irradiated in the longitudinal direction. The craniocaudal imaging length (CCIL) can be specified to have a value between  $\sim 5$  and 27 cm located anywhere within a 27 cm window cen-

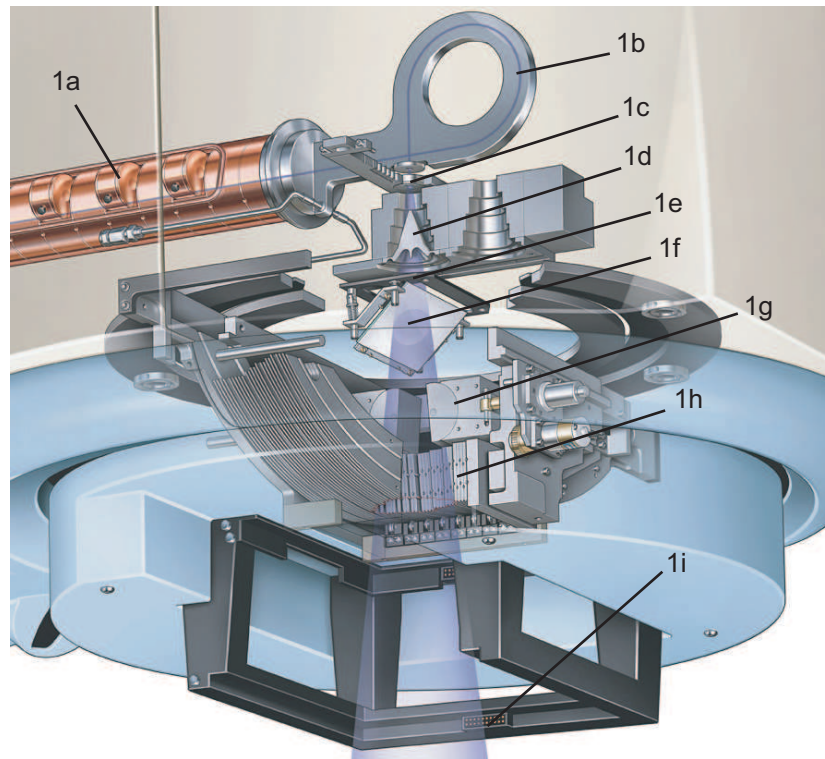


Figure 2.8: Key components in the linac gantry head include the waveguide (1a), the bending magnet (1b), the tungsten target (1c), the flattening filter (1d), the monitor chamber or dosimetry system (1e), the light mirror (1f), the upper Y-jaw (1g), the multileaf collimator (1h) and the accessory tray (1i). Image courtesy of Kevin Hulsey Illustration, Inc.

tered at the isocenter. Next, the MVCBCT field parameters are directly transferred to the control console of the linac to place the system in position for imaging. The linac gantry then rotates in a continuous 200-degree arc ( $270^\circ$  to  $110^\circ$ , clockwise) while acquiring 200 low-exposure ( $< 0.25$  MU) portal images, with one image per  $1^\circ$  increment. For each projection image, the exposure is measured by the dosimetry system (Fig. 2.8, 1e) and recorded in the header of the DICOM file containing the 200 raw projections. Section 2.1 describes the role of the exposure per projection of the 3D reconstruction. The duration of the acquisition procedure increases with

the total exposure specified. For a typical 5 MU, the acquisition lasts approximately 45 seconds. The image reconstruction starts immediately after the acquisition of the first portal image, with a typical  $256 \times 256 \times 274$  voxels completed in 110 seconds. The reconstructed MVCBCT and the raw projection images are saved in the patient database of the computer workstation as DICOM images. Finally, the MVCBCT images are automatically loaded in a 3D alignment application along with its reference CT data. The 3D registration process and couch adjustment also is performed as discussed in Chap. 6.

## 2.6 Technical Summary of MVCBCT

Table 2.1 summarizes the main technical characteristics of MVCBCT imaging presented throughout the chapter. Details of the system are given for the acquisition geometry, the x-ray beam, the flat panel imager, the acquisition procedure and the reconstruction parameters. The bold font specifies the typical values used in clinic because, in our experience, they provide clinically usefull image quality within the time constraint of online positioning.

Table 2.1: Technical characteristics of MVCBCT imaging.

MVCBCT Characteristics	Value
<b>Acquisition Geometry</b>	
Source-axis-distance ( $S_{AD}$ )	100.0 cm
Source-imager-distance ( $S_{ID}$ )	145.0 cm
Cone Angle	7.8°
Projection Field Size	27.4×27.4 cm <sup>2</sup>
Maximum field of view (FOV)	27.0 cm
Craniocaudal length	5 to <b>27.4</b> cm (independent Y jaws)
<b>X-Ray Beam</b>	
Beam energy	6 MeV
Added filtration	Flattening filter
Beam output	1 MU <sub>MVCBCT</sub> = 1 MU <sub>treatment</sub>
Available exposure	2 to 60 MU
<b>Flat Panel Imager</b>	
Detection type	Indirect
Designation	RID 1640 AG9-ES
Array format	1024×1024 pixels
Converter	1mm Copper plate
Scintillator name	Kodak Lanex Fast
Scintillator material	133 mg/cm <sup>2</sup> Gd <sub>2</sub> O <sub>2</sub> S:Tb
Pixel pitch	0.4 μm
Area	40.96 × 40.96 cm <sup>2</sup>
Nominal frame rate	0.16 frame per second
Maximum frame rate	7 frame per second
Readout time	140 ms
<b>Acquisition Procedure</b>	
Number of projections	200
Angular increment	1.0°
Total rotation angle	200.0°
Maximum angular rotation rate	1 rotation per min
<b>Reconstruction Parameters</b>	
Reconstruction matrix size	(128, <b>256</b> , 512) <sup>3</sup>
Voxel size	(2, <b>1</b> , 0.5 mm) <sup>3</sup>
Slice thickness	<b>1</b> , 3, 5 mm
Backprojection filters	Edge enhancing, Edge preserving, <b>Smoothing</b>
Projection binning	1 or <b>2</b>
Pre-processing filter	Median 3×3, Avg. 5×5
Uniformity correction filter	Head and neck, Pelvis

## Chapter 3

# System Performance

The potential clinical applications of MVCBCT directly depend on its physical performance. In this chapter, we therefore discuss how we evaluated the physical performance of MVCBCT and describe how we optimized system and reconstruction settings to achieve the best possible image quality.

Two MVCBCT systems (linac 1: Oncor<sup>TM</sup> and linac 2: Primus<sup>TM</sup>, Siemens Oncology Care Systems, Concord, CA) installed in our clinic were compared. Even though linac 1 is a more recent generation of treatment machine than linac 2, the imaging system components are identical and therefore the physical performances are expected to be similar. Both systems were tuned for treatment and imaging following the same procedure. The physical characterization of MVCBCT presented in the following sections contains results on the time required for imaging and reconstruction, the shape and size of the field of view, the geometric stability, the absolute positioning

Table 3.1: MVCBCT imaging protocol baseline. Abbreviations of protocol components are used throughout the chapter.

Protocol component	Abbreviation	Value
X-ray exposure	expo	9 MU
Projection filtering	projfilt	Avg. $5 \times 5$
Binning	bin	2
Backprojection filter	bckprojfilt	Smoothing
Number of voxels	nvox	$256^3$
Slice thickness	slicethick	3 mm
Craniocaudal imaging length	CCIL	27.4 cm
Normalization factor	$I_{0,\theta}$	$I_{0perMU} \cdot MU_\theta$

accuracy, the image calibration stability, the image quality and the dose delivered to patient.

To avoid specific limitations with the initial MVCBCT clinical product, a separate research platform (using the identical reconstruction algorithm as the product) was used to rapidly test different reconstruction settings and apply filters and corrections developed in-house. Most of the results presented in the dissertation were obtained by performing the image acquisition with the product but by reconstructing and analyzing the MVCBCT images offline with the research platform (see Fig. 2.7).

Different acquisition and reconstruction settings (projection filters, number of voxels, backprojection filter) are compared in the next sections. The reader can review specific terms related to the reconstruction of MVCBCT images such as binning and diffusion filter (Sec. 2.1). Table 3.1 summarizes the baseline MVCBCT imaging protocol components used throughout the chapter. Imaging protocol components were varied to compare the physical performance of the new protocol versus their baseline values. Protocol component abbreviations in Table 3.1 are used throughout the

chapter to save space and avoid repetition.

### 3.1 Duration of Acquisition and Reconstruction

The development of in-room image-guidance techniques must satisfy strict time constraints faced in radiation oncology. Longer time on the treatment table translates into higher probability of reduced treatment accuracy due to patient discomfort [5], and decreased patient through-put. Table 3.2 reports the time required for different acquisition and reconstruction settings.

As expected from the description in Sec. 2.2, Table 3.2 shows that the MVCBCT acquisition is performed faster for lower levels of exposure (MU). MVCBCT images are reconstructed in less than 2 minutes for a volume of  $256^3$  voxels. The time required for reconstruction is fairly constant with exposure since it is mostly limited by the speed performance of the computer workstation. Reconstruction time increases with the number of voxels simply because the reconstruction algorithm loops on the voxels (voxel-based reconstruction). The application of diffusion filtering (noise-reduction filter introduced in Sec. 2.1.2) on the projection images currently increases the time of reconstruction by a factor of 2-3. Specific code development for diffusion filtering as part of the MVCBCT system combined with faster computing may allow on-line clinical application with this projection filter.



Table 3.2: Time required for image acquisition and reconstruction for different imaging protocol. Only the specified protocol component is changed compared to the baseline (Table 3.1).

Modified Imaging Protocol Component			Acquisition Time (s)	Reconstruction Time (s)
expo (MU)	nvox	projfilt		
3	256 <sup>3</sup>	Avg. 5×5	28	118
10	256 <sup>3</sup>	Avg. 5×5	34	119
20	256 <sup>3</sup>	Avg. 5×5	43	116
60	256 <sup>3</sup>	Avg. 5×5	82	117
10	128 <sup>3</sup>	Avg. 5×5	43	100
10	512 <sup>3</sup>	Avg. 5×5	43	344
10	256 <sup>3</sup>	diffusion	43	322

## 3.2 Field of View and Clearance

As a simple definition, only pixels which are illuminated from all projection angles are reconstructed correctly, and they constitute the field of view (FOV). MVCBCT imaging with a large FOV is of particular interest for clinical applications discussed in the dissertation since radiation oncology can demand imaging and treatment across wide areas of the body, in the periphery of the body, or for large patients.

For conventional CT (Fig. 1.2), the cross-sectional FOV forms a circle with a diameter defined by the detector size and the distance between the source and the detector. The longitudinal FOV, that is, the length of the reconstruction volume along the craniocaudal direction, is solely based on the table movement span and can be very large. For MVCBCT however, the FOV dimensions only depends on the detector size, the source-axis-distance (SAD) and the source-imager-distance (SID) (illustrated in Fig. 2.1) since there is no table movement. As illustrated in Fig. 3.1

the shape of the FOV is defined by rotating the source and detector around  $Y_f$ , with the intersection of the divergence of square beams resulting in a cylindrical FOV with two small cones to the opposite ends of the rotational axis. While the FOV of a cross-section in MVCBCT reconstruction is set by the secondary collimator (X-jaw, MLC), the craniocaudal imaging length is based on the primary collimator opening (Y-jaw) during image acquisition. The Y-jaw opening is defined by the creation of the MVCBCT imaging protocol. For the flat panel designed for MV applications, the sensitive electronic components to radiation are generally placed on the periphery of the active area. For this reason, despite a detector area of  $(40.96 \times 40.96 \text{ cm}^2)$ , the current maximum field size allowed for MVCBCT imaging at the detector plane is  $39.7 \times 39.7 \text{ cm}^2$  to help protect the detector electronics from radiation damage. Given the set source-axis-distance and source-imager-distance of 100 and 145 cm respectively, this maximum field size corresponds to  $27.4 \times 27.4 \text{ cm}^2$  at isocenter. There is also an additional small truncation of the projection images to avoid possible reconstruction problem caused by the progressive drop in signal intensity at the field penumbra. Therefore, the current maximum FOV for MVCBCT is approximately  $27 \times 27 \text{ cm}^2$  in the axial plane and a little less than the craniocaudal imaging length (Y-jaw opening) in the longitudinal direction.

We have found that such a FOV is suitable for most clinical cases. Collision issue of the detector with the treatment table or even the patients could occur for patients having a treatment isocenter away from the anatomical mid-planes (lung or breast

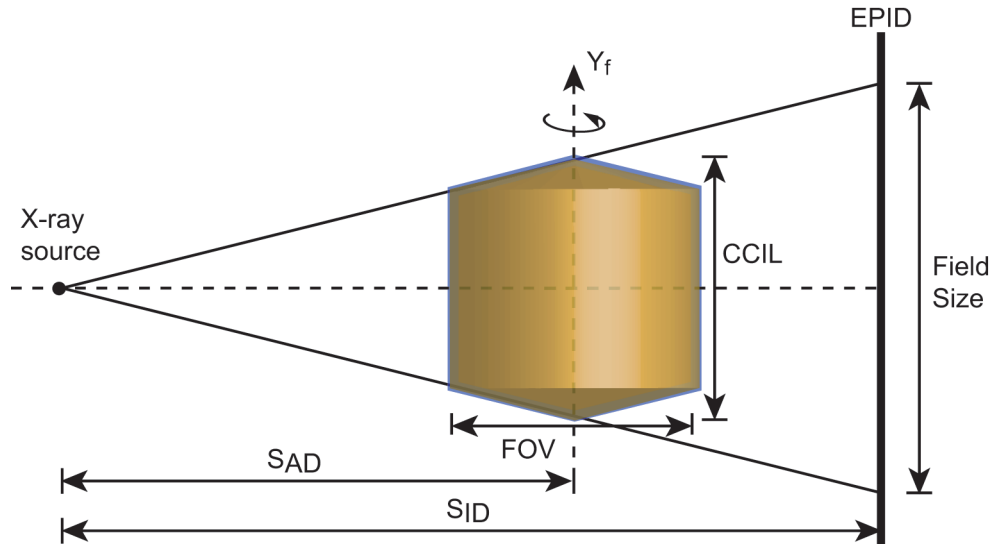


Figure 3.1: Field of view (FOV) for MVCBCT imaging. The source-axis-distance and source-imager-distance are denoted by  $SAD$  and  $SID$  respectively. For the current system design, the maximum craniocaudal imaging length (CILL) and transverse FOV are in the order of 27 cm and  $27 \times 27 \text{ cm}^2$  respectively.

treatment). Applying a voluntary shift to center the patient in the treatment field prior to imaging may be used to avoid this limitation while still providing an accurate set-up using image-guided radiation therapy techniques (IGRT) discussed in Part II of the dissertation.

Finally, the current MVCBCT FOV is mostly limited by the size of the detector. Increasing the  $S_{AD}$  would increase the FOV while increasing the  $S_{ID}$  would decrease the FOV. It has been demonstrated in the literature that shifting the flat panel position in the lateral direction (along the U axis Fig. 2.1) combined with a full rotation of raw projection sampling can increase the transverse FOV of a cross-section by approximately 15 cm [43]. This approach relies on the concept that opposing projection images (e.g.  $0^\circ$  and  $180^\circ$ ) can complement each other since by covering

different sides of the patient anatomy. The increase in transverse FOV provided by this image acquisition and reconstruction approach should improve the image quality due to reduced truncation of the patient anatomy and will open the door to new opportunities of anatomy verification and dose calculation (Chap. 8).

### 3.3 Geometric Stability and Absolute Positioning

The geometric calibration presented in Sec. 2.1.3 plays an important role for absolute positioning and image quality. Simulations performed by our group indicate that lateral deviations from the calibration geometry as small as 2 mm cause streaking artifact around high-contrast regions while longitudinal deviations create shifts in the reconstruction volume, potentially introducing set-up errors [44].

First, the validity of the geometric calibration was evaluated by reconstructing a gold seed placed at isocenter with the room lasers. As expected, the reconstructed position of the seed was located within 1 mm to the central voxel of the reconstruction. Gold seeds are now used as a rapid quality assurance checks for absolute positioning (Sec. 4.2).

Second, the geometric stability of the system over time was investigated by performing then analyzing geometric calibration measurements on our 2 systems over a period of several months. Projection of the isocenter  $\vec{P}_{3d} = (X_0, Y_0, Z_0) = (0, 0, 0)$  to the flat panel plane can be done using the projection matrices in Eq. (2.12) which are obtained during geometric calibration. Figure 3.2 presents the mean projected

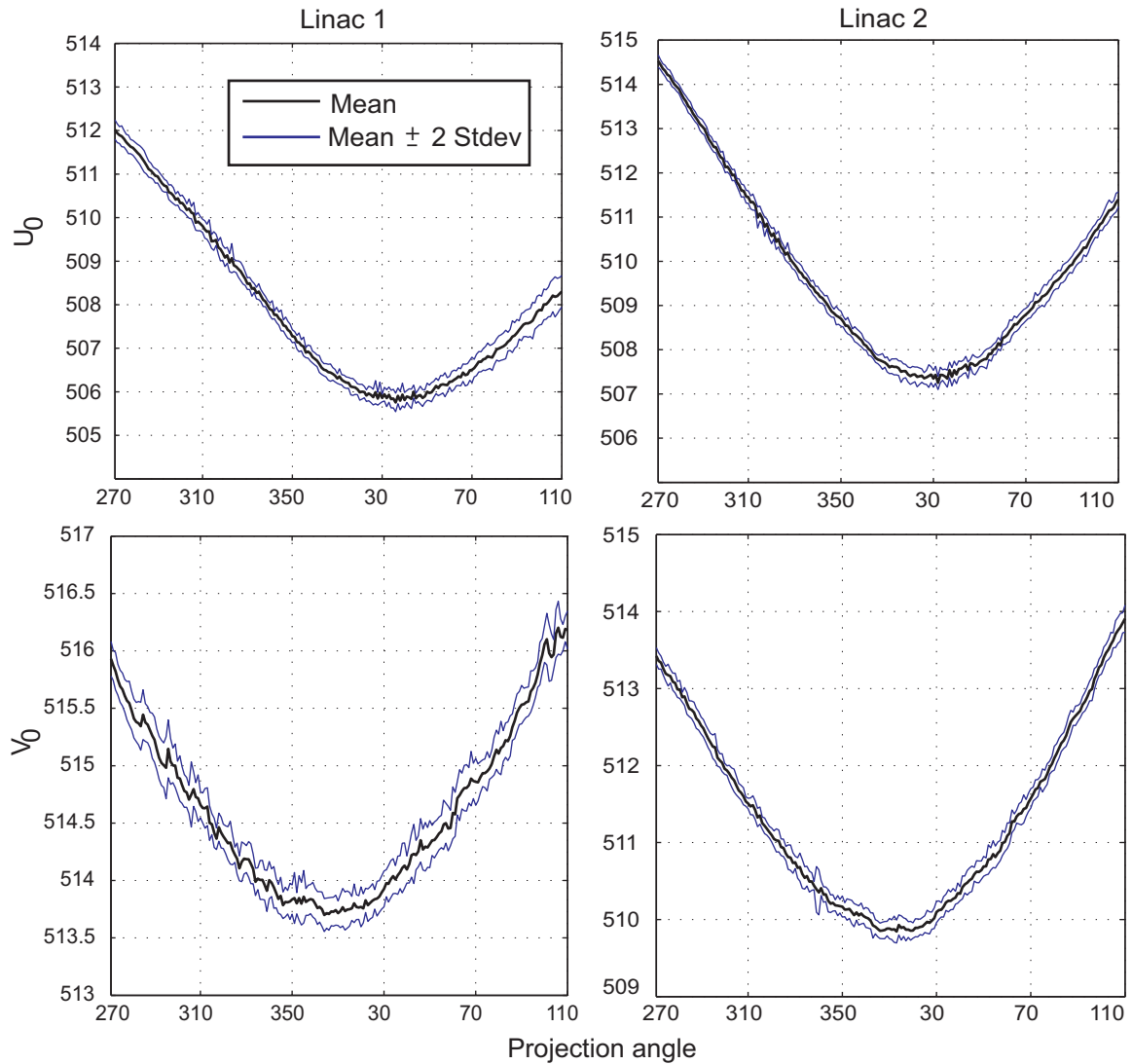


Figure 3.2: Stability of the MVCBCT system geometry in rotation. Projection of the treatment isocenter  $(X_0, Y_0, Z_0)$  on the flat panel  $(U_0, V_0)$  using projection matrices routinely acquired over a period of 8 months. The mean and standard deviation of  $(U_0, V_0)$  are plotted for linac 1 and linac 2.

position of the isocenter  $(U_0, V_0)$  in rotation over a period of 8 months for linac 1 and linac 2. The standard deviation of the projected isocenter position in rotation over time is also displayed. During rotation, the projected position varied smoothly by a maximum of approximately 7 and 3 pixels for the transverse (U) and longitudinal (V) directions respectively. The rigidity of the system is therefore evaluated to be in the order of 1 to 3 mm. The stability of the system geometry as depicted by the standard deviation was excellent. The mean magnitude of 2 standard deviations ( $\sigma$ ) for both directions was less than 0.5 mm. The system geometries were found to be reproducible to better than 1 mm ( $3\sigma < 1$  mm) in both directions over a period of 8 months [45]. These results compared to simulations indicate that excellent stability of the system will help maintain image quality and absolute positioning accuracy in the longitudinal direction.

### 3.4 Stability of CT Number Calibration Factor

The calibration and stability of CT# (image voxel intensities, a quantity representing the linear attenuation coefficient of the material within the voxels) are important in the clinic for applications such as dose calculation and automatic display using user-specified window levels and colormaps. In this section, the stability of the beam output and the flat panel readout were investigated since both affect our ability to control the reconstructed CT# produced by MVCBCT.

Equation (2.1) of the reconstruction describes how the projection data acquired at

an angle  $\theta$  are normalized and logarithmically transformed prior to start of the tomographic reconstruction process. Currently, the non-attenuated beam ( $I_{0,\theta}$ ) is obtained by measuring the fractional exposure delivered per projection ( $MU_\theta$ ) multiplied by a panel sensitivity per unit of exposure ( $I_{0perMU}$ ) derived during gain calibration. In this study, multiple unattenuated (in air) acquisitions were obtained monthly over 8 months to measure the average intensity per frame ( $I_{0perframe}$ ) and the stability of the sensitivity of the detector to 1 MU of exposure ( $I_{0perMU}$ ). Image acquired in air were analyzed by defining a large ( $25 \times 25 \text{ cm}^2$ ) region-of-interest (ROI) in the center of each raw projection. The exposure per projection was extracted from the header of the DICOM file containing the raw projections of the MVCBCT acquisition. Finally, the use of  $I_{0perMU}$  or an average  $I_{0perframe}$  on the reconstructed CT# and image quality was evaluated using the method described in Sec. 3.5.3.

Figure 3.3 illustrates the projection intensity variations of linac 1 acquisitions performed in air at different exposures. Repeated data were produced and plotted over a period of 8 months to investigate the beam output and flat panel stability. Tables 3.3 and 3.4 summarize the statistical analysis generated from the projection images of acquisitions performed in air on linac 1 and linac 2. The percentage deviation from the mean intensity from projection to projection (STD/Mean) increases at low exposure simply because a change of one electron pulse at lower exposure for the x-ray beam creates greater variations in the total intensity per projection. The maximum variation in beam intensity per frame was around 56% at 2.7 MU for linac 2. The

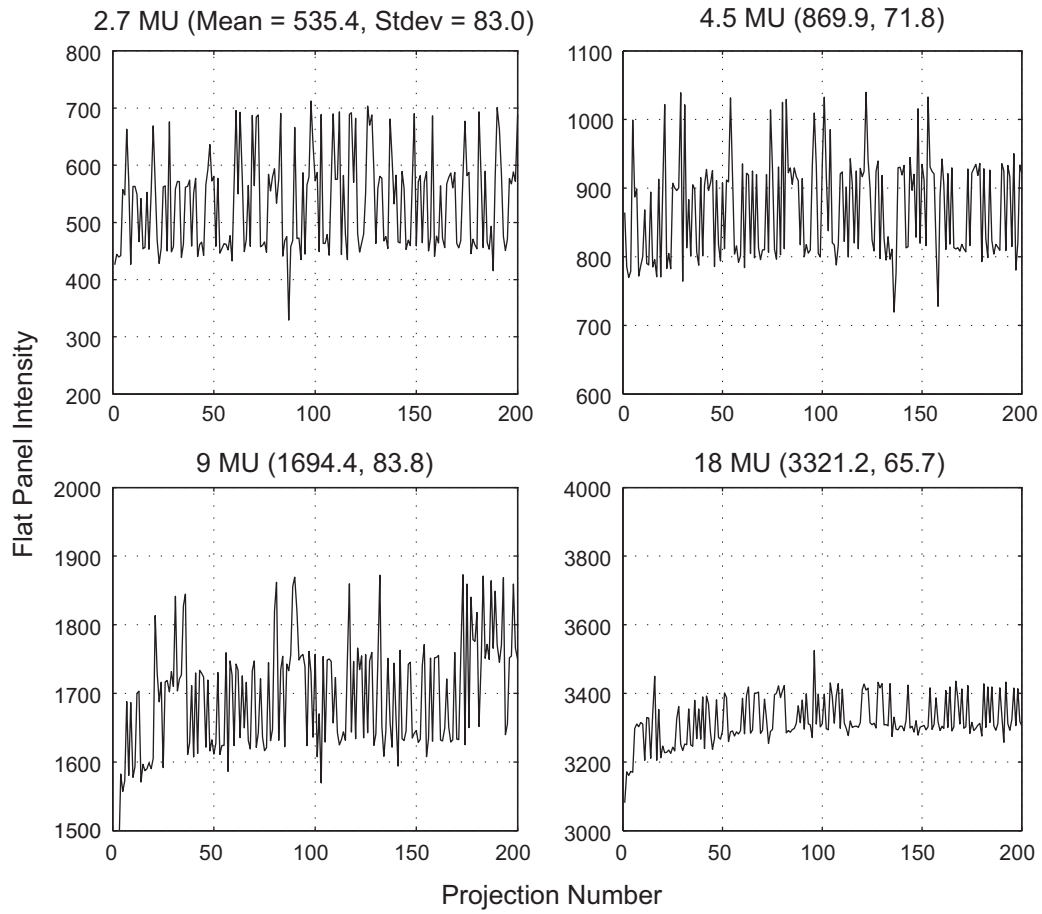


Figure 3.3: Flat panel intensity variation per projection (linac 1) for air acquisitions performed at 2.7, 4.5, 9.0 and 18.0 MU. The mean signal and the standard deviation are displayed above each plot.



stability of the beam output and panel reading was better than 2% at all exposure levels.

Figure 3.4 displays the value of  $I_{0perframe}$  as a function of exposure (MU per projection). The flat panel response at low exposure ( $< 0.1$  MU) was highly linear. The slope was calculated and represents the panel sensitivity for an exposure of 1 MU of the imaging beam ( $I_{0perMU}$ ). The  $I_{0perMU}$  using the different air acquisitions were  $37720 \pm 114$  and  $36584 \pm 916$  for linac 1 and linac 2 respectively. In comparison, the value of  $I_{0perMU}$  using only the normal gain procedure at 8 MU were  $37978 \pm 290$  and  $38857 \pm 344$ . The beam output and panel intensity stability is found to be excellent over a period of 8 months. For the CT# normalization factor, we believe obtaining  $I_{0perMU}$  using only the gain calibration is sufficient to conserve image quality. In addition, using only the gain calibration is more practical than having to acquire several air acquisitions to calibrate the unattenuated detector intensity at several exposures. Usually, the  $I_{0perMU}$  scaling factor is smaller when calculated from several air acquisitions acquired at different exposures. This can easily be observed for linac 2 in Fig. 3.4. This effect may be due to the fact that the flat panel does not entirely clear its dark current. For linac 2, this effect was large enough to change the reconstructed CT# by 3-4%.

Table 3.5 shows the impact of using different  $I_{0,\theta}$  normalization factors on the reconstructed CT#, noise and CNR. The CNR was not greatly affected whether  $I_{0perMU}$  or  $I_{0perframe}$  was used for reconstruction. A 10% over-estimation of  $I_{0perframe}$  re-

Table 3.3: Mean  $I_{0perframe}$  and beam intensity variations over a period of 8 months at different exposure (MU) for linac 1.

Total MU	Mean $I_{0perframe}$	STD/Mean (%)	Min/Mean (%)	Max/Min (%)
2.7	$530 \pm 6$	$15.5 \pm 0.3$	$-35.4 \pm 5.6$	$35.0 \pm 2.3$
4.5	$860 \pm 9$	$8.3 \pm 0.3$	$-21.8 \pm 2.4$	$22.6 \pm 2.6$
9.0	$1690 \pm 13$	$4.3 \pm 0.4$	$-13.7 \pm 2.7$	$10.8 \pm 2.1$
18.0	$3352 \pm 37$	$2.1 \pm 0.2$	$-7.2 \pm 1.1$	$4.8 \pm 1.1$

Table 3.4: Mean  $I_{0perframe}$  and beam intensity variations over a period of 8 months at different exposure (MU) for linac 2.

Total MU	Mean $I_{0perframe}$	STD/Mean (%)	Min/Mean (%)	Max/Min (%)
2.7	$585 \pm 9$	$11.9 \pm 2.6$	$-26.9 \pm 5.8$	$55.8 \pm 5.8$
4.5	$914 \pm 7$	$7.2 \pm 0.8$	$-18.8 \pm 3.0$	$20.2 \pm 5.5$
9.0	$1722 \pm 17$	$4.4 \pm 0.2$	$-13.0 \pm 4.3$	$12.0 \pm 1.9$
18.0	$3301 \pm 32$	$3.0 \pm 0.7$	$-7.0 \pm 1.0$	$7.9 \pm 1.5$

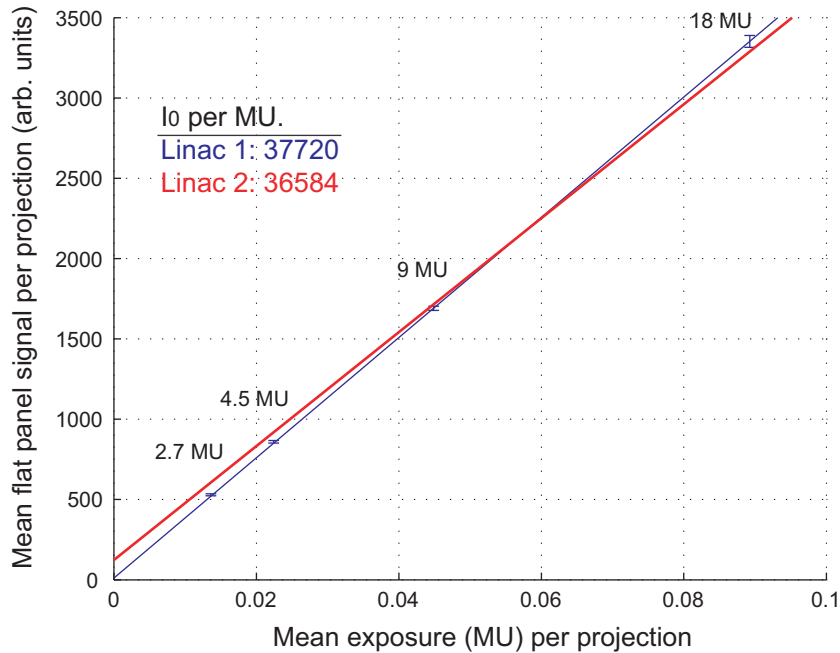


Figure 3.4: Mean detector intensity per projection for air acquisitions performed at 2.7, 4.5, 9.0 and 18.0 MU. Error bar are used to show the standard deviation in mean intensity per frame for measurements done over a period of 8 months.

Table 3.5: Effect of using different  $I_{0,\theta}$  normalization factors on the reconstructed CT#, noise and CNR.

Reconstruction protocol	CT#	Noise	CNR	CNR
	water	water	bone/water	muscle/water
2.7 MU using $I_{0perMU}$	988	43	8.8	1.5
2.7 MU using $I_{0perframe}$	1011	44	8.8	1.6
9.0 MU using $I_{0perMU}$	1051	26	14.2	2.0
9.0 MU using $I_{0perframe}$	1046	26	14.4	2.1
9.0 MU using $I_{0perframe}$ (5% high)	1087	27	13.7	2.0
9.0 MU using $I_{0perframe}$ (10% high)	1115	27	13.5	2.0
9.0 MU using $I_{0perframe}$ (20% high)	1163	27	13.4	2.0
9.0 MU using $I_{0perframe}$ (20% low)	760	46	9.2	1.8

sulted in a CT# increase of approximately 7%. Finally, under-estimation of  $I_{0perframe}$  strongly affected CT# and noise due to saturation of signal for the logarithmic conversion step of the reconstruction.

Given that large beam intensity variations ( $> 30\%$ ) are observed for lower MVCBCT acquisition exposures, it is somewhat surprising that the image quality (CNR) is not affected by the use of a  $I_{0perframe}$  as opposed to the  $I_{0perMU}$  and  $MU_\theta$  reading of the system. This result suggests either that the intensity variation per projection cancels out on the reconstruction, the effect is small compared to other sources of noise or that the  $MU_\theta$  reading of the system is equally erroneous than using a mean  $I_{0perframe}$ .

### 3.5 Image Quality

Image quality is a generic concept that helps quantify what can be expected from an imaging system in a clinical setting. The principal components are uniformity, contrast, spatial resolution and noise. Generally, optimizing image quality signifies

finding the best tradeoff between those components for a given application.

For our system, several parameters were varied to quantify their impact on image quality including the exposure (2.7, 4.5, 9.0, 18.0 and 54.0 MU), the craniocaudal imaging length (2, 5, 15, 27.4 cm), the voxel size (0.5, 1, 2 mm) and the slice thickness (1, 3, 5 mm). For the reconstruction algorithm, we investigated binning, averaging and diffusion filtering of raw projections as well as four different backprojection filters. A simple uniformity correction was developed to reduce a cupping artifact occurring with MVCBCT. The current MVCBCT product settings (Table 3.1) were used as the performance baseline for comparison.

A general discussion about image quality for CT systems with different geometry and x-ray beam energy is necessary at this point to better understand the results of the following sections.

### **Soft-Tissue visualization using kV and MV imaging**

The use of MV photons for imaging is a departure from the general preference for kilo-electron volt (kV) beams in diagnostic imaging. The basic physics of x-ray interaction with matter can be used to explain the tradeoffs between using kV or MV beams for imaging in radiotherapy. The visibility of large low-contrast objects in tomographic images, for example the prostate, depends on the CNR. Contrast is determined by the differential attenuation of the beam through different bodily tissues. In the MV range, Compton scattering provides the majority of the beam attenua-

tion. Due to the small energy dependence of Compton interaction, the contrast in MV imaging is thus relatively constant over a large energy range. However, the greater dose per photon deposited by MV photons reduces the imaging beam intensity that may be applied given patient dose constraints, thus reducing the signal. Moreover, the attenuation coefficients of bodily tissues are lower for MV energies, diminishing image contrast. The other important parameter, noise, includes the statistical fluctuation of photon detection as well as any source of unwanted radiation (i.e., radiation containing no imaging information). In transmission imaging, the x-rays reaching the detector consist of unscattered (primary) and scattered (secondary) components. The primary fluence produces the signal in the resulting image, while the secondary fluence introduces noise and image artifacts and produces quantitative inaccuracies in the reconstructed CT#. The magnitude of scatter reaching the detector depends on the photon energy spectrum, the field size, the object (size and composition), and the object-to-detector distance. The fan beam geometry traditionally used in diagnostic CT rejects a considerable amount of scattered radiation, while the cone-beam geometry used in modern CT scanners and even to a great extent in MVCBCT exposes the detector to greater amounts of scatter radiation. Compared to kV photon beams, MV scattered photons are much less abundant and have a more predictable behavior [46]. To a first approximation, the scatter contribution to a MV projection image will be a smooth dome-shaped signal roughly centered on the imager [28, 47]. Conventional detector gain correction procedures also tend to boost the signal in the center of the

detector to try compensate for a lower detector response measured when there is no object in the beam [48]. This becomes an overcorrection once the patient is placed in the beam, changing the beams energy spectrum. The end result of the amplified signal in the center of the projection images is a cupping artifact, an underestimation of the CT# in the center versus the periphery of the reconstructed MVCBCT image.

### 3.5.1 Uniformity and Cupping Artifact

A head-size water cylinder was used to characterize and correct the cupping artifact occurring for a typical head and neck MVCBCT acquisition. The cylinder diameter and length were 16 cm and 24 cm respectively. The nonuniformity (NU) of MVCBCT was obtained by measuring (with ROIs) the mean signal at the periphery ( $Mean_{periphery}$ ) and in the center ( $Mean_{center}$ ) of the water cylinder. The nonuniformity normalized for the mean reconstruction intensity of the water cylinder ( $Mean_{cylinder}$ ) and in air ( $Mean_{air}$ ) was calculated using the following equation:

$$NU = 100 \times \frac{Mean_{periphery} - Mean_{center}}{Mean_{cylinder} - Mean_{air}} \quad (3.1)$$

The nonuniformity was measured for acquisitions with different craniocaudal imaging lengths and gain calibration types. We compared the nonuniformity from the typical gain calibration acquired in air with a gain calibration using a 1.27-cm lead plate [48] placed in the accessory tray of the linac (Fig. 2.8, 1i). The purpose of the lead plate was to modify the beam on-axis (a nonattenuated beam is harder on-axis due to the preferential attenuation of low-energy x-ray in the flattening filter) to obtain a

Table 3.6: Uniformity performance for different craniocaudal imaging lengths (CCIL) and gain types.

	Full CCIL Air Gain	15 cm CCIL Air Gain	5 cm CCIL Air Gain	2 cm CCIL Air Gain	Full CCIL Lead Plate Gain
Axial	18.8%	16.3%	14.3%	14.2%	7.0%
Sagittal	24.6%	21.9%	17.1%	-	4.3%

more uniform energy fluence during gain calibration. The lead-plate would therefore remove any kind of beam energy spectrum compensation normally captured during gain calibration.

The results are presented in Table 3.6. The nonuniformity of the noncorrected MVCBCT images reaches 19% and 25% in axial and sagittal midsections respectively. The nonuniformity decreased with smaller craniocaudal imaging length but rapidly reached a plateau at lengths of approximately 15 cm. The use of gain calibration acquired with a lead plate greatly reduces nonuniformity, suggesting that the cupping artifact occurring with MVCBCT is mostly ( $\approx 2/3$ ) due to panel response instead of x-ray scatter. As expected, the nonuniformity did not vary with dose, slice thickness, or reconstruction size. The uniformity correction method presented next improves uniformity performance obtained with a lead plate for gain calibration.

### Simple uniformity correction method

A simple postprocessing empirical model was developed to reduce the cupping artifact occurring with MVCBCT. The average reconstructed CT# of a head-size water cylinder was used to assess uniformity obtained across the entire phantom after

correction. A geometrical model of correction factors was defined to characterize the cupping artifact. A basic ellipsoid shape (semiaxes;  $r_x, r_y, r_z$ ) centered on the cylinder ( $x_c, y_c, z_c$ ) was defined. As described in Eq. (3.2), each voxel of the water cylinder MVCBCT ( $x_f, y_f, z_f$ ) falls onto the surface of an ellipsoid  $\alpha$ . Using the water cylinder images, correction factors ( $CF_\alpha$ ) were determined for eight values of  $\alpha$ . Linear interpolation or extrapolation was used to determine the correction factors for values of  $\alpha$  that lie between or beyond the tabulated values.

$$\left(\frac{x_f - x_c}{r_x}\right)^2 + \left(\frac{y_f - y_c}{r_y}\right)^2 + \left(\frac{z_f - z_c}{r_z}\right)^2 = \alpha^2 \Rightarrow CF_\alpha \quad (3.2)$$

Figure 3.5a shows uncorrected MVCBCT images in the axial and sagittal central planes of the water cylinder. Figure 3.5c displays intensity profiles for this image taken along the directions defined by dotted white lines on the images of Fig. 3.5a. The magnitude of cupping artifact presented in these images is approximately 19% and 25% of the cylinder mean value for axial and longitudinal profiles respectively. As illustrated on Fig. 3.5a, a given CT# value approximately falls onto the surface of an ellipsoid centered in the cylinder. Several ellipsoid contours, defined by Eq. (3.2), are displayed on Fig. 3.5a along with their associated correction factors. The correction factors for the profiles of the phantom are also displayed using a dashed line (scale shown on the right of the plots of Fig. 3.5c). The uniformity correction method greatly reduced the cupping artifact as seen in the images (Fig. 3.5b) and profiles (Fig. 3.5d) for the corrected MVCBCT. Figure 3.6 shows the improvement in uniformity obtained with the correction factors applied to the images of a head and neck patient. The



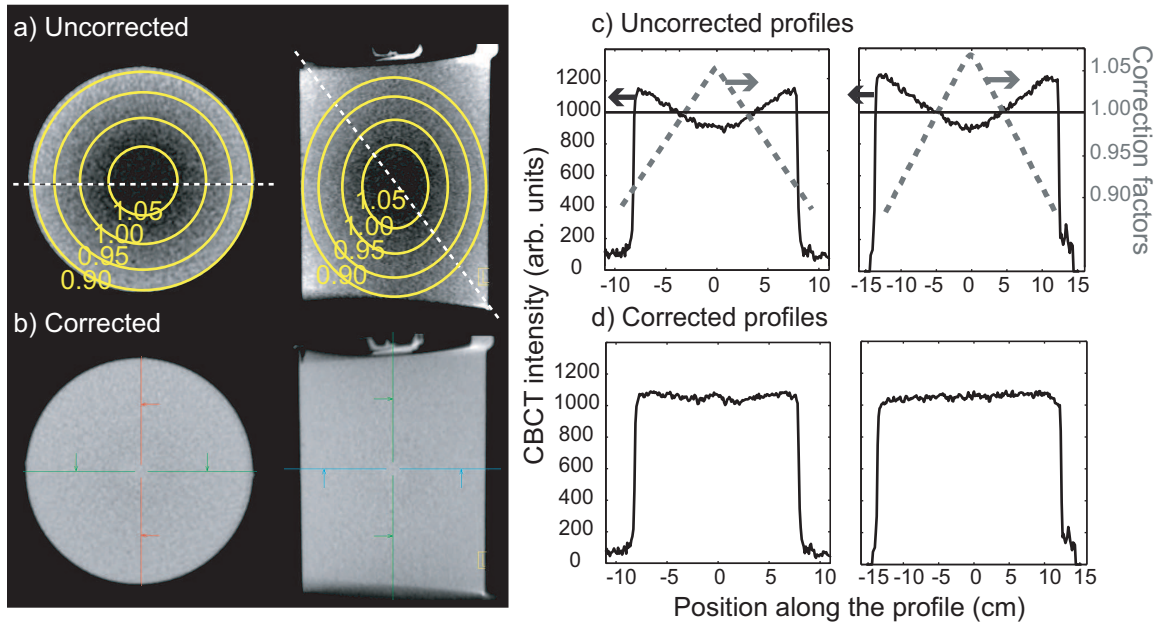


Figure 3.5: MVCBCT acquisitions and intensity profiles for a head-size water cylinder. The uncorrected images (a) contain a strong cupping artifact. Axial and sagittal profiles (c), taken along directions defined by white dashed lines in (a), display the magnitude of the cupping. Derived correction factors are overlaid on images in (a). Dashed lines in (c) plot the correction factors derived from the data. Corrected images (b and d) are much more uniform. Both sets of MVCBCT images are displayed with the same window and level.

remaining cupping artifact, estimated using the soft-tissue intensity along selected profiles, was less than 5% in any direction.

Although there are limitations inherent to this uniformity correction method, especially with respect to where the patient needs to be placed for imaging (roughly centered as in the case of the water cylinder), this simple correction greatly reduces the nonuniformity in the MVCBCT images. Other more robust preprocessing methods to correct projection images for x-ray scatter and other effects (e.g. beam hardening) have also been proposed [28, 47]. These methods would likely further reduce the

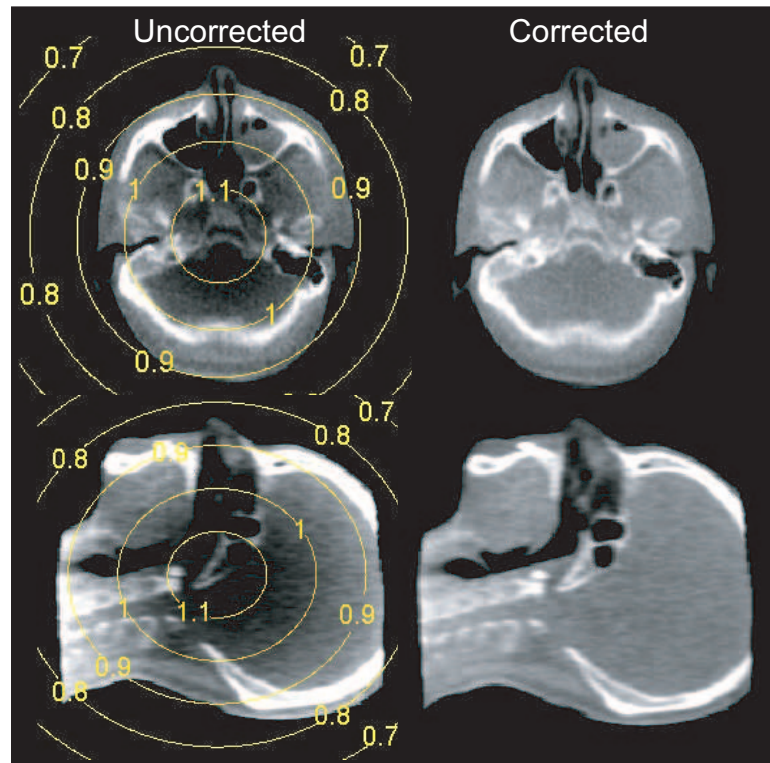


Figure 3.6: Improvement in image uniformity for a head and neck acquisition using a simple geometrical (ellipsoid) model of correction factors. (*left*) Uncorrected image with correction factors overlaid. (*right*) Corrected image. The images are displayed using the same window and level.

cupping artifact. However, the results of this study suggest that a first order correction of the MVCBCT cupping artifact may already be sufficient for dose calculation applications presented in Chap. 8.

### 3.5.2 Spatial Resolution

The ability to visualize small high-contrast objects is governed by the spatial resolution of an imaging system. In general, diagnostic applications such as mammography require better spatial resolution performance than in-room image-guidance in RT simply because of the task and the object-of-interest size. Advance diagnostic system can easily identify object size of a few millimeters, whereas mammography can identify objects having a size of a few hundred microns. The objective of this section is to quantify the spatial resolution of MVCBCT for different imaging protocols.

Several methods have been developed to evaluate the spatial resolution of an imaging system. Subjective methods using line pair patterns are commonly used but have limited accuracy and repeatability. More quantitative methods include an indirect approach using line pair patterns [49] (this approach is used for quality assurance in Chap. 4) and direct methods using point source [50] or edges [51]. For the purpose of optimizing image quality, we used an iterative edge blurring technique [52] to calculate the point-spread function (PSF) of our MVCBCT system. The PSF describes the response of an imaging system to a point-stimulus, and it theoretically is a thorough description of the system's spatial resolution. For some imaging system,

however, it is difficult to experimentally design a point-stimulus. The iterative edge blurring method avoid this difficult by using *a priori* knowledge of the object size used as input to the imaging system. Figure 3.7 illustrates the main steps of the method.

**Iterative edge blurring technique for PSF calculation (illustrated in Fig. 3.7):**

1. Use MVCBCT to image a ball or a wire having a diameter larger than but close to the spatial resolution of the MVCBCT system.
2. Measure the wire diameter precisely (with micrometer). An object having this diameter theoretically represents the ideal input to the system.
3. Extract a transverse image slice.
4. Draw several profiles in the image across the center of the wire.
5. Average all the profiles (this correspond to the response of the MVCBCT system to the ideal input of a specific size).
6. Iteratively blur (with Gaussian functions of different standard deviation "width"  $\sigma$ ) the ideal input to minimize the different between the profile average and the blurred ideal input.
7. The best Gaussian function (described with  $\sigma$  causing the least error) corresponds to the PSF of the system.

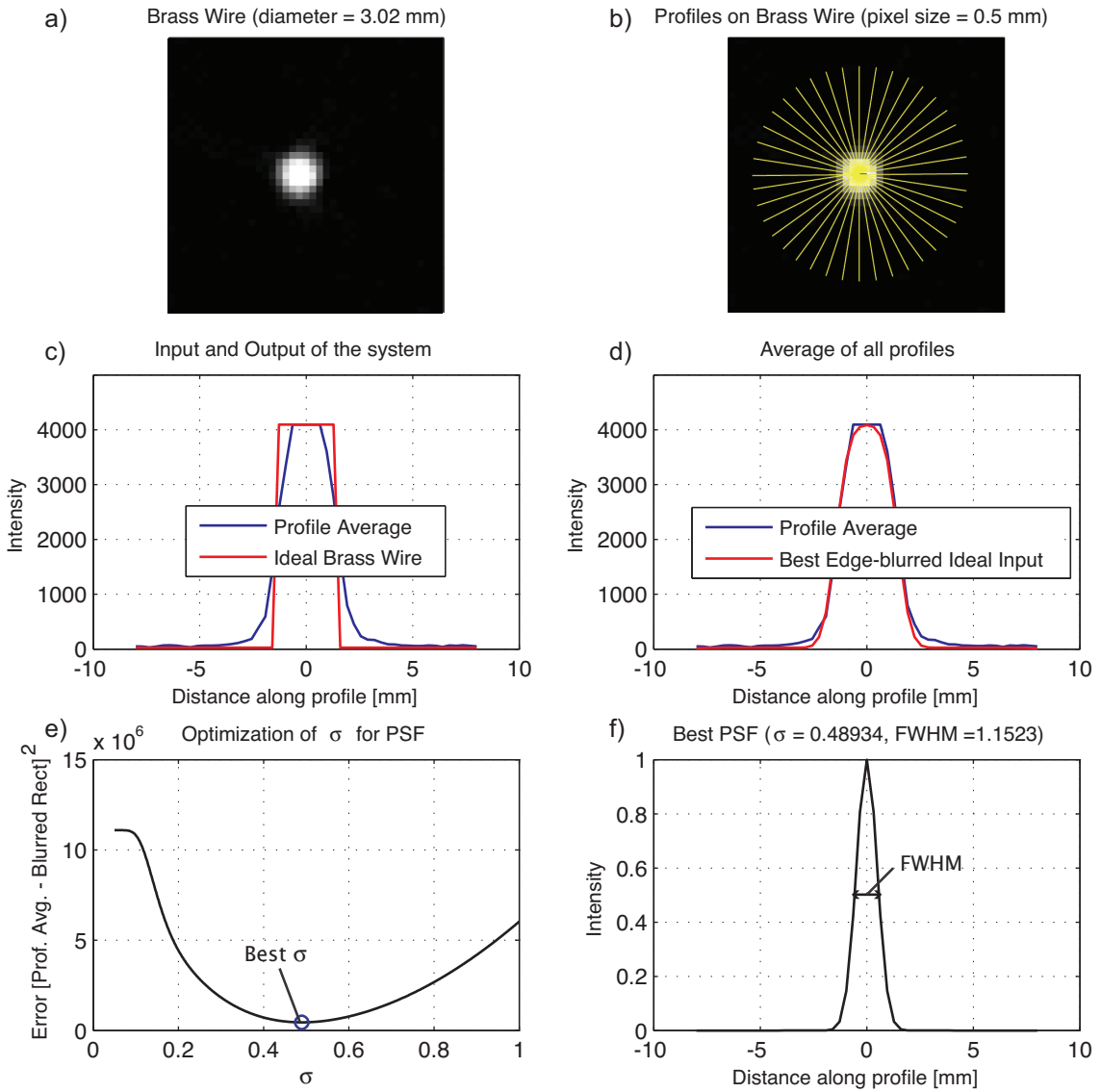


Figure 3.7: Summary of the method used to measure the spatial resolution ( $PSF_{FWHM}$ ) of MVCBCT. (a) Represents a cross-section of the brass wire imaged at isocenter with MVCBCT. (b) Several profiles were drawn passing through the center of mass of the wire. (c) Shows the ideal input (red) measured with the micrometer and the true input (blue) obtained by averaging all the profiles from b. (d) The ideal input is convoluted with Gaussian functions to maximize the similarities with the true input. (e) Shows the optimization of the Gaussian function (trying different standard deviation  $\sigma$ ) minimizing the error between the blurred ideal input and the true input. (f) Plots the best Gaussian function representing the point-spread function (PSF) of the imaging system.

A brass wire located at isocenter along the longitudinal axis was imaged with MVCBCT. The raw images were used to test different reconstruction protocols on the PSF. Only one component of the acquisition or reconstruction was varied per protocol to compare with the baseline (Table 3.1).

The full-width at half maximum (FWHM) of the PSF is summarized in Table 3.7. The FWHM of the point spread function ( $PSF_{FWHM}$ ) varied only between 1.50 and 2.11 mm for all the reconstruction protocols tested. Such a small difference has very little impact on the possible clinical applications with MVCBCT compared to the contrast-to-noise ratio improvement observed in the next section. For this reason, the contrast-to-noise ratio was used as leading component to optimize image quality. The primary blurring sources for MVCBCT are believed to be the x-ray source size ( $\sim 1-2$  mm), the reconstruction program (smoothing filters), the intrinsic spatial resolution of the scintillator and flat panel detector, and the image magnification. In addition, positions in space away from the central transverse plane would likely have lower spatial resolution than reported due to the approximation occurring with the FDK algorithm.

### 3.5.3 Contrast-to-Noise Ratio

The visibility of large low-contrast structures with cone-beam CT is mostly governed by the contrast-to-noise ratio (CNR). This is a key image quality component for all the clinical applications that requires the resolution of soft-tissue structures.

Table 3.7: Spatial resolution performance for different reconstruction protocols. The full-width at half maximum of the point spread function ( $\text{PSF}_{FWHM}$ ) is reported. Only the specified protocol component is changed compared to the baseline specified in Table 3.1.

Reconstruction Protocol Component	$\text{PSF}_{FWHM}$ (mm)	% $\text{PSF}_{FWHM}$ Improvement from baseline
Baseline (Table 3.1)	1.96	—
bin = 1	1.67	-14.8
projfilt = none	1.82	-7.2
projfilt = Avg. 3×3	1.91	-2.6
projfilt = Avg. 7×7	2.02	3.1
projfilt = no Avg., Diffusion	2.06	5.2
projfilt = Avg. 5×5, Diffusion	2.11	7.9
bckprojfilt = Edge Enhancing	1.50	-23.6
bckprojfilt = Edge Preserving	1.53	-21.7
bckprojfilt = Smoothing 2	1.60	-18.3
nvox = 128×128	2.01	2.7
nvox = 512×512	1.92	-2.1
slicethick = 1mm	1.96	0
slicethick = 5mm	1.97	0.4
$I_{0,\theta}$ = Mean $I_{0perframe}$	1.94	-0.8
$I_{0,\theta}$ = Mean $I_{0perframe}$ 5% high	2.00	2.2

In theory, assuming a Gaussian distribution for the noise of the imaging system, a structure should be visible if its CNR is greater than 2, that is, the contrast between the structure and its background is twice as big as the local noise distribution. In reality, defining what is visible on clinical images is highly subjective. In addition, it practically is impossible to design a phantom that contain the tissue complexity of the human anatomy, although animal studies remain an option. This section aims at quantifying the CNR performance on phantoms for different MVCBCT acquisition and reconstruction protocols in order to optimize soft-tissue resolution in the clinic.

A head-size water cylinder implanted with CT inserts was used to measure the CNR performance of MVCBCT. The following CT inserts with relative electron densities to H<sub>2</sub>O (rED) were implanted in the water cylinder: ROI<sub>1</sub>: dense bone (51.3%), ROI<sub>2</sub>: lung inhale (-81.0%), ROI<sub>3</sub>: liver (5.3%), ROI<sub>4</sub>: trabecular bone (11.7%), ROI<sub>5</sub>: adipose (-4.8%), ROI<sub>6</sub>: lung exhale (-51.1%) and ROI<sub>7</sub>: muscle (4.3%). ROIs were drawn for all inserts and their respective background signal in water. Figure 3.8 shows the water cylinder with the ROIs drawn for CNR calculation. A MVCBCT of 60 MU was acquired to precisely draw the ROIs. MVCBCT of different exposures and craniocaudal imaging lengths were then acquired with the phantom in the same position. The MVCBCT reconstructions were corrected for uniformity using the method presented in Sec. 3.5.1. Finally, the ROIs drawn on the 60 MU MVCBCT were copied on each MVCBCT to extract statistics and calculate the CNR.

The CNR of insert  $i$  ( $CNR_i$ ) was calculated using the mean ROI pixel value



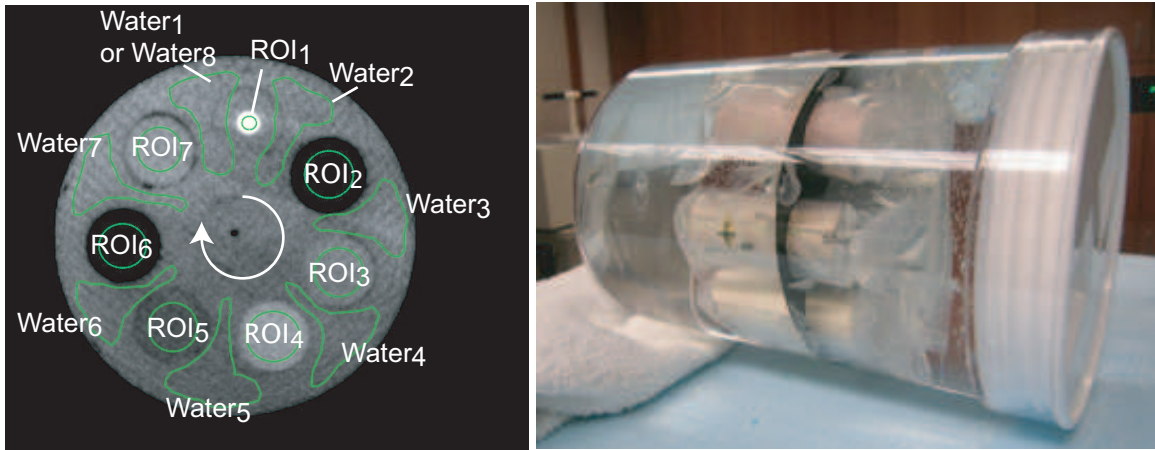


Figure 3.8: Phantom designed for measurements of contrast-to-noise ratio. Inserts mimicking bodily tissues were implanted in a head-size water cylinder. The image on the left is a transverse slice of the MVCBCT reconstruction and shows the regions-of-interest that were defined for CNR measurements.

of insert  $i$  ( $\text{mean}(\text{ROI}_i)$ ) with the mean and standard deviation of the ROI pixel values in background regions ( $\text{mean}(\text{Water}_i)$ ,  $\text{Stdev}(\text{Water}_i)$ ,  $\text{mean}(\text{Water}_{i+1})$  and  $\text{Stdev}(\text{Water}_{i+1})$ ) defined in water on both sides of insert  $i$ . As illustrated in Fig. 3.8, the index  $i$  ranges from 1 to 7 for the inserts and from 1 to 8 for the background regions in water. The CNR of insert  $i$  was calculated using the following equation:

$$\text{CNR}_i = \frac{\text{Mean}(\text{ROI}_i) - 1/2 \cdot (\text{Mean}(\text{Water}_i) + \text{Mean}(\text{Water}_{i+1}))}{1/2 \cdot (\text{Stdev}(\text{Water}_i) + \text{Stdev}(\text{Water}_{i+1}))} \quad (3.3)$$

The results are summarized in Table 3.8. Only one component of the acquisition or reconstruction was varied per protocol compared to the baseline. Reconstruction protocols combinations that resulted in clear suboptimal CNR performance (e.g. bin = 1, projfilt = none, bckprojfilt = edge enhancing) were removed from the table. Averaging or diffusion filtering of the raw projections greatly improves CNR. The smoothing backprojection filter with strong removal of high frequency components

Table 3.8: Contrast-to-noise ratio (CNR) performance for different reconstruction protocols. Only the specified protocol component is changed compared to the baseline defined in Table 3.1. The CNR performances are reported for three electron density differences relative to water (rED).

Reconstruction Protocol Component	CNR for different rED			Mean CNR	% CNR improvement from baseline
	51.3%	11.7%	4.3%		
Baseline (Table 3.1)	18.0	5.7	2.0	8.5	—
bin = 1	10.8	3.3	1.1	5.1	-40.9
projfilt = none	12.5	3.8	1.3	5.9	-31.5
projfilt = Avg. 3×3	14.5	4.5	1.5	6.8	-20.3
projfilt = Avg. 7×7	21.2	7.4	2.2	10.3	19.9
projfilt = no Avg., Diffusion	30.8	11.0	3.8	15.2	77.8
projfilt = Avg. 5×5, Diffusion	34.2	12.5	4.4	17.0	99.3
bckprojfilt = Edge Enhancing	8.1	2.3	0.8	3.7	-56.2
bckprojfilt = Edge Preserving	8.6	2.5	0.9	4.0	-53.4
bckprojfilt = Smoothing low	9.0	2.8	0.8	4.2	-50.8
nvox = 128×128	13.6	4.6	1.5	6.6	-23.1
nvox = 512×512	25.0	8.2	2.5	11.9	39.4
slicethick = 1 mm	10.0	3.3	1.1	4.8	-43.7
slicethick = 5 mm	23.1	7.2	2.3	10.9	27.5
$I_{0,\theta}$ = Mean $I_{0perframe}$	17.8	5.8	1.8	8.5	-1.0
$I_{0,\theta}$ = Mean $I_{0perframe}$ 5% high	17.3	5.7	1.7	8.2	-3.8

provided the best CNR. Because the reconstruction is voxel-based, it is optimal to reconstruct with a size of  $512 \times 512$  with 1 mm slice thickness and resample images to 3 or 5 mm slices. Smaller voxel size or a larger number of voxels (nvox) during reconstruction results in a larger number of sampling on the detector thus improving CNR.

Finally, compared the CNR produced by the best two reconstruction protocols and from the baseline protocol as a function of exposure. The results are illustrated in Fig. 3.9 and plotted in Fig. 3.10.

The CNR varied with the square root of exposure ( $\sqrt{MU}$ ) for the baseline recon-

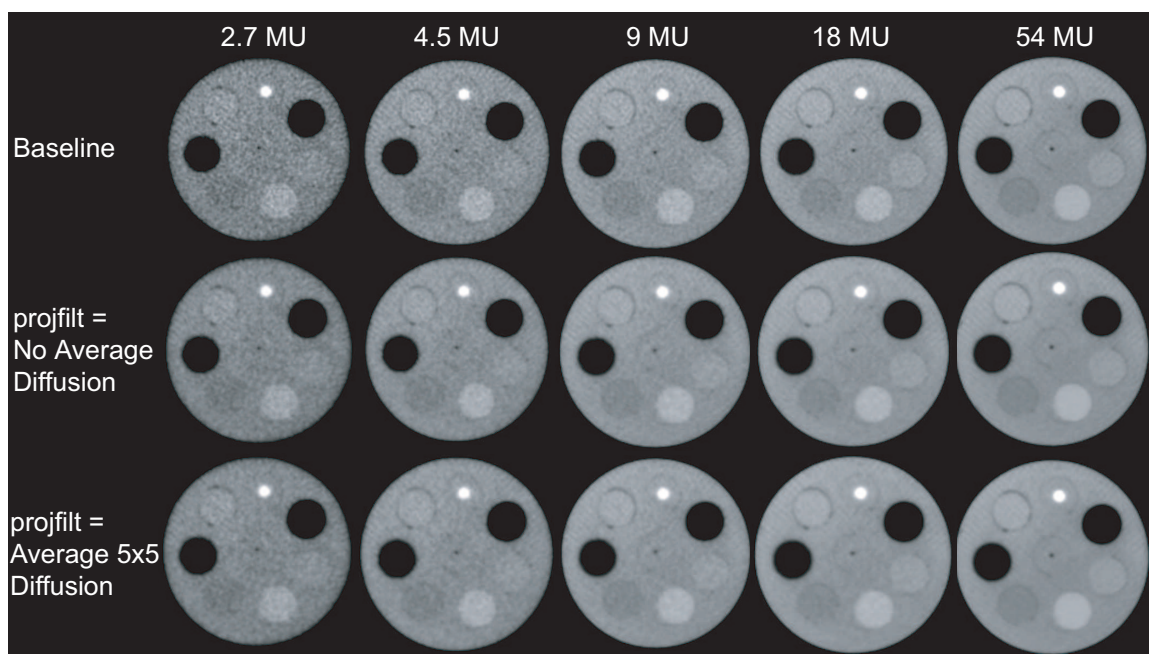


Figure 3.9: Axial images of the phantom Fig. 3.8 showing the CNR performance as a function of MVCBCT exposure (MU) for three different reconstruction protocols: baseline, projfilt = diffusion and projfilt = Average and diffusion.

structions. Diffusion filtering at 9 MU produced a similar CNR improvement as using 5 times more dose versus the baseline protocol. This is a significant improvement for clinical applications that requires soft-tissue visualization. Despite the improvement in imaging performance provided by diffusion filtering, the calculation time for filtering increases the total reconstruction time by a factor of 2 to 3. However, faster computer and possible optimization of the diffusion algorithm has the potential to improve CNR with the ultimate goal of achieving rapid online applications. Until then, the diffusion filter should only be used for applications that do not impose any practical or clinical time constraint.

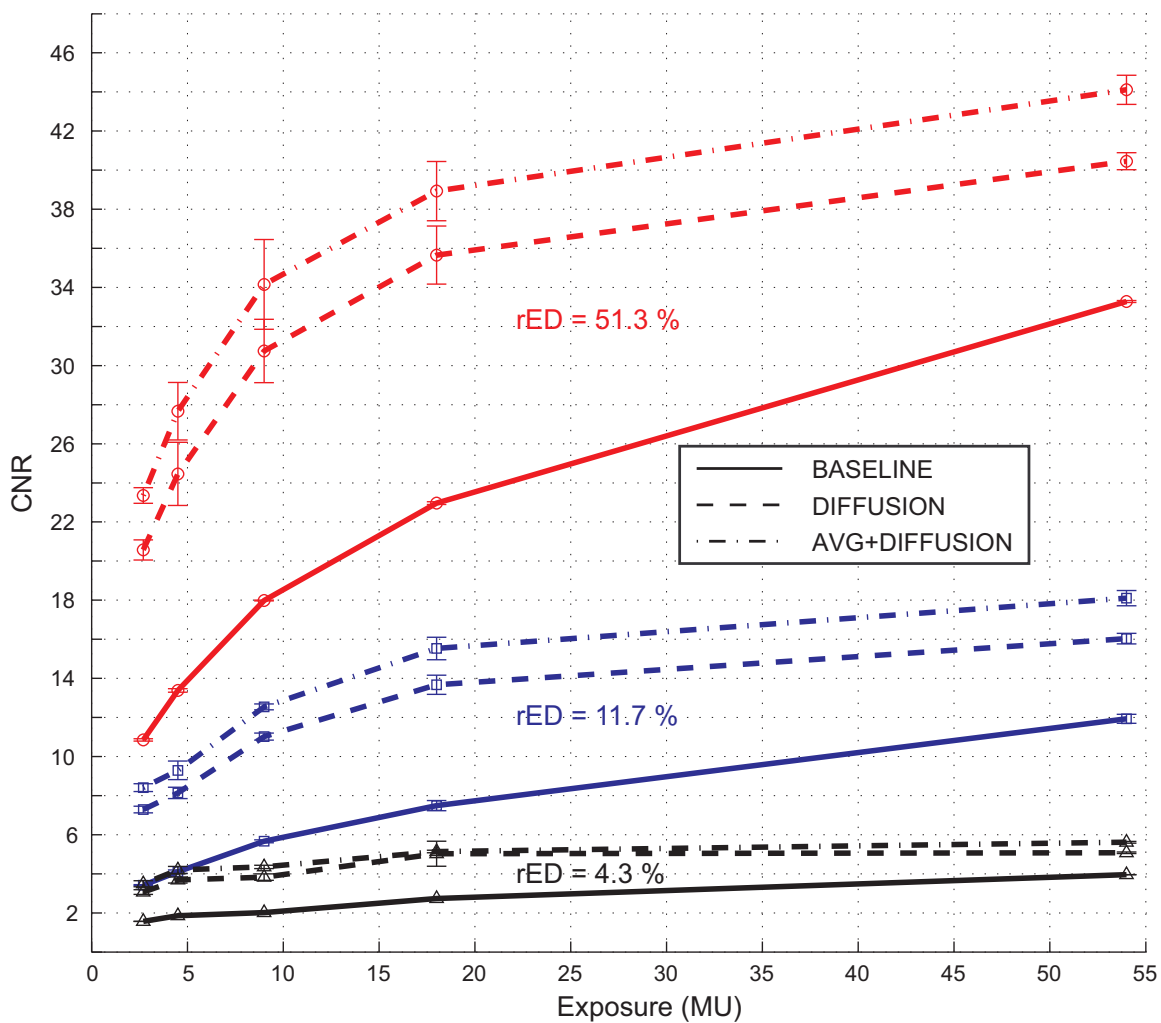


Figure 3.10: CNR performance as a function of MVCBCT exposure (MU) for three different imaging protocols identified: baseline, projfilt = diffusion and projfilt = Avg. and diffusion. The CNR performances are reported for three electron densities relative to water (rED = 51.3% (dense bone), 11.7% (trabecular bone) and 4.3% (muscle)). Error bars represent the standard deviation of the CNR for axial images analyzed over a length of 2 cm.

## 3.6 Electron Density Calibration

Electron density calibration of MVCBCT images is a requirements for several clinical applications. For example, 3D alignment could use a specific intensity of the reconstruction for image registration and MVCBCT images calibrated for electron density then could be used for dose calculation (Chap. 8).

Electron density calibration is derived by converting the CT# in each voxel of the reconstruction into relative electron density. This is usually done empirically by scanning a tissue equivalent phantom (CIRS model 062, Norfolk, VG) with inserts of known electron density. For the calibration of MVCBCT however, this small phantom could not be used as is because it did not reproduce the scatter environment of the water cylinder used to define the uniformity correction factors in Sec. 3.5.1. Instead, we utilized the head-size water cylinder phantom with inserts used for CNR calculation in Sec. 3.5.3. MVCBCT were acquired at three exposures (4.5, 9.0 and 18.0 MU). The CT inserts were placed in 4 different configurations in the water cylinder. The MVCBCT nonuniformity was reduced using the ellipsoid model of correction factors described in Sec. 3.5.1. The water phantom was also imaged 3 cm away from the isocenter in the lateral direction to investigate the efficacy of the uniformity correction method on patient images acquired with an imaging isocenter away from the anatomical midplanes. ROIs were drawn on the inserts of both CT scans to extract the mean intensities.

Figure 3.11a presents the CT# calibration for different MU acquisitions. The

calibrations were not adjusted to obtain a CT# of 0 in air. The linearity of the MVCBCT reconstruction intensity with electron density was excellent. This result is expected for MV imaging where Compton interaction dominates [53]. The CT# calibrations for the 9.0 and 18.0 MU acquisitions were nearly identical. There was a small systematic difference ( $\sim 20$  CT#) for the 4.5 MU acquisition. Figure 3.11b shows the CT calibration for different insert configurations and phantom positions. The mean absolute difference in CT# was only 1.3%. The maximum difference in CT# was 5.1%. The maximum difference in CT# for the phantom placed 3 cm away from the isocenter laterally was 4.2%.

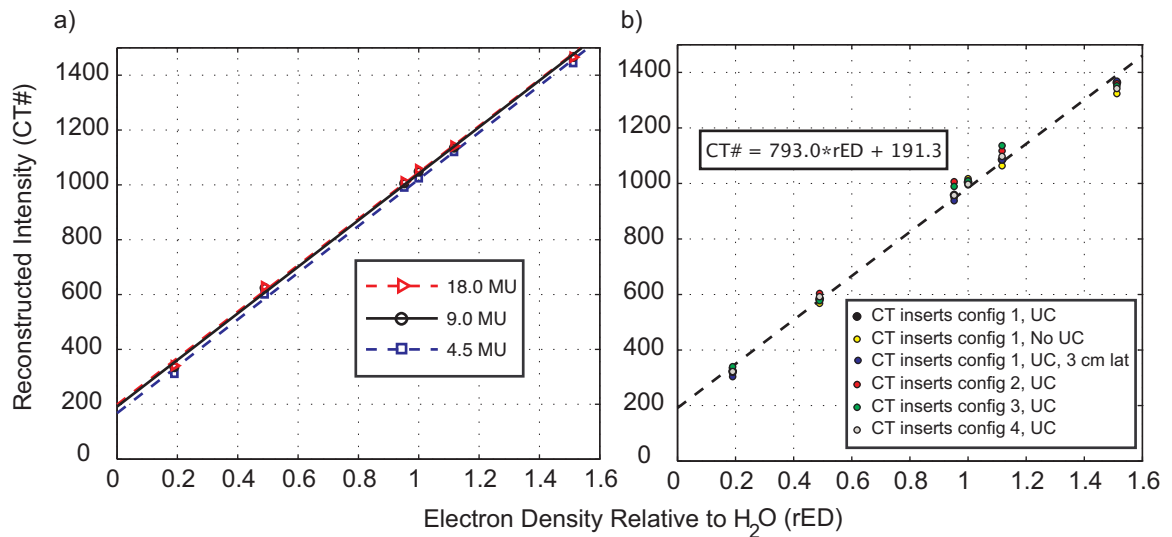


Figure 3.11: Electron density calibration of MVCBCT for different a) exposures (4.5, 9.0 and 18.0 MU) and b) CT insert configurations and phantom positions.

A small gradient in CT# ( $< 6\%$ ) was observed on the MVCBCT reconstruction in the anterior-posterior direction. The reason for this small error may be due to the higher dose delivered in the anterior portion or the Parker weighting of the recon-

struction which cannot perfectly accounts for redundant angles of the reconstruction. Finally, the small variation of the CT# calibration with MU and insert configurations and phantom position may facilitate the development of dose re-calculation applications (Chap. 8).

## **3.7 Dose Delivered to Patients**

In radiation therapy, the patient dose from IGRT is generally small compared to the treatment dose. However, the increasing frequency of CT imaging may result in clinically significant dose to normal tissue. For the patients safety and to optimize the benefits of IGRT, the additional dose delivered from in-room CT imaging systems should be understood and controlled. The objectives of this section are to evaluate the image acquisition dose delivered to patients for MVCBCT and to develop a simple method to reduce the additional dose resulting from routine MVCBCT imaging. The content of this section has been recently published [54].

### **3.7.1 Measurements vs. Simulations**

The first objective of this study was to demonstrate that a commercial treatment planning system (TPS: Pinnacle v7.6, Philips, Bothell, WA) can accurately calculate the patient dose for an MVCBCT acquisition. This is possible because MVCBCT uses the linac treatment beam, which has already been characterized in the TPS for dose

calculation on CT images. A water-equivalent cylindrical phantom made for IMRT quality assurance displayed in Fig. 3.12 was used to validate the MVCBCT dose simulated in our TPS. First, the phantom was imaged with conventional CT, with the resulting CT images then imported in to the TPS. The position of the phantom on the CT table was marked with fiducials. An arc treatment ( $270^\circ$  to  $110^\circ$ ) using a  $27.4 \times 27.4 \text{ cm}^2$  field-size was simulated. The phantom was then aligned on the treatment couch using the fiducials and a MVCBCT acquisition was delivered. The radiation dose was measured with metal-oxide-semiconductor field-effect transistor (MOSFET) detectors placed at 10 different locations in the cylindrical phantom. An ion chamber was placed in the center of the phantom to measure the delivered radiation exposure as well. The calculated dose and measurements were compared.

The delivered MVCBCT dose to the IMRT quality assurance cylinder was calculated in the TPS and compared with measurements performed with MOSFET detectors and an ion chamber. Figure 3.12 shows the comparison of simulated/calculated versus measured dose. The calculated MVCBCT dose formed a slight posterior-anterior gradient ranging from 0.8 to 1.1 cGy per MVCBCT MU. The dose percentage differences between the calculation and the measurement points are displayed on Fig. 3.12. The dose percentage differences between the calculation and the MOSFET points were all better than 3%. The dose percentage difference for the ion chamber placed in the center of the phantom was only 0.2%. These results confirm that a TPS can be used to calculate the full imaging dose distribution delivered to patients.



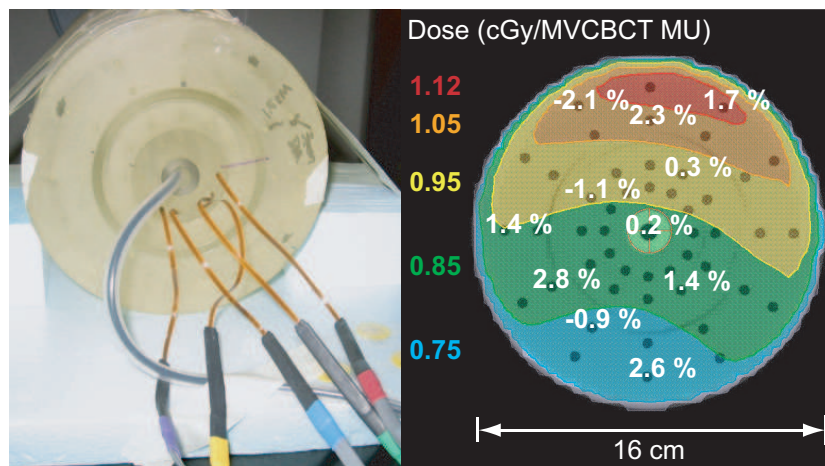


Figure 3.12: Comparison of dose measurements and the simulation of an MVCBCT acquisition performed on an IMRT quality assurance phantom. Dose measurements were performed with an ion chamber (center point) and MOSFET detectors (other points) as depicted in the left image. The simulation of the MVCBCT was done in our commercial TPS. Percent differences between calculated and measured doses are overlaid on the dose distribution displayed on the right.

### 3.7.2 Patient Dose

Conventional CT scans of patients already imported in the TPS were used to simulate the delivered dose for MVCBCT and portal imaging. The treatment isocenter location as well as the target and critical structures were already specified on the patients CT image. Having this information in the TPS results in minimal additional work to obtain a complete assessment of the MVCBCT dose. A MVCBCT imaging plan was simulated as an arc treatment using a specific arc range, total number of MU and a desired field-size. MVCBCT dose simulations were performed on CT images of two prostate patients and one head and neck patient. Simulations were done using the arc acquisition currently allowed by the MVCBCT system (arc:  $270^\circ$  to  $110^\circ$ ) the current maximum field-size of  $27.4 \times 27.4 \text{ cm}^2$ , and assuming a total delivery of 1 MU

to obtain the dose per MU.

The dose delivered for portal imaging or film was also simulated with an anterior-posterior beam added to a lateral beam. The field-size for portal imaging was the same as for MVCBCT (27.4 cm). For a relative comparison with the MVCBCT dose, the calculations were performed assuming a total delivery of 1 MU (0.5 MU for each portal image) to obtain the total dose per MU. Dose-volume histograms were obtained for all patients. Finally, the absolute doses to the main pelvic and head and neck structures delivered at our institution for setup using MVCBCT, CR film and portal imaging were compared. An average of 6 MU ( $2 \times 3$  MU) is currently used to align prostate patients with implanted gold seeds using daily portal imaging. As for head and neck patients, verification of position and bony anatomy is done weekly using CR film ( $2 \times 4$  MU = 8 MU) or the flat panel detector ( $2 \times 2$  MU = 4 MU).

### **Prostate patient**

Relative dose distributions per MU for MVCBCT and portal imaging on an average size pelvis patient are displayed in Fig. 3.13. Isodose lines are displayed on the axial, coronal and sagittal planes crossing the treatment isocenter, which was located in the prostate. For MVCBCT acquisition (top row), the dose formed a posterior-anterior gradient ranging from 0.4 to 1.2 cGy per MVCBCT MU. The DVHs analysis revealed that the dose received by the main pelvic structures for MVCBCT using the current arc acquisition ranges between 0.6 and 1.2 cGy per MVCBCT MU. The dose

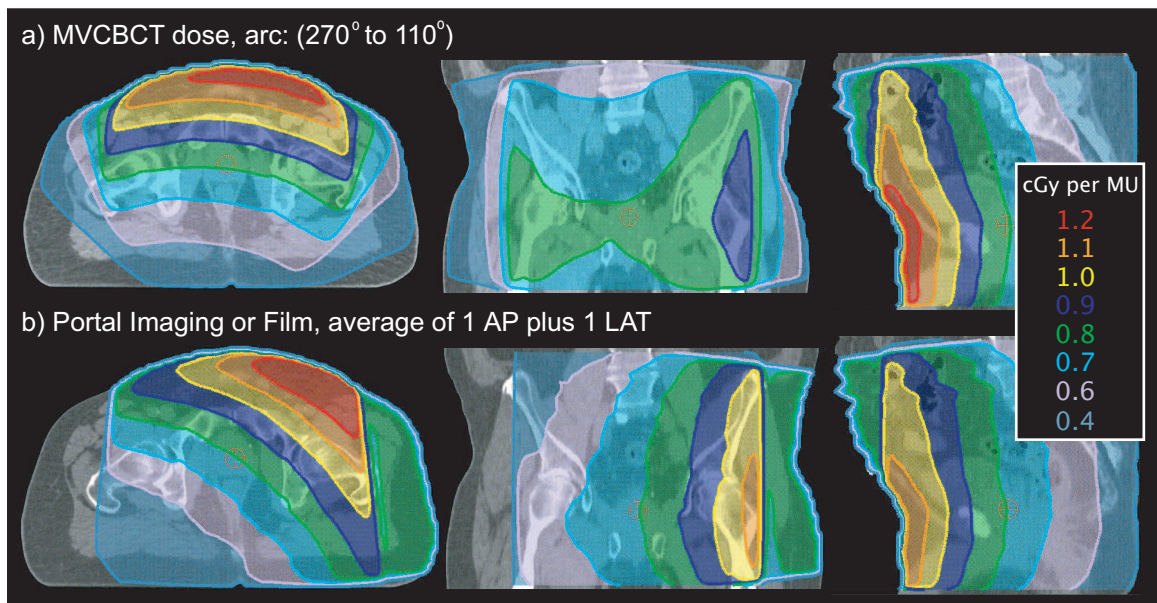


Figure 3.13: Dose delivered per MU to an average size pelvis patient for MVCBCT and portal imaging. On the top row, the current MVCBCT arc acquisition (270° to 110°) using a total of 1 MU was simulated. The bottom row shows the dose distribution per MU for electronic portal imaging or film. An anterior-posterior beam of 0.5 MU was added to a lateral beam of 0.5 MU.

Table 3.9: Dose delivered to a prostate patient for daily alignment verification. MVCBCT (9 MU) and portal imaging ( $2 \times 3$  MU = 6 MU).

Anatomical Structures	MVCBCT (cGy)			Portal Imaging (cGy)		
	Min	Mean	Max	Min	Mean	Max
Prostate	6.4	6.9	7.6	4.1	4.6	5.0
Seminal Vesicles	6.3	6.4	6.8	4.1	4.4	4.7
Nodes	5.2	6.8	10.1	3.3	4.6	7.5
Rectum	5.3	5.9	6.8	3.6	4.1	4.7
Bladder	6.7	7.8	9.5	4.4	5.1	6.2
Penile Bulb	6.5	6.9	7.6	4.4	4.7	5.0
Left Femoral	6.4	7.8	8.9	4.7	6.2	6.8
Small Bowel	2.7	8.3	11.2	2.3	5.4	8.1
Spinal Cord	0.9	3.9	5.2	0.6	2.6	3.8

distribution per MU observed with portal imaging or film in Fig. 3.13 (bottom row) was similar to current MVCBCT imaging. Table 3.9 compares the absolute dose for a 9 MU MVCBCT to what is currently delivered to prostate patients at our institution for daily verification of setup using portal imaging. On average, the main pelvic structures receive 6.8 and 4.6 cGy for MVCBCT and portal imaging respectively. The maximum doses to the rectum were 6.8 and 4.7 cGy for MVCBCT and portal imaging respectively.

### Head and neck patient

The patient dose for a typical head and neck patient formed a posterior-anterior gradient ranging from 0.4 to 1.1 cGy per MVCBCT MU. The dose distribution per MU observed with portal imaging was very similar to MVCBCT imaging. Table 3.10 compares the absolute dose delivered to a head and neck patient for a 5 MU MVCBCT

Table 3.10: Dose delivered to a typical head and neck patient for weekly verification of alignment and anatomy. MVCBCT (5 MU), CR film ( $2 \times 4$  MU = 8 MU) and portal imaging ( $2 \times 2$  MU = 4 MU).

Anatomical Structures	MVCBCT (cGy)			CR Film (cGy)			Portal Imaging (cGy)		
	Min	Mean	Max	Min	Mean	Max	Min	Mean	Max
GTV	4.8	5.2	5.8	6.6	8.1	9.5	2.4	4.0	4.8
CTV1	2.7	5.0	5.8	3.8	7.8	9.6	2.0	3.8	4.8
CTV2	4.5	4.8	5.1	6.6	7.6	8.6	3.2	3.8	4.2
Esophagus	3.9	4.5	5.0	6.1	6.6	7.1	3.0	3.4	3.6
Mandible	3.5	5.4	6.0	5.5	8.6	9.7	2.8	4.2	4.8
Spinal Cord	3.3	4.2	4.8	5.1	6.5	7.5	2.6	3.2	3.8
Left Parotid	2.4	4.9	5.3	4.2	8.8	9.4	2.0	4.4	4.8
Brain Stem	4.2	4.4	4.6	6.6	7.2	7.9	3.2	3.6	4.0
Brain	0.9	4.1	5.6	1.3	6.5	9.3	0.6	3.2	4.6
Skin	0.0	4.4	5.7	0.0	7.0	9.4	0.0	3.6	4.6
Left Eye	1.6	5.5	5.8	2.5	9.2	9.8	1.2	4.6	5.0
Right Lens	3.6	5.1	5.5	5.4	7.5	8.0	2.6	3.8	4.0

with what is currently delivered at our institution for weekly verification of setup and anatomy using CR film and portal imaging. On average, the main head and neck structures received 4.8, 7.6 and 3.8 cGy for MVCBCT, CR film and portal imaging respectively. The maximum doses to the right lens were 5.5, 8.0 and 4.0 cGy for MVCBCT, CR film and portal imaging respectively. Methods to further reduce or eliminate the dose to critical structures with low radiation tolerance, such as the eyes, will be described next.

### 3.7.3 Plan Compensation for Routine MVCBCT Imaging

To investigate the possible clinical impact of the additional MVCBCT imaging dose to the patient and a method to compensate for it, several dose calculations were

compared. In addition to the treatment plan alone, two composite plans were defined. The uncompensated plan consisted of the treatment plan plus daily MVCBCT imaging. For the compensated plan, the treatment plan MUs were reduced by a compensation factor (percentage less than 100%) and added to the MVCBCT imaging dose such that the mean dose to the target remained the same as with the treatment plan dose alone. Equation (3.4) describes how the compensation factor is calculated.

$$T_{Tx} = CF_{MVCBCT} \cdot T_{Tx} + T_{MVCBCT} \cdot n_{MU} \cdot n_f \quad (3.4)$$

The left side of Eq. (3.4) is the target mean dose for the original treatment plan alone ( $T_{Tx}$ ). The right side of Eq. (3.4) is the mean target dose reduced by the compensation factor ( $CF_{MVCBCT}$ ) plus the mean target dose received during the MVCBCT imaging. The imaging dose is calculated by multiplying the mean target MVCBCT dose ( $T_{MVCBCT}$ ) times the number of MVCBCT MU per fraction ( $n_{MU}$ ) and the number of fractions ( $n_f$ ) where MVCBCT imaging is performed. The doses  $T_{Tx}$  and  $T_{MVCBCT}$  are calculated from the TPS, and Eq. (3.4) can be solved to find  $CF_{MVCBCT}$ , the compensation factor that keeps the mean target dose the same in the compensated plan as in the original treatment plan. The compensation factor reduces the number of MU per treatment beam per fraction. Both the number of fractions and the beam arrangement are kept unchanged. This compensation method was tested on the plans of two prostate patients and one head and neck patient. Dose distributions and DVHs for the plans (treatment alone, uncompensated and compensated) were compared. The compensation method described was applied on

the plans of three patients.

### **Prostate patient treated with 4-field box plus conformal boost**

Figures 3.14 and 3.15 show dose distributions and DVHs for uncompensated and compensated plans for daily 9 MU MVCBCT imaging on a pelvis patient treated with a 4-field box plus conformal boost. As seen with Fig. 3.14 (middle column) and Fig. 3.15 (left) simply adding daily 9 MU MVCBCT to the treatment dose results in a uniform dose increase of approximately 2.7 Gy (40 fractions  $\times$  6.8 cGy). The volume of tissue receiving more than 77 Gy between the left and middle column of Fig. 3.14 is clearly increased. The compensation factor of the first compensated plan was 96%. As observed in Fig. 3.14 (right column), the compensation method reduces the dose in the high-dose region such that the amount of tissue receiving a high dose ( $\sim$ 50 Gy or more) remained the same. Despite the compensation method, the volume of tissue receiving doses less than 50 Gy in the compensated plan was still slightly greater than with the treatment plan alone.

### **Prostate patient treated with IMRT**

Figure 3.16 presents DVHs of uncompensated and compensated plans for daily 9 MU MVCBCT imaging on a pelvis patient treated with IMRT. Similarly to the previous case, a uniform increase in dose was observed for all structures for the uncompensated plan (top). The mean increase in structure mean dose was 2.1 Gy (33

fractions  $\times$  6.5 cGy). The compensation factor found using Eq. (3.4) was 96.8%. As observed in Fig. 3.16 (right), the compensated plan showed no increase in the high dose region and a small increase in the low dose region.

### **Head and neck patient treated with IMRT**

Figures 3.17 and 3.18 show dose distributions and DVHs of uncompensated and compensated plans for daily 5 MU MVCBCT imaging on a head and neck patient treated with IMRT. As seen with Fig. 3.17 (middle column) and Fig. 3.18 (left) simply adding daily 5 MU MVCBCT to the treatment dose results in a uniform dose increase of 1.8 Gy (33 fractions $\times$ 5.5 cGy). The volume of tissue receiving more than 74 Gy between the left and middle column of Fig. 3.17 is slightly increased. The compensation factor of the compensated plan using only the current arc was 97.7%. As observed in Fig. 3.18 (right), the compensation method reduces the dose in the high-dose region such that the amount of tissue receiving a high dose ( $\sim$ 40 Gy or more) remained the same. Despite the compensation method, the volume of tissue receiving less than 40 Gy in the compensated plan was still slightly greater than with the treatment plan alone. The mean difference in structure mean dose between the treatment alone and the compensated treatment plus imaging plan was 0.6 Gy. A simple method to completely eliminate the imaging dose delivered to the lenses will be presented next.



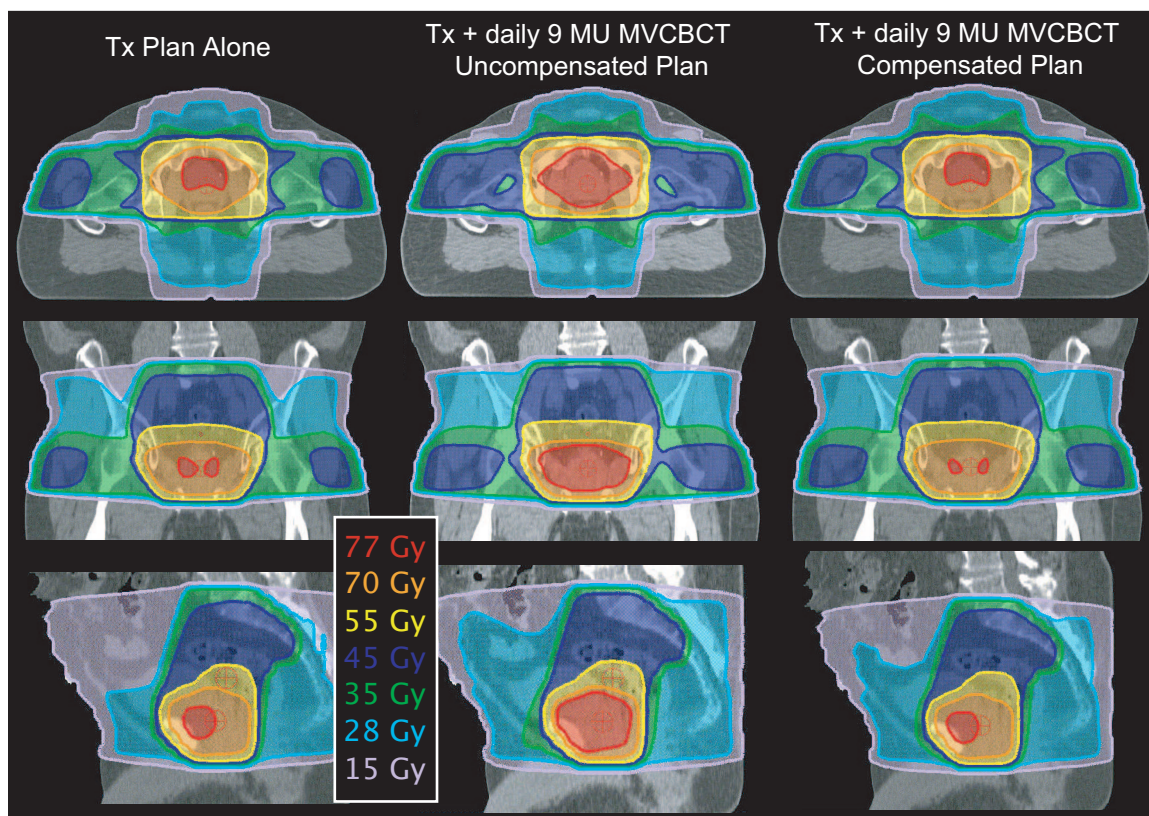


Figure 3.14: Dose distributions calculated on a pelvis patient for different plans combining treatment and MVCBCT imaging dose. This prostate patient was treated with a 4 field box (25 fractions) to the whole pelvis followed by two boosts; the first one including seminal vesicles and prostate (5 fractions), and the second including only the prostate (10 fractions). The treatment plan alone (treatment dose alone) (left) is compared with an uncompensated plan (treatment dose +  $40 \times 9$  MU MVCBCT) (middle) and a compensated plan (96% treatment dose +  $40 \times 9$  MU MVCBCT) (right).

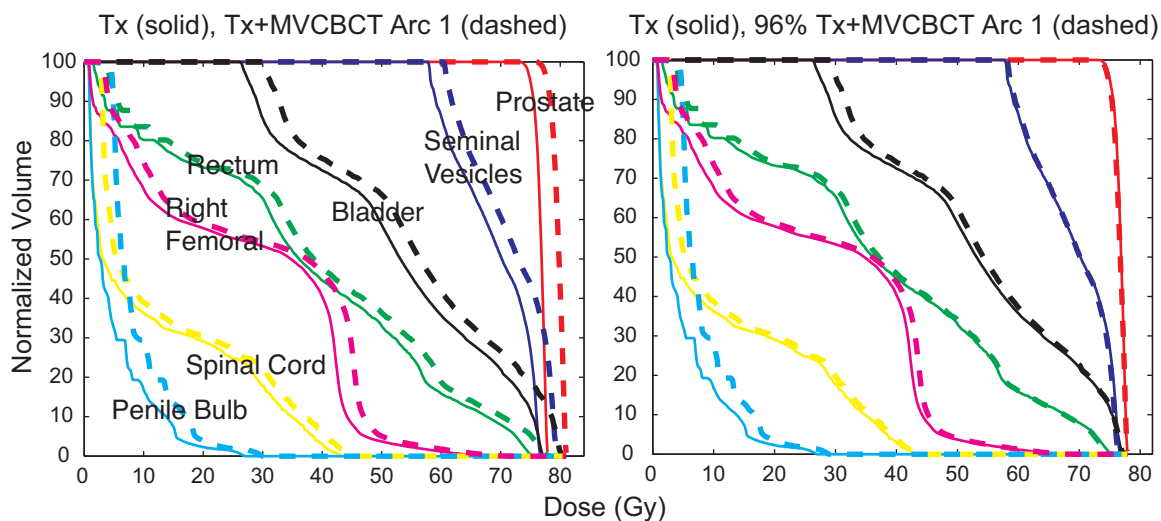


Figure 3.15: DVHs for the prostate patient plans presented in Fig. 3.14. DVHs for the treatment dose alone (solid) were compared with different combinations of treatment and imaging dose (dashed). The treatment plan alone (treatment dose alone) was compared with left - an uncompensated plan (treatment dose +  $40 \times 9$  MU MVCBCT), right - a compensated plan (96% treatment dose +  $40 \times 9$  MU MVCBCT).

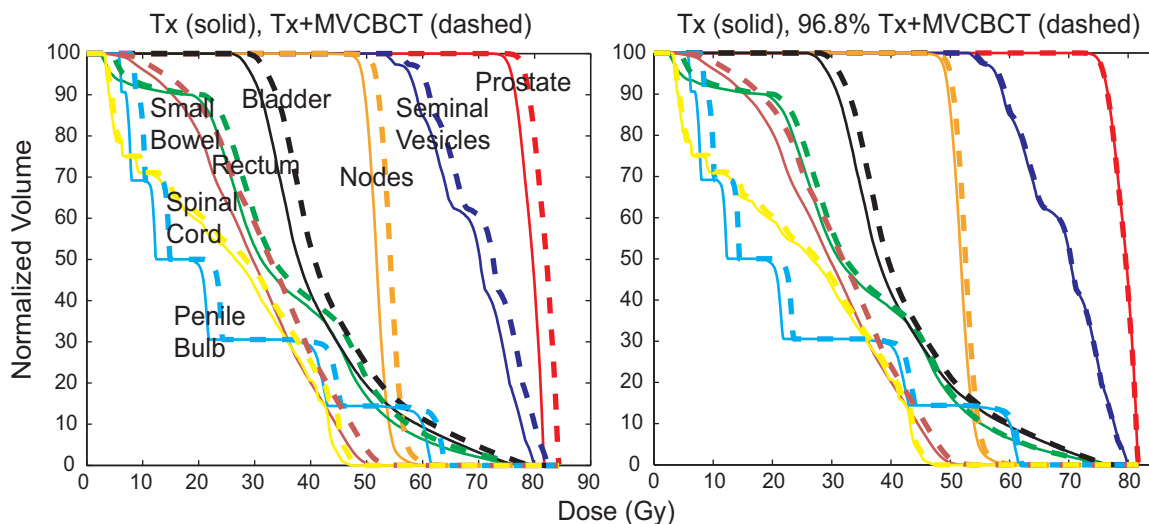


Figure 3.16: DVHs for a prostate patient treated with IMRT. DVHs for the treatment dose alone (solid) were compared with left - the treatment dose added to daily 9 MU MVCBCT (dashed) and right - a compensated treatment dose added to daily 9 MU MVCBCT (dashed).

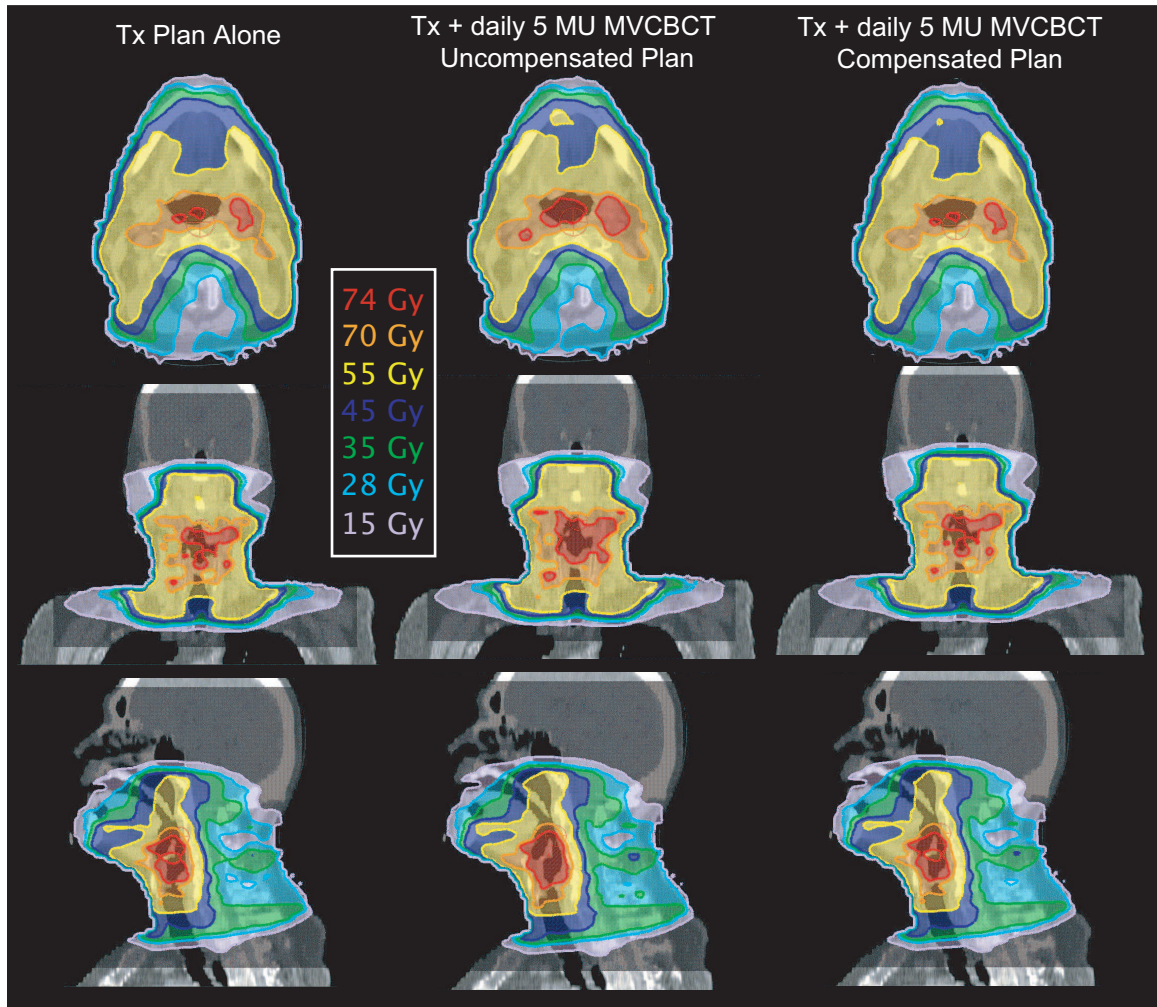


Figure 3.17: Dose distributions simulated on a head and neck patient for different combinations of treatment and MVCBCT imaging dose. The patient was treated with IMRT. The treatment plan alone (treatment dose alone) (left) is compared with an uncompensated plan (treatment dose +  $33 \times 5$  MU MVCBCT) (middle) and a compensated plan (97.7% treatment dose +  $33 \times 5$  MU MVCBCT) (right).

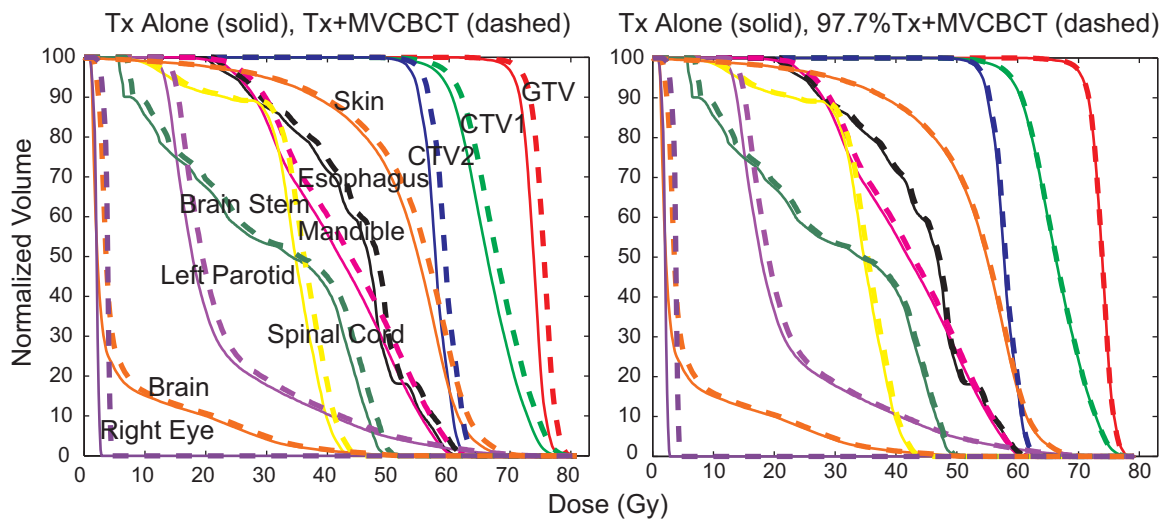


Figure 3.18: Dose volume histograms (DVHs) for the head and neck patient plans presented in Fig. 3.17. DVHs for the treatment dose alone (solid) were compared with left - the treatment dose added to daily 5 MU MVCBCT (dashed) and right - a compensated treatment dose added to daily 5 MU MVCBCT (dashed).

### Plan to minimize the dose to patients

Our approach to minimize the dose delivered from routine MVCBCT imaging has been to incorporate the imaging and the treatment dose in a composite plan. This can be done because MVCBCT uses the same beam for treatment and imaging. Using the treatment and imaging plans simulated in the TPS, a compensation factor was introduced to keep the target mean dose unchanged. This compensation factor can be obtained in less than 10 minutes for all patients. The method was tested on two prostate patients and one head and neck patient. All compensated plans compared to the initial plan without imaging showed no increase in the high dose region and small increases at low dose. For the cases examined, the additional dose in the low-dose region for the compensated plan is considered clinically insignificant. For the head-

and-neck case presented, the maximum doses to the spinal cord for the treatment plan alone and the compensated plan were 44.0 and 44.4 Gy respectively. However, the question whether the compensation method should be applied is still open. Most of our physicians feel no need to compensate for routine MVCBCT because the delivered dose is similar to portal imaging or film, neither of which have been compensated for in the past. However, given the ease of use of the method presented, the additional dose from IGRT could be greatly reduced or documented. Another direct method to reduce the dose to normal tissue, which has been used in our clinic, is to reduce the amount of tissue imaged in the craniocaudal direction. All simulations performed were done using the maximum field size. Closing the Y jaw for imaging can be used to focus on a specific target, such as prostate or to completely avoid dose to critical structures such as the eyes. In addition, collimating the beam reduces the amount of scatter radiation reaching the detector, which slightly improves the image quality. Finally, the most direct method to reduce the MVCBCT dose is to use fewer MU per acquisition. This will become possible with the development of more sensitive detectors for MV imaging [42]. Preliminary investigations also suggest that an optimized beamline for MVCBCT imaging will provide significant improvement in CNR thus allowing a significant reduction of the MVCBCT imaging exposure [55].

## Chapter 4

# Quality Assurance

MVCBCT is now widely used in the community of radiation oncology. The objective of the work presented in this chapter was to evaluate the stability of MVCBCT in order to define a quality assurance (QA) protocol. The criteria used to design the QA protocol included (a) can be done in the radiation oncology clinic, (b) can be performed quickly so that the MVCBCT is not taken out of clinical use, (c) can be performed by therapists or physics staff members, (d) does not require any elaborate equipment and (e) produces quantifiable results that can be documented and followed in time.

This paragraph gives an overview of the method and materials used to assess stability of a MVCBCT imaging system. Our two MVCBCT systems (linac 1 & 2) were followed for a period of 8 months. The systems were fully calibrated (geometry, CT# normalization factor and flat panel corrections) and analyzed daily on the first

week, weekly for a month and monthly thereafter. We specifically investigated the MVCBCT system stability with respect to the beam output, the absolute positioning and the image quality. To investigate how frequently calibration of the MVCBCT system is needed, phantom images were reconstructed on each day of QA using freshly acquired calibrations and only the initial calibration of the system. This chapter establishes a system performance baseline for MVCBCT QA. Our QA recommendations are summarized in Sec. 4.5. Based on the development of the last 5 years, a practical list of possible artifacts occurring with the MVCBCT system was also generated (Sec. 4.4). The library gives insights on how to identify, understand and possibly resolve image artifacts that can occur with the MVCBCT imaging system.

## 4.1 Beam output in MVCBCT mode

The x-ray beam intensity output in MVCBCT mode needs to be characterized and stable for patient safety and to conserve CT# calibration as discussed in Sec. 3.4. Differences in patient dose resulting from a given exposure in MVCBCT and standard treatment mode may occur over time since the dose delivery modes use different tuning parameters in the control console of the linac.

We used a Framer chamber (Model BC 2581 A (0.6 cc), CNMC Company Inc., TN), to verify that the exposure in MVCBCT mode is equivalent to the exposure in standard treatment mode (1 MU MVCBCT = 1 MU treatment) under normal treatment conditions (1 MU = 1 cGy at  $d_{max} = 1.5$  cm for a  $10 \times 10$  cm<sup>2</sup> field size).

Farmer chamber readings in MVCBCT and treatment mode were acquired on each day of QA using the same field size and exposure.

The results showed that the treatment and MVCBCT exposures remained within 3% of each other for a period of 8 months. The maximum variation in exposure for ten consecutive MVCBCT acquisitions was 2%. Therefore, we conclude that the stability of the linac output in MVCBCT mode is excellent.

## 4.2 Absolute Positioning

As discussed in Sec. 3.3, the absolute positioning accuracy and stability of MVCBCT is based on the geometrical relationship between the x-ray source and the EPID in rotation. This relationship is captured in a geometrical calibration procedure described in Sec. 2.1.3. The phantom used for geometric calibration is showed on the left side of Fig. 4.1. The phantom is described in details in Sec. 2.1.3. The geometry must then only be reproducible for the geometrical calibration and the position of the MVCBCT reconstruction volume to remain accurate in the radiation field. The stability of the system geometry was previously demonstrated to be better than 1 mm over a period of 8 months.

To further investigate absolute positioning accuracy, system stability and a simple method for positioning QA, we routinely acquired MVCBCT projection images of a gold seed placed at isocenter with the room lasers. We used an exposure of 20 MU for MVCBCT acquisition to minimize the noise near the reconstructed gold



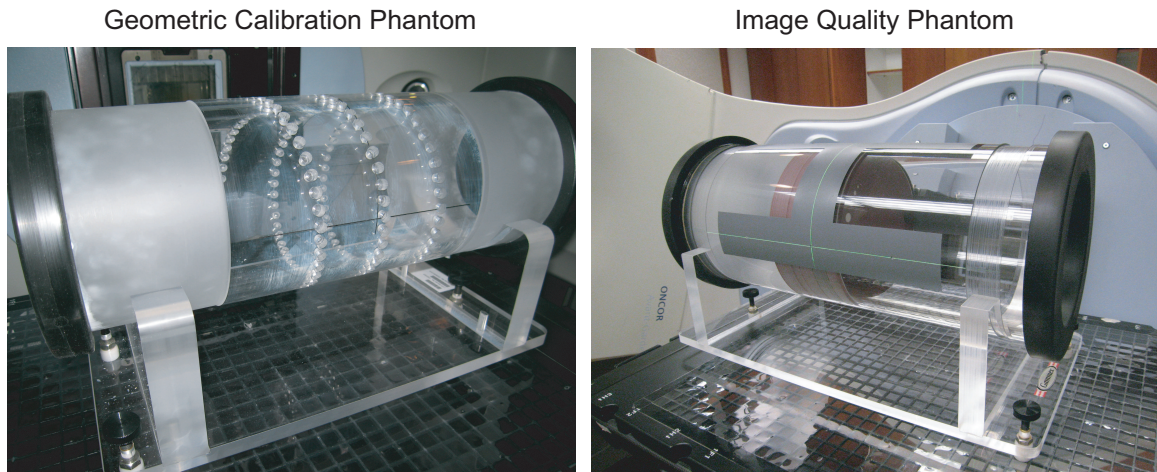


Figure 4.1: Geometric calibration and image quality assurance phantom.

seed. For each day of QA we compared the reconstructed position of the seed using either the initial geometric calibration (acquired on Nov. 4<sup>th</sup>, 2006) or newly acquired geometric calibration. The position of the gold seed relative to the central voxel of the reconstruction can be obtained using the computer workstation (Fig. 2.7).

The reconstructed gold seed positions of linac 1 are presented in Fig. 4.2. The results show great accuracy and stability of the system absolute positioning. The reconstructed seed position remained within 1 mm of the laser point (treatment isocenter) for a duration of 8 months (dates not all showed in the figure). Using only the initial geometric calibration of the system did not cause noticeable reduction in absolute positioning accuracy or image quality. Similar results were observed for linac 2. Therefore, the absolute positioning accuracy and stability of both of our systems was better than 1 mm over a period of 8 months.

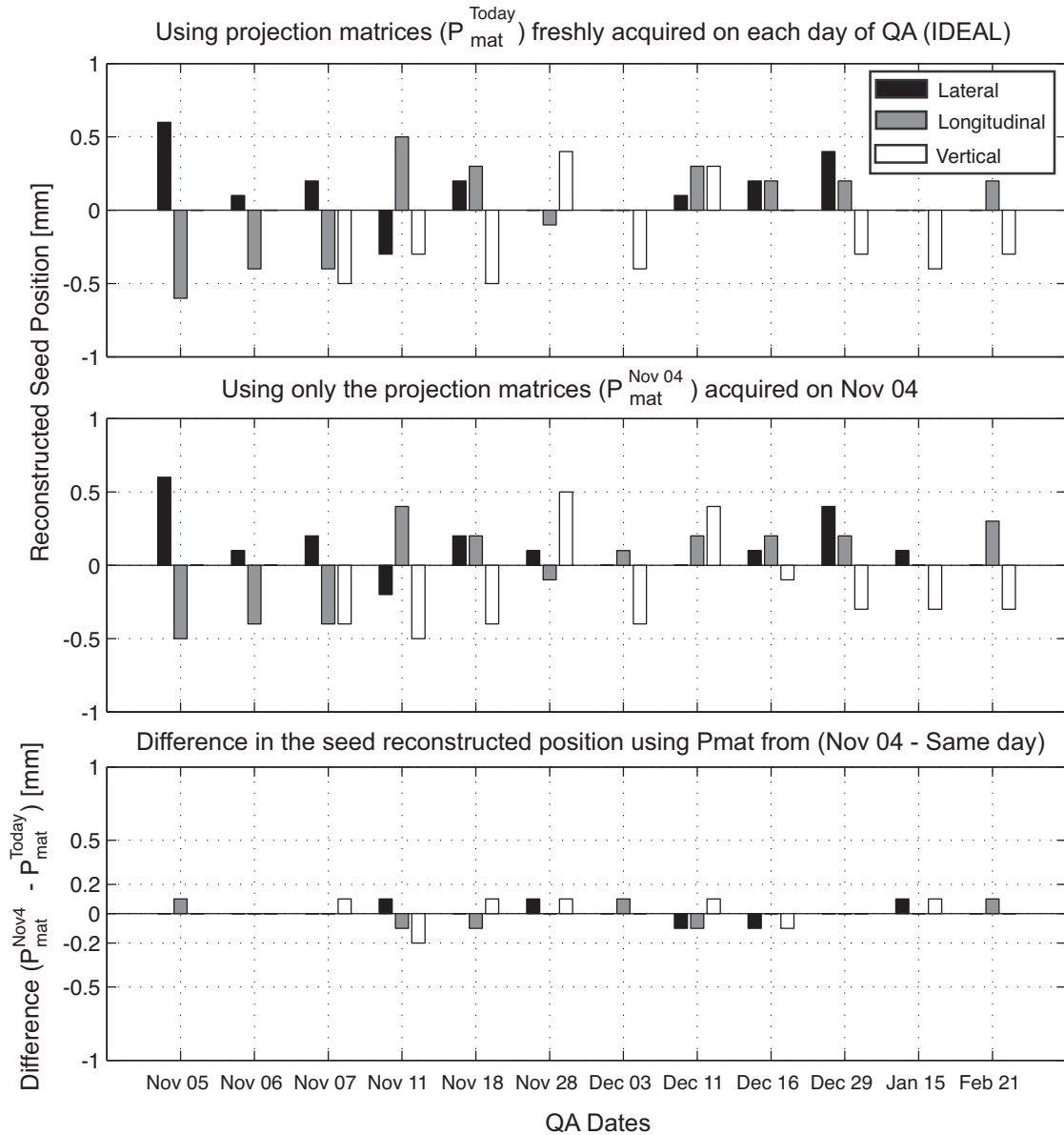


Figure 4.2: Reconstruction position (lateral, longitudinal and vertical) of a gold seed placed at isocenter. For each day of QA, the gold seed was reconstructed using the geometric calibration of the day (top) and the initial geometric calibration (middle) to investigate the required frequency of geometric calibration. The plot at the bottom is the difference between the first two plots. It shows that the geometry stability is excellent (better than 0.5 mm).

### 4.3 Image Quality

Image quality plays an important role in all the clinical applications of MVCBCT. For positioning, the clinical decision often depends on the visualization of a particular bone in the MVCBCT image. It is predictable that components in the MVCBCT system, such as the flat panel detector, will degrade over time thus reducing the MVCBCT image quality. Establishing an imaging performance baseline and a quality assurance protocol are key to define when components of the system are no longer performing optimally.

To assess imaging performance over time we acquired routine images of an image quality phantom (EMMA) provided by Siemens (Siemens Oncology Care Systems, Concord, CA) as part of the MVision™ product. EMMA (displayed on the right of Fig. 4.1) was specifically designed for imaging QA. We developed a graphical user interface (called MVCBCT<sub>QA</sub>) with Matlab (The Mathworks, Inc., Natick, MA) to semiautomatically analyze EMMA. The graphical user interface illustrated in Fig. 4.3 automatically extracts the sections of interest in the MVCBCT image of the phantom, lets the user adjust the position of predrawn (or predefined) regions-of-interest (ROI) and finally produces quantitative assessment on the main image quality components.

The phantom contains 4 sections: high-contrast, low-contrast, spatial resolution and uniformity & noise. A complete description of the phantom specifications is provided in Fig. 4.3. EMMA is a cylindrical phantom measuring 20 cm in diameter and 60 cm in length. The phantom is made of special plastic mimicking the electron

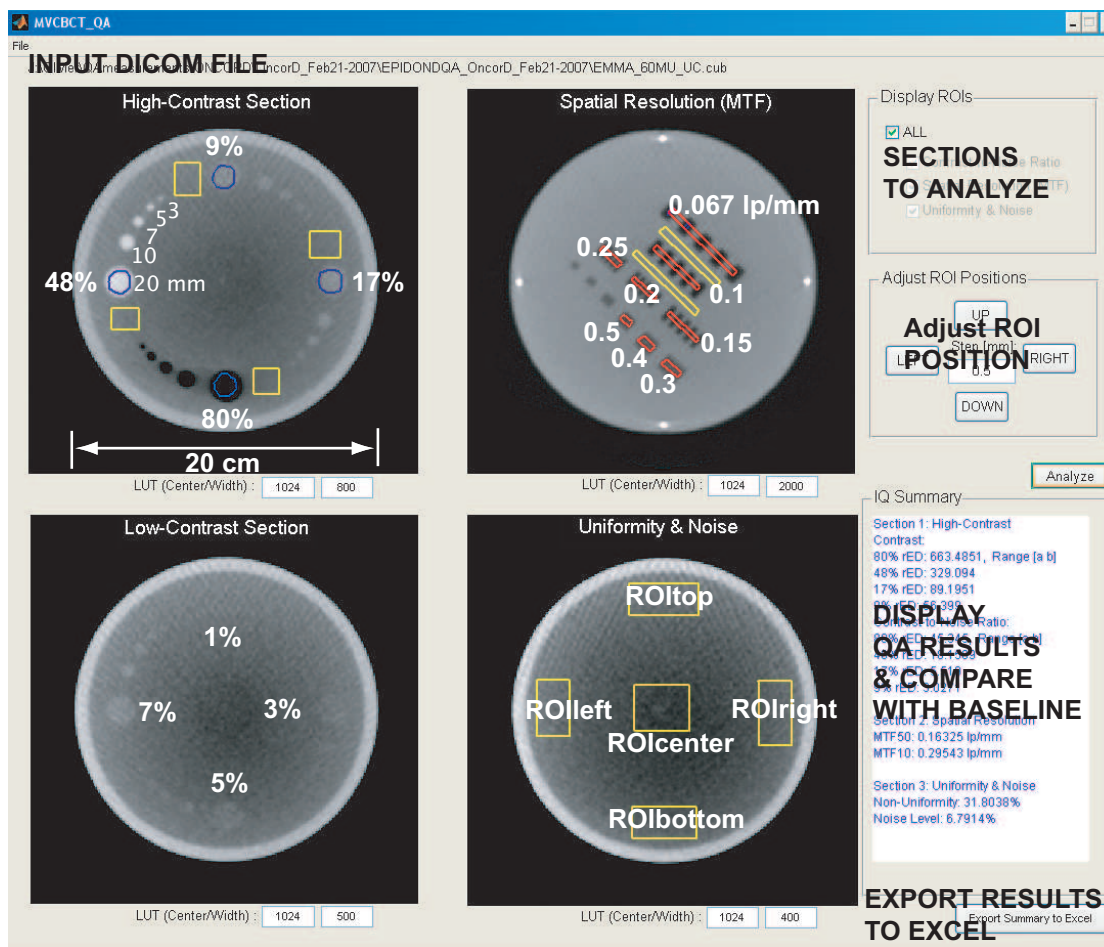


Figure 4.3: Graphical user interface developed to automatically analyze EMMA images.

density of water. Such plastic is often called a solid water material.

The high-contrast section contains inserts of varying size (20, 10, 7, 5, 3 mm) and electron density relative to solid water ( $rED = 80\%$ ,  $48\%$ ,  $17\%$  and  $9\%$ ), which were used to assess stability of the reconstructed CT# and the contrast-to-noise ratio (CNR). The reconstructed CT# for a  $rED$  is simply the mean signal of the largest ROI. The CNR of insert  $i$  ( $CNR_i$ ) was calculated using the mean ROI pixel value of insert  $i$  ( $\text{mean}(\text{ROI}_i)$ ) with the mean and standard deviation of the ROI pixel values

in a background region ( $\text{mean}(\text{ROI}_b)$ ,  $\text{std}(\text{ROI}_b)$ ) drawn in solid water near insert  $i$ .

The CNR of insert  $i$  was calculated using

$$\text{CNR}_i = \frac{\text{mean}(\text{ROI}_i) - \text{mean}(\text{ROI}_b)}{\text{std}(\text{ROI}_b)} \times 100 \quad (4.1)$$

The low-contrast section has inserts of smaller differences in electron density relative to solid water (rED = 7%, 5%, 3% and 1%). Performances in the low-contrast section were not reported due to high subjectivity in assessing the inserts' positions. The section could have been used to define the smallest low-contrast insert that can be visualized on MVCBCT images for each rED. Such task is highly user and display condition dependent and therefore we decided not to report those results.

The spatial resolution section contains line pairs of different spatial frequencies (0.067, 0.10, 0.15, 0.20, 0.25, 0.30, 0.40, 0.50, 0.60, 0.80, 1.00 line pairs per mm or lp/mm). To assess the spatial resolution of the system quantitatively, we calculated the modulation transfer function (MTF) using the method developed by Droege *et al* [49]. We report the MTF at 50% (MTF<sub>50</sub>) and 10% (MTF<sub>10</sub>) of the maximum.

The uniformity and noise section is simply a large circular slab of solid water. It can not only be used to measure the noise and uniformity but also to potentially observe image artifact. ROIs were drawn at the periphery and in the center of the section. The noise (expressed in % of the mean signal) was calculated using the average mean and standard deviation (stdev) values of all the ROI (ROIs) in the section which include ROI<sub>bottom</sub>, ROI<sub>left</sub>, ROI<sub>top</sub>, ROI<sub>right</sub> and ROI<sub>center</sub>. The noise

was calculated with the following equation.

$$Noise = 100 \times \frac{stdev(ROIs)}{mean(ROIs)} \quad (4.2)$$

The nonuniformity (NU) (expressed in % of the mean signal) was calculated with the mean ROI pixel value at the periphery of the phantom ( $ROI_{periphery}$  consists of the average mean and standard deviation from the following ROI:  $ROI_{bottom}$ ,  $ROI_{left}$ ,  $ROI_{top}$  and  $ROI_{right}$ ) with the mean ROI pixel value in the center ( $ROI_{center}$ ). The NU was obtained with the following equation.

$$NU = 100 \times \frac{mean(ROI_{periphery}) - mean(ROI_{center})}{mean(ROIs)} \quad (4.3)$$

EMMA was imaged over a period of 8 months using an exposure of 9 MU, a reconstruction size of  $(512 \times 512)$  for transverse images and a slice thickness of 0.5 mm. Transverse slices were combined with a Gaussian averaging filter to obtain a new slice thickness of 5 mm. Images were obtained using the initial calibrations and fresh calibrations acquired at the day of QA. All images were imported in  $MVCBCT_{QA}$  to extract the imaging performance over time. The image quality results were exported to Microsoft Excel for further data analysis.

Tables 4.1, 4.2 and 4.3 summarize the imaging performance results of our 2 linacs over a period of 8 months. For linac 1, the results on the image quality components (CT#, CNR, MTF, uniformity and noise) were nearly identical whether an old calibration of the system or daily recalibration were used. Linac 2 showed more variability (larger standard deviation) in the CT# values than linac 1 for images

Table 4.1: Contrast-to-noise ratio (CNR) quality assurance performance for inserts of different electron density relative to water (rED).

Using fresh calibrations			Using only the initial calibration	
<b>Linac 1</b>				
rED	Mean	CNR	Mean	CNR
48%	$1216.2 \pm 7.5$	$18.7 \pm 1.5$	$1217.6 \pm 6.4$	$18.2 \pm 1.4$
17%	$969.7 \pm 5.8$	$6.1 \pm 0.4$	$970.9 \pm 7.3$	$5.8 \pm 0.4$
9%	$957.6 \pm 5.9$	$3.1 \pm 0.3$	$959.2 \pm 7.1$	$3.1 \pm 0.2$
<b>Linac 2</b>				
rED	Mean	CNR	Mean	CNR
48%	$1173.9 \pm 7.6$	$19.1 \pm 2.6$	$1163.2 \pm 23.1$	$17.5 \pm 2.1$
17%	$948.6 \pm 7.0$	$5.7 \pm 0.6$	$938.4 \pm 24.6$	$6.6 \pm 0.6$
9%	$926.4 \pm 8.5$	$3.5 \pm 0.4$	$916.8 \pm 25.9$	$3.7 \pm 0.3$

acquired using only the initial calibration of the system. These results indicate that linac 2 may require the CT# to be calibrated more often (probably once a month). The other components of image quality for linac 2 showed similar stability than linac 1. Only small performance differences were observed between linacs. For example, the percentage differences in CNR, MTF, uniformity, and noise were all better than 3%. The noise and nonuniformity were smaller than 2%.

Overall, both system showed excellent stability over a period of 8 months. Monthly acquisition of images with EMMA will continue to be acquired to follow the long-term (> 2 years) imaging performance stability of MVCBCT.

Table 4.2: Spatial resolution quality assurance performance. The modulation transfer function (MTF in line pairs per mm) is reported at 50% (MTF<sub>50</sub>) and 10% (MTF<sub>10</sub>) of the maximum value.

Using fresh calibrations		Using only the initial calibration
<b>Linac 1</b>		
MTF <sub>50</sub>	$0.16 \pm 0.00$	$0.16 \pm 0.00$
MTF <sub>10</sub>	$0.29 \pm 0.01$	$0.29 \pm 0.01$
<b>Linac 2</b>		
MTF <sub>50</sub>	$0.16 \pm 0.00$	$0.16 \pm 0.01$
MTF <sub>10</sub>	$0.29 \pm 0.01$	$0.29 \pm 0.02$

Table 4.3: Uniformity and noise quality assurance performance.

Using fresh calibrations			Using only the initial calibration	
<b>Linac 1</b>				
ROI positions	Mean	Std	Mean	Std
Top	$940.4 \pm 3.6$	$17.2 \pm 0.8$	$941.0 \pm 3.6$	$17.5 \pm 0.9$
Right	$916.8 \pm 4.1$	$16.3 \pm 0.9$	$917.9 \pm 4.2$	$15.8 \pm 0.5$
Center	$940.4 \pm 4.2$	$21.7 \pm 0.9$	$940.1 \pm 4.2$	$21.6 \pm 0.3$
Uniformity (%)	$1.6 \pm 0.1$		$1.5 \pm 0.2$	
Noise (%)	$1.9 \pm 0.0$		$1.8 \pm 0.0$	
<b>Linac 2</b>				
ROI positions	Mean	Std	Mean	Std
Top	$902.5 \pm 8.2$	$15.4 \pm 0.6$	$889.3 \pm 26.0$	$15.9 \pm 0.8$
Right	$891.9 \pm 5.6$	$14.3 \pm 0.7$	$882.7 \pm 23.6$	$14.0 \pm 0.8$
Center	$910.8 \pm 4.8$	$19.2 \pm 1.1$	$900.8 \pm 22.9$	$19.1 \pm 0.8$
Uniformity (%)	$1.8 \pm 0.2$		$1.8 \pm 0.3$	
Noise (%)	$1.7 \pm 0.0$		$1.7 \pm 0.1$	



## 4.4 Practical Artifact Library

Over the last 4-5 years of development, image artifacts and their causes were documented. This section summarizes the possible artifacts occurring with MVCBCT. For each artifact, we describe the imaging defect, explain the possible causes, evaluate its severity and likelihood of occurring in the clinic and give possible remedies. The artifacts are illustrated in Figs. 4.4 and 4.5.

### A) Truncation

*Description:* As illustrated in Fig. 4.4a, truncations in the projection data and therefore in the MVCBCT reconstruction cause an overestimation of the CT# near the truncated anatomy and an underestimation of the CT# in the center of transverse slices for longitudinal positions affected by truncation of anatomy. The reconstruction noise is also increased in the affected transverse slices. Images may be reconstructed having streaks near truncated bony structures. *Cause(s):* The patient body extends beyond the field-of-view of the imaging system. Parts of the anatomy are therefore missing on some projections of the acquisitions. i.e. the attenuation occurring in the shoulders and pelvis are not completely represented for image reconstruction (incomplete Fourier domain). The truncation causes addition of high frequency components (noise) in the reconstruction. *Likelihood:* Occurs longitudinally when the anatomy extends the current field-of-view of 27 cm. In the clinic, truncation artifacts will occur in the shoulders, the thorax and pelvis. *Severity:* Dependent on anatomical site and strongly reduce image quality. *Remedy:* None. An extrapolation technique

is currently used in the reconstruction but does not eliminate the artifact.

### **B) Bad gain**

*Description:* As illustrated in Fig. 4.4b, improper gain calibration creates rings with discontinuous CT#. The central point of transverse slices show a clear underestimation of the CT#. *Cause(s):* The gain calibration of the flat panel detector is no longer valid. Simulations performed by mathematically imposing gain calibration errors demonstrated that the gain needs to be off by at least 20% to see this artifact. A difficulty of obtaining a gain calibration may be a sign of detector aging causing unstable amplification of the detector sections. Electrical noise in the wire has also been identified (observed by changing a stretched power cable connected to the flat panel detector) as a cause of difficult gain calibration. *Likelihood:* Extremely rare but should increase over the life-span of the detector. *Severity:* Strongly reduce image quality, which may hinder the ability to see anatomical structures. Reacquiring the image on a patient would likely not help due to errors in gain calibration. *Remedy:* Recalibrate the flat panel gain and verify the stability of the panel sensitivity after several deployment of the flat panel positioner. Deployment of the positioner may be used to diagnose a difficulty to acquire gain calibration due to a stretched or damaged cable.

### **C) Offset**

*Description:* As illustrated in Fig. 4.4c, offset artifacts are characterized by an underestimation of the CT# along the longitudinal axis at isocenter. The artifact may

be discontinuous along the longitudinal axis. *Cause(s)*: The dark current of the flat panel not being properly removed before backprojection. *Likelihood*: Extremely rare. *Severity*: This artifact can significantly complicate the process of identifying anatomical structure at and around the isocenter (e.g. prostate, bladder and rectum wall). *Remedy*: Wait 5-10 minutes with the x-ray beam off to let the flat panel refresh its offset for all integration time. This calibration is updated automatically when the beam is off. Contact vendor, the system may not acquire the offset for the full range of integration times needed during MVCBCT imaging.

#### **D) Dead pixels**

*Description*: As illustrated in Fig. 4.4d, dead pixels result in streaking and faint ring artifacts concentric to isocenter. *Cause(s)*: Transient cluster of dead pixels. *Likelihood*: Extremely rare. *Severity*: The median filter applied to the projections makes this a rare event. *Remedy*: Reacquire dead pixel map.

#### **E) Missing projection(s)**

*Description*: As illustrated in Fig. 4.4e, a missing projection artifact is characterized with lines visible along strong anatomical features. *Cause(s)*: Linac and/or hardware failure. The systems allows up to ten missing projections. *Likelihood*: Extremely rare. Simulations of removing projection images on purpose have indicated that the artifact is only visible if three or more subsequent projections are missing. *Severity*: Increase image noise and reduce soft-tissue resolution. *Remedy*: Reduce speed of the gantry and verify acquisition card of flat panel.

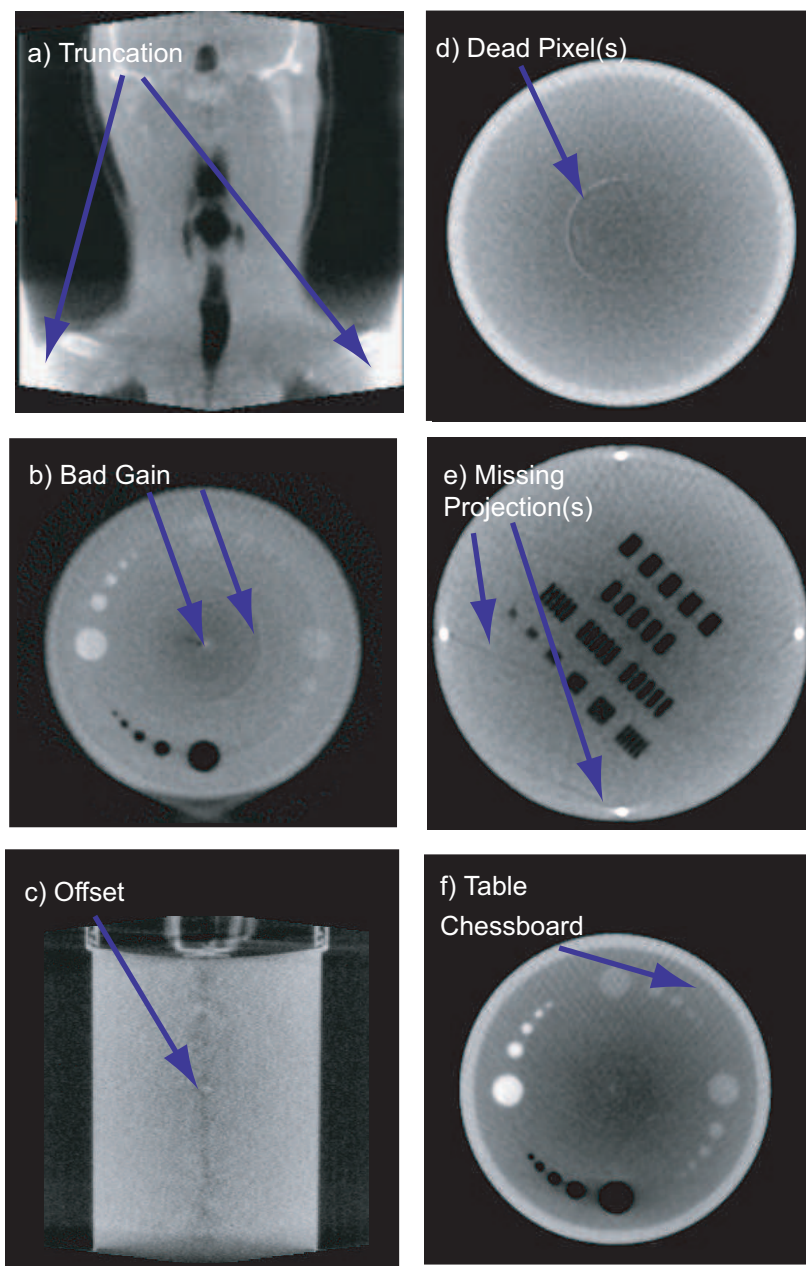


Figure 4.4: Library of image artifacts possibly occurring with MVCBCT imaging.

## **F) Table Chessboard**

*Description:* As illustrated in Fig. 4.4f, the current patient table causes a faint fine mesh ( $3 \times 3 \text{ mm}^2$ ) with generally 2 specific angles for the mesh lines. *Cause(s):* This artifact is related to truncation since it is caused by the fact that the table is only seen on some projections of the acquisition. *Likelihood:* Always present. Less severe for table causing a more uniform attenuation. *Severity:* Increase image noise and reduce soft-tissue resolution. *Remedy:* None. Future tabletop should attenuate the x-ray beam more uniformly thus causing less artifact.

## **G) Flat panel shifts**

*Description:* As illustrated in Fig. 4.5g, shifts in the position of the flat panel cause artifacts that are difficult to visualize. Longitudinal shift of the flat panel out of calibration will cause positioning error and are practically invisible. A lateral shift will cause crescent-shaped shadow and streaks around regions with strong contrast. *Cause(s):* Mechanical failure of the flat panel positioner potentially caused by physical contact. The geometric calibration of the system becomes no longer valid. *Likelihood:* Rare. *Severity:* Warning. Longitudinal shift will result in positioning error of the same magnitude as the flat panel shift. *Remedy:* Recalibrate the flat panel position and the MVCBCT system geometry. Perform the proposed daily or weekly QA with gold seed to capture this possible problem.

## **H) Cupping**

*Description:* As illustrated in Fig. 4.5h, the cupping artifact is characterized by an

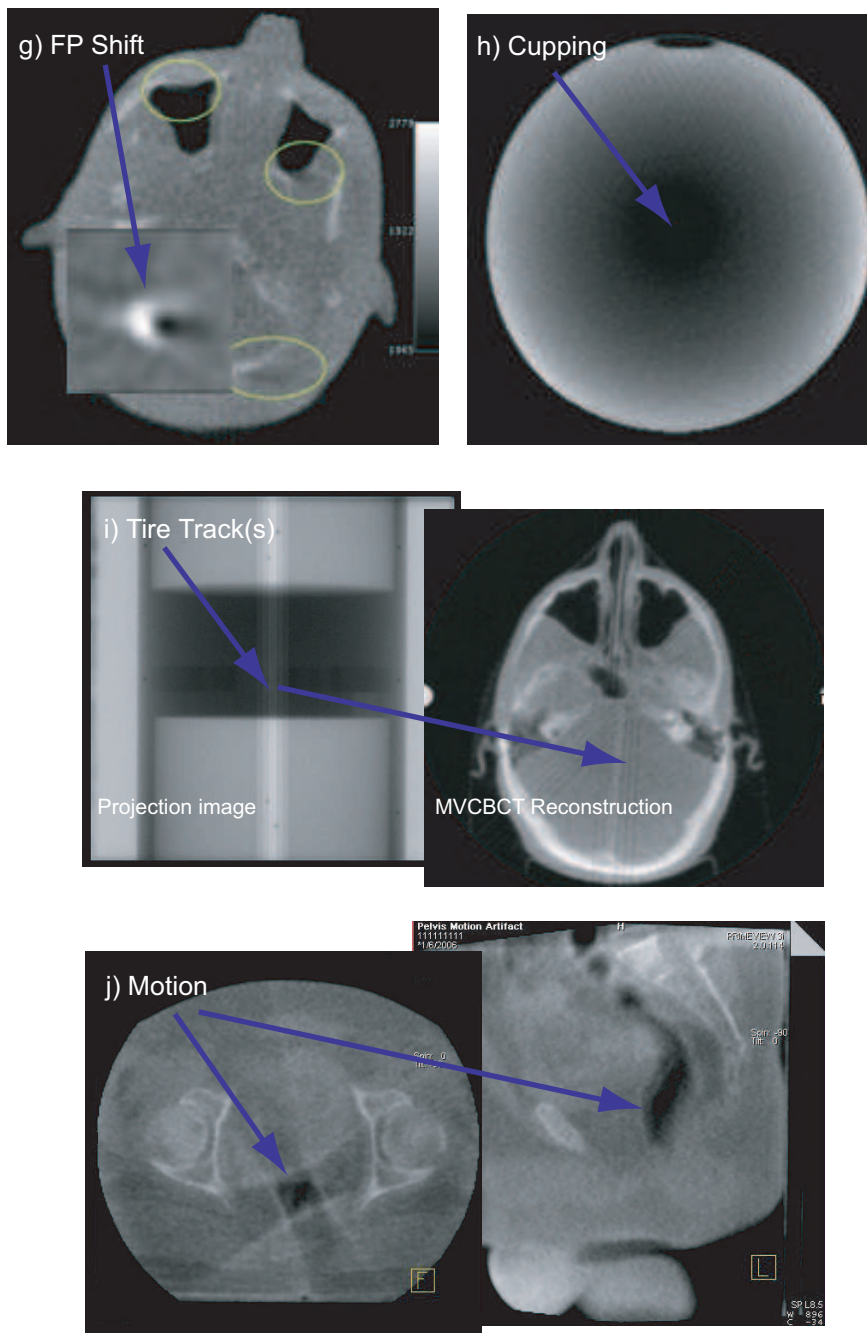


Figure 4.5: Library of image artifacts possibly occurring with MVCBCT imaging -continued.

overestimation of the CT# at the periphery of transverse slices and an underestimation of the CT# in the center of the reconstruction. Such artifact reduces the uniformity of MVCBCT. In 3D the cupping has an elliptical profile as previously illustrated in Fig. 3.5. *Cause(s)*: The panel response with energy added to x-ray scattered photons accumulating on the center of projections. The gain calibration done in air compensates for the harder beam on-axis which in turns amplifies the presence of scatter during image acquisition. *Likelihood*: Always present. *Severity*: Makes the window/level adjustment difficult and therefore the simultaneous visualization of anatomy at the periphery and in the center of transverse images is strongly reduced. *Remedy*: Reducing the craniocaudal field size for imaging slightly reduces the artifact (Sec. 3.5.1). The user can also acquire the gain calibration with a 1.27 cm lead plate in the accessory tray. Finally, this artifact can be nearly eliminated by choosing proper postprocessing uniformity correction filter (head and neck or pelvis).

### **I) Tire Track (s)**

*Description*: As illustrated in Fig. 4.5i, tire tracks consist of oblique alternating white and dark lines affecting the CT# for the specific projection angles affected by the problem. The lines are best seen in axial images. *Cause(s)*: One or several projections were not perfectly synchronized with the beam output. Subsequent projections have pulse artifact in the center of the projection image. *Likelihood*: Small. *Severity*: Strong artifact that can hinder the ability to align anatomical structure close to target. *Remedy*: Reduce speed factor of the gantry for MVCBCT acquisition.

## J) Motion

*Description:* As illustrated in Fig. 4.5j, patient or anatomical motion occurring during image acquisition result in a lost of sharpness around high-contrast anatomical structures (bone and air cavities). *Cause(s):* Patient or internal organ motion. *Likelihood:* Patient-specific but rare. *Severity:* Difficult to rely on the image due to uncertainty in patient position. May need to repeat acquisition. *Remedy:* None. Communicate with patient to notify the start of imaging and treatment.

## 4.5 Recommendations for Quality Assurance

Our recommendations for quality assurance are summarized in Table 4.4. The recommended tasks for daily, monthly and binannual QA are specified with an approximation of the time required for the tasks.

### Beam output

The beam output should be verified as part of the linac monthly QA or anytime the treatment beam is adjusted. We use a Farmer chamber (or an ion chamber) to measure the beam output in both the MVCBCT and treatment mode. Our tolerance is currently fairly loose (5%) in the allowable difference in beam output between the two modes since 5% error in MVCBCT exposure has nearly no effect on the patient dose even for routine MVCBCT imaging (Sec. 3.7).



Table 4.4: Recommendations for quality assurance of MVCBCT. Daily, monthly and binannual QA tasks are specified with an approximation of the total time required for the tasks.

	Daily	Monthly	Every 6 months
Task	-EPID positioning with x-reticule	-Absolute positioning (seed) -Image quality (EMMA)	-System calibrations -MVCBCT dose
Time	3-5 minutes	5-10 minutes	2-3 hours

### **Absolute positioning**

The geometric calibration of MVCBCT should be done twice a year or anytime the flat panel detector position is adjusted. We still recommend that the position of the flat panel detector (EPID) should be verified daily using an accessory (x-reticule) imaged at gantry position  $0^\circ$  and  $90^\circ$  to prevent geometric misalignments caused by sudden mechanical failures. We also recommend imaging a fiducial (gold seed) with MVCBCT on a monthly basis to verify absolute positioning with the MVCBCT system.

### **Image quality**

Given the current lack of tool provided by Siemens OCS to perform QA imaging with EMMA, it is difficult to give recommendations to nonacademic institutions. Assuming that an image quality application will be provided in a near future, we recommend acquiring and analyzing monthly images of EMMA to establish a baseline of QA performance for the main components of image quality (CT#, CNR, MTF, uniformity, noise). More than one image of EMMA should be acquired every month to assure a proper analysis of the system imaging performance. At our institution,

we currently acquire two images of EMMA per MVCBCT system each month. These two images can then be analyzed and compared to the performance baseline of a typical imaging protocol used in the clinic. Flat panel calibrations (gain and dead pixel map) should be acquired twice a year unless clear image quality degradation is observed in data monthly acquired with EMMA.

## Part II

# Clinical Applications

# Chapter 5

## Overview

The clinical applications of in-room volumetric imaging are increasingly advancing the speciality of radiation oncology. For the first time, these methods allow radiotherapy to have direct use of the wealth of information from 3D imaging for diagnostic, treatment planning and patient anatomy verification. Changes in tumor position, size, and shape that take place during radiotherapy can now be measured and accounted for each particular patient to fully benefit from the highly conformal treatment provided by 3DCRT and IMRT.

In advances over the last 10 years, institutions have started exposing numerous cases of clinically significant organ motion, anatomy changes and positioning errors that simply could not be corrected using conventional methods. Although the technological advances in IGRT have potential to improve clinical outcomes, no one of the six IGRT technology presented in the introduction is appropriate for all clinical sce-

narios. This dissertation illustrates the potential uses of MVCBCT through selected clinical examples.

Our simple system presented in Fig. 2.7 opens the possibility for new mechanisms of verification and feedback into the clinical processes or radiation oncology. Figure 5.1 outlines different IGRT strategies made possible by the system. One possibility is the monitoring of intra-fraction motion of high-contrast features or fiducial markers using the flat panel in ciné mode [5]. This could be used to continually modify (gate) treatments for anatomical sites where motion may be problematic during the course of a single treatment session.. This application is not yet possible with current technology, but remains a goal for future research. With the same system, portal imaging can be used to ensure setup based on bony anatomy or gold seeds. Finally, with the introduction of an MVCBCT acquisition mode, it is possible to perform 3D setup based on bony anatomy and soft tissues to determine patient specific anatomical variation using images. This new information can be used to tailor the treatment plan for future fractions to account for the individuals variation.

The following chapters describe the work that has been done to introduce MVCBCT in the clinic. Chapter 6 compares two positioning methods using phantom and head and neck data. We also show the use of MVCBCT to locate and position stationary tumor in the lung. Finally, the use of MVCBCT to align particular patients with pelvis and spinal tumor is investigated. Chapter 7 evaluates the capability of monitoring changing anatomy over the course of treatment with MVCBCT. Chapter 8

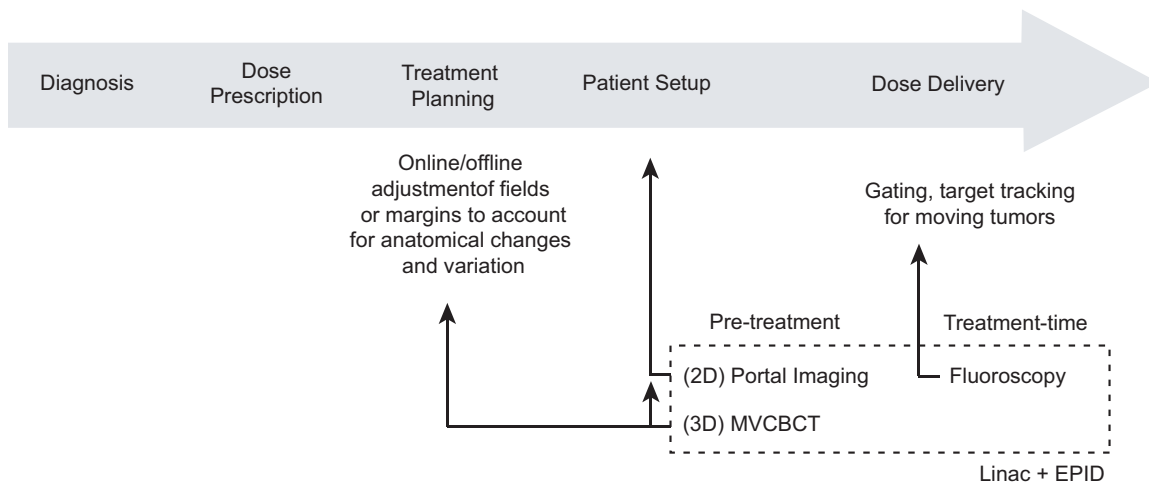


Figure 5.1: An overview of various image-guided radiation therapy schemes using only a conventional linac and a flat-panel EPID. The large grey arrow represents the conventional flow of treatment with the main radiotherapy processes, and the small arrows indicate the possible points of feedback into the processes.

aims at validating MVCBCT for dosimetric applications. Chapter 9 describes other possible applications with MVCBCT.

## 5.1 Examples of Clinical Images

Since the first patient imaged with MVCBCT in 2003 at our institution, 400 acquisitions have been performed on a total 95 patients. The anatomical sites imaged include head and neck, lung, pelvis, breast and spine. The exposure used for MVCBCT imaging ranges from 2 and 15 MU for patient alignment and 10 and 20 MU for planning purpose. Figure 5.2 shows side-by-side views of conventional CT and MVCBCT for typical pelvis (right) and head and neck (left) patients. For example, soft tissue structures such as the trapezius, the obturator internus, the gluteus

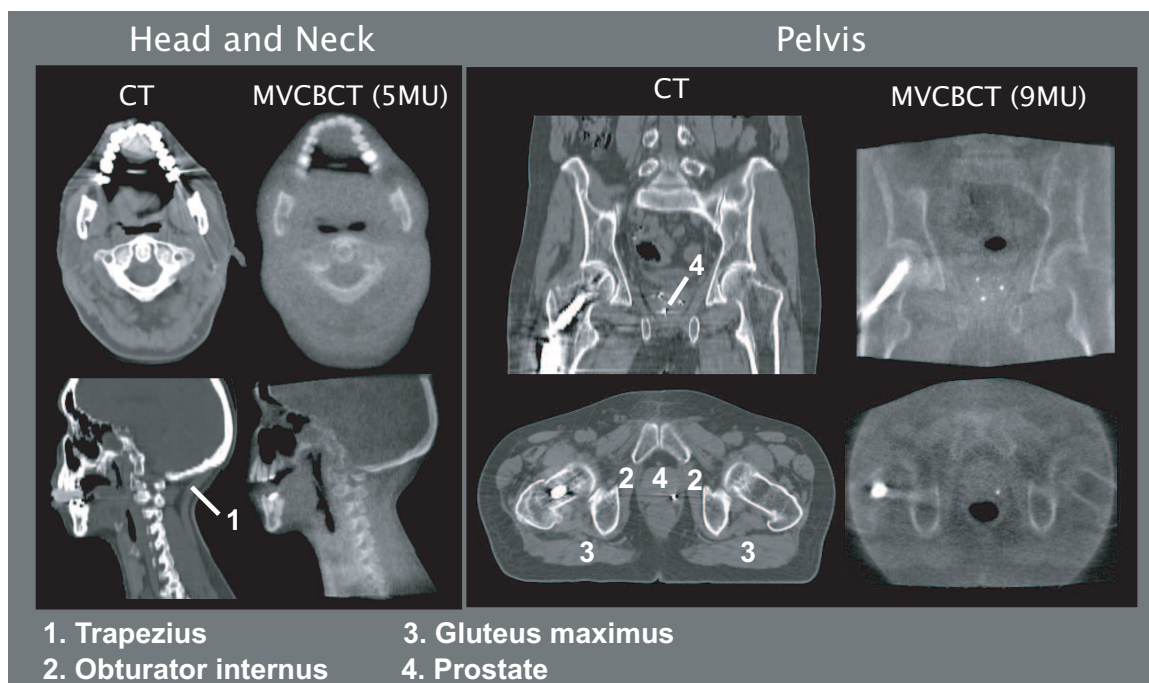


Figure 5.2: Typical MVCBCT images for head and neck (5MU) and prostate (9 MU) patients compared to conventional CT. The image quality of MVCBCT is sufficient to perform a 3D alignment based on bony anatomy and soft tissue. Several muscles and the prostate can be identified on both the CT and MVCBCT images. CT and MVCBCT images are not displayed with the same window and level.

maximus and the prostate gland are identified on both the CT and MVCBCT images of Fig. 5.2. MVCBCTs with exposure as low as 2 MU and 10 cm imaging length in the craniocaudal direction have been used in the clinic for simpler setup cases such as prostate patients with implanted gold seeds. The next section summarizes the MVCBCT imaging protocols used in the clinic for specific applications and body site.

## 5.2 Proposed Imaging Protocols

The explored clinical applications of MVCBCT presented in the next sections have different requirements for imaging performance. Patient setup generally necessitates the best image quality within the usual tight time constraint while using MVCBCT for off-line treatment planning can be performed over more extended periods of time. Using the work presented in Chap. 3 and our clinical experience of the last 4-5 years, we summarized the imaging protocol to use for a specific application and body site. The main factors affecting the image quality of MVCBCT are the radiation exposure, the voxel size, the final slice thickness and the body site imaged. Table 5.1 specifies the exposure, the reconstruction size, the slice thickness, the longitudinal FOV and the reconstruction kernel that provide the best imaging performance. Because the reconstruction algorithm is voxel-based, it is always better to reconstruct using 1 mm slice thickness but in a way that allows the slices to be averaged over 3 or 5 mm for planning applications. In our clinic, we use Matlab and MeVisLab to combine the numerous slices (up to 274) obtained from computer workstation. Averaging slices improves the CNR and reduces the number of slices to import in the treatment planning system. Finally, the future availability of diffusion filtering also should reduce the exposure needed to perform a clinical task.



Table 5.1: MVCBCT acquisition protocol recommendations for a specific clinical application and body site. The radiation exposure used in our clinic is slightly lower than reported since all reconstructions are processed with diffusion filtering. The right arrow ( $\Rightarrow$ ) signifies that the user should resample or combine transverse slices before analysis.

	Patient Setup <i>Daily or weekly imaging</i>	Planning or DGRT <i>Imaging once or twice</i>
Head & neck	Exposure (MU): 5-10 (bone) Recon Size: 256×256 Slice Thickness: 1 $\Rightarrow$ 3 mm FOVz: exclude eyes if possible Kernel: Smoothing - H&N	Exposure: 10-20 MU Recon Size: 512×512 Slice Thickness: 1 $\Rightarrow$ 5 mm FOVz: exclude eyes if possible Kernel: Smoothing - H&N
Chest or breast	Exposure (MU): 5-10 (bone) Recon Size: 256×256 Slice Thickness: 1 $\Rightarrow$ 3 mm FOVz: full length Kernel: Smoothing - Pelvis	Exposure: 15-20 MU Recon Size: 512×512 Slice Thickness: 1 $\Rightarrow$ 5 mm FOVz: full length Kernel: Smoothing - Pelvis
Pelvis	Exposure (MU): 3-5 (seeds) 5-10 (bone), 10-15 (soft-tissue) Recon Size: 256×256 Slice Thickness: 1 $\Rightarrow$ 3 mm FOVz: full length Kernel: Smoothing - Pelvis	Exposure: 15-20 MU Recons Size: 512×512 Slice Thickness: 1 $\Rightarrow$ 5 mm FOVz: full length Kernel: Smoothing - Pelvis

## Chapter 6

# Patient Positioning

Patient immobilization and control of target position still remain critical problems in the radiotherapy processes. As a consequence, fairly large security margin (1 cm or more) are used around the tumor during treatment planning but which can increase dose delivery to normal tissues and compromise the potential sparing capabilities of modern conformal radiation delivery techniques. Poor tumor position control on a daily basis and the lack of confidence for tumor delineation are now clearly recognized as the two main sources of error that limit the implementation of new dose escalation protocols which could improve cure rates and/or reduce normal tissue complications.

This chapter compares the performance of the gold standard method for patient alignment with a new method using MVCBCT imaging. Phantom measurements are used to compare the absolute positioning accuracy at which a given setup error is measured. The setup methods are also compared using patient data. Finally, selected

clinical examples are used to show the clinical advantage of 3D imaging over current methods for patient positioning.

## 6.1 Patient Positioning Methods

For decades, patients have been positioned with simple immobilization devices (masks, head holder, knee cushion, etc) and by inferring the location of internal anatomy from surface landmarks (temporary tattoos). Points are aligned to a set of laser-defined crosshairs, which indicate the machine isocenter. It has been demonstrated that external marks limit gross setup error but may not properly represent the internal anatomy [56]. Radiographic 2D images produced on film by the treatment beam have been the standard method to look at the internal anatomy. The dose per image and the time required to develop the films have limited the frequency of setup verification. For these reasons, most radiation oncology departments still continue to verify the position of their patients only once a week using films. The development of digital EPID system based on video-camera or flat panel detectors has improved the efficiency of setup verification. A complete assessment of patient alignment with 2D portal images can now be performed in less than 5 minutes with a fraction of the dose required for films. Bony anatomy, which is the most visible structure on portal images is examined for alignment. For cases such as prostate, it has been documented that bony anatomy may not be a suitable structure to assure tumor localization [56]. The prostate may shift by more than 1 cm relative to the pelvis

bone due to bladder and rectum filling. For this reason, fiducial markers (gold seeds) implanted through a minimally invasive procedure have also been used as surrogate to locate prostate, lung, liver, pancreatic, and paraspinal cancers [57, 58, 59, 60]. To avoid such procedure soft-tissue structures must be available in the image used for setup. For head and neck however, alignment based on bony anatomy (maxilla, base of skull and spinal vertebrae) may be adequate for most situations.

The system presented in Fig. 2.7 gives two options to complement the initial alignment performed using external markings. The two positioning methods are illustrated in Fig. 6.1.

## **2D Method: Portal Imaging with Digital Radiographs**

The first is a 2D method that compares digitally reconstructed radiographs (DRR) and portal images acquired with the EPID. DRRs are generated with the treatment planning system using the CT image and at the location of the treatment isocenter using a realistic source-detector-distance to artificially create 2D radiographs of the anatomy. Every 2D image localizes the patient anatomy in two dimensions and estimating the setup errors in 3D requires two or more image comparisons. Usually, image comparisons are done at gantry positions  $0^\circ$  (anterior-posterior) and  $90^\circ$  (lateral). The exposure required for a portal image ranges between 1 and 5 MU. The 3D shift is obtained using the treatment verification application available in the Syngo Station (Fig. 2.7) of the system. Due to the nature of the portal images, alignment can only

be based on projection of bony anatomy or fiducial markers.

### **3D Method: MVCBCT with CT**

The 3D setup technique consists of comparing the diagnostic CT image used as reference for planning with a MVCBCT image acquired with the patient in treatment position. Automatic 3D image registration can be performed using a maximization of mutual information algorithm. Manual adjustment of the images is generally required. Anatomical contours and points-of-interest are also available in the adaptive targeting application of the computer workstation (Fig. 2.7) to guide the 3D alignment procedure. Bony anatomy and soft-tissue can be used for setup. More advanced registration techniques have been implemented by others and are discussed in the concluding chapter (Sec. 10.3).

## **6.2 Patient Alignment: 2D vs. 3D**

The objective of this work was to compare the 2D and 3D setup methods. The alignment methods were compared in terms of absolute positioning accuracy as well as capability to measure a setup error based on phantom data. The two methods were also compared for positioning of head and neck patients undergoing treatment.

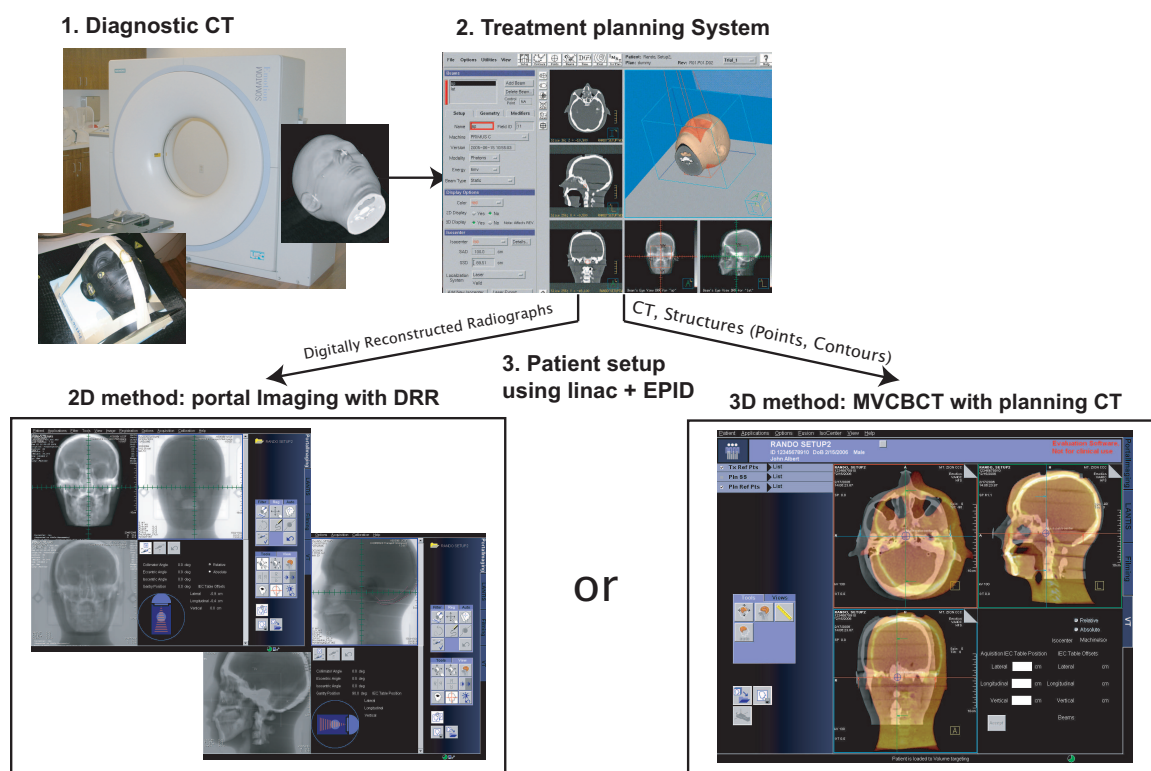


Figure 6.1: Comparison of the patient alignment methods using only a linac equipped with an EPID.

### 6.2.1 Absolute Positioning Accuracy

A gold seed was placed at the laser position and imaged with portal imaging and MVCBCT once a week for a period of 8 months (Sec. 3.3). The distances (in 3D) away from the calibrated image center were recorded. The mean and standard deviation of the measurements were  $(0.2 \pm 0.8)$  and  $(-0.1 \pm 0.4)$  mm for portal imaging and MVCBCT respectively. These results indicate that both the 2D and the 3D method can achieve absolute positioning with an accuracy better than 1 mm.

### 6.2.2 Phantom Positioning Studies

To compare the setup methods, orthogonal portal images and MVCBCT images of a phantom with 3 embedded gold seeds were obtained with the phantom positioned at 30 different known locations in the treatment field. The initial alignment of the seeds served as the reference position. Similar measurements were performed using an anthropomorphic head phantom (Rando). A CT scan was first acquired of Rando. The CT room laser alignment was marked on Rando using three small fiducials. The image was imported into the planning system and a simple 2-field plan was created using the fiducials to define the treatment isocenter. DRRs were generated at  $0^\circ$  and  $90^\circ$  gantry position. Finally, the plan, the CT scan, the treatment isocenter point and the DRRs were transferred to the treatment unit. Portal images and MVCBCT were acquired with the phantom placed at 16 positions. Only the automatic registration was used to align the MVCBCT acquisitions with the CT scans.

The mean and standard deviation of the differences between the applied shift and the measured shift using the phantom with gold seeds were 0.0 mm and 0.3 mm, respectively for both setup methods. Figure 6.2 compares the positioning method using the head phantom. The shift measured with the 2D method (EPI Shift) is plotted versus the shift measured with the 3D method (MVCBCT Shift) for the longitudinal, lateral and vertical directions. The standard deviations of the differences between the applied shift and the measured shift measured with the head phantom were 0.9 mm and 0.4 mm for the 2D method and the 3D method respectively. The mean differences of the differences obtained from the head phantom between the applied and measured shifts were close to zero for both methods. A linear fit of all the measurement points showed a unit slope (intercept close to zero) with a high correlation coefficient ( $R^2 > 0.96$ ) in all directions.

Both techniques (2D and 3D) were capable to measure positioning shifts with sub-millimeter precision when performed with a anthropomorphic head phantom. Because the phantom is stationary and rigid, the registration can be based entirely on bony anatomy. It therefore is not surprising that there was no difference in the setup accuracy using the 2D or 3D method.

### **6.2.3 Patient Positioning Study**

A total of 18 MVCBCT acquisitions (2-10 MU) and orthogonal pairs of portal images (2 MU) were acquired on 8 patients undergoing treatment for head and neck



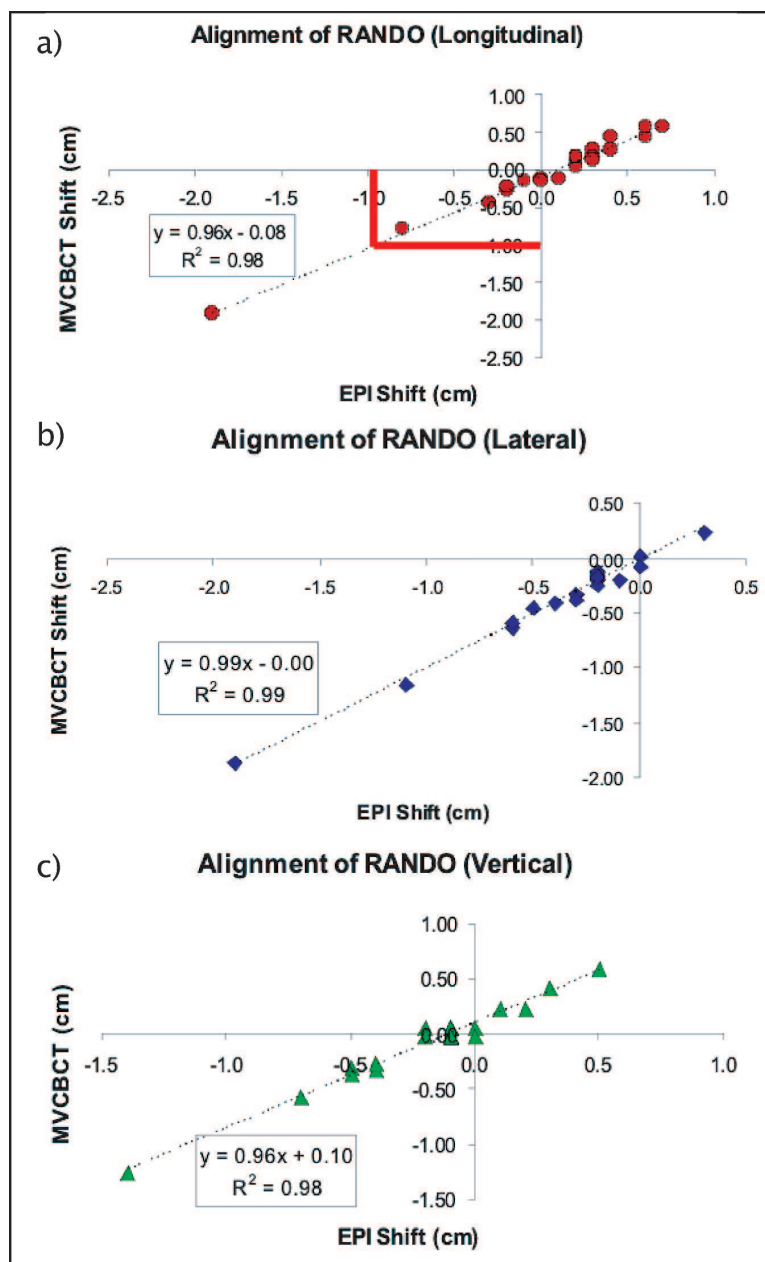


Figure 6.2: Setup method comparison using an anthropomorphic head phantom (Rando). A shift measured with a 2D method (EPI Shift) is plotted against the shift measured with the 3D method (MVCBCT Shift) in the a) longitudinal, b) lateral and c) vertical directions. The treatment couch was moved to image Rando at 16 different locations around the isocenter. A linear fit on all the points was performed for each direction. The goodness of the linear fit is displayed with the correlation factor  $R^2$ .

cancers. The slice thickness of the CT and MVCBCT were 3 and 1 mm respectively. Patients were immobilized using aquaplast head and shoulder masks. Automatic registration and manual fine tuning were used to align the MVCBCT acquisitions with the CT scans.

Bony anatomy and overall soft tissue were visualized on the MVCBCTs while only bony structures could be used for alignment on portal images. Figure 6.3 summarizes the positioning error assessments. The shift measurements made with the two methods were within 2 mm of each other in 76% of all cases. Portal imaging resulted in shifts up to 3 mm whereas MVCBCT positioning resulted in shifts up to 4.3 mm in a single direction. The plots shows that more shift would have been applied using MVCBCT suggesting better sensitivity to positioning error. The differences in the shifts measured (2D vs. 3D) on patients may be due to the capability of MVCBCT to perform local alignment accounting for rotations, distortions and weight loss. In one case (Sec. 6.3), the portal imaging did not match with the DRRs, and no shift could be determined that would make the films align satisfactorily. The corresponding MVCBCT showed that there was an alignment issue with respect to head tilt which was not clear on portal imaging. In two other cases, large variations in neck position (up to 6 mm) were observed once the bony anatomy was aligned with the planning CT. In these cases, local alignments were performed based on the anatomy in proximity to the treatment isocenter. The following sections describe specific cases where a 3D setup method has clear advantage.

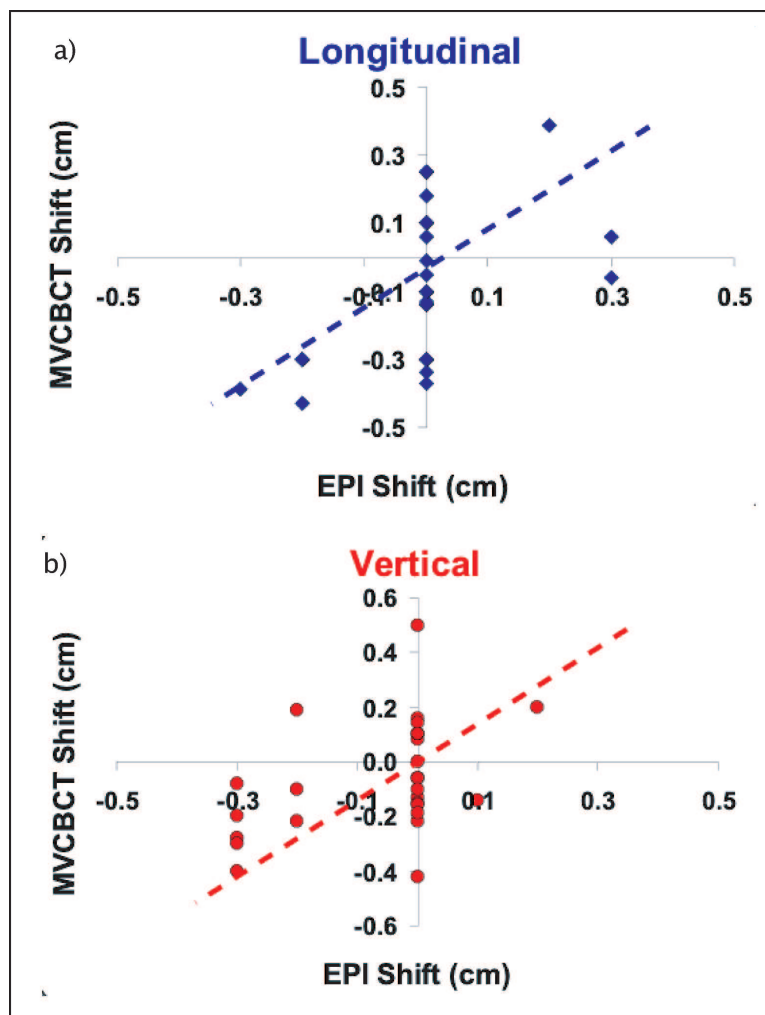


Figure 6.3: Setup method comparison for head and neck patients. A shift measured with a 2D method (EPI Shift) is plotted against the shift measured with the 3D method (MVCBCT Shift) in the a) longitudinal and b) vertical directions. The line represents the relationship that was observed with a solid phantom. Clearly head and neck patients present a more complex problem for setup.

## 6.3 Evaluating Complex Spinal Cord Displacement During Setup

In this example, a patient with a T2N2b squamous cell carcinoma of the hypopharynx was imaged during radiation treatment using MVCBCT. The patient was positioned using an aquaplast head and shoulder mask indexed to the treatment couch. Originally, a TIMO-C head holder was used, which provided a more pronounced angle of neck flexion during treatment. A set of standard CT scans were used to obtain images for IMRT treatment planning. MVCBCT images were acquired at various times during treatment. Orthogonal pairs of 2D portal images were also obtained at the time of MVCBCT acquisition in order to compare the two modalities.

Figure 6.4a displays a DRR of the patient as initially simulated and planned. Easily visible structures such as the posterior vertebral bodies, base of skull, anterior maxilla, and aquaplast mask are outlined. Several weeks into the treatment, an MVCBCT image and a corresponding set of portal images were acquired for this patient. Figure 6.4b shows the outlines from Fig. 6.4a superimposed on this portal image. Although the base of skull and mask line up well, the line of the anterior maxilla is not aligned with the current position of the anterior maxilla. Additionally, the line of the posterior vertebral bodies is difficult to compare with the spinal anatomy. Figure 6.4c displays a sagittal image from MVCBCT (gray scale) overlaid on the planning CT images (color). The two sets of images have been registered to obtain

an overall alignment based on the anatomy of the skull and face, as was similarly done using the 2D technique.

As seen in Fig. 6.4c, the patient alignment using the MVCBCT and planning CT images allows for further assessment of not only global position, but also the relative positions of internal anatomical structures. Although the base of the skull is well aligned, a 6 mm difference in the position of the anterior vertebral bodies between the planning CT images and the MVCBCT data is clearly visible. The patient was subsequently resimulated using a neck holder with less flexion (TIMO B) in order to place the patient in a robust and more comfortable position. Once this plan was complete, an additional MVCBCT was obtained, as seen overlying the new planning CT images in Fig. 6.4d. Comparison of the new MVCBCT and planning CT image data indicates that overall alignment, from the base of skull and along the vertebral bodies, was significantly improved using the new set up.

In this case, MVCBCT provided clear, informative images that allowed a more complete evaluation of the patient set up in comparison to 2D portal imaging. The 2D portal images did show some variation in patient positioning, but did not reveal the origin and the full magnitude of the misalignment. Using MVCBCT images, we were able to measure the magnitude of the misalignment, identify its source (a distortion of the neck), and confirm the correction of the problem. MVCBCT was a critical tool that led to replanning for more accurate treatments for this patient.

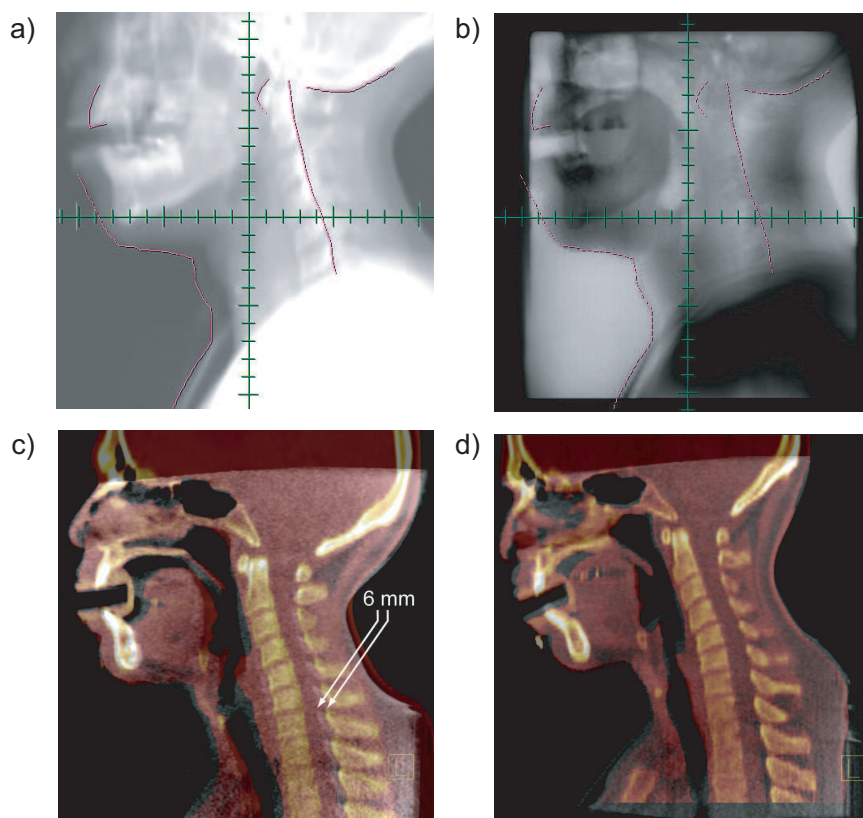


Figure 6.4: Assessment and correction of a complex neck distortion using MVCBCT. On the same day, a head and neck patient positioned with a TIMO C head holder was imaged using portal imaging (b) and MV CBCT (c). A difference in the arching of the neck is difficult to detect using the lateral digitally reconstructed radiograph (DRR) (a) overlaid on to the portal image (b). Registration of the patient MVCBCT (gray scale) with the kV CT (color) in (c) revealed a complex distortion of the lower neck region which creates a 6 mm misalignment of the vertebral bodies and spinal cord. A new MVCBCT (color) compared with the new CT (gray) in (d) showed improvement in the 3D alignment.

## 6.4 Performing Setup of a Patient with a Lung Tumor

An MVCBCT was used to position a patient with a T2N0M0 squamous cell carcinoma of the lung. The patient had refused surgery, and, therefore, was treated with definitive radiation therapy. At the time of fluoroscopic simulation, the tumor was noted to be immobile. This is obviously not the case for most lung tumors [4]. The isocenter was placed within the tumor volume and planning CT images were obtained without respiratory gating.

A hypofractionated course of radiation was prescribed, and it was therefore exceedingly important to ensure accurate set up of the tumor within the field. For this reason, and because of the reduced number of fractions, MVCBCT was used for daily set up.

On the first day of treatment, a pair of orthogonal portal images and an MVCBCT were acquired. The MVCBCT images were aligned with the planning CT using the soft tissue mass itself in order to ensure adequate tumor dose. On the first treatment day, two additional MVCBCTs were obtained to verify this positioning method; the first following the applied shift, and the second after treatment delivery to evaluate any intrafraction motion during the 20 minutes of IMRT treatment. The post shift MVCBCT showed excellent alignment with the planning CT, and the post treatment MVCBCT remained well aligned. On subsequent days a single MVCBCT procedure

was performed for positioning.

To illustrate the potential pitfalls associated with relying on portal imaging for patient positioning, the measured shift that could have been made using only 2D portal images for positioning was applied to the MVCBCT and reference CT images. As can be seen in Fig. 6.5, if the sternum is aligned (6.5c), the tumor in the right lung is not (6.5a and 6.5b), and would have been underdosed. A similar misalignment of tumor happens when the MVCBCT and the planning CT images are aligned based on vertebral body position, a common way to verify the position of thoracic patients.

## **6.5 Setup of Patient with Paraspinous Tumor in the Presence of Orthopedic Hardware**

With conventional CT or MR imaging in the setting of paraspinous metallic hardware, artifact and image degradation create obstacles to the accurate delivery of high doses of radiation without compromising spinal cord tolerance. A new technique was developed using MVCBCT images to direct IGRT for treatment of paraspinous tumors in the presence of orthopedic hardware.

A patient with a resected paraspinous high-grade sarcoma was treated to 58 Gy in 29 fractions with an IMRT plan. Due to the steep isodose lines in close proximity to the spinal cord, daily MVCBCT imaging was used to ensure accurate patient positioning before each treatment. The MVCBCT and planning CT images (illustrated



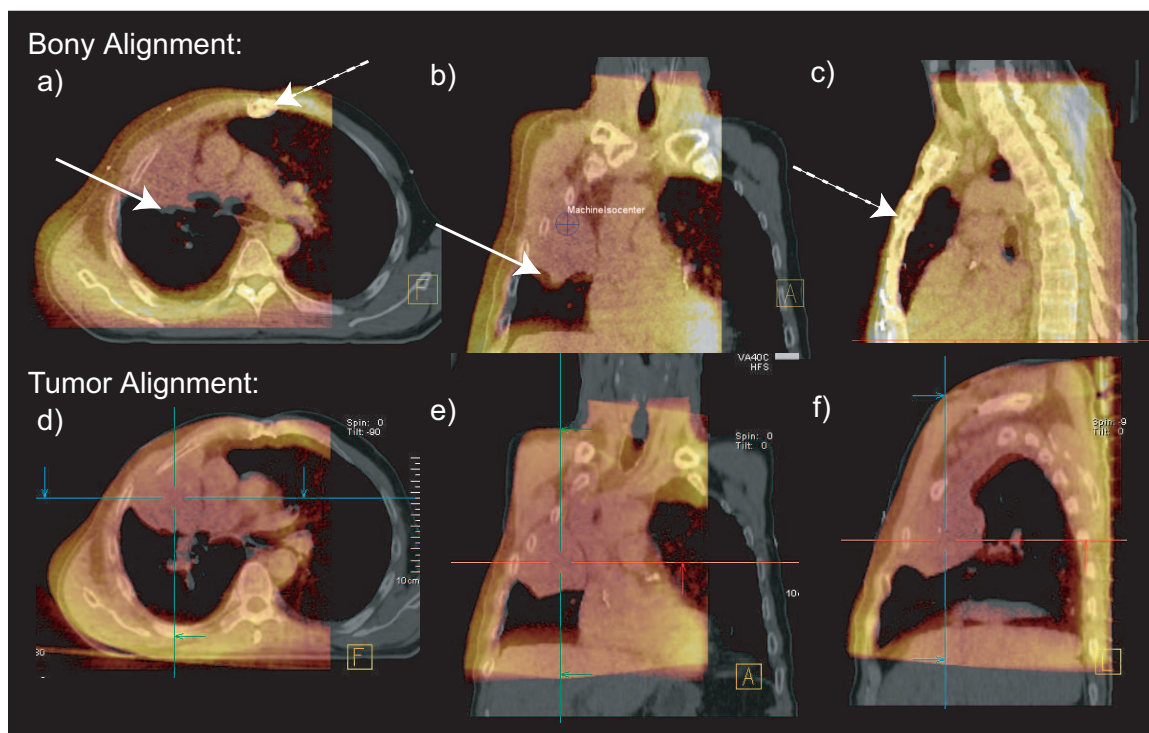


Figure 6.5: Images comparing the use of MVCBCT and portal imaging for setup of a hypo fractionated lung patient with a large and relatively immobile tumor. On the first fraction, the shift assessment was done using the sternum on portal images. This shift was then applied to a MVCBCT acquired the same day. Three views of the CT (gray scale) fused with the MVCBCT (color) are shown. While the sternum is well aligned on (c) the tumor is not on (a) and (b). For this reason, the patient was aligned using the soft-tissue information on the MVCBCT images.

in Fig. 6.6) were automatically registered and fine-tuned by physicians, and the displacement between the image sets was applied remotely to the table. To estimate the impact of the daily MVCBCT shifts on dosimetry, the dose-volume histograms of the original IMRT plan and a hybrid IMRT plan (created by shifting the isocenter of the original IMRT plan by the mean absolute shifts in the lateral, longitudinal, and vertical directions) were compared.

The mean absolute daily table shifts obtained on the basis of the MVCBCT in the lateral, longitudinal, and vertical directions were 3.6 mm (95% C.I., 2.6-4.6 mm), 4.1 mm (95% C.I., 3.2-5.0 mm), and 1.0 mm (95% C.I., 0.6-1.3 mm), respectively. When comparing the original IMRT plan to the hybrid IMRT plan, the dose to 0.1 cc of the spinal cord increased from 51.5 Gy to 60.9 Gy; and, the doses to 95% of clinical target volumes 1 and 2 were reduced from 51.6 Gy to 47.6 Gy and 49.5 Gy to 44.7 Gy, respectively.

MVCBCT greatly reduces technical problems associated with the treatment of paraspinal tumors in the presence of orthopedic hardware. MVCBCT provides 3D anatomical information in the treatment position with clear imaging of metallic objects without compromising soft-tissue information, thereby allowing accurate delivery of high doses of radiation. MVCBCT played a key role in this example of IGRT, where optimal setup was achieved for a patient who might otherwise be treated with doses unlikely to provide long-term local control or not be treated at all.

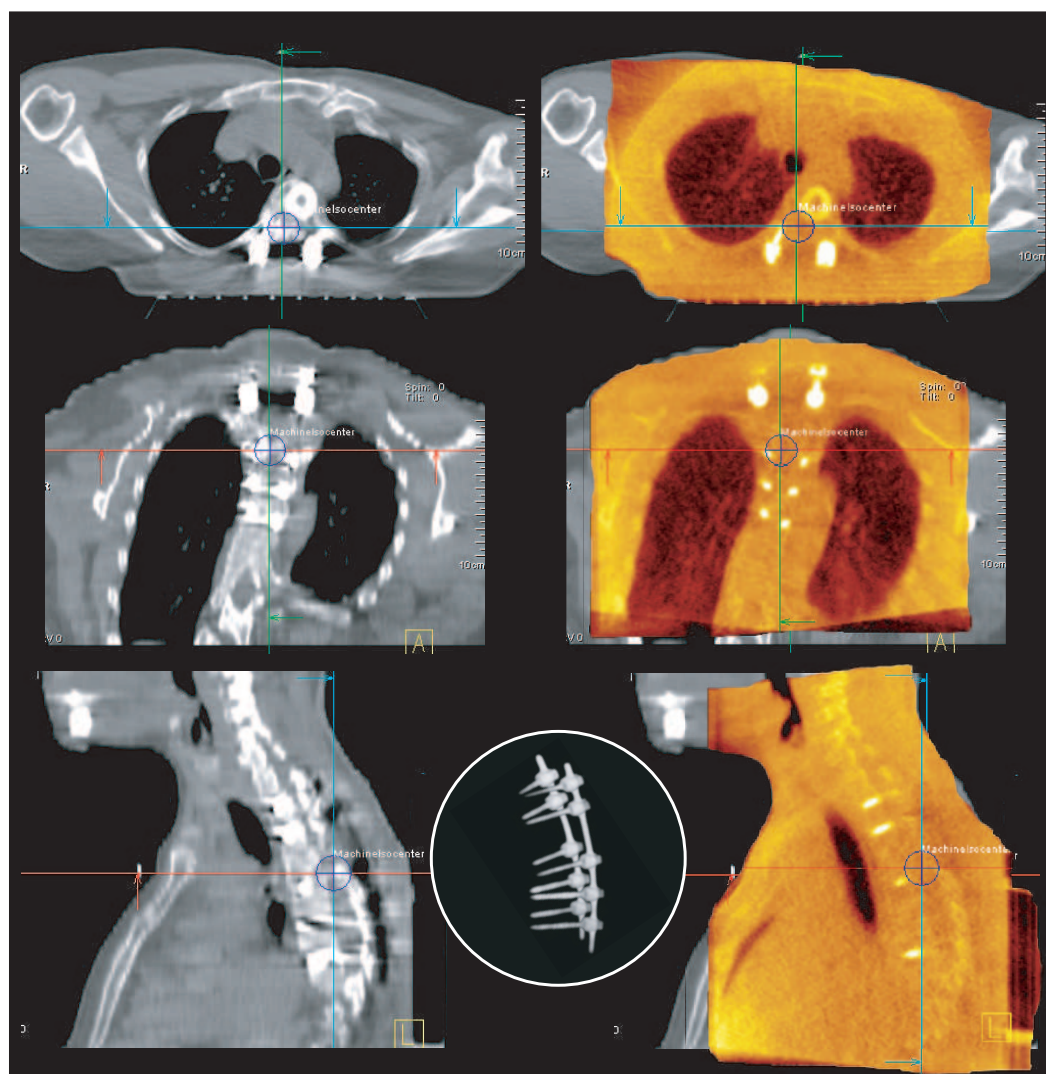


Figure 6.6: Example of daily 3D image registration of MVCBCT (orange) with planning CT (grayscale) in axial, coronal, and sagittal planes. Inset demonstrates 3D MVCBCT reconstruction of hardware, without artifact typically associated with kV CT.

## 6.6 Alignment of Prostate Patients

Daily portal imaging on patients with implanted gold markers in the prostate can locate the gland with 1-2 mm accuracy [61, 62, 63]. However, this 2D positioning method cannot be used for all cases. For example, the gold markers are often not visible on the lateral portal image of patient with a hip prosthesis. It has been demonstrated that the lateral portal image contains information relative to the most frequent setup error of prostate patient [64]. In addition, the presence of surgical clips for patients undergoing prostatectomy also can hide the location of gold markers implanted in the prostate bed and make them difficult to identify. For these reasons, physicians in our clinic have started requesting that specific patients undergoing radiation therapy for prostate cancer are aligned with MVCBCT rather than portal imaging.

A positioning method using MVCBCT was developed to solve these problems. The method is illustrated in Fig. 6.7. With MVCBCT, gold markers are easily identified on all patients with an exposure as low as 2 MU. The corresponding CT image is displayed in grayscale color map to display the seeds in white while the MVCBCT is displayed using an inverse grayscale color map to render the seeds in black. Using a 50% CT, 50% MVCBCT transparency level, the gold seeds visualized in the axial, sagittal and coronal planes can easily be superimposed with each other. Even at low MVCBCT exposure, patient specific variables potentially causing poor coverage of the target have been identified, including the level of rectum and bladder filling

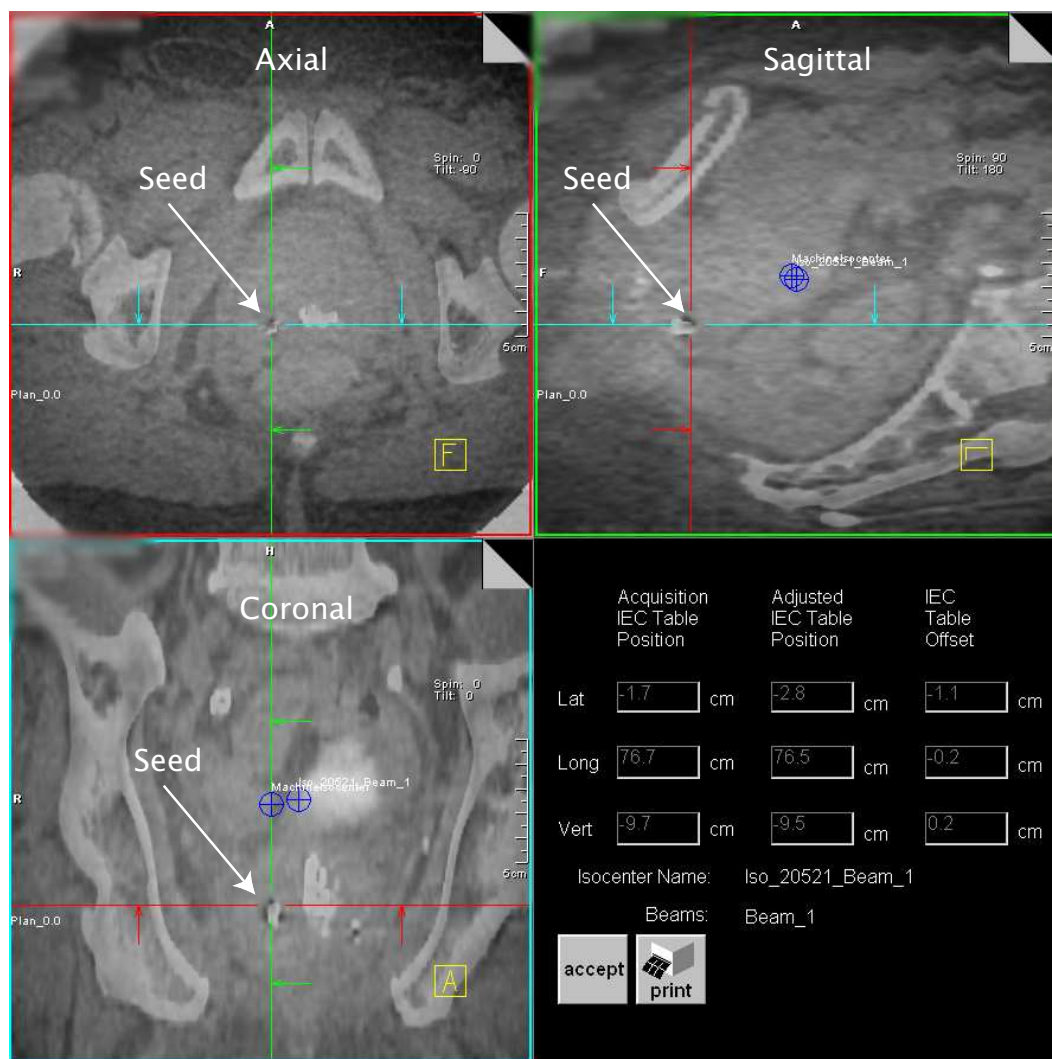


Figure 6.7: Example of prostate patient alignment using gold markers. The CT image is displayed in grayscale color map (seeds shown in white) while the MVCBCT image is displayed using an inverse grayscale color map with the seeds shown in black. Using a 50% CT, 50% MVCBCT transparency level, the gold seeds visualized in the axial, sagittal and coronal planes can easily be superimposed with each other in a combined displays. Gold markers can easily be identified on MVCBCT using only 2 MU of patient exposure.

that now can be assessed on a daily basis. The use of higher MVCBCT exposure to better visualize the prostate is under study and could allow soft-tissue alignment without the need of the invasive procedure of gold marker implantation.

## Chapter 7

# Monitoring Patient Anatomy Over Time

The use of routine 3D imaging before treatment exposes the dynamic nature of patient anatomy. Measuring such variation is the first step towards implementing more dynamic RT processes. This chapter describes two cases of anatomical variation that can be quantified with MVCBCT imaging. Other cases of anatomical variation that were observed in the clinic include daily rectal distention of prostate patient and the evolution of the size of a lung tumor.

### 7.1 Soft-Tissue Variation in the Nasal Cavity

In this next example, a patient with a T4bN1 squamous cell carcinoma of the nasal cavity was imaged using MVCBCT at various times while under treatment with

external radiation therapy. The tumor involved the right nasal cavity and extended anterolaterally into the maxillary sinus and posteriorly to the nasopharynx. Prior to treatment, the extent of tumor was only evaluable on CT or MRI examination. The tumor was unresectable, and the patient was treated definitively with concurrent chemoradiation. A conventional noncontrast CT was used to obtain base images for treatment planning. Four MVCBCTs were obtained during the course of radiation treatment in an effort to assess tumor anatomy variation that could not otherwise be easily visualized.

Representative images of the planning CT and 2 subsequent MVCBCTs are shown in Fig. 7.1. The point indicated by  $T_0$  represents the start of radiation treatment. Examination of the MVCBCT images revealed an obvious soft tissue density within the right maxillary sinus. The air interface present anteriorly provided excellent contrast with this soft tissue density. In comparison, the left maxillary sinus was completely air filled, as seen on the planning CT and subsequent MVCBCT images. These images show that there is more soft tissue density within the right maxillary sinus on the first MVCBCT evaluation ( $T_0 + 6$  days) as compared to the original planning CT ( $T_0 - 14$  days). This may indicate that there was tumor growth between the time of treatment planning and start of treatment. A comparison of the first ( $T_0 + 6$  days) and second ( $T_0 + 14$  days) MVCBCT images shows some decrease in the amount of soft tissue in the cavity.

The amount of air filling for each side of the maxillary sinus at the given time-



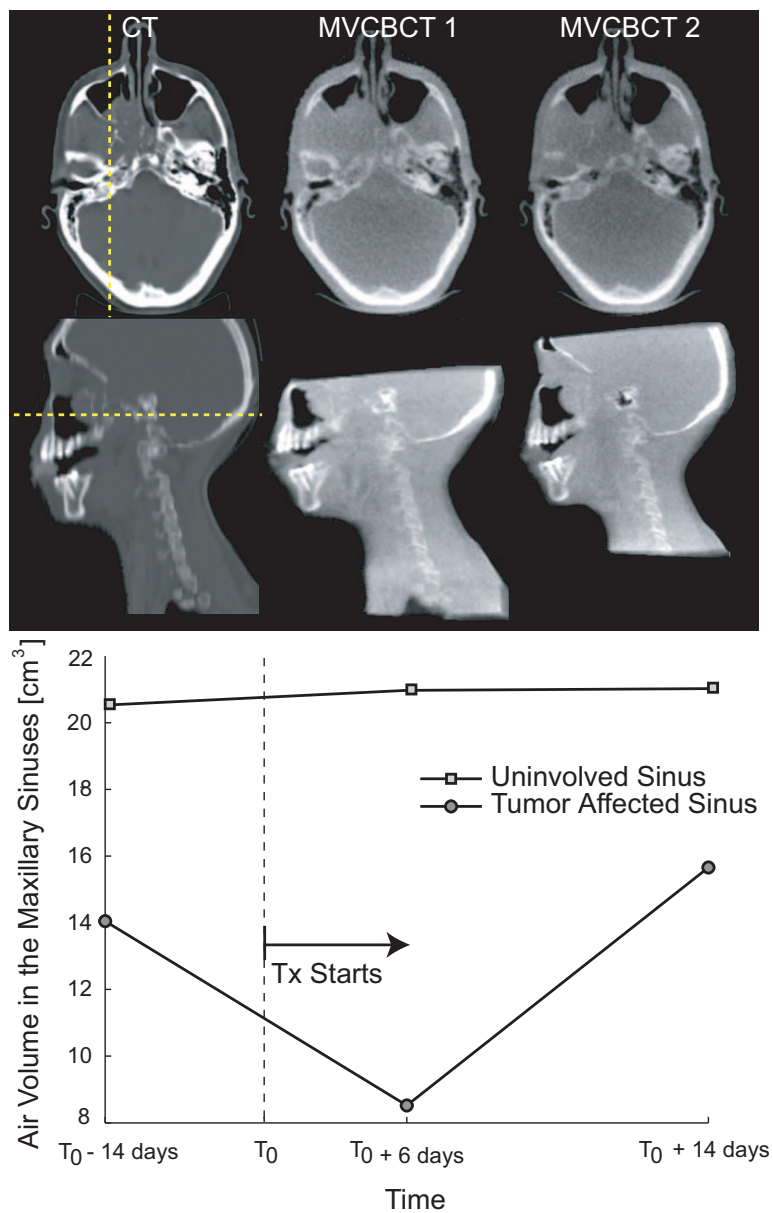


Figure 7.1: Tumor size variation during the course of radiotherapy. The planning CT (left) of a patient affected by a right maxillary sinus tumor was acquired 14 days before the beginning of the treatment fractions  $T_0$ . Two MVCBCTs (middle and right) were acquired 6 days and 14 days after  $T_0$ . The evolution of the tumor size is visible on the axial (top) and sagittal (middle) views. The bottom plot presents the air volume in the cavities as a function of time.

points was calculated with automatic contouring. This is plotted for the right (tumor affected sinus) and the left maxillary sinus (uninvolved sinus) in Fig. 7.1. If we were to assume that the soft tissue density within the affected sinus were exclusively tumor, rather than a combination of tumor and secretions, this quantitative assessment of air volume within the sinuses may serve as a surrogate for tumor response. This example demonstrates the potential of this imaging modality to monitor changes in target volume that are not otherwise evaluable using conventional techniques such as portal imaging.

## 7.2 Weight Loss for a Head and Neck Patient

Today's concurrent chemoradiation therapy for head and neck patients are so aggressive that patients frequently suffer from side effects that alter normal nutrition. It is fairly common ( $\sim 33\%$ ) for head and neck patients to observe weight loss of up to 58% of pretreatment body weight [65] over the course of radiotherapy. Figure 7.2 presents a case of weight loss observed for a patient treated for a base of tongue carcinoma with IMRT. The initial CT image (grayscale) is compared with an MVCBCT image (color) acquired 22 days after the beginning of therapy. The patient lost up to 4 cm of soft tissue on the side of the neck after only half of the total number of treatment fractions.

Despite the frequent occurrence of such variation, it is currently difficult to define when these patients need to be reimaged with conventional CT and replanned.

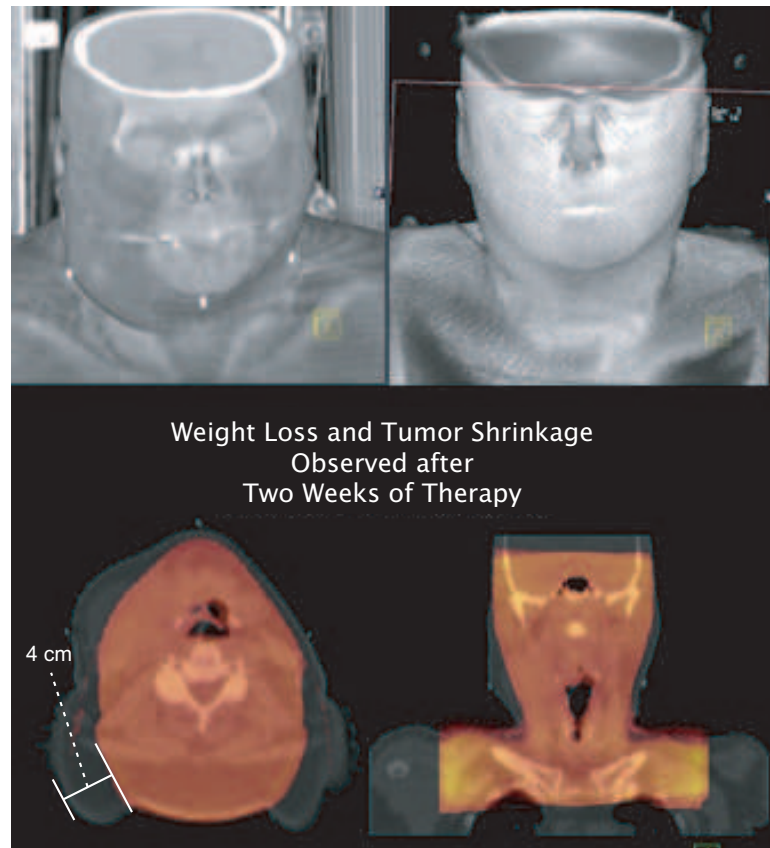


Figure 7.2: Example of weight loss for a patient treated for a base of tongue tumor with IMRT.

The following chapter explores the possibility of using MVCBCT to quantify the dosimetric impact of such variation in anatomy.

## Chapter 8

# Dose Calculation

Variations in target volume and anatomy presented in the last chapter may have dosimetric consequences that require re-planning. At what point during treatment a patient needs to be re-planned is currently difficult to determine. Commonly, treatment plans are revised only when the set up is no longer reproducible, the mask used to positioning the patient no longer fits, or significant weight loss is noted. Weekly physical examination and total body weight measurements are performed but are unable to quantify changes that occur locally at the target or along the treatment beams. Most importantly, these methods do not quantify the dosimetric impact of the changing anatomy or patient positioning inaccuracies.

While MVCBCT was primarily developed to provide accurate 3D positioning of the patient moments before dose delivery, the images obtained could also be used to perform dose calculation. This would open the possibility to monitor the dosimetric

impact of changes in anatomy or position as compared to the reference CT by applying the initial treatment plan on the MVCBCT images.

The objective of this chapter is to demonstrate the feasibility of performing dose calculation using MVCBCT. A complete article describing the work done in this chapter has recently been published [66]. Because of the current limitations in the MVCBCT imaging volume, this study focused on dose calculations performed in the head and neck region. First, phantom experiments were performed to investigate the effect of MVCBCT cupping artifacts on dose calculation accuracy and to develop a method to reduce this effect. We then calibrated the corrected MVCBCT images for electron density and entered the calibration data into a commercial planning system. To test the dosimetric accuracy of using MVCBCT for a clinical case, we compared the doses calculated using MVCBCT and using a conventional CT for a patient who exhibited minimal anatomical changes between the two image acquisitions. Finally, we used two sets of CT and MVCBCT images to track the changes in delivered dose distributions for a patient who lost considerable weight during the course of IMRT.

### **Requirements for dose calculation**

A 3D image data set has to fulfill two requirements before being used for dose calculation. First, the image volume has to include all the patient tissue along the treatment beams. Second, the treatment planning system requires the image to be calibrated for electron density, which is a radiological parameter related to dose de-

position in radiotherapy. Prior to image calibration, any artifact inherent to the imaging modality must be minimized. Calibration of CT images for electron density has been robustly demonstrated on kV and MV CT systems using fan-beam geometry [67, 53]. Only recently have groups begun investigating the possibility of calibrating cone-beam images. The calibration of MVCBCT is presented in Sec. 3.6.

## 8.1 Effect of Cupping Artifact

A head size water cylinder phantom was used to investigate the impact of the MVCBCT cupping artifact on the accuracy of dose calculation. The water cylinder was first imaged with the conventional CT scanner. The phantom alignment in the CT room was marked with three small fiducials. MVCBCT images of the cylinder then were acquired in the treatment room using the fiducials for alignment. The kVCT, the MVCBCT with cupping artifact and a MVCBCT corrected for nonuniformity (correction method presented in Sec. 3.5.1) were all imported to the treatment planning system. The CT voxel intensities of each scan were converted to relative electron density to water using the calibration curves. A plan with a single anterior-posterior  $10 \times 10 \text{ cm}^2$  square beam was applied on all three image sets. The three dose distributions were obtained using identical dose grid positions and a resolution of 2 mm. Finally, the dose distributions obtained using the two MVCBCT scans (with and without uniformity correction) were compared with the reference dose distribution calculated using the conventional CT. To obtain a complete quantitative

evaluation of dose distributions in both the low and high dose gradient regions, we computed dose percentage differences and a gamma index [68]. We used typical acceptance criteria of 3% in dose and 3 mm in distance-to-agreement for the gamma index.

Figure 8.1 presents a quantitative analysis of the effect of the cupping artifact on the dose calculation accuracy for a cylindrical water phantom. As seen in Fig. 8.1 (top), the dose percentage differences between the doses calculated on the CT and on the uncorrected MVCBCT scans (left) showed a systematic deviation, which increased with depth. The nonuniformity caused the dose calculated in the in-field region (field edge reduced by 4 mm) to be less on average by 0.95% and by a maximum of 4.5%. Differences larger than  $\pm 10\%$  were observed at the field penumbra and along the phantom edge. These differences were likely due to slight error in the setup ( $< 2$  mm) of the phantom or in the placement of the treatment isocenter in the treatment planning system. The calculation of the gamma index on the uncorrected water cylinder (Fig. 8.1 bottom) showed that despite the large cupping artifact only 1% of the whole dose distribution did not meet the acceptance criteria of 3% and 3 mm. When the water cylinder was corrected for nonuniformity, 98% of the in-field region was within 1% difference in dose and 92% of the entire dose distribution, including phantom edges and penumbra, was within 2% in dose and 2 mm in distance-to-agreement.

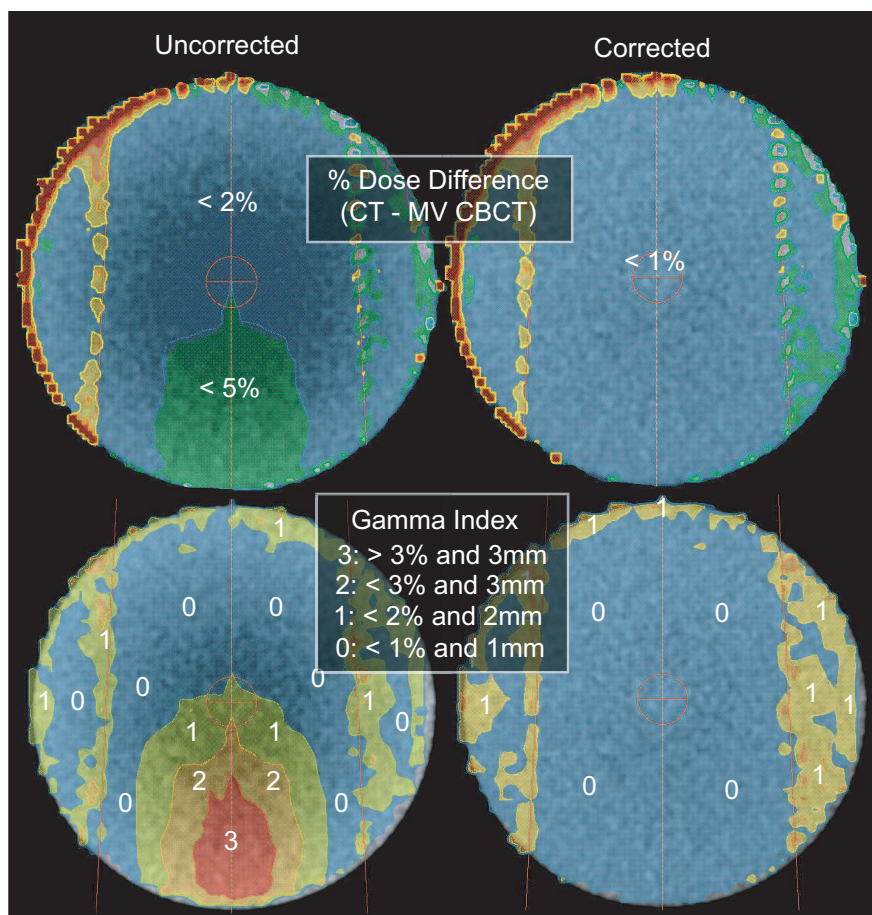


Figure 8.1: Dose percentage differences (CT - MVCBCT) (top) and gamma indices (bottom) for the head-size water cylinder uncorrected (left) and corrected (right) for uniformity.



## 8.2 Validation of MVCBCT

To assess the dose calculation accuracy achieved with MVCBCT on a patient, a head and neck patient treated with IMRT for a recurrent nasopharyngeal carcinoma was selected. This patient was imaged in the first week of therapy and no major change or deformation in anatomy from the time of the reference CT was seen. This observation was also verified with the 3D registration of the MVCBCT image with the CT results. Manual registration was performed until the best match was achieved by visual comparison. The MVCBCT image was corrected for nonuniformity using the ellipsoid correction factors previously described. The IMRT treatment plan (isocenter, beams and contours) defined on the kVCT image was applied to the MVCBCT image. None of the beam passed through the patients shoulders, parts of which extended beyond the MVCBCT field of view. The dose distributions calculated with the conventional CT and the MVCBCT images were compared using dose percentage difference and gamma index distributions. Because the anatomy and position of the patient was nearly identical on both images after 3D registration, contours drawn on the conventional CT images (spinal cord, left parotid, right eye, brain stem and gross tumor volume, etc.) were directly copied on to the MVCBCT images. The dose-volume histograms (DVH) of the structures were compared.

Figure 8.2 displays isodose lines produced using conventional CT (left) and MVCBCT (right) for the first test patient. There is good qualitative agreement between the two dose distributions. For doses higher than 10 Gy (14% of the prescription dose) the

maximum percent difference in dose was 8%. More than 90% of the volume had a percent difference of 5% or less. Percent differences between 5-8% were observed in the left air cavity and are believed to be due to slight misalignment or local anatomic variation. Reviewing the gamma index, 98% of the complete volume was within 3% and 3 mm, and 88% of the volume was within 2% and 2 mm. Overall, as seen in Fig. 8.2, the DVHs calculated from conventional CT and from MVCBCT were also in excellent agreement.

### **8.3 Dosimetrical Impact of Anatomical Changes**

A patient treated with IMRT for a base of tongue carcinoma was selected to evaluate the capability of MVCBCT to monitor the dosimetric impact of weight loss. The patient was first imaged with conventional CT (CT1) for planning. The treatment plan created for this patient contained beams passing partly through the patient shoulders to cover the cervical lymph nodes. Parts of these beams extended beyond the MVCBCT field of view. A MVCBCT (MVCBCT1) was acquired during the first week of therapy, twelve days after CT1. Additional CT (CT2) and MVCBCT (MVCBCT2) images were acquired on week 3 (22 days after MVCBCT1) of treatment. The patient was displaced by 2 cm in the vertical direction for MVCBCT imaging to obtain better uniformity correction from the method presented in this paper. MVCBCT images were corrected for nonuniformity and transferred to the treatment planning system. As with the previous test case, the MVCBCT images

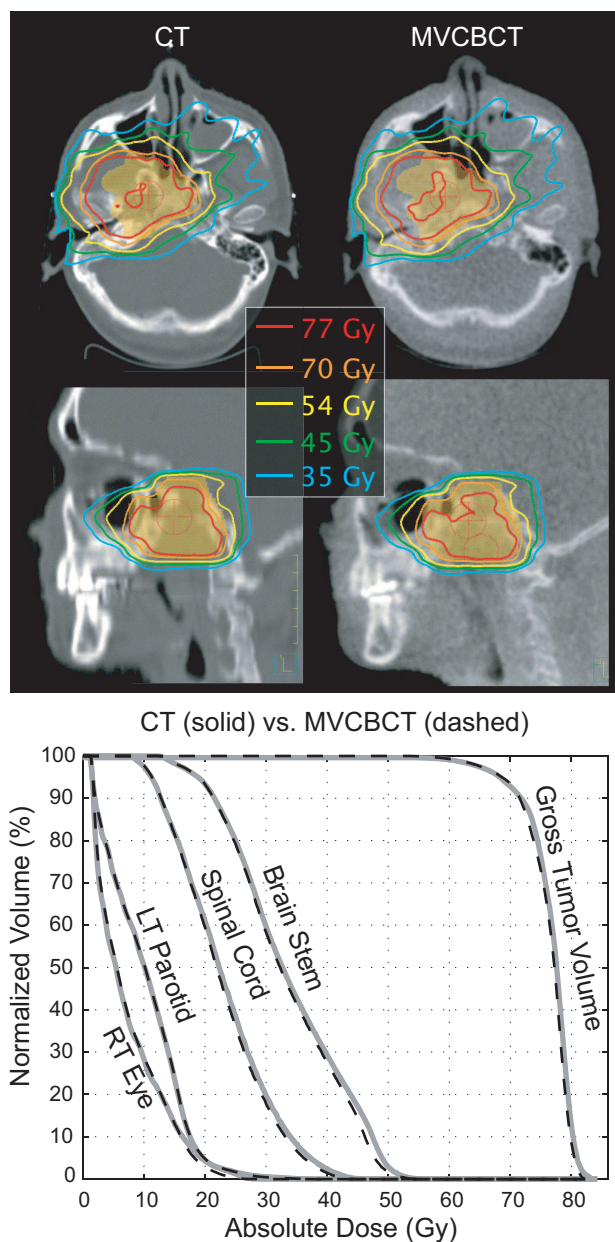


Figure 8.2: Dose calculation on a patient treated for a recurrent nasopharyngeal carcinoma with IMRT. No weight loss or anatomical deformation was observed between CT and MVCBCT images. Isodose lines at the treatment isocenter planes on the conventional CT and MVCBCT are presented (above). Good qualitative agreement is observed with DVHs (below) obtained from dose calculations performed using CT (solid lines) and MVCBCT (dashed lines).

were aligned precisely with their corresponding reference CT images (MVCBCT1 with CT1 and MVCBCT2 with CT2) using 3D registration. A dosimetrist and a physician contoured the target and critical structures on CT1 and CT2. These contours were copied to the corresponding MVCBCT images. For comparison, critical structures (parotids, spinal cord, brain stem, larynx and right temporomandibular joint (TMJ)) were also drawn directly on the images from MVCBCT2 by the dosimetrist. CT1 but not CT2 was used as a visual reference to guide the contouring on MVCBCT2. To compensate for parts of the patients shoulders and chest that extended outside the MVCBCT field of view, tissue and lung contours were drawn on CT1 and copied onto MVCBCT1 and MVCBCT2 after 3D registration. The missing tissue and lungs were assigned a density relative to water of 1 and 0.4 respectively. Dose distributions were then obtained by applying the initial treatment plan to data from CT1, MVCBCT1, CT2, and MVCBCT2. The four dose distributions were produced using identical dose grid positions and a resolution of 3 mm. Dose percentage difference and gamma index distributions were computed for different combinations of dose distributions (CT1-MVCBCT1, CT2-MVCBCT2, CT1-CT2, MVCBCT1-MVCBCT2, and CT1-MVCBCT2). Dose volume histograms were obtained for several structures (left TMJ, parotids, spinal cord, larynx, clinical target volume (CTV) and gross tumor volume (GTV)).

For the second patient, the weight loss between week 1 and week 3 of therapy can easily be seen on the axial images of Figs. 7.2 and 8.3. The patient lost up

to 4 cm of soft tissue on both sides of the neck between CT1 and CT2. First, we compared dose calculation on MVCBCT images versus their respective CT images. Minor anatomical changes were observed on the posterior aspect of the neck between CT1 and MVCBCT1 (see axial images Fig. 8.3). No observable anatomical changes were observed between CT2 and MVCBCT2. Isodose lines displayed on the axial and sagittal central planes of the conventional CTs and MVCBCTs (Fig. 8.3) show good qualitative agreement between the dose distributions obtained from images acquired closely in time (CT1 with MVCBCT1 and CT2 with MVCBCT2). For doses greater than 20 Gy (29% of the prescription dose), 78% and 84% of the dose calculation performed on MVCBCT1 compared with CT1 and MVCBCT2 compared with CT2 respectively fell within the acceptance criteria of 3% in dose and 3 mm in distance-to-agreement. The portion that failed the criteria was almost entirely located posteriorly below the fifth cervical vertebrae (C5) where the MVCBCT images were acquired with missing tissue. This will be addressed in more detail in the Discussion section. The percentages passing the acceptance criteria increase to 96% and 97% when the anatomy below C5 is excluded. Figure 8.4 (top) displays the percentage difference in dose for CT1-MVCBCT1 (a) and CT2-MVCBCT2 (b). The majority of the dose distributions were within 3% in dose. The dose in the shoulder area was on average 6.3% higher on the MVCBCTs. The DVHs calculated on CTs and their corresponding MVCBCT are compared on Fig. 8.4 (below). Overall, the agreement was excellent because the anatomical structures in the head and neck area are mostly situated

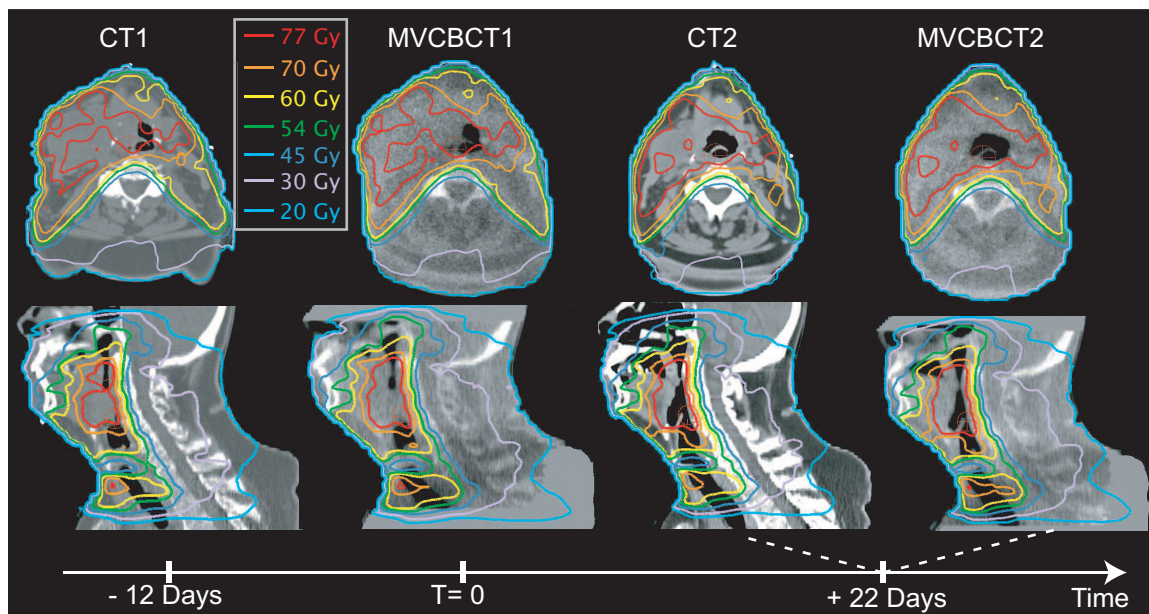


Figure 8.3: Dose calculation on a patient treated for a base of tongue tumor with IMRT. The initial plan defined on the initial CT (CT1) was applied on a MVCBCT acquired in the first week of treatment (MVCBCT1) and additional CT (CT2) and MVCBCT (MVCBCT2) acquired 22 days after the beginning of therapy. Axial and sagittal images crossing the isocenter show good qualitative agreement between the isodose lines (CT1 with MVCBCT1 and CT2 with MVCBCT2).

above C5.

Figure 8.5 (top) displays the percentage difference in dose for CT1-CT2 (a) and MVCBCT1-MVCBCT2 (b). A comparison of CT1 with MVCBCT2 was also performed and yielded very similar results to those presented in Fig. 8.5. Both the CT and the MVCBCT data sets show a large volume of tissue receiving more than a 3% increase in dose due to the patient weight loss. In the CT data set, the mean percentage increase in dose between week 1 and week 3 was 5.2%. Approximately 20% of the dose distribution did not fall within the passing criteria of 3% in dose and 3 mm in distance-to-agreement. In the MVCBCT data set, the mean percentage

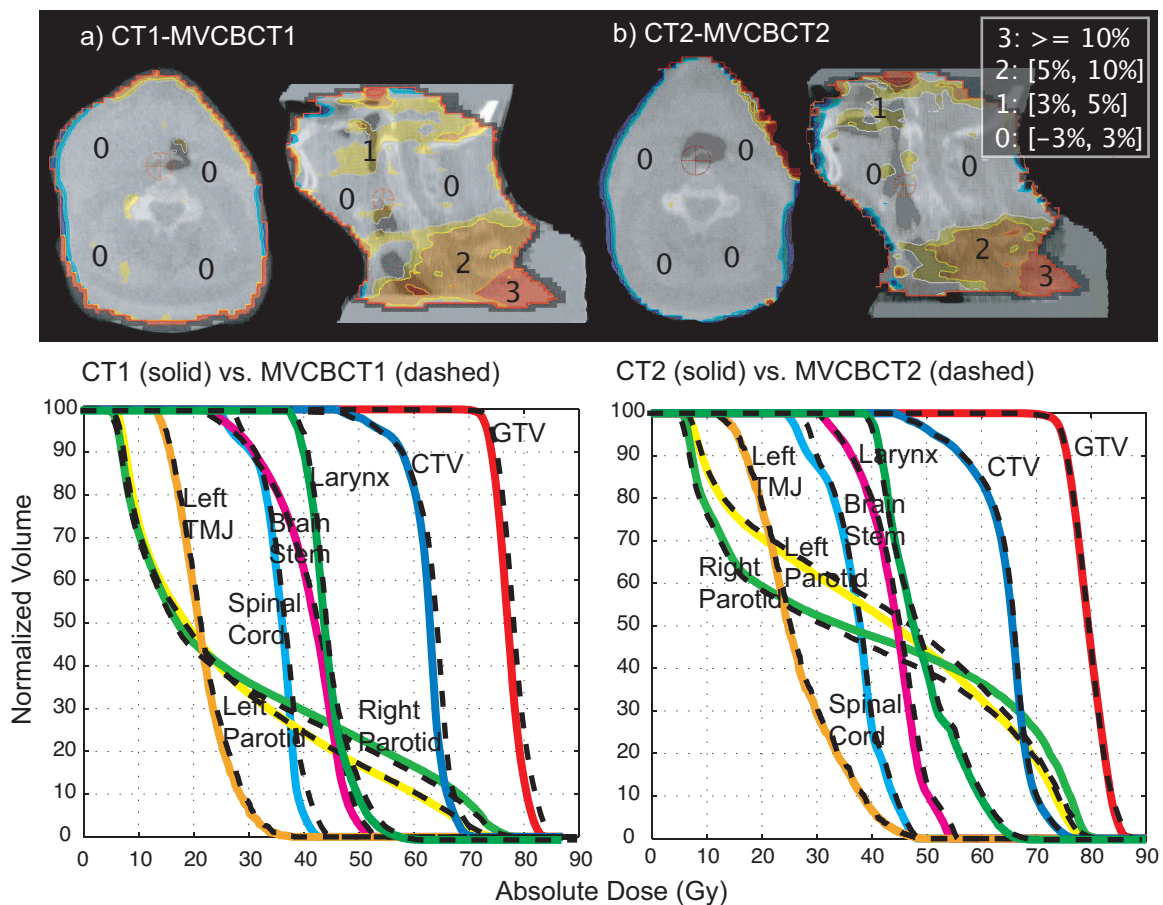


Figure 8.4: Top- Axial and sagittal images crossing the isocenter showing dose percentage difference distributions for CT1 compared to MVCBCT1 (left) and CT2 compared with MVCBCT2 (right). Most of the dose calculation on MVCBCT was within 3% of the dose calculation on CT. The shoulder area, where MVCBCT suffers from missing tissue was, on average 6.3% higher in dose with MVCBCT. Below DVH comparisons showing excellent agreement for CT (solid) and MVCBCT (dashed) acquired closely in time. All contours producing the DVHs were drawn on the CT images and applied on MVCBCT after registration

increase in dose between week 1 and week 3 was 4.6%. There was good qualitative agreement between CT1-CT2 (Fig. 8.5a) and MVCBCT1-MVCBCT2 (Fig. 8.5b) in the anatomical locations receiving more than a 5% increase in dose. Fig. 8.5 (below) shows the dosimetric impact of weight loss assessed using DVH comparisons between CT1-CT2 (left) and MVCBCT1-MVCBCT2 (right). Again, contours on MVCBCT were transferred from the corresponding CT data. All critical structures and target volumes showed similar increases in dose using CT (left) or MVCBCT (right). For example, the maximum dose to the spinal cord increased from 42.9 to 48.3 Gy using CT1-CT2 (left) while increasing from 44.1 to 48.9 Gy using MVCBCT1-MVCBCT2. Similarly, the left parotid mean dose increased from 26.2 to 41.8 Gy using CT data while increasing from 26.0 to 42.1 Gy using data from MVCBCT. The largest qualitative DVH difference was observed with the right parotid, which was located in a high-dose gradient region.

Figure 8.6 evaluates the possibility of contouring critical structures directly on the MVCBCT image. The DVHs shown were obtained from two independent sets of contours (Fig. 8.6 top). One set was obtained from contouring on CT2 and copying the contours on MVCBCT2 after 3D registration (blue contours), and the other set by direct contouring on MVCBCT2 (white contours). Overall, the agreement between the two sets of contours and DVHs was good. Again, the largest difference was observed with the right parotid. Contouring the right parotid directly on MVCBCT2 improved the DVH agreement with CT2 (see Fig. 8.4a).



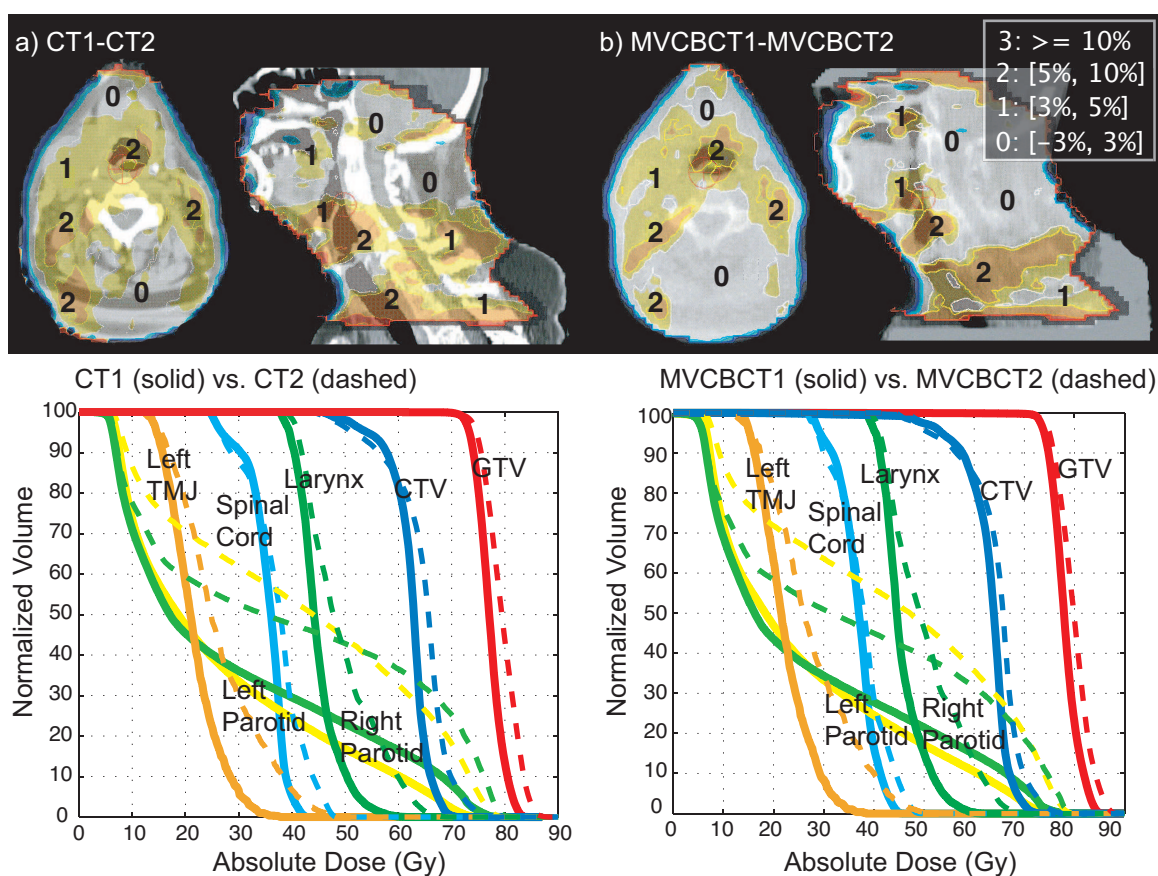


Figure 8.5: Top- Axial and sagittal images crossing the isocenter showing dose percentage difference distributions for CT1 compared to CT2 (left) and MVCBCT1 compared with MVCBCT2 (right). There are large anatomical areas where the dose increased by 5% or more. The locations of these areas are in good agreement between CT (left) and MVCBCT (right). Below DVH comparisons. All contours producing the DVH were drawn on the CT images and applied on to the MVCBCT after registration. The impact of weight loss on the DVHs is very similar when calculated using either CT or MVCBCT.

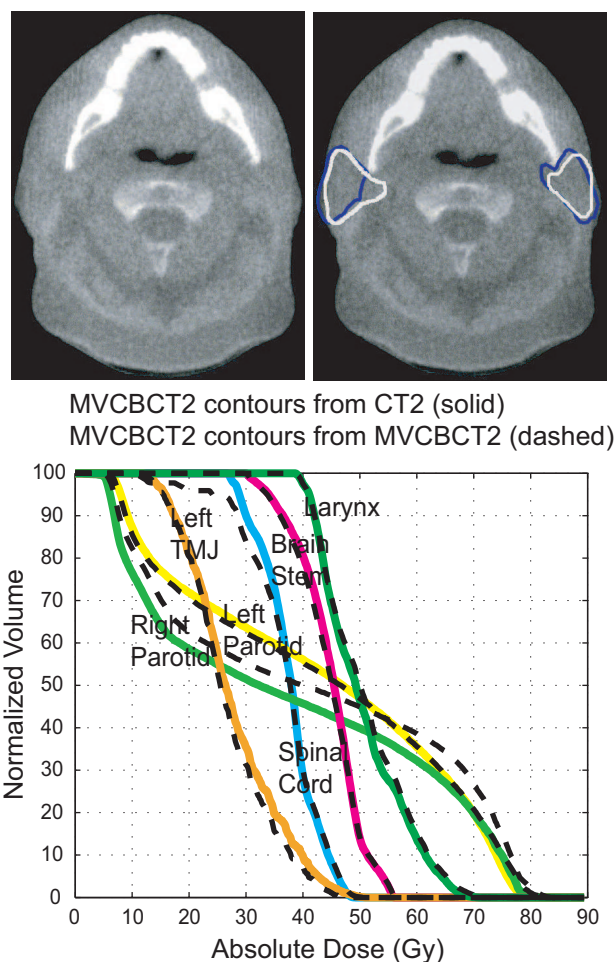


Figure 8.6: Evaluating the feasibility of contouring critical structures on MVCBCT. Top - One set of DVH was obtained from contours drawn on CT2 and copied to MVCBCT2 (blue contours) while the other set was obtained by direct contouring on MVCBCT2 (white contours). Below- The largest DVH difference was observed within the right parotid, which was located in a high-dose gradient region. Contouring directly on MVCBCT improved the DVH qualitative agreement compared to the right parotid on CT2 (Fig. 8.5). The overall good agreement in DVHs demonstrates the contouring capability of many head and neck structures on MVCBCT.

## 8.4 Discussion

### 8.4.1 Dose calculation accuracy achieved with MVCBCT

Calibration of CT images for physical or electron density is the main factor influencing dose calculation accuracy [69]. Because of a large cupping artifact produced by scatter radiation and beam hardening, the calibration of cone-beam CT images is more complex than calibration for conventional fan-beam CT. Fortunately, the lower amounts of scatter and the reduced energy dependence of the photon interactions in the MeV versus the keV range produce a cupping artifact that is somewhat predictable. In this work, a simple empirical method was used as a first order correction to improve the uniformity of MVCBCT reconstructions for the head and neck region. Although there are limitations inherent to the method with respect to where the patient needs to be placed for imaging (roughly centered as in the case of the water cylinders), this simple correction greatly reduces the nonuniformity in the CBCT images. Other more robust preprocessing methods to correct projection images for scatter have also been proposed [28, 47]. These methods would likely further reduce the cupping artifact. However, the results of this study suggest that a first order correction of the MVCBCT cupping artifact may already be sufficient for clinically useful dosimetric accuracy. The simulations performed with the head-sized water cylinder demonstrated that the dosimetric error caused by the MVCBCT cupping artifact is much less than the cupping artifact itself. This trend has also been observed

using a pelvis-sized water cylinder [70]. For multiple beam configurations, dosimetric errors would be further reduced due to averaging over different beam angles. With the uniformity-correction method that we have developed (see Sec. 3.5.1), dose calculation accuracy better than 3% in dose and 3 mm in distance-to-agreement was demonstrated for a head and neck patient treated with IMRT.

#### **8.4.2 Expanding dose calculation to more clinical sites**

The other factor that determines dosimetric accuracy is the size and location of field of view of the MVCBCT images. Using the current MVCBCT system, only the head and neck region can be fully imaged. One option to compensate for the limited field of view of MVCBCT is to merge the images from the kVCT and MVCBCT [53] in order to supplement truncated image data. In this study, tissue contours from the kVCT were used to compensate for using missing tissue in the MVCBCT images of the second patient. However there was still a 5 to 10% dosimetric over estimation related to missing data artifact, the assumption of rigid body deformation and the lack of heterogeneity correction in the missing data region. Despite this problem, the fact that most critical structures in the head and neck area are situated above the shoulders allowed the use of MVCBCT to accurately monitor the dosimetric impact of weight loss on clinically important structures. A dosimetric accuracy better than 3% in dose and 3 mm in distance-to-agreement was demonstrated above the shoulders. As larger detectors are manufactured or new image acquisition schemes developed, CBCT

should become capable of completely imaging the anatomy along the beams. Simply allowing a lateral shift of the detector for acquisition would increase the field of view to image shoulders or an average sized pelvis [43]. The good imaging performance and calibration possibility of MVCBCT in the presence of metallic objects could also be used to obtain better dose calculations in areas near a hip prosthesis or tooth fillings [71].

### **8.4.3 MVCBCT to monitor the dosimetric impact of weight loss**

During the course of external beam radiation treatment, many head and neck patients develop significant anatomic changes that may be related to multiple factors, including shrinkage of the tumor and/or nodal masses, weight loss, and resolution of postoperative changes [8]. For these cases, it has been demonstrated that repeat CT imaging and replanning is essential to ensure adequate doses to target volumes and safe doses to critical normal tissues [7]. One goal of this study was to learn if MVCBCT imaging could be used to detect when replanning becomes necessary. With MVCBCT already in use for patient setup, the user performing the CT-MVCBCT alignment may more readily notice when a change in anatomy has become potentially significant clinically. As this study demonstrates, dose recalculation on MVCBCT is also possible and can be used to estimate the percentage in dose differences within the target volume or normal tissues. Structures such as spinal cord, brain stem, larynx

and all of the bony structures can be contoured directly with MVCBCT. Although soft-tissue contouring is more difficult, nevertheless it was found to be feasible even in structures such as the parotids. Using the initial reference CT (CT1) as a guide, the dosimetrist was able to contour the parotids with MVCBCT with reasonable confidence. Using these contours, it was possible to estimate a mean dose increase from 26 to 42 Gy in the left parotid of the second patient. Although weight loss occurred throughout treatment, if the patient's anatomy from week 3 was assumed to represent the anatomy for the remaining treatment fractions (18 of 33 fractions), the right and left parotid mean doses would be increased by 7 and 9 Gy respectively. These estimates are in good agreement with the mean dose increase calculated using the conventional CT images. Although weight loss may be expected in these patients [65], many continue to be treated with the original treatment plan since the dosimetric impact of the weight loss is rarely assessed.

Several head and neck patients are now being imaged weekly with CT and MVCBCT to monitor the dose to critical structures and further study the dose calculation accuracy achieved with MVCBCT. Despite the fact that dose calculation can be performed on MVCBCT, repeating the kVCT is now still required for replanning. Currently MVCBCT does provide some soft-tissue information but conventional CT is preferred for recontouring the target volumes (GTV and CTV). Precise soft-tissue contouring on MVCBCT should become feasible as image quality continues to improve [55], which combined with a larger reconstructed volume may eliminate the need

for repeat kVCT scans on the patient undergoing radiation treatment procedures.

## Chapter 9

# Other Applications

Other applications using MVCBCT have been studied or implemented in the clinic. The following sections briefly describe some of the work performed by members of our group that extend the application of MVCBCT beyond those already discussed in this thesis.

### 9.1 Organ Delineation in Presence of Metallic Implants

Metal artifacts cause a significant problem for identifying structures when images are acquired with conventional diagnostic CT techniques. Several postprocessing algorithms have been developed to reduce the image degradation [72]. However, the level of artifact reduction is still only adequate on images affected by small metal



objects, such as gold seeds, and cannot resolve artifacts that accompany the use of larger metallic structures such as femoral and spinal implants, dental fillings, and arterial stents. In comparison to the keV energy range, the presence of high atomic number ( $Z$ ) material has relatively little impact on the image quality of MVCBCT. Therefore, MVCBCT images can be used to complement missing information during planning or patient position verification.

Figure 9.1 demonstrates the superiority of MVCBCT over conventional diagnostic CT in the presence of metal objects. An MVCBCT was performed on a patient that underwent major reconstruction of the left portion of the pelvis. Figure 9.1a and Fig. 9.1b compare the same sagittal and axial slices on the diagnostic CT (left) and the MVCBCT (right). Figure 9.1c shows that only the MV cone-beam image, which was displayed (with appropriate window and level settings) to show the metal pieces, can render the 3D object correctly.

The presence of metal artifacts in CT makes it impossible to use the CT numbers quantitatively for dose calculations. For these cases the treated volume is usually assumed to be water-equivalent in the treatment plan calculations. Treating the volume as water and ignoring the presence of metal may cause severe deviations between the planned dose distribution and the real dose delivered. Ongoing research is being performed to calibrate the MVCBCT for direct use in dose calculations, thus with the goal of achieving more accurate dose calculations using inhomogeneity corrections. Currently at UCSF, most prostate patients with hip prosthesis undergo a

MVCBCT acquisition to complement the CT procedure during the contouring process in the planning system [71]. Other cases where MVCBCT could be used include patients with dental amalgam or implants, orthopedic implants or prostheses, and high-dose rate brachytherapy catheters.

## 9.2 Tomosynthesis

Megavoltage Cone-Beam Digital Tomosynthesis (MVCB DT) is an in-room imaging technique, which enables the reconstruction of several 2D slices from a set of projection images acquired over an arc of  $20^\circ$  to  $40^\circ$ . The limited angular range reduces the acquisition time and the dose delivered to the patient, but affects the image quality of the reconstructed tomograms. A recent technical note describing some imaging characteristics of MVCB DT was published by our group [73]. The image obtained with MVCB DT are somewhere between MVCBCT and portal imaging in terms of image quality and dose to the patient. While it is not clear at this point what role MVCB DT will play in RT, potential clinical applications include lung patient setup and the development of breath holding techniques for gated imaging.

## 9.3 High-Dose Rate Brachytherapy

MVCBCT has recently been used to identify catheters and to complement the regular CT for target definition for high dose rate (HDR) brachytherapy in patients with

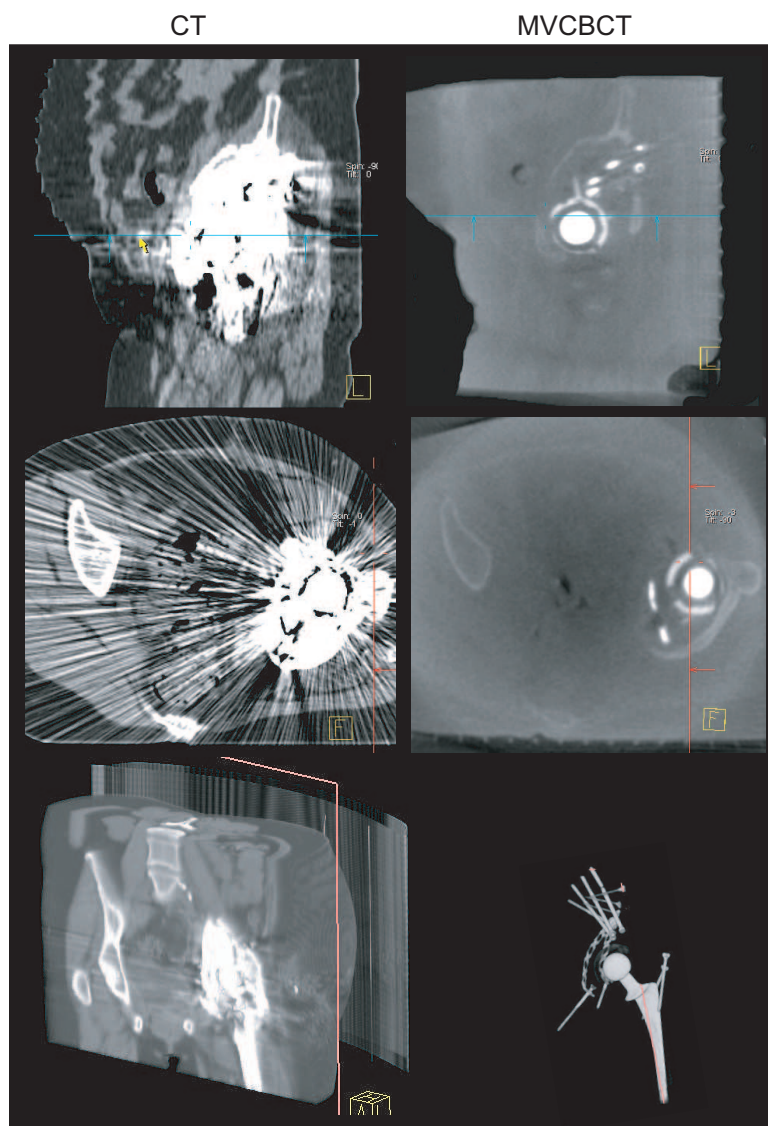


Figure 9.1: Images showing the superior performance of MVCBCT (right) over CT (left) in the presence of dense metal objects. All metal pieces used for this hip reconstruction are clearly visible on the MVCBCT 3D rendering (bottom).

implanted metallic objects. A method was developed for prostate patient in which routine transrectal ultrasound guided catheter implant and recovery, MVCBCT, and regular CT acquisitions were performed within few minutes. Metallic wires were inserted in the catheters during the MVCBCT image acquisition. A series of filters (averaging and diffusion) were applied on the MVCBCT image to maximise spatial resolution and image quality. The MVCBCT and CT images were registered with the Anatomy Modelling module of the planning system using the catheters as landmarks. The fused images were used to delineate the target and organs at risk. Then, the MVCBCT and the volumes of interest were transferred to the brachytherapy planning system where catheters were identified solely from the MVCBCT image. The dose distribution was optimized by following our standard technique using the inverse planning. Fused MVCBCT-CT images greatly facilitated target delineation. The registration precision was better than 1.5 mm in the prostate and catheter areas. Catheters were easily visible and accurately defined on the MVCBCT images. The same dosimetric criteria used for regular HDR prostate planning were used and achieved on this patient.

HDR treatment based only on CT is not possible for patients with bilateral hip replacements. For these reasons, the use of MVCBCT for planning offers prostate and other pelvic patients with hip prosthesis an advanced form of HDR brachytherapy that is not possible using existing conventional techniques.

# Chapter 10

## Conclusion and Future Directions

### 10.1 Clinical Significance of Thesis

The end goal of this research is an in-room 3D imaging system for image-guidance of external beam radiation therapy. The work presented in this thesis has accomplished many of the key steps towards achieving this end goal. In the last 5 to 6 years, the first clinical MVCBCT imaging system has been developed, studied and integrated in the clinic. Such fast implementation of a new technology can largely be attributed to a conjoint effort between academia (UCSF) and the industry (Siemens OCS). In only 4 years, our group has published nine peer-reviewed articles with three more under preparation and at least 50 abstracts presented at meetings of international caliber. To the best of our knowledge, this is the first thesis to report on a clinical MVCBCT imaging system used in radiation oncology. In this section, I give

my personal opinion on the significance of the thesis scientific contributions described in this thesis. These contributions are described in the same chronological order in which the work was performed. This dissertation describes new contributions in MVCBCT with respect to system development, the description and optimization of the system physical performance, clinical applications, and clinical implementation.

My first year on this project was mostly dedicated to learning the basics of the imaging system and to understanding the clinical motivation to develop in-room image guidance techniques. There were several late evenings with incremental progress. As a student, it was a wonderful experience to be surrounded by such good scientists and clinicians. I was able to tackle small projects that motivated the development of software tools for image reconstruction and analysis. During that time, image acquisitions were done in a purely manual fashion which allowed testing of different acquisition modes, image calibrations and flat panel detectors. My role was to reconstruct images offline using a primitive set of applications developed at Siemens (Siemens Oncology Care Systems, Concord, CA). This experience truly solidified my understanding of the system and helped me establish the basic software tools to perform research. One of my image analysis application written with Matlab (The Mathworks, Inc., Natick, MA) is still used by members of our team. In addition, this experience was key to understand the final implementation of MVCBCT as part of a commercial product. Being able to view and extract relevant information from the system is monumental for research and clinical work.

In the second year, switch boxes were installed on one linac to change the control console software version so that the rapid and safe acquisition of MVCBCT images could be performed. Patients were enrolled in different clinical studies under approval of the UCSF Institutional Review Board. My role was to prepare the patients' reference images, run the MVCBCT image acquisitions, assist in the setup decision making and review images offline. Most of the clinical cases presented in part II of the dissertation were obtained during that time. The first experience with a clinical MVCBCT system was published in a dedicated issue of the Medical Dosimetry journal on IGRT [74]. The paper is included in the Appendix B. It briefly discussed several aspects of MVCBCT including the system hardware and software, the image quality, and the dose delivered to patients but clearly focused on what can be done in the clinic with MVCBCT imaging. For the first time at our institution, patients were followed with in-room 3D imaging for both positioning errors (Chap. 6) and changes in anatomy (Chap. 7) occurring over the course of therapy. Prostate patients implanted with hip prostheses were imaged with MVCBCT for planning purposes (Sec. 9.1). These applications are becoming the new standard for clinical practice at our institution and elsewhere.

During the same period, we started to evaluate the possibility of using MVCBCT images for dose calculation. The first requirement for such application was to calibrate MVCBCT for electron density. Any artifact occurring with the imaging system had to be eliminated or reduced. Using the water-filled cylindrical phantom, we iden-

tified the flat panel energy response and scattered x-ray photons as main sources of a cupping artifact in MVCBCT images. A simple post-processing method based on an elliptical model of nonuniformity was developed to improve image uniformity. The dose calculation accuracy achieved with MVCBCT was evaluated on phantoms and with patient data representing a simple head and neck case. Finally, we demonstrated the feasibility of quantifying the dosimetric impact of anatomical variations. Another important technical contribution to our group has been to develop a method to import MVCBCT images in a treatment planning system, apply a reference plan, review the dose grids, and compare dose-volume histograms. Programs were written to compare dose distributions and evaluate the accuracy of dose calculation on MVCBCT. The work presented at the American Society for Therapeutic Radiology and Oncology meeting and published in the International Journal of Radiation Oncology, Biology, Physics (i.e., "The Red Journal") [66] clearly showed the feasibility and the current limitations of dose calculation using MVCBCT. This paper is also included in Appendix B. A larger study is under way to identify patients that would benefit the most from such application.

The dose delivered to patients from imaging has always been a sensitive subject. Even though the imaging dose from IGRT is generally small compared to the treatment dose, the increasing frequency of CT imaging may result in clinically significant dose to normal tissue. For the patients safety and to optimize the benefits of IGRT, the additional dose delivered from MVCBCT imaging was studied. Using the same



beam for treatment and imaging offers clear advantages in assessing patient dose. The treatment planning system was first validated as a tool to evaluate patient dose by comparing phantom measurements and simulations. We developed a method to quickly assess the dose received by any patient undergoing MVCBCT imaging. We also proposed in a recent paper [54] (included in Appendix B) methods to compensate the treatment plan to account for the dose received from routine MVCBCT imaging. This topic of MVCBCT imaging is also presented in Sec. 3.7. The paper demonstrates that dose from both treatment and imaging can be administered effectively and safely for patients treated with MVCBCT image guidance.

The physical performance of the system was characterized and optimized for image quality. While the work presented in the dissertation comes from recent measurements (phantom images acquired in the last year), and describes the experience gained from several measurements performed over the last 4-5 years. The most significant contribution is identifying the system settings (summarized in Table 5.1) that provide the best image quality for specific clinical applications and body sites. We also specified the MVCBCT exposure to use for alignment based on fiducials, bony anatomy or soft-tissue. Diffusion filtering on raw projections before reconstruction demonstrated substantial improvement in soft-tissue resolution and allows reduction of the radiation exposure. All this work was presented at the 2007 American Association of Physicists in Medicine meeting [75] and will be the subject of a scientific paper.

Finally, we evaluated the stability of the imaging system and developed a complete

QA procedure [76]. The system demonstrated superb stability which indicates that minimal work is needed for QA. Positioning accuracy should ideally be verified daily while other aspects such as geometry, radiation exposure, and system calibrations can be verified only twice a year. A future paper on the subject will greatly help the community to maintain the performance of the system with minimal workload.

## 10.2 Management of New Technology

I had the opportunity to study the management of technology at UC Berkeley Haas School of Business during the PhD. This section discusses both the opportunities and the challenges facing Siemens OCS in promoting and marketing MVCBCT.

The market of radiation oncology worldwide is divided between four major players: Varian/GE, Siemens, Elekta/Philips and Tomotherapy. All vendors offer a treatment machine potentially equipped with an in-room 3D imaging system ready for IGRT applications. From the different IGRT scientific events that I participated internationally, I have been able to observe the fierce competition of the industry and also have grasped the general community's opinion on the technologies available for IGRT.

Siemens has faced difficult challenges in marketing MVCBCT to the radiation oncology field. Varian, as the incontestable industry leader, has been able to take advantage of excellent development on kVCBCT imaging conducted by Elekta and collaborators two years prior to the release of MVCBCT. Both Elekta and Varian offer kVCBCT as main technology for IGRT. Siemens with MVCBCT has two strong

competitive industry leaders to face in promoting MVCBCT. While the simplicity and robustness of MVCBCT have always been strong features, the competitors and the general community have had doubts about the image quality and the dose delivered to patients. For image quality, it is becoming obvious that the kVCBCT and MVCBCT technologies complement each other. While kVCBCT performs well for small regularly-shaped objects, MVCBCT shows advantages for large objects and can be calibrated for electron density, a mandatory feature for dose calculation. The soft-tissue resolution of kVCBCT is generally superior than MVCBCT but the kVCBCT images exhibit large local variations of CT# due to strong scatter contamination to the detector's signal. In general, the community expectations have been high for the development of new imaging system systems that are integrated with radiation therapy machines. To the exception of CT-on-rail, all in-room CT systems have lower performance than modern conventional CT. It is important to keep in mind that the goal is not to replace conventional CT but to obtain 3D representations of the patient in treatment position to assure accurate administration of the treatment plan. With that said, all IGRT options are young technologies and will continue to improve. As for the imaging dose, our group has recently reported on this subject for MVCBCT. Not only can it be in the same order of magnitude than kVCBCT for alignment purpose, but a complete imaging dose distribution can be simulated in the planning system to create a composite plan. What once was a weakness for MVCBCT is now becoming an asset. Only publications and presentations at meetings will help educate

the community.

MVCBCT has several characteristics of a disruptive technology. Contrary to a sustaining technology, a disruptive technology is generally less attractive due to lower performance on certain aspects of the system and therefore it provides lower profit margin than competitors. However, they often offer a new set of attributes that eventually becomes of great value to mainstream customers. Historical examples include the compact disc, digital photography and semiconductors. Dose calculation and dose guided radiation therapy, discussed next, may represent competitive advantages for Siemens in the future. The business potential of disruptive technology are usually difficult to define and lower investment is generally attributed. For many years, Siemens generally has followed rather than led innovation in the radiation oncology field. The company has been the first to offer MVCBCT and should continue to invest in the development of new imaging systems and features. Only time will tell if their current portfolio approach of multiple investments will result in a sustainable competitive advantage.

### **10.3 Future Development**

MVCBCT imaging, through the development of IGRT protocols, is increasingly personalizing the administration of radiotherapy. Patients showing more variations in positioning and anatomy are now better followed throughout the treatment course. This allow treatment plans with reduced margins and new dose escalation protocols,

with the goal of developing procedures in which the patients will directly benefit from higher cure rates and fewer side effects. Some institutions, especially those that are smaller or are community based, must decide whether the clinical benefits are worth the investment and the current additional workload associated with in-room 3D imaging.

In this last section, I describe ways to improve the imaging system and discuss future developments.

The time required for patient set-up could easily be reduced by 1 to 2 minutes with proper tools for 3D image registration. The current automatic registration based on maximization of mutual information using the whole image is inefficient and inappropriate for most clinical cases. One immediate improvement would be to allow the user to specify a 3D region-of-interest that allows the automatic registration to converge faster and that localizes the alignment produced around the target. Head and neck patients showing anatomical distortion would clearly benefit from such capability. Another registration option should be to have the automatic registration only use a specified range of CT#. With such functionality, alignment of prostate patients implanted with gold seeds could be performed in few seconds with little or no human assistance. Finally, more options for simultaneous viewing two 3D images must be developed. Magnifying glass and chess board viewing tools would complement well the current image fusion with level of transparency.

There are currently several active areas of research aimed at improving the image

quality of MVCBCT. One direct method would be to use a more sensitive detector in MV imaging. Very little investment in the past have been made for MV imaging due to the much higher demand of kV flat panel detectors. In fact, the detector currently used for MVCBCT is a kV flat panel detector slightly modified for MV imaging. With the large number of MVCBCT system sold, there is now increasing level of incentive to invest in research and development of new detectors designed specifically for MV imaging. New detectors have already showed substantial improvement for MV imaging [42]. Another possible avenue for improving the imaging performance of MVCBCT is to modify the beam line in order to slightly increase the low-energy component of the x-ray beam. Preliminary investigations using a lower energy beam with no flattening filter and a carbon target suggest a factor of 3.5 improvement in CNR thus allowing a significant reduction of the exposure to obtain a given MVCBCT image quality [55]. Routine MVCBCT image acquisition on patients using this new imaging beam line and a new detector is currently underway at our institution.

Considerable research focuses on developing adaptive methods to fully personalize the administration of radiotherapy. The main issue with the current clinical practice is that the planned dose differs from the actual delivered dose due to errors in target position, anatomical changes and machine delivery. While the response of specific human cells to radiation has been well documented, there is currently no means to assure that the dose has been delivered as planned. The long term goal of our group is to link radiobiology studies and human cell response from functional imaging with

an accurate quantification of the true delivered dose during treatment. More aggressive and definitive treatment (dose escalation) could be prescribed with improved confidence thus bringing complete information to understand treatment outcomes. Since 2003, our group has been working on dose-guided radiation therapy (DGRT), an extension of adaptive radiation therapy where dosimetric considerations constitute the basis of treatment modification [77]. The main component of this strategy is a procedure to reconstruct the dose delivered to the patient based on treatment-time portal images [78] and pre-treatment MVCBCT images of the patient to obtain in-situ 3D dose distribution. The status of our research on DGRT has been recently published in a special issue of the British Journal of Radiology [79]. DGRT enabled by MVCBCT and exit-dosimetry combined with functional imaging may bring a new level of customized treatment and verification leading to improved cure rates and lower morbidity in patients receiving radiation therapy for cancer.

# Appendix A

## Summary of Terms and Abbreviations



Table A.1: Summary of Terms and Abbreviations.

Term or Abbreviation	Description
3DCRT	3-Dimensional Conformal Radiation Therapy
CCIL	Craniocaudal Imaging Length
CNR	Contrast-to-noise ratio
CT	Computerized Tomography
DRR	Digitally Reconstructed Radiograph
DVH	Dose-Volume Histogram
EBRT	External-Beam Radiation Therapy
EPID	Electronic Portal Imaging Device
FOV	Field-of-view
FWHM	Full Width at Half Maximum
IGRT	Image-Guided Radiation Therapy
IMRT	Intensity Modulated Radiation Therapy
kVCBCT	kiloVoltage Cone-Beam CT
Linac	Linear Accelerator
MOSFET	Metal-Oxide-Semiconductor Field-Effect Transistor
MRI	Magnetic Resonance Imaging
MTF	Modulation transfer function
MU	Monitor Unit
MVCBCT	Megavoltage Cone-Beam CT
NU	Non Uniformity
PET	Photon-Emission Tomography
PRF	Pulse Rate Frequency
PSF	Point Spread Function
QA	Quality Assurance
ROI	Region Of Interest
RT	Radiation Therapy
STD	Standard deviation
TFT	Thin Film Transistor
TPS	Treatment Planning System
UCSF	University of California San Francisco

## Appendix B

### Published Papers



## MEGAVOLTAGE CONE-BEAM CT: SYSTEM DESCRIPTION AND CLINICAL APPLICATIONS

OLIVIER MORIN, B.S.E., AMY GILLIS, M.D., JOSEPHINE CHEN, PH.D.  
 MICHÈLE AUBIN, M.S.E.E., M. KARA BUCCI, M.D., MACK ROACH, III, M.D. and  
 JEAN POULIOT, PH.D.

University of California San Francisco Comprehensive Cancer Center, Department of Radiation Oncology, San Francisco, CA; and University of California San Francisco/University of California Berkeley Joint Graduate Group in Bioengineering, San Francisco, CA

(Accepted 21 December 2005)

**Abstract**—In this article, we describe a clinical mega-voltage cone-beam computed tomography (MV CBCT) system, present the image acquisition and patient setup procedure, discuss the positioning accuracy and image quality, and illustrate its potential use for image-guided radiation therapy (IGRT) through selected clinical examples. The MV CBCT system consists of a standard linear accelerator equipped with an amorphous-silicon flat panel electronic portal-imaging device adapted for mega-electron volt (MeV) photons. An integrated computer workspace provides automated acquisition of projection images, image reconstruction, CT to CBCT image registration, and couch shift calculation. The system demonstrates submillimeter localization precision and sufficient soft-tissue resolution to visualize structures such as the prostate. In our clinic, we have used the MV CBCT system to detect nonrigid spinal cord distortions, monitor tumor growth and shrinkage, and locate and position stationary tumors in the lung. MV CBCT has also greatly improved the delineation of structures in CT images that suffer from metal artifacts. MV CBCT has undergone significant development in the last few years. Current image quality has already proven sufficient for many IGRT applications. Moreover, we expect the range of clinical applications for MV CBCT to grow as imaging technology continues to improve. © 2006 American Association of Medical Dosimetrists.

**Key Words:** External beam, Image-guided radiation therapy, Radiotherapy imaging, MV cone-beam CT.

### INTRODUCTION

Image-guided radiation therapy (IGRT) refers to the use of patient imaging in the treatment room to increase the conformality of the radiation dose to the tumor, improving tumor control, and reducing normal tissue complications.

The development of image-guidance tools and techniques in radiotherapy has been greatly motivated by the continual advances in external beam radiation delivery. With 3-dimensional (3D) conformal radiotherapy and intensity-modulated radiotherapy (IMRT), it is now possible to deliver radiation doses that conform tightly to the tumor volume. Many clinical studies and simulations indicate that these more conformal, higher dose treatments can decrease both the spread of disease and normal tissue complications.<sup>1-5</sup> However, as the planned dose distributions conform more closely to the pre-treatment planning computed tomography (CT), the precision of dose delivery becomes limited by the validity of using the planning CT to represent the patient on the treatment table throughout an extended course of treatment. Organs may change in size, shape, and position

from day to day and week to week due to normal anatomical variability, as well as due to the patient's reaction to radiation therapy, such as tumor shrinkage or weight loss.<sup>6-10</sup> Therefore, patient anatomical and positional information that can be obtained immediately before treatment is extremely valuable.

Imaging has long played a key role in assuring the accuracy of radiation therapy treatment. Recent implementation of highly sensitive and automated on-board electronic portal imaging devices (EPIDs) now enables daily low-dose portal imaging to visualize and adjust the patient position before each treatment. However, the utility of portal imaging to adjust the patient position is limited by reduced soft-tissue and 3D geometrical visualization caused by projection onto a 2-dimensional (2D) plane. This has motivated the development of 3D imaging of the patient while lying on the treatment table. Because CT is the current standard for localization of soft-tissue organs and target in treatment planning, there is a growing interest in CT imaging in the treatment room. Several systems have been developed including (1) a "CT on rails" system<sup>11,12</sup> requiring an additional diagnostic (CT) machine in the treatment room; (2) a kilovoltage cone-beam CT (kV CBCT) system<sup>13,14</sup> consisting of an additional kV x-ray source and detector attached to the treatment gantry; (3) a mobile C-arm

Reprint requests to: Jean Pouliot, UCSF Comprehensive Cancer Center, Department of Radiation Oncology, 1600 Divisadero Street, Suite H1031, San Francisco, CA 94143. E-mail: Pouliot@radonc17.ucsf.edu

kilovoltage imager<sup>15</sup>; (4) a megavoltage cone-beam CT (MV CBCT) system<sup>16,17</sup> using the pre-existing treatment machine and EPID for imaging; (5) an MV CT system<sup>18,19</sup> using the pre-existing treatment machine with an attached change arc of detectors; and (6) a tomotherapy system<sup>20</sup> replacing the traditional treatment machine (beam) with a CT ring and an MV beam source. The potential clinical applications of these IGRT technologies will depend on imaging performance, which continues to improve for many of the systems. As we learn more about patient anatomical variability using in-room 3D imaging, more clinical applications will also become apparent. In general, the goal is to provide more accurate and reproducible patient setup. The possibility of delivered dose verification combined with in-room imaging is also being explored and should provide an extra level of verification in the radiotherapy processes.

We present the recent developments in MV CBCT, describe an MV CBCT system, including the time required for acquisition and setup, the positioning accuracy, and the image quality. Then, a few chosen clinical examples are presented to illustrate how MV CBCT can be used for patient setup based on bony anatomy and/or soft tissue, to identify non-rigid deformation of the patient anatomy on the treatment couch and to monitor anatomical changes due to weight loss or tumor response. The superiority of MV volumetric imaging in presence of metallic objects is also demonstrated. Finally, ongoing research to improve image quality is discussed, as well as research to combine image guidance with dose verification.

## BASICS OF MEGAVOLTAGE CONE-BEAM CT

A cone-beam CT image is reconstructed from a set of open-field projection images acquired at different positions around the patient. The process is similar to conventional CT, which uses the signal from a single row of detectors to reconstruct a slice. For conventional CT, the 3D image is formed by translating the patient and imaging several slices. For CBCT, a 2D detector array is used and the reconstructed data set is a direct 3D image without multiple gantry rotations, table movement, or slice artifact. For MV CBCT, projection images are acquired using a radiotherapy linear accelerator (linac) with photons primarily in the mega-electron volt (MeV) energy range.

### *Historical perspective of 3D MV imaging*

Approximately 20 years ago, researchers in radiation oncology first used a linac beam for 3D imaging. These early systems reconstructed 2D slices using a fan-beam geometry.<sup>21,22</sup> Recently, MV fan-beam CT has been integrated into the helical tomotherapy system (Tomotherapy Inc., Madison, WI).<sup>20,23</sup> As the technology of 2D x-ray detectors has advanced,<sup>24</sup> cone-beam reconstruction systems have become increasingly feasible.

Several researchers have acquired MV CBCT images using standard linacs with liquid-filled ionization chamber detectors,<sup>25</sup> video-based EPIDs,<sup>25,26</sup> and amorphous silicon (a-Si) flat panel detectors.<sup>27,28</sup> In much of the early work, signal was maximized by applying high doses (50–200 cGy). Strategies such as the development of more sensitive detectors<sup>29,30</sup> and the restriction of the imaging volume to the treatment volume<sup>31,32</sup> have reduced these doses to clinically acceptable values and will continue to decrease imaging doses. Other developments include the adaptation of MV CBCT for lung tumor visualization by synchronizing image acquisition with respiration.<sup>16</sup>

The University of California San Francisco (UCSF), in collaboration with Siemens Oncology Care Systems, has been working on the clinical implementation of MV CBCT for the last 5 years. Our first MV CBCT imaging system has been previously described.<sup>17</sup> During this time, we have reduced exposure and improved image quality using a special triggered acquisition,<sup>33</sup> reduced the acquisition time, demonstrated soft-tissue contrast<sup>34</sup> and, recently, initiated a clinical patient setup study comparing portal imaging to MV CBCT.

### *Soft-tissue visualization using kV and MV imaging*

The shared use of the linac beam for treatment and imaging is inexpensive and convenient. However, the use of MeV photons for imaging is a departure from the general preference for kilo-electron volt (keV) beams in diagnostic imaging. The basic physics of x-ray interaction with matter can be used to explain the tradeoffs between using keV or MeV beams for imaging in radiotherapy. The visibility of large low-contrast objects in tomographic images, for example the prostate, depends on the contrast-to-noise ratio. Contrast is determined by the differential attenuation of the beam through different bodily tissues. In the MeV range, Compton scattering provides the majority of the beam attenuation. Due to the small energy dependence of Compton interaction, the contrast in MeV imaging is thus relatively constant over a large energy range. However, the greater dose per photon deposited by MeV photons reduces the imaging beam intensity that may be applied given patient dose constraints, thus reducing the signal. Moreover, the attenuation coefficient differences between bodily tissues are smaller for MeV energies, diminishing image contrast. The other important parameter, noise, includes the statistical fluctuation of photon detection as well as any source of unwanted radiation (*i.e.*, radiation containing no imaging information). In transmission imaging, the x-rays reaching the detector consist of unscattered (primary) and scattered (secondary) components. The primary fluence produces the signal in the resulting image, while the secondary fluence introduces noise and image artifacts and produces quantitative inaccuracies in the reconstructed CT numbers. The magnitude of scatter reaching the detector depends on the photon energy, the

field size, the object (size and composition), and the object-to-detector distance. The fan beam geometry rejects a considerable amount of scattered radiation, while the cone-beam geometry exposes the detector to scatter radiation. For a typical kV CBCT pelvic image (cone angle  $\sim 10^\circ$ ) acquired with the optimal air gap, the scatter-to-primary ratio (SPR) is greater than 170%, leading to CT number inaccuracies on the order of 40%.<sup>35</sup> Methods of reducing the effects of scatter include changing the acquisition parameters (dose, field-of-view, voxel size, etc.), using an antiscatter grid, performing pre-processing of the 2D projection raw images, and applying post-processing on the 3D reconstruction. Antiscatter grids have been studied for kV images but, so far, have not greatly improved the contrast-to-noise ratio for high-scatter acquisitions.<sup>36</sup> For an MV projection image of a pelvis (cone angle  $\sim 14^\circ$ ), the SPR is much smaller, on the order of 20–40%.<sup>37</sup> The small energy dependence of MeV photon interaction also makes the scatter fluence less dependent on the patient internal anatomy. The reduced effect of scatter for MeV images greatly narrows the difference in kV and MV cone-beam imaging quality. The lower dependence of the scatter on the exact patient anatomy may also make it easier to correct MV CBCT for scatter and allows for the accurate calibration of the voxel intensities into electron or physical density. Simple MV CBCTs of 2 water cylinders (pelvis and head-size cylinders) have been used with good results to develop geometric models of correction factors that reverse the spatially-induced cupping artifact. This correction of the nonuniformity caused by scatter allows dose calculation to be performed directly on the MV CBCT image.

#### Imaging system

Our clinic has 2 in-room MV imaging systems capable of portal imaging and cone-beam CT. Both systems consist of a standard treatment unit, one Primus™ and one ONCOR™ linear accelerator (Siemens Medical Solutions, Concord, CA) equipped with an amorphous silicon (a-Si) flat-panel adapted for MV photons. The  $41 \times 41 \text{ cm}^2$  flat-panel x-ray detector (AG9-ES, PerkinElmer, Optoelectronics) consists of a 1-mm copper plate and a Kodak Lanex Fast scintillator plate ( $\text{Gd}_2\text{O}_2\text{S:Tb}$ ) overlaid on top of light-sensing and charge-integrating thin-film transistor (TFT) array. The flat panel has  $1024 \times 1024$  TFT detector elements with a pitch of 0.4 mm. The detector is mounted on a retractable support, which deploys in less than 10 seconds with a positional reproducibility of 1 mm in any direction.<sup>38</sup> The entire imaging system, presented in Fig. 1, operates under a prototype SYNGO™-based COHERENCE™ therapist workspace, which communicates to the control console, the linac, and a local patient database. The workspace contains applications allowing for the automatic acquisition of projection images, image reconstruction, CT-to-CBCT image registration, and couch position adjustment. Each projection of the CBCT acquisition



Fig. 1. MV CBCT imaging system using a conventional linac and a flat-panel EPID adapted for the detection of MeV photons. In 45 seconds, the gantry rotates  $200^\circ$  around the patient acquiring one image per degree. The shift required to register the daily MV CBCT with the reference planning CT is available approximately 3 minutes after the beginning of the image acquisition.

is corrected for defective pixels, as well as for pixel-to-pixel offset and gain variations before 3D reconstruction.

#### Imaging geometry

In conventional CT, the relative source and detector positions are constant during rotation, and analytical equations can be used to describe the geometry of the reconstruction. The linac x-ray source and an EPID positioner, however, often lose their ideal isocentric positions as the gantry rotates, due to sagging of the mechanical supports. A geometric calibration<sup>17,39</sup> is performed to correct for this effect and conserve image quality. The position of the EPID must then only be reproducible for the calibration to remain geometrically accurate. The absolute position of the reconstruction volume isocenter is determined by the placement of the calibration phantom during geometric calibration. The room lasers are used to accurately place the phantom at the isocenter. The validity of the calibration method was verified by reconstructing a gold seed placed at isocenter with the room lasers. The center of the seed was located at the central voxel of the reconstruction, as expected. Simulations indicate that lateral deviations from the calibration geometry as small as 1 mm cause streaking artifact around high-contrast regions, while longitudinal deviations create shifts in the reconstruction volume, potentially introducing setup errors.<sup>40</sup> Our system was found to be reproducible to better than 1 mm in both directions over several months.<sup>38</sup> Routine geometrical calibra-

tions are conducted to assure image quality and will be used to track the system long-term geometrical stability.

#### Imaging procedure

An MV CBCT acquisition is similar to an arc treatment. The user first creates imaging template protocols by specifying the total dose for a CBCT acquisition (2–60 monitor units [MU]), the reconstruction size (128, 256, or 512), and the slice interval (1, 2, or 3 mm). A CBCT acquisition field is added to the existing patient treatment field list using one of the pre-defined CBCT protocols, which contain all the information needed by the system to perform the acquisition (field size, start and end angle, total dose, flat panel distance, etc.). The field parameters are directly transferred to the control console of the linac and the user can rapidly place the system in position for imaging. The linac gantry then rotates in a continuous 200° arc (270° to 110°, clockwise), acquiring one portal image for each angle. This acquisition procedure lasts 45 seconds. The image reconstruction starts immediately after the acquisition of the first portal image, and a typical  $256 \times 256 \times 274$  reconstruction volume ( $1.1 \times 1.1 \times 1.0 \text{ mm}^3$  voxel size) is completed in 110 seconds. The reconstructed MV CBCT and the raw projection images are saved in the patient database as DICOM images.

#### 3D setup method

The MV CBCT imaging procedure is well integrated in the clinical workflow for patient alignment. Upon start of the MV CBCT acquisition, the reference planning CT of the patient is automatically loaded into the COHERENCE™ Adaptive Targeting registration software, with the anatomical contours and the points of interest (Fig. 2a) defined in the planning system. Immediately after reconstruction, the software automatically registers the MV CBCT with the reference CT using a maximization of mutual information algorithm. Further manual adjustment of the registration in any of the typical planes (axial, coronal, and sagittal) is possible. In the current software version, rotations have been disabled from the registration. The system can display each CT with different color scheme, and the transparency levels can be adjusted to visualize either CT or the MV CBCT image sets. The table shift correction is constantly updated as the user fine-tunes the registration. The shift represents the distance between the planned treatment isocenter as specified on the CT image during planning and the true treatment isocenter, which corresponds intrinsically to the center voxel of the MV CBCT reconstruction. The table shift needed to align the treatment image with the diagnostic CT is typically available 3 minutes after the start of the MV CBCT acquisition.

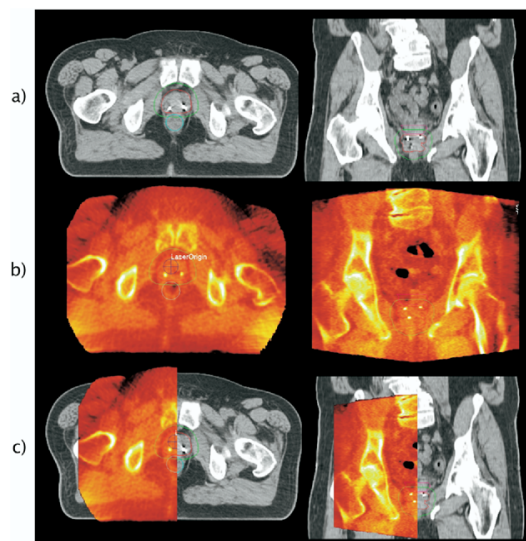


Fig. 2. A comparison of (a) a reference planning CT (gray) of a prostate patient, (b) an MV CBCT of the patient lying on the treatment table (color), and (c) a fusion of the 2 images. With an MV CBCT of 14.4 MUs, structures such as the prostate, rectum, fat, muscles, bone, and gold seeds are visible. Registration can be done automatically or manually using the 3 typical views (axial, sagittal, and coronal). The planning contours and the points of interest can be displayed on the MV CBCT to facilitate the registration.

#### System validation

To validate the new setup method, MV CBCT images ( $1 \text{ mm}^3$  voxel size) and orthogonal portal images of a phantom with 3 embedded gold seeds were obtained with the phantom positioned at 30 different known locations in the treatment field. The initial alignment of the seeds served as the reference position. The Syngo-based COHERENCE™ therapist workspace was used to measure the applied translations using the Portal Imaging (2D-2D) and the Adaptive Targeting (3D-3D) registration applications. The mean and standard deviation of the differences between the applied shift and the measured shift were 0.0 mm and 0.25 mm, respectively, for both data sets. This indicates that MV CBCT used with the Adaptive Targeting tool has the potential to verify patient shifts with submillimeter precision. Portal imaging was also demonstrated to be highly accurate in identifying translations of gold seeds.

Similar measurements were performed using an anthropomorphic head phantom (Rando) to compare a 2D setup technique using digitally-reconstructed radiographs (DRR) and portal images with a 3D setup technique using a diagnostic CT and MV CBCT images. Two CT scans were acquired on Rando using (A) a typical spiral 3-mm slice thickness, and (B) a fine sequential 1-mm slice thickness. The CT room laser alignment was marked on Rando using 3 small fiducials. The images

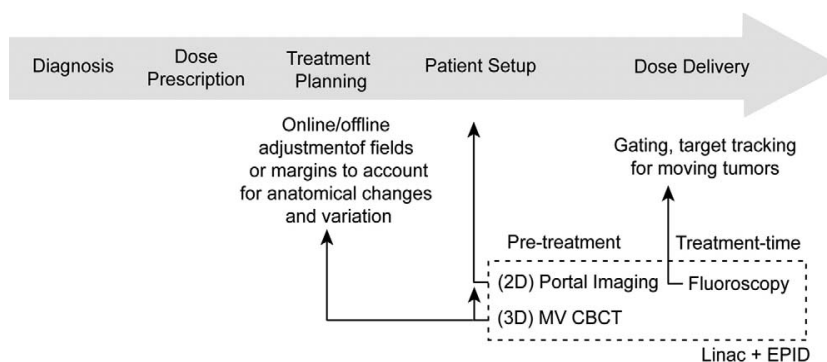


Fig. 3. An overview of various image-guided radiation therapy schemes using only a conventional linac and a flat-panel EPID. The large gray arrow represents the conventional flow of treatment with the main radiotherapy processes, and the small arrows indicate the possible points of feedback into the processes.

were imported into the planning system and a simple 2-field plan was created using the fiducials to define the treatment isocenter. Two pairs of orthogonal DRRs were created using CT scans (A) and (B). Finally, the plan, the CT scans, the treatment isocenter points, and the DRRs were transferred to the treatment unit. The Rando head was then aligned on the treatment table and translated to 30 different locations in the treatment field. For each position, a pair of orthogonal portal images was acquired to compare with the coarse (A) and fine (B) DRR references. MV CBCT images were also acquired at each position to compare with CT scans (A) and (B) in the Adaptive Targeting application. Only the automatic registration was used to align the MV CBCT acquisitions with the CT scans. The standard deviation of the differences between the applied shift and the measured shift was 0.4 mm and 0.9 mm for the 3D registration using the fine and the typical CT scans, respectively. This suggests that finer CT scans are more accurate for patient positioning using 3D alignment. Because the registration was almost entirely based on bony anatomy, there was no difference in the setup accuracy using the 2D or 3D method. However, the possibility of verifying setup in every plane in 3D greatly facilitated the process of obtaining the shift. Three-dimensional alignment should also provide an added benefit in the case of object rotation, which was excluded in the 2 described studies. Future work will include small rotations to study how they affect the shift assessments made using the 2D and 3D methods.

### CLINICAL APPLICATIONS

The MV CBCT system described above offers several image-guided techniques outlined in Fig. 3. One possibility is the monitoring of intrafraction motion of high-contrast features or fiducial markers using the flat panel in ciné mode.<sup>7</sup> This could be used to gate treatments for anatomical sites where in-treatment motion

may be problematic. With the same system, portal imaging can be used to ensure setup based on bony anatomy or gold seeds. Finally, with the introduction of an MV CBCT acquisition mode, it is possible to perform 3D setup based on bony anatomy and soft tissues to determine patient specific anatomical variation using images. This new information can be used to tailor the treatment plan for future fractions to account for the individual's variation. The application of this technique to different anatomical sites will depend on the ability to visualize the relevant organs.

The following sections describe the work that has been done to introduce MV CBCT in the clinic. Our IGRT objectives are to improve target positioning and to monitor anatomical changes as the treatment progresses. The patient acquisitions performed so far have demonstrated that MV CBCT provides information about the patients that was not available with portal imaging. Several studies are underway to determine the best usage of these new images.

### Patient acquisitions

To date, 90 acquisitions have been performed on a total of 45 patients. The anatomical sites imaged include head and neck, lung, and pelvis. All patients imaged with MV CBCT are required to give informed consent, and the image acquisitions are performed in accordance with the institutional review board's ethical standards. The patients enrolled in our setup study are positioned on the table using traditional immobilization devices and markings and are aligned with the room lasers. Both an MV CBCT and an orthogonal pair of 2D portal images are acquired in this initial position. The patients are then aligned using the orthogonal portal images compared with the reference DRRs. The applied shift is recorded and compared offline with the shift that would have been applied using MV CBCT. The dose used for MV CBCT

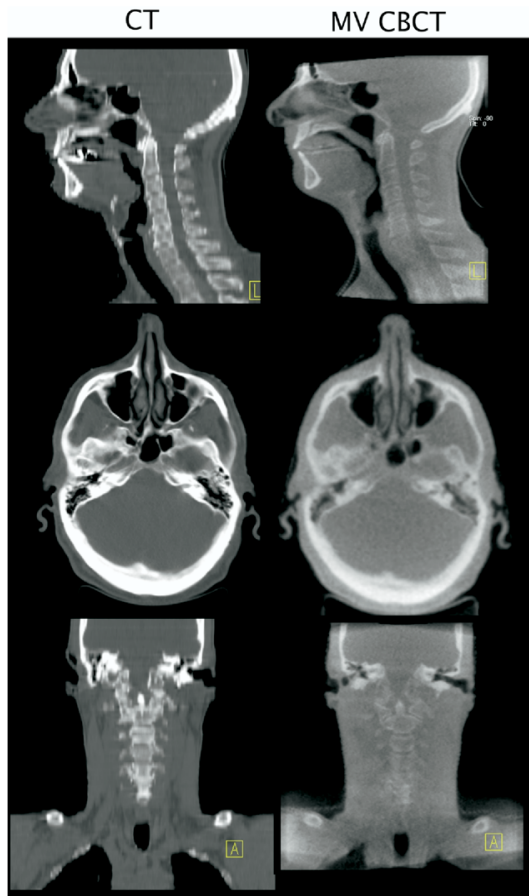


Fig. 4. Comparison of a diagnostic CT (left) with a 7-MU MV CBCT (right) for a typical head-and-neck patient. The window level of both sets of images was adjusted to provide the best soft-tissue contrast.

images ranges from 2 to 15 MUs depending on the frequency of the acquisition and on the anatomical site.

Figure 4 provides a comparison of a diagnostic CT (left) with the MV CBCT (right) performed on the first day of treatment for a typical head-and-neck patient. The window level of both sets of images was adjusted to allow the best soft-tissue contrast. Only 7 MU was delivered for the MV CBCT.

#### Patient dose in MV CBCT

The dose delivered to the patient during the MV CBCT was estimated using a commercial treatment planning software (Philips Pinnacle, Bothell, WA). An arc treatment was simulated on typical prostate and head-and-neck patients. With our current acquisition settings (projection angles and field size), the dose at the centers of the head and prostate were 0.9 and 0.75 cGy per MU, respectively. The maximum dose reached 1.24 cGy/MU

in a small anterior portion of the field of view. Although the dose delivered during MV CBCT imaging is generally negligible compared to the therapy dose, this extra dose could easily be taken into account in the patient's treatment plan.

#### MV CBCT for prostate patient setup

The prostate can shift daily up to 1 cm relative to pelvic bones due to gas and variations in rectal/bladder filling.<sup>7</sup> The variability in rectal distension can decrease the probability of biochemical control, local control, and rectal toxicity in patients who are treated without daily image-guided prostate localization.<sup>8</sup> At UCSF, most prostate patients treated by external beam radiotherapy have 3 gold markers implanted in the prostate, which are visualized daily on orthogonal portal images for alignment.<sup>41</sup> Gold seeds are implanted via a minor invasive procedure, usually well tolerated; however, this may not be feasible or appropriate in all circumstances. Patients are asked to have their bladder full and an empty rectum at the time of treatment to place the gland at the most inferior and posterior position in the body. In the example we present below, a typical prostate patient was aligned using the 3 markers on portal images. After setup but prior to treatment, the patient was imaged with MV CBCT. A total dose of 10.8 cGy (in the center of the prostate) was used to obtain the MV CBCT image. A large portion of the nonuniformity effect caused by scattered radiation was removed from the MV CBCT reconstruction using a gain calibration performed with solid water in the field of view. This had the effect of compensating for the additional signal in the center of the panel caused by scattered radiation on a given projection. The axial and coronal views of the patient diagnostic CT with anatomical contours are presented on Figs. 2a. Figure 2b shows that MV CBCT is capable of volumetric imaging with a good amount of soft-tissue information. Structures such as the prostate, the rectum, muscles, fat, air cavities, and gold seeds can be seen. It is clear by comparing the gold seeds on Fig. 2a and 2b that MV imaging performs better in the presence of metal objects. Figure 2c represents the patient anatomy prior to treatment fused with the reference anatomy and the anatomical contours of the planning. Despite some minor change in the rectum filling, the prostate shape and position at the time of treatment matches well with the anatomy on the diagnostic CT. In the presence of gold seeds, we have found that MV CBCT acquisitions of less than 2 MU can be used for direct 3D alignment. Figure 2c, however, shows the potential of using MV CBCT to align the patient based on soft tissue without the need of gold seeds. MV CBCT acquisitions of approximately 9 MU are currently required on typical pelvic patients for consistent prostate visualization without the need of gold seeds. By superimposing the anatomical contours on the CBCT image, the user may verify the impact of daily changes in rectum filling on the definition of the gross



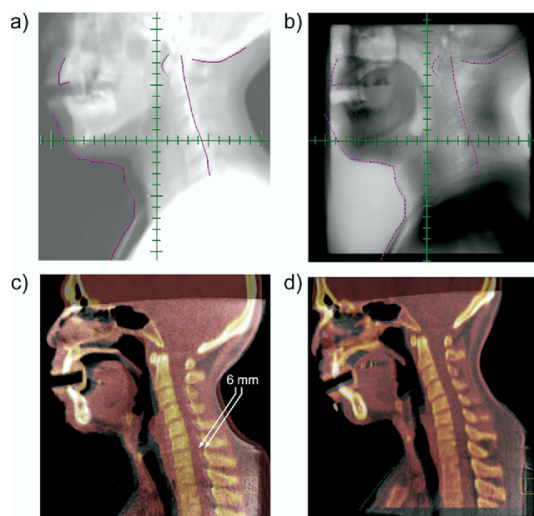


Fig. 5. Assessment and correction of a complex neck distortion using MV CBCT. On the same day, a head-and-neck patient positioned with a TIMO-C head holder was imaged using portal imaging (b) and MV CBCT (c). A difference in the arching of the neck is difficult to detect using the lateral DRR (a) overlaid onto the portal image (b). Registration of the patient MV CBCT (gray scale) with the kV CT (color) in (c) revealed a complex distortion of the lower neck region, which creates a 6-mm misalignment of the vertebral bodies and spinal cord. A new MV CBCT (color) compared with the new CT (gray) in (d) showed improvement in the 3D alignment.

tumor volume (GTV). More accurate treatment schemes using MV CBCT images could be studied by displaying anatomical contours and isodose lines from the treatment plan on the MV CBCT. Therapists could ensure, for example, that the rectal wall would not receive more than a limit dose on a given day of treatment.

#### *MV CBCT for evaluating complex spinal cord displacement during setup*

In this example, a patient with a T2N2b squamous cell carcinoma of the hypopharynx was imaged during radiation treatment using MV CBCT. The patient was positioned using an aquaplast head-and-shoulder mask indexed to the treatment couch. Originally, a TIMO-C head holder was used, which provided a more pronounced angle of neck flexion during treatment. A standard CT was used to obtain images for IMRT treatment planning. MV CBCT images were acquired at various times during treatment. Orthogonal pairs of 2D portal images were also obtained at the time of MV CBCT acquisition to compare the 2 modalities.

Figure 5a displays a DRR of the patient as initially simulated and planned. Easily visible structures such as the posterior vertebral bodies, base of skull, anterior maxilla, and aquaplast mask are outlined. Several weeks into the treatment, an MV CBCT and a corresponding set

of portal images were acquired for this patient. Figure 5b shows the outlines from Fig. 5a superimposed on this portal image. Although the base of skull and mask line up well, the line of the anterior maxilla is not aligned with the current position of the anterior maxilla. Additionally, the line of the posterior vertebral bodies is difficult to compare with the spinal anatomy. Figure 5c displays a sagittal image from the MV CBCT (gray scale) overlaid on the planning CT (color). The 2 sets of images have been registered to obtain an overall alignment based on the anatomy of the skull and face, as was similarly done using the 2D technique.

As seen in Fig. 5c, the patient alignment using the MV CBCT and planning CT allows for further assessment of not only global position, but also the relative positions of structures. Although the base of the skull is well aligned, a 6-mm difference in the position of the anterior vertebral bodies between the planning CT and the MV CBCT is clearly visible. The patient was subsequently resimulated using a head holder with less flexion (TIMO-B) to place the patient in a robust and more comfortable position. Once this plan was complete, an additional MV CBCT was obtained, as seen overlying the new planning CT in Fig. 5d. Comparison of the new MV CBCT and planning CT indicates that overall alignment, from the base of skull and along the vertebral bodies, was significantly improved using the new setup.

In this case, MV CBCT provided clear, informative images that allowed a more complete evaluation of patient setup. The 2D portal images did show some variation in patient positioning, but did not reveal the origin and the full magnitude of the misalignment. Using MV CBCT images, we were able to measure the magnitude of the misalignment, identify its source (a distortion of the neck), and confirm the correction of the problem. MV CBCT was a critical tool that led to replanning for more accurate treatments.

#### *MV CBCT to monitor anatomical changes*

In this next example, a patient with a T4bN1 squamous cell carcinoma of the nasal cavity was imaged using MV CBCT at various times while under treatment with external radiation therapy. The tumor involved the right nasal cavity and extended anterolaterally into the maxillary sinus and posteriorly to the nasopharynx. Prior to treatment, the extent of tumor was only evaluable on CT or magnetic resonance imaging examination. The tumor was unresectable, and the patient was treated definitively with concurrent chemoradiation. A conventional noncontrast CT was used to obtain base images for treatment planning. Four MV CBCTs were obtained during the course of radiation treatment in an effort to assess tumor anatomy variation that could not otherwise be easily visualized.

Representative images of the planning CT and 2 subsequent MV CBCTs are shown in Fig. 6. T<sub>0</sub> represents the start of radiation treatment. Examination of the

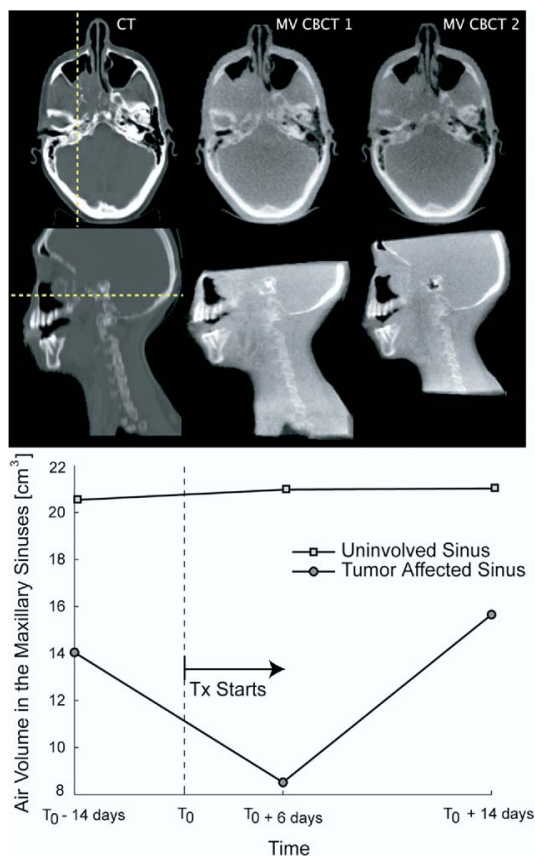


Fig. 6. Tumor size variation during the course of radiotherapy. The planning CT (left) of a patient affected by a right maxillary sinus tumor was acquired 14 days before the beginning of the treatment fractions  $T_0$ . Two MV CBCTs (middle and right) were acquired 6 days and 14 days after  $T_0$ . The evolution of the tumor size is visible on the axial (top) and sagittal (middle) views. The bottom plot presents the air volume in the cavities as a function of time.

MV CBCTs revealed an obvious soft-tissue density within the right maxillary sinus. The air interface present anteriorly provided excellent contrast with the soft-tissue density. In comparison, the left maxillary sinus was completely air filled, as seen on the planning CT and subsequent MV CBCTs. These images show that there is more soft-tissue density within the right maxillary sinus on the first MV CBCT ( $T_0 + 6$  days) as compared to the original planning CT ( $T_0 - 14$  days). This may indicate that there was tumor growth between planning and start of treatment. A comparison of the first ( $T_0 + 6$  days) and second ( $T_0 + 14$  days) MV CBCT shows some decrease in the amount of soft tissue in the cavity.

The amount of air filling for each side of the maxillary sinus at the given timepoints was calculated. This is plotted for the right (tumor affected sinus) and the left maxillary sinus (uninvolved sinus) in Fig. 6. If we were

to assume that the soft-tissue density within the affected sinus were exclusively tumor, rather than a combination of tumor and secretions, this quantitative assessment of air volume within the sinuses may serve as a surrogate for tumor response. This example demonstrates the potential of this imaging modality to monitor changes in target volume that are not otherwise evaluable.

The variation in target volume over a course of treatment may have important dosimetric consequences that require replanning. At what point during treatment a patient needs to be replanned is currently difficult to define. Because the MV CBCT images are obtained in the treatment position, it is possible to project the radiation treatment plan onto these images to assess the exact daily delivered dose.<sup>42</sup>

#### Dose calculation using MV CBCT

A recent validation study of dose calculation using MV CBCT in a commercial planning system was performed to assess the dose calculation accuracy.<sup>42</sup> An IMRT plan for a nasopharyngeal carcinoma was first defined using a conventional CT. On the first day of treatment, an MV CBCT acquisition was acquired. The patient anatomy and position on the MV CBCT was in good agreement with the initial CT. The same plan (isocenter, contours, and beams) was applied to the MV CBCT image, which had been corrected for nonuniformity and calibrated for electron density. The isodoses and the dose-volume histograms from the regular CT and the MV CBCT were in very good agreement. A gamma function<sup>43</sup> was computed to compare quantitatively the 2 dose distributions. The dose calculation accuracy using MV CBCT was better than 3% or 3 mm everywhere. This result opens the possibility of using MV CBCT to monitor the dosimetrical impact of setup errors, local deformations, weight loss, and soft-tissue shrinkage/swelling.

#### MV CBCT to perform setup for lung tumor

An MV CBCT was used to position a patient with a T2N0M0 squamous cell carcinoma of the lung. The patient had refused surgery and, therefore, was treated with definitive radiation therapy. At the time of fluoroscopic simulation, the tumor was noted to be immobile. This is obviously not the case for most lung tumors.<sup>6</sup> The isocenter was placed within the tumor volume and a nongated planning CT was obtained.

A hypofractionated course of radiation was prescribed, and it was therefore exceedingly important to ensure accurate set up of the tumor within the field. For this reason, and because of the reduced number of fractions, MV CBCT was used for daily setup.

On the first day of treatment, a pair of orthogonal portal images and an MV CBCT was acquired. The MV CBCT images were aligned with the planning CT using the soft-tissue mass itself to ensure adequate tumor dose. On the first treatment day, 2 additional MV CBCTs were

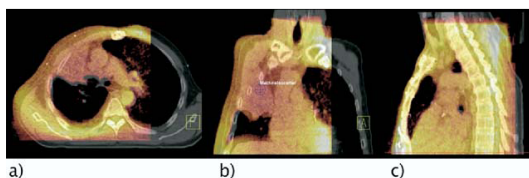


Fig. 7. Images comparing the use of MV CBCT and portal imaging for setup of a hypofractionated lung patient with a large and relatively immobile tumor. On the first fraction, the shift assessment was done using the sternum on portal images. This shift was then applied to an MV CBCT acquired the same day. Three views of the CT (gray scale) fused with the MV CBCT (color) are shown. While the sternum is well aligned on (c) the tumor is not on (a) and (b). For this reason, the patient was aligned using the soft-tissue information on the MV CBCT images.

obtained to verify this positioning method; the first following the applied shift, and the second after treatment delivery to evaluate any intrafraction motion during the 20 minutes of IMRT treatment. The post-shift MV CBCT showed excellent alignment with the planning CT, and the post-treatment MV CBCT remained well aligned. On subsequent days, a single MV CBCT was performed for positioning.

As an academic exercise, the measured shift that could have been made using only 2D portal images for positioning was applied to the MV CBCT and reference CT images. As can be seen in Fig. 7, if the sternum is aligned (Fig. 7c), the tumor in the right lung is not (Figs. 7a and 7b), and would be underdosed. A similar misalignment of tumor happens when the MV CBCT and the planning CT are aligned based on vertebral body position, a common way to verify the position of thoracic patients.

#### *MV CBCT to complement planning for patient with dense metal objects*

Metal artifacts on diagnostic CT images cause a significant problem for identifying structures. Several post-processing algorithms have been developed to reduce the image degradation.<sup>44</sup> However, the level of artifact reduction is still only adequate on images affected by small metal objects, such as gold seeds. In comparison to the keV energy range, the presence of high atomic number ( $Z$ ) material has relatively little impact on the image quality of MV CBCT. Therefore, MV CBCT images can be used to complement missing information during planning or patient position verification. Figure 8 demonstrates the superiority of MV CBCT in the presence of metal objects. An MV CBCT was performed on a patient who underwent major reconstruction of the left portion of the pelvis. Figures 8a and 8b compare the same sagittal and axial slices on the diagnostic CT (left) and the MV CBCT (right). Figure 8c shows that only the MV cone-beam image, which was

window leveled to show the metal pieces, can render the 3D object correctly.

The presence of metal artifacts in CT makes it impossible to use the CT numbers quantitatively for dose calculations. For these cases the treated volume is usually assumed to be water-equivalent in the treatment plan calculations. Treating the volume as water and ignoring the presence of metal may cause severe deviations between the planned dose distribution and the real dose delivered. Ongoing research is being performed to calibrate the MV CBCT for direct use in dose calculations, thus allowing for more accurate dose calculations using inhomogeneity corrections. Currently at UCSF, most prostate patients with hip prosthesis undergo an MV CBCT acquisition to complement the CT during the contouring process in the planning system.<sup>45</sup> Other cases where MV CBCT could be used include patients with dental amalgam or implants, orthopedic implants or prostheses, and high-dose-rate brachytherapy catheters.

#### FUTURE DIRECTIONS

We have described the performance of a clinical MV CBCT system and discussed some of its possible

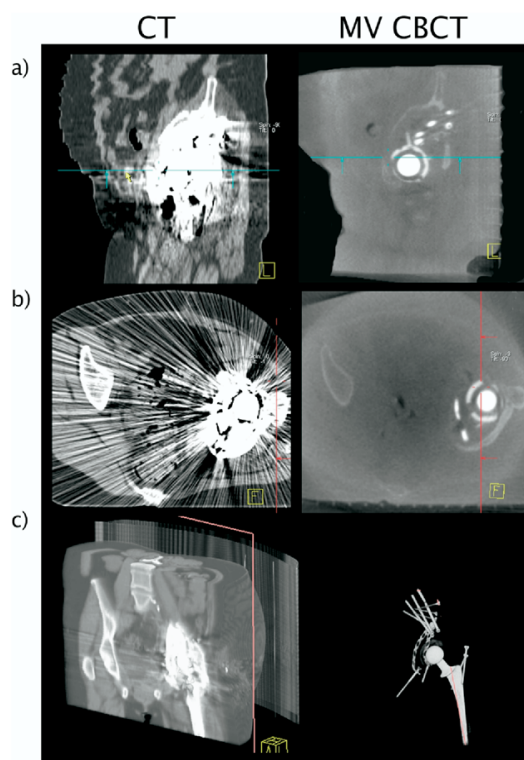


Fig. 8. Images showing the superior performance of MV CBCT (right) over CT (left) in the presence of dense metal objects. All metal pieces used for this hip reconstruction are clearly visible on the MV CBCT 3D rendering (bottom).

uses in IGRT. Despite the simplicity of the system, which consists of a conventional linac with an attached EPID, we have been able to locate objects with millimeter accuracy and visualize a variety of organs, including the prostate. Clinically, MV CBCT has already proven useful to evaluate the alignment of the spinal cord, locate and position immobile lung tumors, track the evolution of tumors in the sinus, and improve the delineation of structures in CT images that suffer from metal artifacts. These examples demonstrate the potential for MV CBCT to increase our understanding of the patient position on the treatment table and improve tumor targeting.

Soft-tissue resolution is key for in-room 3D imaging to complement the offering of portal imaging. Using our current MV CBCT system, we are able to visualize the prostate using approximately 9 MU. Ongoing research to improve image quality will further increase soft-tissue resolution. Monte Carlo simulations and experiments have demonstrated that using a lower-Z target generates more low-energy photons and enhances the contrast of portal images significantly.<sup>46,47</sup> In fact, simply removing the flattening filter causes contrast improvement in the order of 200%.<sup>48</sup> Combinations of target and flattener have been studied to optimize the combined applications of therapy and high-contrast megavoltage imaging.<sup>44</sup> Recent acquisitions of MV CBCT on a sheep head and on a CT contrast phantom using a carbon target and no flattening filter showed contrast resolution on the order of 0.5% for a dose of 3.5 cGy. The difference in density between the prostate and the surrounding tissues is in the order of 1–4%. With the improved beam line, one could project the resolution of the prostate and optic nerve with 1–2 cGy. Clinical images will soon be acquired with the new beam line to determine the extent of soft-tissue resolution.

New adaptive filtering schemes for MV imaging have also been developed and showed important noise reduction on projection images.<sup>30</sup> Finally, the biggest improvement in image quality might come from the detector itself, using denser and new scintillation materials, which would push the detection efficiency peak toward the photon energies of the treatment beam. The net result of all these efforts is that the contrast-to-noise ratio can still be significantly improved, which will allow MV CBCT to become a routine option for a wider range of clinical applications.

While the use of 3D imaging to account for the patient anatomy at treatment time is a great advance in assuring radiotherapy accuracy, the true determining factor for treatment outcomes is the dose delivered to the patient. MV CBCT may also play a key role in tracking the dose distributions delivered to the patient. As previously mentioned, we are currently researching the correction of MV CBCT image artifacts and the calibration of MV CBCT for electron or physical density. The calibrated MV CBCT images could be used to recalculate the dose delivered by the treatment plan to obtain a

more accurate estimate of the true delivered dose.<sup>42</sup> Another possibility under investigation is the additional use of the EPID during treatment to measure the energy fluence delivered by the linac. The measured fluence and the MV CBCT of the patient would be used together to estimate the delivered dose.<sup>49–51</sup> In this case, the effect of both patient anatomical changes as well as linac delivery errors could be assessed. These dosimetric verifications may provide additional information, which can be used to further optimize and improve radiation therapy treatments.

*Acknowledgment*—The authors thank the following persons for their valuable contributions, enlightening discussions, and active participation on the acquisition of the clinical cone-beam images: Albert Chan, Michael Ballin, Chris Malfati, Ping Xia, and Lynn Verhey at UCSF; and Ali Bani-Hashemi and his team at Siemens OCS. This research was supported by Siemens Oncology Care Systems (OCS). One of the authors (O.M.) acknowledges a doctoral scholarship from the National Sciences and Engineering Research Council of Canada (NSERC).

## REFERENCES

- Jacob, R.; Hanlon, A.; Horwitz, E.; *et al.* The relationship of increasing radiotherapy dose to reduced distant metastases and mortality in men with prostate cancer. *Cancer* **100**:538–43; 2004.
- Lee, N.; Xia, P.; Fischbein, N.J.; *et al.* Intensity-modulated radiation therapy for head-and-neck cancer: The UCSF experience focusing on target volume delineation. *Int. J. Radiat. Oncol. Biol. Phys.* **57**:49–60; 2003.
- Kuban, D.; Pollack, A.; Huang, E.; *et al.* Hazards of dose escalation in prostate cancer radiotherapy. *Int. J. Radiat. Oncol. Biol. Phys.* **57**:1260–8; 2003.
- Hurkmans, C.W.; Cho, B.C.J.; Damen, E.; *et al.* Reduction of cardiac and lung complication probabilities after breast irradiation using conformal radiotherapy with or without intensity modulation. *Radiother. Oncol.* **62**:163–71; 2002.
- Tubiana, M.; Eschwege, F. Conformal radiotherapy and intensity-modulated radiotherapy: Clinical data. *Acta Oncol.* **39**:555–67; 2000.
- Shih, H.A.; Jiang, S.B.; Aljarrah, K.M.; *et al.* Internal target volume determined with expansion margins beyond composite gross tumor volume in three-dimensional conformal radiotherapy for lung cancer. *Int. J. Radiat. Oncol. Biol. Phys.* **60**:613–22; 2004.
- Lometti, M.W.; Morin, O.; Aubin, M.; *et al.* Intra- fractional and inter/intra-field organ motion and a proposal for a new patient set-up protocol. American Association of Physicists in Medicine 47th Annual Meeting, Seattle, WA. *Med. Phys.* **32**:2160; 2005.
- de Crevoisier R.; Tucker, S.L.; Dong, L.; *et al.* Increased risk of biochemical and local failure in patients with distended rectum on the planning CT for prostate cancer radiotherapy. *Int. J. Radiat. Oncol. Biol. Phys.* **62**:965; 2005.
- Hansen, E.K.; Xia, P.; Quivey, J.; *et al.* The roles of repeat CT imaging and re-planning during the course of IMRT for patients with head and neck cancer. *Int. J. Radiat. Oncol. Biol. Phys.* **60**:S159; 2004.
- Barker, Jr.; J.L., Garden, A.S.; Ang, K.K.; *et al.* Quantification of volumetric and geometric changes occurring during fractionated radiotherapy for head- and-neck cancer using an integrated CT/ linear accelerator system. *Int. J. Radiat. Oncol. Biol. Phys.* **59**: 960–70; 2004.
- Ma, C.-M.; Paskalev, K.; *et al.* In-room CT techniques for image-guided radiation therapy. *Med. Dosim.* **31**:30–9; 2006.
- Wong, J.R.; Cheng, C.W.; Grimm, L.; *et al.* Clinical implementation of the world's first Primatom, a combination of CT scanner and linear accelerator, for precise tumor targeting and treatment. *Med. Phys.* **17**:271–6; 2001.
- Jaffray, D.A.; Siewerdsen, J.H.; Wong, J.W.; *et al.* Flat-panel cone-beam computed tomography for image-guided radiation therapy. *Int. J. Radiat. Oncol. Biol. Phys.* **53**:1337–49; 2002.

14. Oelfke, U.; Tucking, T.; Nill, S.; *et al.* Linac-integrated KV cone-beam CT: Technical features and first applications. *Med. Dosim.* **31**:62–70; 2006.
15. Sorensen, S.P.; Chow, E.; Kriminski, S.; *et al.* Image guided radiotherapy using a mobile kilovoltage x-ray device. *Med. Dosim.* **31**:40–50; 2006.
16. Sillanpaa, J.; Chang, J.; Mageras, G.; *et al.* Developments in megavoltage cone beam CT with an amorphous silicon EPID: Reduction of exposure and synchronization with respiratory gating. *Med. Phys.* **32**:819–29; 2005.
17. Pouliot, J.; Bani-Hashemi, A.; Chen, J.; *et al.* Low-dose megavoltage cone-beam CT for radiation therapy. *Int. J. Radiat. Oncol. Biol. Phys.* **61**:552–60; 2005.
18. Gildersleve, J.; Dearnaley, D.P.; Evans, P.M.; *et al.* A randomised trial of patient repositioning during radiotherapy using a megavoltage imaging system. *Radiother. Oncol.* **31**:161–8; 1994.
19. Evans, P.M.; Gildersleve, J.Q.; Rawlings, C.; *et al.* Technical note: The implementation of patient position correction using a megavoltage imaging device on a linear accelerator. *Br. J. Radiol.* **66**:833–8; 1993.
20. Mackie, T.R.; Kapatoes, J.; Ruchala, K.; *et al.* Image guidance for precise conformal radiotherapy. *Int. J. Radiat. Oncol. Biol. Phys.* **56**:89–105; 2003.
21. Swindell, W.; Simpson, R.G.; Oleson, J.R.; *et al.* Computed tomography with a linear accelerator with radiotherapy applications. *Med. Phys.* **10**:416–20; 1983.
22. Nakagawa, K.; Akanuma, A.; Aoki, Y.; *et al.* A quantitative patient set-up and verification system using megavoltage CT scanning. *Int. J. Radiat. Oncol. Biol. Phys.* **21**:228; 1991.
23. Ruchala, K.J.; Olivera, G.H.; Schloesser, E.A.; *et al.* Megavoltage CT on a tomotherapy system. *Phys. Med. Biol.* **44**:2597–621; 1999.
24. Mosleh-Shirazi, M.A.; Evans, P.M.; Swindell, W.; *et al.* A cone-beam megavoltage CT scanner for treatment verification in conformal radiotherapy. *Radiother. Oncol.* **48**:319–28; 1998.
25. Midgeley, S.; Millar, R.M.; Dudson, J. A feasibility study for megavoltage cone beam CT using a commercial EPID. *Phys. Med. Biol.* **43**:155–69; 1998.
26. Spies, L.; Ebert, M.; Groh, B.A.; *et al.* Correction of scatter in megavoltage cone-beam CT. *Phys. Med. Biol.* **46**:821–33; 2001.
27. Ford, E.C.; Chang, J.; Mueller, K.; *et al.* Cone-beam CT with megavoltage beams and an amorphous silicon electronic portal imaging device: Potential for verification of radiotherapy of lung cancer. *Med. Phys.* **29**:2913–24; 2002.
28. Groh, B.A.; Siewerdsen, J.H.; Drake, D.G.; *et al.* A performance comparison of flat-panel imager-based MV and kV cone-beam CT. *Med. Phys.* **29**:967–75; 2002.
29. Seppi, E.J.; Munro, P.; Johnsen, S.W.; *et al.* Megavoltage cone-beam computed tomography using a high-efficiency image receptor. *Int. J. Radiat. Oncol. Biol. Phys.* **55**:793–803; 2003.
30. Ghelmansarai, F.; Bani-Hashemi, A.; Pouliot, J.; *et al.* Soft tissue visualization using a highly efficient megavoltage cone beam CT imaging system. Proceedings of the International Society for Optical Engineering Meeting, San Diego, 2003. San Diego: Medical Imaging; **5745**:159–70; 2005.
31. Sidhu, K.; Ford, E.C.; Spirou, S.; *et al.* Optimization of conformal thoracic radiotherapy using cone-beam CT imaging for treatment verification. *Int. J. Radiat. Oncol. Biol. Phys.* **55**:757–67; 2003.
32. Anastasio, M.A.; Daxin, S.; Xiaochuan, P.; *et al.* A preliminary investigation of local tomography for megavoltage CT imaging. *Med. Phys.* **30**:2969–80; 2003.
33. Ghelmansarai, F.A.; Misra, S.; Pouliot, J. Electronic readout of a-Si EPIDs for optimum signal-to-noise ratio. Proceedings of the International Society for Optical Engineering Meeting, San Diego, 2003. San Diego: Medical Imaging; **5030**:788–98; 2003.
34. Pouliot, J.; Bani-Hashemi, A.; Aubin, M.; *et al.* Clinical integration of a MV cone-beam system for image-guided treatment. American Association of Physicists in Medicine 47th Annual Meeting, Seattle, WA. *Med. Phys.* **32**:1938; 2005.
35. Siewerdsen, J.H.; Jaffray, D.A. Cone-beam computed tomography with a flat-panel imager: Magnitude and effects of x-ray scatter. *Med. Phys.* **28**:220–31; 2001.
36. Siewerdsen, J.H.; Moseley, D.J.; Bakhtiar, B.; *et al.* The influence of antiscatter grids on soft-tissue detectability in cone-beam computed tomography with flat-panel detectors. *Med. Phys.* **31**:3506–20; 2004.
37. Jaffray, D.A.; Battista, J.J.; Fenster, A.; *et al.* X-ray scatter in megavoltage transmission radiography: Physical characteristics and influence on image quality. *Med. Phys.* **21**:45–60; 1994.
38. Morin, O.; Chen, J.; Aubin, M.; *et al.* Evaluation of the mechanical stability of megavoltage imaging system using a new flat panel positioner. Proceedings of the International Society for Optical Engineering Meeting, San Diego, 2005. San Diego: Medical Imaging; **5745**:704–10; 2005.
39. Wiesent, K.; Barth, K.; Navab, N.; *et al.* Enhanced 3D-reconstruction algorithm for C-arm systems suitable for interventional procedures. *IEEE Trans. Med. Imaging* **19**:391–403; 2000.
40. Morin, O.; Bose, S.; Chen, J.; *et al.* The impact of portal imager shifts and the assumption of rigid isocentricity on megavoltage cone-beam CT images. American Association of Physicists in Medicine 47th Annual Meeting, Seattle, WA. *Med. Phys.* **32**:1916; 2005.
41. Downs, T.M.; Roach, M.; Grossfeld, G.D.; *et al.* The University of California, San Francisco (UCSF) experience with permanently implanted gold markers for daily prostate realignment during radiation therapy. *Int. J. Radiat. Oncol. Biol. Phys.* **54**:280; 2002.
42. Morin, O.; Chen, J.; Aubin, M.; *et al.* Dose calculation using megavoltage cone-beam CT. American Society for Therapeutic Radiology and Oncology 47th Annual Meeting, Denver, CO. *Int. J. Radiat. Oncol. Biol. Phys.* **63**:S62–3; 2005.
43. Low, D.A.; Harms, W.B.; Mutic, S.; *et al.* A technique for the quantitative evaluation of dose distributions. *Med. Phys.* **25**:656–61; 1998.
44. Mahnken, A.H.; Raupach, R.; Wildberger, J.E.; *et al.* A new algorithm for metal artifact reduction in computed tomography: In vitro and in vivo evaluation after total hip replacement. *Invest. Radiol.* **38**:769–75; 2003.
45. Aubin, M.; Morin, O.; Bucci, K.; *et al.* Effectiveness of MV CBCT for patients with implanted high-Z material. American Association of Physicists in Medicine 47th Annual Meeting, Seattle, WA. *Med. Phys.* **32**:1933; 2005.
46. Nishimura, K.; Svatos, M.; Zheng, Z.; *et al.* Target flattener combinations for combined therapy and high contrast megavoltage imaging. American Association of Physicists in Medicine 47th Annual Meeting, Seattle, WA. *Med. Phys.* **32**:1909; 2005.
47. Flampouri, S.; Evans, P.M.; Verhaegen, F.; *et al.* Optimization of accelerator target and detector for portal imaging using Monte Carlo simulation and experiment. *Phys. Med. Biol.* **47**:3331–49; 2002.
48. Zheng, Z.; Ghelmansarai, F.; Svatos, M. Simplified beamlines for high performance portal imaging. American Association of Physicists in Medicine 46th Annual Meeting, Pittsburgh, PA. *Med. Phys.* **30**:1474; 2003.
49. Chen, J.; Chuang, C.F.; Morin, O.; Aubin, M.; Pouliot, J. Calibration of an amorphous-silicon flat panel portal imager for exit-beam dosimetry. *Med. Phys.* **33**:584–94; 2006.
50. Partridge, M.; Ebert, M.; Hesse, B.M. IMRT verification by three-dimensional dose reconstruction from portal beam measurements. *Med. Phys.* **29**:1847–58; 2002.
51. Pouliot, J.; Chen, J.; Zheng, Z.; *et al.* Dose reconstruction from MV conebeam CT for dose-guided radiation therapy. American Association of Physicists in Medicine 46th Annual Meeting, Pittsburgh, PA. *Med. Phys.* **31**:1832; 2004.



## PHYSICS CONTRIBUTION

## DOSE CALCULATION USING MEGAVOLTAGE CONE-BEAM CT

OLIVIER MORIN, B.Sc.,\*<sup>†</sup> JOSEPHINE CHEN, PH.D.,\* MICHÈLE AUBIN, M.S.E.E.,\* AMY GILLIS, M.D.,\*  
 JEAN-FRANÇOIS AUBRY, M.Sc.,\* SUPRATIK BOSE, PH.D.,<sup>‡</sup> HONG CHEN, PH.D.,\*  
 MARTINA DESCOVICH, PH.D.,\* PING XIA, PH.D.,\*<sup>†</sup> AND JEAN POULIOT, PH.D.\*<sup>†</sup>

\*Comprehensive Cancer Center, Department of Radiation Oncology, University of California, San Francisco, San Francisco, CA;

<sup>†</sup>University of California San Francisco and Berkeley, Joint Graduate Group in Bioengineering, San Francisco, CA; <sup>‡</sup>Siemens Medical Solutions, Oncology Care Systems Group, Concord, CA

**Purpose:** To demonstrate the feasibility of performing dose calculation on megavoltage cone-beam CT (MVCBCT) of head-and-neck patients in order to track the dosimetric errors produced by anatomic changes.

**Methods and Materials:** A simple geometric model was developed using a head-size water cylinder to correct an observed cupping artifact occurring with MVCBCT. The uniformity-corrected MVCBCT was calibrated for physical density. Beam arrangements and weights from the initial treatment plans defined using the conventional CT were applied to the MVCBCT image, and the dose distribution was recalculated. The dosimetric inaccuracies caused by the cupping artifact were evaluated on the water phantom images. An ideal test patient with no observable anatomic changes and a patient imaged with both CT and MVCBCT before and after considerable weight loss were used to clinically validate MVCBCT for dose calculation and to determine the dosimetric impact of large anatomic changes.

**Results:** The nonuniformity of a head-size water phantom (~30%) causes a dosimetric error of less than 5%. The uniformity correction method developed greatly reduces the cupping artifact, resulting in dosimetric inaccuracies of less than 1%. For the clinical cases, the agreement between the dose distributions calculated using MVCBCT and CT was better than 3% and 3 mm where all tissue was encompassed within the MVCBCT. Dose–volume histograms from the dose calculations on CT and MVCBCT were in excellent agreement.

**Conclusion:** MVCBCT can be used to estimate the dosimetric impact of changing anatomy on several structures in the head-and-neck region. © 2007 Elsevier Inc.

Dose calculation, Cone-beam CT, Planning with megavoltage cone-beam CT, Anatomic changes, Weight loss.

## INTRODUCTION

Image-based treatment planning has become the gold standard in radiotherapy (RT). In current practice, a kilovoltage CT (kVCT) scanner is used to acquire a three-dimensional (3D) snapshot of the patient anatomy before the beginning of therapy. This 3D image is imported, as a reference, to a treatment planning system to define the treatment isocenter, contour anatomic structures (target and organs at risk), and choose a beam arrangement to deliver a dose distribution that conforms to the given dose prescriptions and limitations. Ideally, the dose delivered upon completion of RT would be identical to the planned dose. In reality, sources of

error exist related to patient positioning, anatomic variations over time, the dose calculation engine, and the treatment machine output that will make the dose delivered differ from what was intended. These variables may potentially reduce the probability of tumor control and increase the severity of any side effects. Numerous investigators have reported that organs may shift in size, shape, and position from day to day and week to week because of normal anatomic variability, as well as clinical changes over time, such as tumor shrinkage, edema, or weight loss (1–3). It is fairly common (~33%) for head-and-neck cancer patients to have severe weight loss of up to 58% of their pretreat-

Reprint requests to: Olivier Morin, B.Sc., Comprehensive Cancer Center, Department of Radiation Oncology, University of California San Francisco, 1600 Divisadero St., Suite H1031, San Francisco, CA 94143. Tel: (415) 353-7167; Fax: (415) 353-9883; E-mail: Morin@radonc17.ucsf.edu

Presented in part at the 47th Annual Meeting of the American Society for Therapeutic Radiology and Oncology (ASTRO), Denver, CO, October 16–20, 2005.

This research was partly funded by Siemens Oncology Care Systems.

O. Morin and J.-F. Aubry received a scholarship from the

National Sciences and Engineering Research Council of Canada (NSERC).

Conflict of interest: none.

**Acknowledgments**—The authors acknowledge the following persons for their valuable contributions: at UCSF, Chris Malfatti for the acquisition of phantom images as well as Jeff Bellerose and Clayton Akazawa for planning and contouring on CT and MVCBCT images. At Siemens Oncology Care Systems (OCS), Ali Bani-Hashemi and his team.

Received May 25, 2006, and in revised form Sept 22, 2006. Accepted for publication Oct 20, 2006.

ment body weight (4). Such variations in target volume during the treatment course have dosimetric consequences that require repeat treatment planning. At what point during treatment a patient needs to undergo repeat planning is difficult to determine. Commonly, treatment plans are revised only when the setup is no longer reproducible, the mask used to position the patient no longer fits, or significant weight loss has been noted. Weekly physical examinations and total body weight measurements are performed but are unable to quantify changes that occur locally at the target or along the treatment beams. Most importantly, these methods do not quantify the dosimetric impact of the changing anatomy or patient positioning inaccuracies.

Several in-room CT systems have recently been developed, including (1) "CT on rails" (5), (2) a kilovoltage cone-beam CT system (6), (3) a mobile C-arm kilovoltage imager (7), (4) a megavoltage (MV) cone-beam (CB) CT (MVCBCT) system (8), and (5) a tomotherapy system (9). This study used a MVCBCT image, which utilizes the treatment beam from a conventional linear accelerator and an electronic portal imager to obtain an accurate 3D representation of the patient in the treatment position. Although this new imaging technology was primarily developed to provide accurate 3D positioning of the patient moments before dose delivery, the images obtained could also be used to perform dose calculations. This would open the possibility to monitor the dosimetric affect of changes in anatomy or position compared with the reference CT by applying the initial treatment plan to the MVCBCT images.

#### *Dose calculation requirements*

A 3D image data set must fulfill two requirements before being used for dose calculation. First, the image volume must include all the patient tissue along the treatment beams. Second, the treatment planning system requires the image to be calibrated for electron density, a radiologic parameter related to dose deposition in RT. Before image calibration, any artifact inherent to the imaging modality must be minimized. The calibration of CT images for electron density has been robustly demonstrated on kV and MV CT systems using fan-beam geometry (10, 11). Only recently have groups begun investigating the possibility of calibrating cone-beam images.

Using a large, open field for CBCT acquisition is an efficient way to obtain a 3D image without the need for multiple gantry rotations and couch movements. However, it exposes the detector to scattered radiation. In transmission imaging, the unscattered (primary) photons produce the image, and the scattered (secondary) photons introduce noise and image artifacts. Consequently, quantitative inaccuracies can be present in the reconstructed CT numbers. Although the problem caused by scatter to CBCT images is not new (12–14), the method to correct its effect is still an active area of research. Several authors have studied correcting kVCBCT images for scatter (15–17). The methods of reducing the artifacts include changing the acquisition parameters (*e.g.*, dose, field-of-view, voxel size), using an

anti-scatter grid and performing preprocessing of the two-dimensional projection images. All these methods have shown promising results for specific cases. Compared with kV photon beams, MV scattered photons are much less abundant and have more predictable behavior (12). To a first approximation, the scatter contribution to a MV projection image will be a smooth dome-shaped signal roughly centered on the imager (18, 19). Conventional detector gain correction procedures also tend to boost the signal in the center of the detector to try to compensate for a lower detector response measured when no object is present in the beam (20). This becomes an overcorrection once the patient has been placed in the beam, changing the beam's energy spectrum. The end result of the amplified signal in the center of the projection images is a cupping artifact, an underestimation of the CT values in the center of the reconstructed MVCBCT image. The magnitude of the cupping artifact increases with object size, and the location of the cupping is also dependent on the object's position relative to the isocenter. Before electron density calibration and dose calculation, MVCBCT images need to be corrected for this nonuniformity.

The objective of this research was to demonstrate the feasibility of performing dose calculations using MVCBCT. Because of the current limitations in the MVCBCT imaging volume, we focused this study on the dose calculations performed in the head-and-neck region. First, we performed phantom experiments to investigate the effect of MVCBCT cupping artifacts on dose calculation accuracy and to develop a method to reduce this effect. We then calibrated the corrected MVCBCT images for electron density and entered the calibration data into a commercial planning system. To test the dosimetric accuracy of using MVCBCT for a clinical case, we compared the doses calculated using MVCBCT and using a conventional CT for a patient who exhibited minimal anatomic changes between the two image acquisitions. Finally, we used two sets of CT and MVCBCT images to track the changes in the delivered dose distributions for a patient who had lost considerable weight during the course of intensity-modulated RT (IMRT).

## METHODS AND MATERIALS

### *Imaging and planning equipment*

Our clinic has two in-room MV imaging systems capable of CBCT (MVison, Siemens Medical Solutions, Concord, CA). Both systems consist of a standard medical linear accelerator equipped with an amorphous silicon flat panel detector adapted for MV photons. Details on the imaging system have been described previously (21). The relatively small contribution of scatter in the mega-electron volt energy range, compared with the kiloelectron volt range, allows the full use of the detector longitudinally (superior to inferior) without significant reductions in image quality. Therefore, with the current size of the detector ( $41 \times 41 \text{ cm}^2$ ), a volume of approximately  $27 \times 27 \times 27 \text{ cm}^3$  can be imaged. The MVCBCT acquisition is similar to an arc treatment. The linear accelerator gantry rotates in a continuous  $200^\circ$  arc ( $270^\circ$  to  $110^\circ$ , clockwise) acquiring one portal image for each angle. This acqui-

sition procedure lasts 45 s. The image reconstruction starts immediately after the acquisition of the first portal image and is completed in 110 s. All the MVCBCT acquisitions presented in this report were performed using a total exposure of 7.2 monitor units.

For treatment planning purposes, patients undergoing external beam RT at our hospital are imaged using a CT SOMATOM Emotions scanner (Siemens Medical Solutions, Malvern, PA). Predefined imaging protocols are used to tune the X-ray beam characteristics for the best image quality for specific body regions. Quality assurance tests are done to ensure accurate calibration of the reconstructed CT numbers for electron density. The obtained calibration look-up table is entered in Pinnacle version 7.6 (Philips Medical Solutions, Bothell, WA), the treatment planning system used by the department.

#### Uniformity correction

The predictability of scatter in the MV range allows for the use of a simple postprocessing method to improve the uniformity of MVCBCT. For this study, we first imaged a head-size water cylinder to characterize and correct the artifact produced during a typical head-and-neck MVCBCT acquisition. The cylinder diameter and length was 16 cm and 24 cm, respectively. The average CT number of the whole cylinder was used as the CT value desired after correction. A geometric model of correction factors was defined to characterize the cupping artifact. A basic ellipsoid shape (semiaxes;  $r_x$ ,  $r_y$ ,  $r_z$ ) centered on the cylinder ( $x_c$ ,  $y_c$ ,  $z_c$ ) was defined. As described in Eq. 1, each voxel of the water cylinder MVCBCT ( $x,y,z$ ) falls onto the surface of an ellipsoid  $\alpha$ . Using the water cylinder images, correction factors ( $CF_\alpha$ ) were determined for eight values of  $\alpha$ . Linear interpolation or extrapolation was used to determine the correction factors for values of  $\alpha$  that lie between, or beyond, the tabulated values.

$$\left(\frac{x-x_c}{r_x}\right)^2 + \left(\frac{y-y_c}{r_y}\right)^2 + \left(\frac{z-z_c}{r_z}\right)^2 = \alpha^2 \rightarrow CF_\alpha \quad (1)$$

#### Electron density calibration

Tissue inhomogeneity is derived by converting the CT value in each voxel of the reconstruction into relative electron density or physical density, depending on the treatment planning system. This is usually done empirically by scanning a tissue equivalent phantom (CIRS model 062, Norfolk, VA) with inserts of known electron density. For the calibration of MVCBCT, however, this small phantom could not be used as is, because it did not reproduce the scatter environment of the water cylinder used to define the uniformity correction factors. Instead, electron density inserts (*i.e.*, air, lung inhale, lung exhale, adipose, water, trabecular bone, and dense bone) were placed in the same water cylinder used to define the uniformity correction factors. The water cylinder with inserts was imaged using both conventional CT and MVCBCT. The MVCBCT nonuniformity was reduced using the ellipsoid model of correction factors described. Regions of interest were drawn on the inserts of both CT scans to extract the mean intensities.

#### Estimating the dosimetric inaccuracies produced by MVCBCT nonuniformity

The water cylinder phantom was used to investigate the impact of the MVCBCT cupping artifact on the accuracy of dose calculation. The water cylinder was first imaged with the conventional CT scanner. The phantom alignment in the CT room was marked

with three small fiducials. A MVCBCT of the cylinder was acquired in the treatment room using the fiducials for alignment. The kVCT, MVCBCT with cupping artifact, and MVCBCT corrected for nonuniformity were all imported into the treatment planning system. The CT voxel intensities of each scan were converted to relative electron density to water using the calibration curves. A plan with a single anterior-posterior  $10 \times 10\text{-cm}^2$  square beam was applied on all three image sets. The three dose distributions were obtained using identical dose grid positions and a resolution of 2 mm. Finally, the dose distributions obtained using the two MVCBCT scans (with and without uniformity correction) were compared with the reference dose distribution calculated using the conventional CT. To obtain a complete quantitative evaluation of dose distributions in the low- and high-dose gradient regions, we computed dose percentage differences and a  $\gamma$  index (22). We used typical acceptance criteria of 3% in dose and 3 mm in the distance-to-agreement for the  $\gamma$  index.

#### Clinical test case for validation

To assess the dose calculation accuracy achieved with MVCBCT on a patient, a head-and-neck patient treated with IMRT for recurrent nasopharyngeal carcinoma was selected. This patient was imaged in the first week of therapy and no major change or deformation in the anatomy from the time of the reference CT was seen. This observation was also verified with 3D registration of the MVCBCT image with the CT. Manual registration was performed until the best match was achieved by visual comparison. The MVCBCT was corrected for nonuniformity using the ellipsoid correction factors previously described. The IMRT plan (isocenter, beams, and contours) defined on the kVCT image was applied to the MVCBCT image. None of the beam passed through the patient's shoulders, parts of which extended beyond the MVCBCT field of view. The dose distributions calculated with the conventional CT and MVCBCT were compared using the dose percentage differences and  $\gamma$  index distributions. Because the anatomy and position of the patient was nearly identical on both images after 3D registration, contours drawn on the conventional CT (*e.g.*, spinal cord, left parotid, right eye, brainstem, and gross tumor volume) were directly copied onto the MVCBCT. The dose-volume histograms (DVH) of the structures were compared.

#### Testing the ability of MVCBCT to determine dosimetric changes caused by weight loss

One patient treated with IMRT for a base of tongue carcinoma was selected to evaluate the capability of MVCBCT to monitor the dosimetric affect of weight loss. The patient was first imaged with conventional CT (CT1) for planning. The treatment plan created for this patient contained beams passing partly through the patient's shoulders to cover the cervical lymph nodes. Parts of these beams extended beyond the MVCBCT field of view. A MVCBCT (MVCBCT1) was acquired during the first week of therapy, 12 days after CT1. Additional CT (CT2) and MVCBCT (MVCBCT2) images were acquired on Week 3 (22 days after MVCBCT1) of treatment. The patient was displaced by 2 cm in the vertical direction for MVCBCT imaging to obtain better uniformity correction from the method presented in this report. MVCBCTs were corrected for nonuniformity and transferred to the treatment planning system. As with the previous test case, the MVCBCTs were aligned precisely with their corresponding reference CT (MVCBCT1 with CT1 and MVCBCT2 with CT2) using 3D registration. A dosimetrist and physician contoured the target and



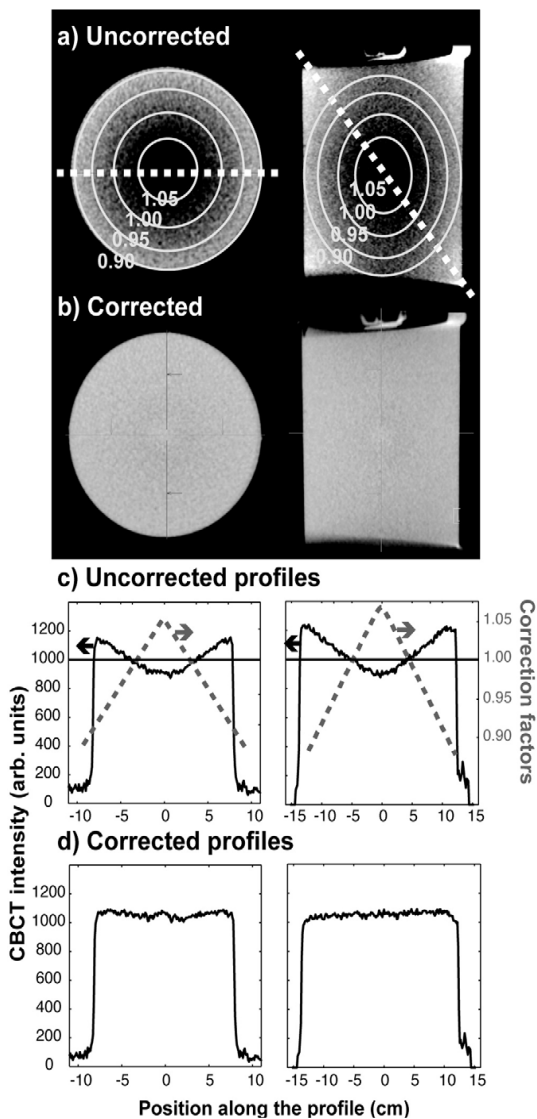


Fig. 1. Megavoltage cone-beam CT (MVCBCT) acquisitions and intensity profiles for a head-size water cylinder. Uncorrected images (a) contain strong cupping artifact. Axial and sagittal profiles (c), taken along directions defined by white dashed lines in (a), display magnitude of cupping. Derived correction factors are overlaid on images in (a). Dashed lines in (c) plot correction factors derived from data. Corrected images (b,d) are much more uniform. Both sets of MVCBCT images displayed with same window and level.

critical structures on CT1 and CT2. These contours were copied onto the corresponding MVCBCTs. For comparison, critical structures (*i.e.*, parotid glands, spinal cord, brainstem, larynx, and right temporomandibular joint) were also drawn directly on MVCBCT2 by the dosimetrist. CT1, but not CT2, was used as a visual reference to guide the contouring on MVCBCT2. To compensate for parts of the patient's shoulders and chest that extended outside the MVCBCT field of view, tissue and lung contours were drawn

on CT1 and copied onto MVCBCT1 and MVCBCT2 after 3D registration. The missing tissue and lungs were assigned a density relative to water of 1 and 0.4, respectively. Dose distributions were then obtained by applying the initial treatment plan onto CT1, MVCBCT1, CT2, and MVCBCT2. The four dose distributions were produced using identical dose grid positions and a resolution of 3 mm. The dose percentage differences and  $\gamma$  index distributions were computed for different combinations of dose distributions (CT1-MVCBCT1, CT2-MVCBCT2, CT1-CT2, MVCBCT1-MVCBCT2, and CT1-MVCBCT2). Dose-volume histograms were obtained for several structures (*i.e.*, left temporomandibular joint, parotid glands, spinal cord, larynx, clinical target volume, and gross tumor volume).

## RESULTS

### Uniformity correction

Figure 1a shows the uncorrected MVCBCT images in the axial and sagittal central planes of the water cylinder. Figure 1c displays the intensity profiles for this image taken along the directions defined by the dotted white lines on the images of Fig. 1a. The magnitude of cupping artifact present in these images was approximately 28% and 32% of the cylinder mean value for the axial (left) and longitudinal (right) profiles, respectively. As illustrated in Fig. 1a, a given gray value falls approximately onto the surface of an ellipsoid centered in the cylinder. Several ellipsoid contours, defined by Eq. 1, are displayed in Fig. 1a, along with their associated correction factors. The correction factors for the profiles of the phantom are also displayed using a dashed line (scale shown on the right of the plots of Fig. 1c). The uniformity correction method greatly reduced the cupping artifact, as seen in the images (Fig. 1b) and profiles (Fig. 1d) for the corrected MVCBCT. Figure 2 shows the improvement in uniformity obtained with the correction factors applied to the images of a head-and-neck patient. The remaining cupping artifact, estimated using the soft-

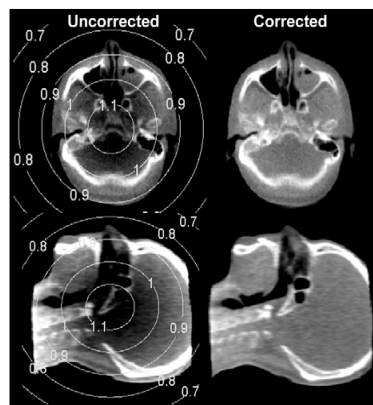


Fig. 2. Improvement in image uniformity for head-and-neck acquisition using simple geometric (ellipsoid) model of correction factors. (Left) Uncorrected image with correction factors overlaid. (Right) Corrected image. Images displayed using same window and level.

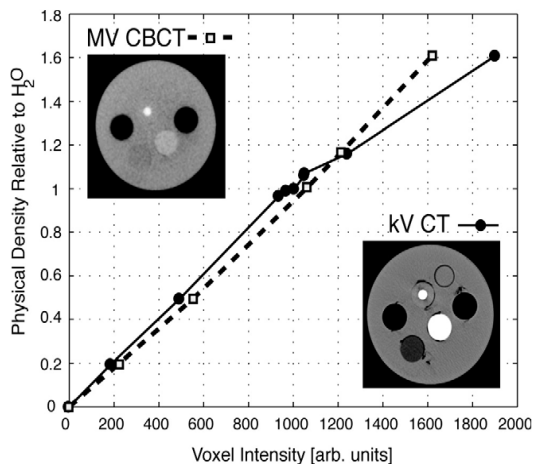


Fig. 3. Physical density calibration of conventional CT (solid line) and megavoltage cone-beam CT (MVCBCT) (dashed line). Representative cross-sectional images of phantom used for calibration shown for each modality.

tissue intensity along selected profiles, was  $<5\%$  in any direction.

#### Image calibration

Figure 3 shows the physical density calibration of the conventional CT and MVCBCT. These two calibration curves were entered in the treatment planning system. The curves were used with their respective image data set for all the dose calculations performed in this study.

#### Dosimetric inaccuracies produced by MVCBCT nonuniformity

Figure 4 presents a quantitative analysis of the effect of the cupping artifact on the dose calculation accuracy for a cylindrical water phantom. As seen in Fig. 4 (top), the dose percentage differences between the doses calculated on the CT and on the uncorrected MVCBCT (Fig. 4, left) showed a systematic deviation, which increased with depth. The nonuniformity caused the dose calculated in the in-field region (field edge reduced by 4 mm) to be less, on average, by 0.95% and by a maximum of 4.5%. Differences larger than  $\pm 10\%$  were observed at the field penumbra and along the phantom edge. These differences were likely to be due to a slight error in the setup ( $<2$  mm) of the phantom or in the placement of the treatment isocenter in the treatment planning system. The calculation of the  $\gamma$  index on the uncorrected water cylinder (Fig. 4, bottom) showed that despite the large cupping artifact only 1% of the whole dose distribution did not meet the acceptance criteria of 3% and 3 mm. When the water cylinder was corrected for nonuniformity, 98% of the in-field region was within 1% difference in dose, and 92% of the entire dose distribution, including phantom edges and penumbra, was within 2% in dose and 2 mm in distance-to-agreement.

#### Clinical test case

Figure 5 displays the isodose lines produced using the conventional CT and MVCBCT for the first test patient. Good qualitative agreement was found between the two dose distributions. For doses  $>10$  Gy (14% of the prescription dose), the maximal percentage difference in the dose was 8%. More than 90% of the volume had a percentage difference of  $\leq 5\%$ . Percentage differences of 5–8% were observed in the left air cavity and are believed to be due to slight misalignments or local anatomic variations. Reviewing the  $\gamma$  index, 98% of the complete volume was within 3% and 3 mm and 88% of the volume was within 2% and 2 mm. Overall, as seen in Fig. 5, the DVHs calculated on the conventional CT and on the MVCBCT were also in excellent agreement.

#### Estimating the dosimetric effect of weight loss using MVCBCT

For the second patient, the weight loss between Weeks 1 and 3 of therapy can be easily seen on the axial images of Fig. 6. The patient lost up to 4 cm of soft tissue on both sides of the neck between CT1 and CT2. First, we compared the dose calculation on the MVCBCTs with their respective CTs. Minor anatomic changes were observed in the posterior aspect of the neck between CT1 and MVCBCT1 (Fig. 6, axial images). No observable anatomic changes were observed between CT2 and MVCBCT2. Isodose lines displayed on the axial and sagittal central planes of the conventional CT and MVCBCT scans (Fig. 6) showed good qualitative agreement between the dose distributions obtained from images acquired closely in time (CT1 with

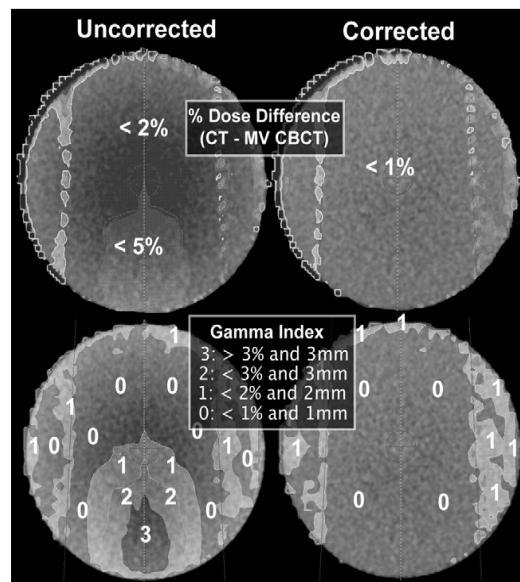


Fig. 4. (Top) Dose percentage differences (CT-megavoltage cone-beam CT [MVCBCT]) and (Bottom)  $\gamma$  indexes for head-size water cylinder (Left) uncorrected and (Right) corrected for uniformity.

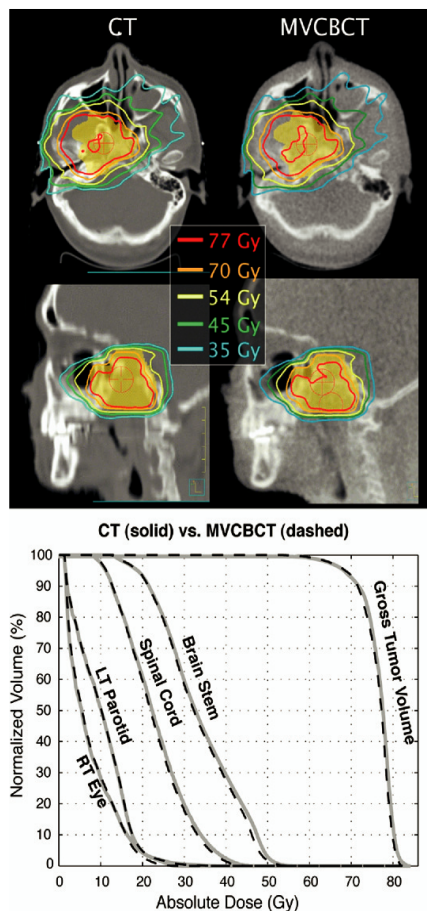


Fig. 5. Dose calculation on patient treated for recurrent nasopharyngeal carcinoma with intensity-modulated radiotherapy. No weight loss or anatomy deformation observed between CT and megavoltage cone-beam CT (MVCBCT). (Above) Isodose lines at treatment isocenter planes on conventional CT and MVCBCT. (Below) Good qualitative agreement observed with dose–volume histograms obtained from dose calculations performed using CT (solid lines) and MVCBCT (dashed lines).

MVCBCT1 and CT2 with MVCBCT2). For doses  $>20$  Gy (29% of the prescription dose), 78% and 84% of the dose calculation performed on MVCBCT1 compared with CT1 and MVCBCT2 compared with CT2, respectively, fell within the acceptance criteria of 3% in dose and 3 mm in the distance-to-agreement. The portion that failed the criteria was almost entirely located posteriorly below the fifth cervical vertebrae (C5), where the MVCBCT had missing tissue. This has been addressed in more detail in the “Discussion” section. The percentages passing the acceptance criteria increased to 96% and 97% when the anatomy below C5 was excluded. Figure 7 displays the percentage difference in dose for CT1-MVCBCT1 and CT2-MVCBCT2. Most of the dose distributions were within 3% in dose. The dose in the shoulder area was, on average, 6.3% greater on the MVCBCTs. The DVHs calculated on the CT and their

corresponding MVCBCT images are compared in Fig. 7. Overall, the agreement was excellent because the anatomic structures in the head-and-neck area are mostly situated above C5.

Figure 8 displays the percentage difference in dose for CT1-CT2 and MVCBCT1-MVCBCT2. A comparison of CT1 with MVCBCT2 was also performed and yielded very similar results to those presented in Fig. 8. The CT and MVCBCT data sets both showed a large volume of tissue receiving more than a 3% increase in dose because of patient weight loss. In the CT data set, the mean percentage increase in dose between Weeks 1 and 3 was 5.2%. Approximately 20% of the dose distribution was not within the passing criteria of 3% in dose and 3 mm in distance-to-agreement. In the MVCBCT data set, the mean percentage increase in dose between Weeks 1 and 3 was 4.6%. Good qualitative agreement was found between CT1-CT2 (Fig. 8a) and MVCBCT1-MVCBCT2 (Fig. 8b) in the anatomic locations receiving more than a 5% increase in dose. Figure 8 also shows the dosimetric effect of weight loss, as assessed using DVH comparisons between CT1-CT2 and MVCBCT1-MVCBCT2. Again, the contours on MVCBCT images were transferred from the corresponding CT images. All critical structures and target volumes showed similar increases in dose using CT and MVCBCT. For example, the maximal dose to the spinal cord increased from 42.9 to 48.3 Gy using CT1-CT2 and increased from 44.1 to 48.9 Gy using MVCBCT1-MVCBCT2. Similarly, the left parotid mean dose increased from 26.2 to 41.8 Gy using CT and increased from 26.0 to 42.1 Gy using MVCBCT. The largest qualitative DVH difference was observed with the right parotid, which was located in a high-dose gradient region.

Figure 9 shows the evaluation of the possibility of contouring critical structures directly on the MVCBCT image. The DVHs shown were obtained from two independent sets of contours (Fig. 9, top). One set was obtained from contouring on CT2 and copying the contours on MVCBCT2 after 3D registration and the other set by direct contouring on MVCBCT2. Overall, the agreement between the two sets of contours and DVHs was good. Again, the largest difference was observed with the right parotid. Contouring the right parotid directly on MVCBCT2 improved the DVH agreement with CT2 (Fig. 7a).

## DISCUSSION

### *Dose calculation accuracy achieved with MVCBCT*

Calibration of the CT images for physical or electron density is the main factor influencing dose calculation accuracy (23). Because of a large cupping artifact produced by scatter radiation and beam hardening, the calibration of cone-beam CT images is more complex than calibration for conventional fan-beam CT. The lower amounts of scatter and the reduced energy dependence of the photon interactions in the mega-electron voltage range produce a cupping artifact that is somewhat predictable. In this study, a simple empirical method was developed as a first-order correction

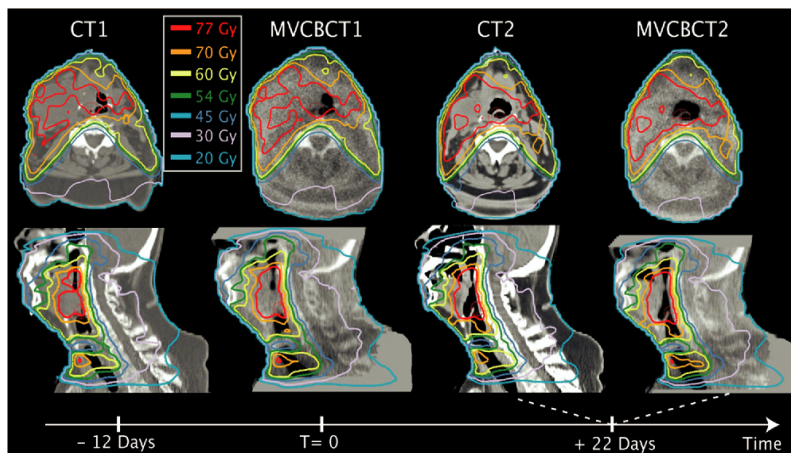


Fig. 6. Dose calculation for patient treated for base-of-tongue tumor with intensity-modulated radiotherapy. Initial plan defined on initial CT (CT1) applied on megavoltage cone-beam CT (MVCBCT) acquired in first week of treatment (MVCBCT1) and additional CT (CT2) and MVCBCT (MVCBCT2) acquired 22 days after beginning of therapy. Axial and sagittal images crossing isocenter show good qualitative agreement between isodose lines (CT1 with MVCBCT1 and CT2 with MVCBCT2).

to improve the uniformity of MVCBCT reconstructions for the head-and-neck region. Although limitations are inherent

to this method with respect to where the patient needs to be placed for imaging (roughly centered, as in the case of the

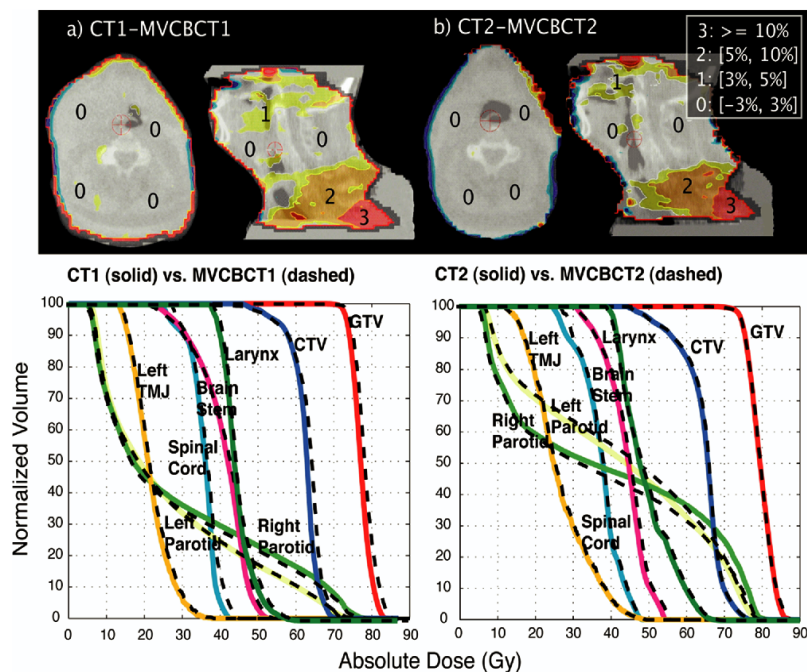


Fig. 7. (Top) Axial and sagittal images crossing isocenter showing dose percentage difference distributions for (a) CT1 compared with megavoltage cone-beam CT (MVCBCT1) and (b) CT2 compared with MVCBCT2. Most dose calculation on MVCBCT was within 3% of dose calculation on CT. Shoulder area, where MVCBCT had missing tissue was, on average, 6.3% greater in dose with MVCBCT. (Below) Dose-volume histogram comparisons showing excellent agreement for CT (solid line) and MVCBCT (dashed line) acquired closely in time. All contours producing dose-volume histograms drawn on CT images and applied on MVCBCT after registration. CTV = clinical target volume; GTV = gross target volume.

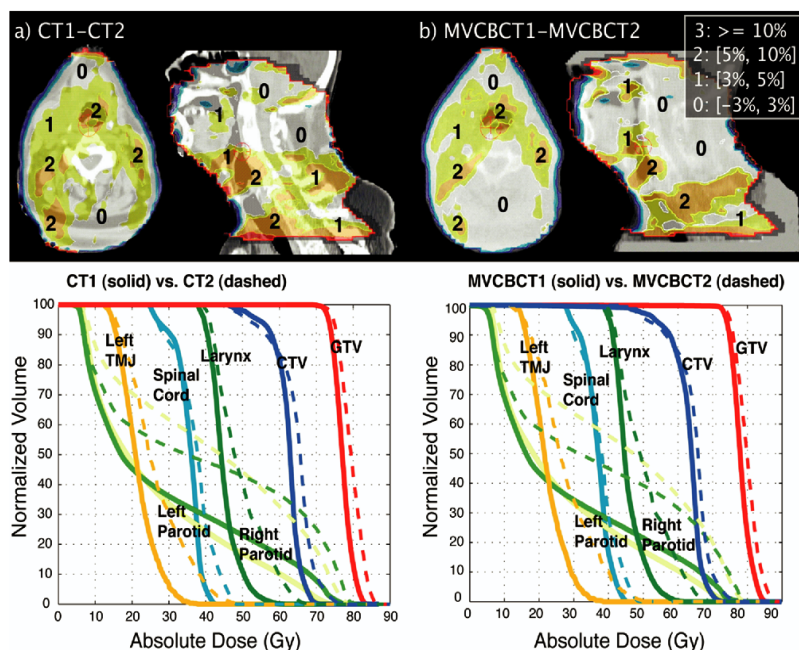


Fig. 8. (Top) Axial and sagittal images crossing isocenter showing dose percentage difference distributions for (a) CT1 compared with CT2 and (b) MVCBCT1 compared with MVCBCT2. Large anatomic areas had the dose increased by  $\geq 5\%$ . These areas' locations were in good agreement between (Left) CT and (Right) MVCBCT. (Below) Dose-volume histogram (DVH) comparisons. All contours producing DVHs were drawn on CT images and applied to MVCBCT images after registration. Effect of weight loss on DVHs was very similar when calculated on either CT or MVCBCT.

water cylinders), this simple correction greatly reduces the nonuniformity in the CBCT images. Other more robust preprocessing methods to correct projection images for scatter have also been proposed (18, 19). These methods would likely further reduce the cupping artifact. However, the results of this study have suggested that a first-order correction of the MVCBCT cupping artifact may already be sufficient for clinically useful dosimetric accuracy. The simulations performed with the head-size water cylinder demonstrated that the dosimetric error caused by the MVCBCT cupping artifact was much less than the cupping artifact itself. This trend has also been observed using a pelvis-size water cylinder (24). For multiple beam configurations, dosimetric errors would be further reduced because of averaging over different beam angles. With the uniformity-correction method presented in this report, a dose calculation accuracy better than 3% in dose and 3 mm in distance-to-agreement was demonstrated for a head-and-neck patient treated with IMRT.

#### Expanding dose calculation to more clinical sites

The other factor that determines dosimetric accuracy is the field of view of the MVCBCT images. Using the current MVCBCT system, only the head-and-neck region can be fully imaged. One option to compensate for the limited field of view of MVCBCT is to merge the images from the kVCT and MVCBCT (10) to supplement the truncated image data. In this study, tissue contours from the kVCT were used to

compensate for using missing tissue in the MVCBCT images of the second patient. However, a 5–10% dosimetric overestimation still occurred related to missing data artifact, the assumption of rigid body deformation, and the lack of heterogeneity correction in the missing data region. Despite this problem, the fact that most critical structures in the head-and-neck area are situated above the shoulders allowed the use of MVCBCT to accurately monitor the dosimetric effect of weight loss on clinically important structures. A dosimetric accuracy better than 3% in dose and 3 mm in distance-to-agreement was demonstrated above the shoulders. As larger detectors are manufactured or new image acquisition schemes are developed, CBCT should become capable of completely imaging the anatomy along the beams. Simply allowing a lateral shift of the detector for acquisition would increase the field of view to image the shoulders or an average size pelvis (25). The good imaging performance and calibration possibility of MVCBCT in the presence of metallic objects could also be used to obtain better dose calculations in areas near a hip prosthesis or tooth fillings (26).

#### MVCBCT to monitor dosimetric effect of weight loss

During the course of external beam RT, many head-and-neck patients develop significant anatomic changes that may be related to multiple factors, including shrinkage of the tumor and/or nodal masses, weight loss, and resolution of postoperative changes (1). For these cases, it has been

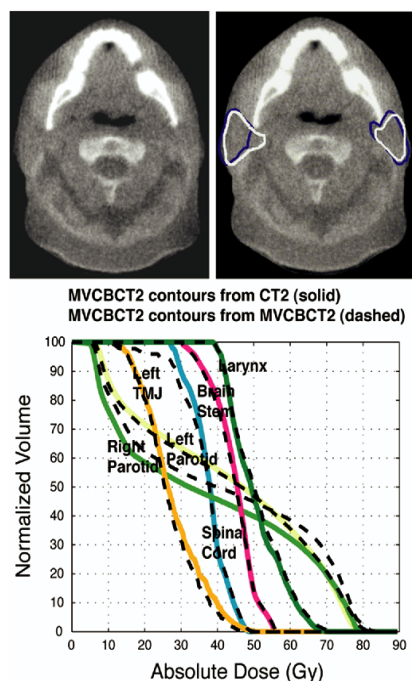


Fig. 9. Evaluating the feasibility of contouring critical structures on MVCBCT. (Top) One set of dose–volume histograms (DVHs) obtained from contours drawn on CT2 and copied to MVCBCT2 (blue contours); other set obtained by direct contouring on MVCBCT2 (white contours). (Below) Largest DVH difference observed within right parotid, located in high-dose gradient region. Contouring directly on MVCBCT improved DVH qualitative agreement compared with right parotid on CT2 (Fig. 8). Overall good agreement in DVHs demonstrated contouring capability of many head-and-neck structures on MVCBCT.

demonstrated that repeat CT imaging and repeat planning is essential to ensure adequate doses to the target volumes and safe doses to critical normal tissues (3). One goal of this study was to determine whether MVCBCT imaging could be used to detect when repeat planning becomes necessary. With MVCBCT already in use for patient setup, the user performing the CT-MVCBCT alignment may more readily notice when a change in anatomy has become potentially clinically significant. As the results of this study have demonstrated, dose recalculation on MVCBCT is also possible and can be used to estimate the percentage dose differences in the target volume or normal tissues. Structures such as spinal cord, brainstem, larynx, and all the bony structures can be contoured directly on MVCBCT. Although soft-tissue contouring is more difficult, it was feasible even in

structures such as the parotids. Using the initial reference CT (CT1) as a guide, the dosimetrist was able to contour the parotids in the MVCBCT with reasonable confidence. Using these contours, it was possible to estimate a mean dose increase from 26 to 42 Gy in the left parotid of the second patient. Although weight loss occurred throughout treatment, if the anatomy from Week 3 was assumed to represent the anatomy for the remaining treatment fractions (18 of 33 fractions), the right and left parotid mean doses would be increased by 7 and 9 Gy, respectively. These estimates match well the mean dose increase calculated using the conventional CT images. Although weight loss may be expected in these patients (4), many continue to be treated with the original treatment plan because the dosimetric affect of the weight loss is rarely assessed.

Several head-and-neck patients now undergo imaging weekly with CT and MVCBCT to monitor the dose to critical structures and further study the dose calculation accuracy achieved with MVCBCT. Even though dose calculation can be performed on MVCBCT, repeating the kVCT is still required for repeat planning. Currently, MVCBCT can provide some soft-tissue information, but conventional CT is preferred for recontouring the target volumes (gross tumor volume and clinical target volume). Precise soft-tissue contouring on MVCBCT should become feasible as the image quality continues to improve (27) and, combined with a larger reconstructed volume, may eliminate the need for repeat kVCT.

## CONCLUSION

In this study, we have demonstrated the clinically applicable dosimetric accuracy of MVCBCT using a simple calibration technique. With the current reconstruction volume, it is possible to obtain accurate dose calculation on MVCBCT acquisitions of head-and-neck patients, provided no anatomy is missing along the treatment beams. A dosimetric accuracy better than 3% in dose and 3 mm in distance-to-agreement was demonstrated above the shoulders. Using MVCBCT, it is now possible to monitor the dosimetric effect of anatomic variations, including weight loss and tumor shrinkage for head-and-neck patients. This is a critical step in adapting RT to anatomic changes during treatment. Several head-and-neck patients have now been selected for a study aimed at monitoring the dose to critical structures and further defining the dose calculation accuracy achieved with MVCBCT. The future availability of a larger MVCBCT field of view will allow MVCBCT to be used for dose calculations on other body sites.

## REFERENCES

1. Barker JL Jr, Garden AS, Ang KK, *et al.* Quantification of volumetric and geometric changes occurring during fractionated radiotherapy for head-and-neck cancer using an integrated CT/linear accelerator system. *Int J Radiat Oncol Biol Phys* 2004;59:960–970.
2. de Crevoisier R, Tucker SL, Dong L, *et al.* Increased risk of biochemical and local failure in patients with distended rectum on the planning CT for prostate cancer radiotherapy. *Int J Radiat Oncol Biol Phys* 2005;62:965–973.
3. Hansen EK, Bucci MK, Quivey JM, *et al.* Repeat CT imaging

- and replanning during the course of IMRT for head-and-neck cancer. *Int J Radiat Oncol Biol Phys* 2006;64:355–362.
4. Beaver MES, Matheny KE, Roberts DB, *et al*. Predictors of weight loss during radiation therapy. *Otolaryngol Head Neck Surg* 2001;125:645–648.
  5. Wong JR, Cheng CW, Grimm L, *et al*. Clinical implementation of the world's first Primatom, a combination of CT scanner and linear accelerator, for precise tumor targeting and treatment. In: Physica M, editor. *Istituti Editoriali e Poligrafici Internazionali*. Vol. 17. Italy: Medica Physica 2001. p. 271–276.
  6. Jaffray DA, Siewerdsen JH, Wong JW, *et al*. Flat-panel cone-beam computed tomography for image-guided radiation therapy. *Int J Radiat Oncol Biol Phys* 2002;53:1337–1349.
  7. Sorensen SP, Chow E, Kriminski S, *et al*. Image guided radiotherapy using a mobile kilovoltage x-ray device. *Med Dosim* 2006;31:40–50.
  8. Pouliot J, Bani-Hashemi A, Chen J, *et al*. Low-dose megavoltage cone-beam CT for radiation therapy. *Int J Radiat Oncol Biol Phys* 2005;61:552–560.
  9. Mackie TR, Kapatotes J, Ruchala K, *et al*. Image guidance for precise conformal radiotherapy. *Int J Radiat Oncol Biol Phys* 2003;56:89–105.
  10. Langen KM, Meeks SL, Poole DO, *et al*. The use of megavoltage CT (MVCT) images for dose recomputations. *Phys Med Biol* 2005;50:4259–4276.
  11. Thomas SJ. Relative electron density calibration of CT scanners for radiotherapy treatment planning. *Br J Radiol* 1999;72:781–786.
  12. Jaffray DA, Battista JJ, Fenster A, *et al*. X-ray scatter in megavoltage transmission radiography: Physical characteristics and influence on image quality. *Med Phys* 1994;21:45–60.
  13. Kanamori H, Nakamori N, Inoue K, *et al*. Effects of scattered X-rays on CT images. *Phys Med Biol* 1985;30:239–249.
  14. Siewerdsen JH, Jaffray DA. Cone-beam computed tomography with a flat-panel imager: Magnitude and effects of X-ray scatter. *Med Phys* 2001;28:220–231.
  15. Ruola N, Xiangyang T, Conover D. X-ray scatter correction algorithm for cone beam CT imaging. *Med Phys* 2004;31:1195–1202.
  16. Siewerdsen JH, Daly MJ, Bakhtiar B, *et al*. A simple, direct method for x-ray scatter estimation and correction in digital radiography and cone-beam CT. *Med Phys* 2006;33:187–197.
  17. Siewerdsen JH, Moseley DJ, Bakhtiar B, *et al*. The influence of antiscatter grids on soft-tissue detectability in cone-beam computed tomography with flat-panel detectors. *Med Phys* 2004;31:3506–3520.
  18. Spies L, Ebert M, Groh BA, *et al*. Correction of scatter in megavoltage cone-beam CT. *Phys Med Biol* 2001;46:821–833.
  19. van Elmpt WJC, Nijsten S, Mijnheer BJ, *et al*. Experimental verification of a portal dose prediction model. *Med Phys* 2005;32:2805–2818.
  20. Maltz J, Gangadharan B, Hristov D, *et al*. Su-FF-I-11: Site-specific image-gain calibration for MV CBCT [Abstract]. *Med Phys* 2006;33:1999.
  21. Morin O, Gillis A, Chen J, *et al*. Megavoltage cone-beam CT: System description and clinical applications. *Med Dosim* 2006;31:51–61.
  22. Low DA, Harms WB, Mutic S, *et al*. A technique for the quantitative evaluation of dose distributions. *Med Phys* 1998;25:656–661.
  23. Seco J, Evans PM. Assessing the effect of electron density in photon dose calculations. *Med Phys* 2006;33:540–552.
  24. Chen J, Morin O, Chen H, *et al*. Su-FF-J-72: The effect of MV cone-beam CT cupping artifacts on dose calculation accuracy [Abstract]. *Med Phys* 2005;32:1936.
  25. Smitsmans MHP, De Bois J, Sonke J-J, *et al*. Automatic prostate localization on cone-beam CT scans for high precision image-guided radiotherapy. *Int J Radiat Oncol Biol Phys* 2005;63:975–984.
  26. Aubin M, Morin O, Chen J, *et al*. The use of megavoltage cone-beam CT to complement CT for target definition in pelvic radiotherapy in presence of hip replacement. *Br J Radiol* 2006;79:918–921.
  27. Faddegon B, Ghelmansarai F, Bani-Hashemi A. Su-FF-J-07: A low-Z target with no flattener and reduced energy for improved contrast in megavoltage cone-beam CT [Abstract]. *Med Phys* 2006;33:2021.

## Patient dose considerations for routine megavoltage cone-beam CT imaging

Olivier Morin<sup>a)</sup>

*Comprehensive Cancer Center, Department of Radiation Oncology, University of California San Francisco, San Francisco, California 94143 and UCSF/UC Berkeley Joint Graduate Group in Bioengineering, San Francisco, California 94158*

Amy Gillis, Martina Descovich, Josephine Chen, Michèle Aubin, Jean-François Aubry, Hong Chen, and Alexander R. Gottschalk

*Comprehensive Cancer Center, Department of Radiation Oncology, University of California San Francisco, San Francisco, California 94143*

Ping Xia and Jean Pouliot

*Comprehensive Cancer Center, Department of Radiation Oncology, University of California San Francisco, San Francisco, California 94143 and UCSF/UC Berkeley Joint Graduate Group in Bioengineering, San Francisco, California 94158*

(Received 14 December 2006; revised 7 March 2007; accepted for publication 8 March 2007; published 26 April 2007)

Megavoltage cone-beam CT (MVCBCT), the recent addition to the family of in-room CT imaging systems for image-guided radiation therapy (IGRT), uses a conventional treatment unit equipped with a flat panel detector to obtain a three-dimensional representation of the patient in treatment position. MVCBCT has been used for more than two years in our clinic for anatomy verification and to improve patient alignment prior to dose delivery. The objective of this research is to evaluate the image acquisition dose delivered to patients for MVCBCT and to develop a simple method to reduce the additional dose resulting from routine MVCBCT imaging. Conventional CT scans of phantoms and patients were imported into a commercial treatment planning system (TPS: Phillips, Pinnacle) and an arc treatment mimicking the MVCBCT acquisition process was generated to compute the delivered acquisition dose. To validate the dose obtained from the TPS, a simple water-equivalent cylindrical phantom with spaces for MOSFETs and an ion chamber was used to measure the MVCBCT image acquisition dose. Absolute dose distributions were obtained by simulating MVCBCTs of 9 and 5 monitor units (MU) on pelvis and head and neck patients, respectively. A compensation factor was introduced to generate composite plans of treatment and MVCBCT imaging dose. The article provides a simple equation to compute the compensation factor. The developed imaging compensation method was tested on routinely used clinical plans for prostate and head and neck patients. The quantitative comparison between the calculated dose by the TPS and measurement points on the cylindrical phantom were all within 3%. The dose percentage difference for the ion chamber placed in the center of the phantom was only 0.2%. For a typical MVCBCT, the dose delivered to patients forms a small anterior-posterior gradient ranging from 0.6 to 1.2 cGy per MVCBCT MU. MVCBCT acquisitions in the pelvis and head and neck areas deliver slightly more dose than current portal imaging but render soft tissue information for positioning. Overall, the additional dose from daily 9 MU MVCBCTs of prostate patients is small compared to the treatment dose (<4%). Dose-volume histograms of compensated plans for pelvis and head and neck patients imaged daily with MVCBCT showed no additional dose to the target and small increases at low doses. The results indicate that the dose delivered for MVCBCT imaging can be precisely calculated in the TPS and therefore included in the treatment plan. This allows simple plan compensations, such as slightly reducing the treatment dose, to minimize the total dose received by critical structures from daily positioning with MVCBCT. The proposed compensation factor reduces the number of MU per treatment beam per fraction. Both the number of fractions and the beam arrangement are kept unchanged. Reducing the imaging volume in the cranio-caudal direction can further reduce the dose delivered for MVCBCT. This is a useful feature to eliminate the imaging dose to the eyes or to focus on a specific region of interest for alignment. © 2007 American Association of Physicists in Medicine. [DOI: 10.1118/1.2722470]

Key words: patient dose compensation, image-guided radiation therapy, megavoltage cone-beam CT



## I. INTRODUCTION

Several computed tomography (CT) imaging systems have been developed in external beam radiation therapy to improve patient positioning and monitor anatomical changes. Clinical evidence suggests that both prostate and head and neck patients would benefit from treatment supported with three-dimensional (3D) image-guided radiation therapy (IGRT) techniques. Prostate patients undergoing treatment with IGRT are likely to have higher probability of local control.<sup>1</sup> Obtaining weekly 3D images of head and neck patients not only provides verification of positioning<sup>2</sup> but also opens the possibility of adapting the treatment course for anatomical changes such as weight loss and/or tumor shrinkage.<sup>3,4</sup> Even though the imaging dose from IGRT is generally small compared to the treatment dose, the increasing frequency of CT imaging may result in clinically significant dose to normal tissue. For the patients' safety and to optimize the benefits of IGRT, the additional dose delivered from in-room CT imaging systems should be understood and controlled.

For many decades, imaging inside the treatment room has played a role in verifying radiation therapy treatment. Portal images, projection images of the patient using the treatment aperture, have been used to confirm the patient position based on bony anatomy or gold markers implanted in or near the tumor. The use of radiographic film for portal imaging has limited the frequency of this verification due to the time required to process the films and a dose of more than 10 cGy to the patient.<sup>5</sup> However, recent implementation of electronic portal imaging devices allows a digital image to be acquired in a few seconds with doses ranging from 2 to 8 cGy.<sup>6</sup> The use of portal imaging to adjust patient position before treatment is limited, however, because soft tissue cannot be visualized and the full 3D geometry is obscured by the projection onto a two-dimensional (2D) plane. Therefore, considerable research of the last years has focused on developing 3D imaging of the patient on the treatment table. Several clinical CT imaging systems are now available including (i) a "CT on rails"<sup>7</sup> system requiring a conventional diagnostic CT machine in the treatment room, (ii) a kilovoltage cone-beam CT (kVCBCT) system<sup>8</sup> consisting of an additional kV x-ray source and detector attached to the treatment gantry, (iii) a tomotherapy system<sup>9,10</sup> replacing the traditional treatment machine (beam) with a MV beam source on a ring gantry equipped with a xenon ion chamber array, and (iv) a megavoltage cone-beam CT (MVCBCT) system<sup>11,12</sup> using the pre-existing treatment machine and an electronic portal imaging device.

The dose delivered by most of these in-room CT imaging systems has been recently reported in the literature. Point measurements have been obtained on phantom as well as skin measurements on patients using the most frequently used imaging protocols. For valid comparison, the absorbed doses summarized here from technologies using diagnostic x rays (CT and kVCBCT) have been adjusted for the variation in photon radiobiological efficiency (RBE) as a function of energy. A typical kV beam (120 kVp) is between 1.8 and 4

times more efficient at creating cell damage than a MV beam.<sup>13</sup> The reported values represent, therefore, maximum equivalent dose delivered by a given technology. With this in mind, a conventional CT is estimated to deliver up to approximately 5.4 cSv ( $3 \text{ cGy} \times 1.8$ ) per scan.<sup>14,15</sup> Recent dosimetric studies done with kVCBCT systems showed maximum delivered doses ranging between 5.4 and 16 cSv ( $3\text{--}9 \text{ cGy} \times 1.8$ ) depending on the manufacturers,<sup>16,17</sup> which use different imaging settings (beam and grid) and number of raw 2D projections. The tomotherapy MVCT system has also been studied and a recent article reported a multiple-scan average dose in the center of a 20 cm cylindrical phantom of only 1.1 cSv.<sup>18</sup> For comparison, four-dimensional CT scans increase the CT maximum delivered dose by a factor ranging between 10 and 15.<sup>19</sup> The patient dose from nonclinical MVCBCT imaging systems has previously been simulated.<sup>12,20,21</sup> Our group presented last year a preliminary study on the dose delivered by a clinical MVCBCT system.<sup>22</sup> Recently, point dose measurements and dose distributions on phantoms were reported for the same MVCBCT system.<sup>23</sup> This article follows with a complete characterization of the delivered dose on patients from MVCBCT. The objective of this work is to evaluate how the MVCBCT system exposure translates into patient dose. Given this information, we investigated a simple plan compensation method to eliminate or minimize the additional dose delivered from routine MVCBCT imaging.

## II. MATERIALS AND METHODS

### II.A. Basics of megavoltage cone-beam CT

Our clinic has two in-room MV imaging systems capable of portal imaging and cone-beam CT (MVision™, Siemens Medical Solutions, Concord, CA). The imaging systems consist of a standard linear accelerator 6 MV beam and an amorphous silicon flat panel detector (Perkin Elmer Optoelectronics, Wiesbaden, Germany) adapted for MV photons. Our two MVCBCT systems have been previously described.<sup>11</sup> The MVCBCT acquisition is similar to an arc treatment. The linear accelerator gantry rotates in a continuous 200° arc (270° to 110°, clockwise) acquiring one low-dose (<0.05 MU) MV portal image per degree. This acquisition procedure lasts 45 s. The image reconstruction starts immediately after the acquisition of the first portal image and is completed in less than 2 min. The total number of monitor units (MU) used for MVCBCT imaging is specified upon the creation of an MVCBCT acquisition field at the therapist station. Any number between 2 and 60 MU can be specified. Depending on the amount of soft tissue resolution required, we are currently using a total exposure ranging between 2 and 10 MU for daily setup imaging. MVCBCTs of higher exposures (up to 20 MU) have been used during the treatment planning process to complement conventional CT or magnetic resonance images for patients with implanted high atomic number material (spinal rods and hip prostheses).<sup>24</sup> With the current size of the detector ( $41 \times 41 \text{ cm}^2$ ) and a source-detector distance of 145 cm, an open field of  $27.4 \times 27.4 \text{ cm}^2$  can be used for MVCBCT imaging, which yields a maximum re-

construction volume of approximately  $27 \times 27 \times 27$  cm<sup>3</sup>. The linear accelerator Y jaws can also be moved independently to reduce the amount of tissue being irradiated in the cranio-caudal direction. The longitudinal reconstructed length can be anything between  $\sim 5$  and 27 cm anywhere within a 27 cm window centered at the isocenter.

### II.B. Comparison of calculated and measured MVCBCT dose

The first objective of this study was to demonstrate that a commercial treatment planning system (TPS: Pinnacle v7.6, Phillips) can accurately calculate the patient dose for a MVCBCT acquisition. This is possible because MVCBCT uses the linear accelerator treatment beam, which has already been characterized in the TPS for dose calculation on CT images. A water-equivalent cylindrical phantom made for intensity-modulated radiation therapy (IMRT) quality assurance was used to validate the MVCBCT dose simulated in our TPS. First, the phantom was imaged with conventional CT and imported into the TPS. The position of the phantom on the CT table was marked with fiducials. An arc treatment ( $270^\circ$  to  $110^\circ$ ) using a  $27.4 \times 27.4$  cm<sup>2</sup> field-size was simulated. The phantom was then aligned on the treatment couch using the fiducials and a MVCBCT acquisition was delivered. Dose measurements were performed with metal-oxide-semiconductor field-effect transistor (MOSFET) detectors placed at ten different locations in the cylindrical phantom. An ion chamber was placed in the center of the phantom as well. The calculated dose and measurements were compared.

### II.C. MVCBCT exposure and soft-tissue information

The absolute dose comparisons presented in this paper assume 9 and 5 MU MVCBCTs are used to image pelvis and head and neck patients, respectively. Although increasing the number of MU for MVCBCT imaging provides a higher contrast-to-noise ratio and thus more soft tissue information, our clinical experience of the last 3 years with MVCBCT suggests that using 9 and 5 MU for pelvis and head and neck patients provides sufficient soft tissue information to guide 3D positioning. Figure 1 shows side-by-side views of conventional CT and MVCBCT for typical pelvis (right) and head and neck (left) patients. For example, soft tissue structures such as the trapezius, the obturator internus, the gluteus maximus, and the prostate gland are identified on both the CT and MVCBCT images of Fig. 1. MVCBCTs with exposure as low as 2 MU and 10 cm reconstruction length in the cranio-caudal direction have been used in the clinic for simpler setup cases such as prostate patients with implanted gold seeds.

### II.D. Dose delivered to patients

Conventional CT scans of patients already imported in the TPS were used to simulate the delivered dose for MVCBCT and portal imaging. The treatment isocenter location as well as the target and critical structures were already specified on

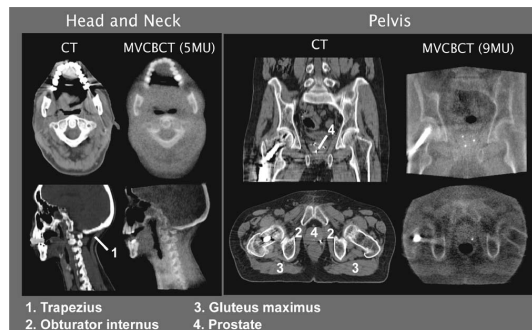


FIG. 1. Typical MVCBCT images for head and neck (5 MU) and prostate (9 MU) patients compared to conventional CT. The image quality of MVCBCT is sufficient to perform a 3D alignment based on bony anatomy and soft tissue. Several muscles and the prostate can be identified on both the CT and MVCBCT images. CT and MVCBCT images are not displayed with the same window and level.

the patients' CT image. Having this information in the TPS results in minimal additional work to obtain a complete assessment of the MVCBCT dose. A MVCBCT imaging plan was simulated as an arc treatment using a specific arc range, total number of MU, and a desired field-size. MVCBCT dose simulations were performed on CT images of two prostate patients and one head and neck patient. Simulations were done using the arc acquisition currently allowed by the MVCBCT system (arc 1:  $270^\circ$  to  $110^\circ$ ) the current maximum field-size of  $27.4 \times 27.4$  cm<sup>2</sup>, and assuming a total delivery of 1 MU to obtain the dose per MU. In addition, an opposed arc acquisition (arc 2:  $90^\circ$  to  $290^\circ$ ) was simulated on the first prostate patient to investigate the benefits of more than one MVCBCT arc acquisition on the imaging dose distribution. The hypothesis was that a more uniform dose distribution could be obtained by alternating arc 1 and arc 2 over the course of treatment. The dose delivered for portal imaging or film was also simulated with an anterior-posterior beam added to a lateral beam. The field-size for portal imaging was the same as for MVCBCT (27.4 cm). For a relative comparison with the MVCBCT dose, the calculations were performed assuming a total delivery of 1 MU (0.5 MU for each portal image) to obtain the total dose per MU. Dose-volume histograms were obtained for the first prostate patient using only arc 1 or a combination of arc 1 and arc 2. Finally, the absolute doses to the main pelvic and head and neck structures delivered at our institution for setup using MVCBCT, CR film, and portal imaging were compared. An average of 6 MU ( $2 \times 3$  MU) is currently used to align prostate patients with implanted gold seeds using daily portal imaging. As for head and neck patients, verification of position and bony anatomy is done weekly using CR film ( $2 \times 4$  MU = 8 MU) or the flat panel detector ( $2 \times 2$  MU = 4 MU).

### II.E. Plan compensation method for routine MVCBCT imaging

To investigate the possible clinical impact of the additional MVCBCT imaging dose to the patient and a method to

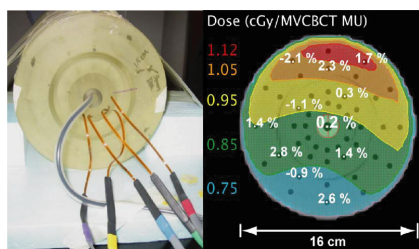


FIG. 2. Comparison of dose measurements and the simulation of an MVCBCT acquisition performed on an IMRT quality assurance phantom. Dose measurements were performed with an ion chamber (center point) and MOSFET detectors (other points) as depicted in the left image. The simulation of the MVCBCT was done in our commercial TPS. Percent differences between calculated and measured doses are overlaid on the dose distribution displayed on the right. The dose percentage differences between the calculation and the MOSFET points were all better than 3%.

compensate for it, several dose calculations were compared. In addition to the treatment plan alone, two “composite” plans were defined. The uncompensated plan consisted of the treatment plan plus daily MVCBCT imaging. For the compensated plan, the treatment plan MUs were reduced by a compensation factor (percentage less than 100%) and added to the MVCBCT imaging dose such that the mean dose to the target remained the same as with the treatment plan dose alone. Equation (1) describes how the compensation factor is calculated. The left side of Eq. (1) is the target mean dose for the original treatment plan alone ( $T_{Tx}$ ). The right side of Eq. (1) is the mean target dose reduced by the compensation factor ( $CF_{MVCBCT}$ ) plus the mean target dose received during the MVCBCT imaging. The imaging dose is calculated by multiplying the mean target MVCBCT dose ( $T_{MVCBCT}$ ) times the number of MVCBCT MU per fraction ( $n_{MU}$ ) and the number of fractions ( $n_f$ ) where MVCBCT imaging is performed. The doses  $T_{Tx}$  and  $T_{MVCBCT}$  are calculated from the TPS, and Eq. (1) can be solved to find  $CF_{MVCBCT}$ , the compensation factor that keeps the mean target dose the same in the compensated plan as in the original treatment plan:

$$T_{Tx} = CF_{MVCBCT} \cdot T_{Tx} + T_{MVCBCT} \cdot n_{MU} \cdot n_f. \quad (1)$$

The compensation factor reduces the number of MU per treatment beam per fraction. Both the number of fractions and the beam arrangement are kept unchanged. This compensation method was tested on the plans of two prostate patients and one head and neck patient. Dose distributions and DVHs for the plans (treatment alone, uncompensated, and compensated) were compared.

### III. RESULTS

#### III.A. Comparison of calculated and measured MVCBCT dose

The delivered MVCBCT dose to the IMRT QA cylinder was calculated in the TPS and compared with measurements performed with MOSFET detectors and an ion chamber (see Fig. 2). The calculated MVCBCT dose formed a slight posterior-anterior gradient ranging from 0.8 to 1.1 cGy per

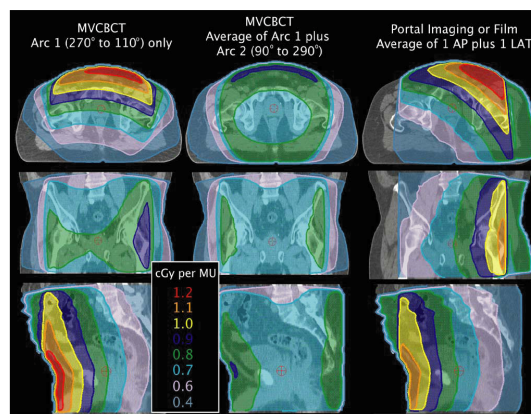


FIG. 3. Dose delivered per MU to an average size pelvis patient for MVCBCT and portal imaging. On the left column, only the current MVCBCT arc acquisition ( $270^\circ$  to  $110^\circ$ ) using a total of 1 MU was simulated. For the middle column, the dose distribution was obtained from the addition of two opposed MVCBCT arcs: arc 1 ( $270^\circ$  to  $110^\circ$ ) and arc 2 ( $90^\circ$  to  $290^\circ$ ) using a total of 0.5 MU each. The right column shows the dose distribution per MU for electronic portal imaging or film. An anterior-posterior beam of 0.5 MU was added to a lateral beam of 0.5 MU.

MVCBCT MU. The dose percentage differences between the calculation and the measurement points are displayed in Fig. 2 (right). The dose percentage differences between the calculation and the MOSFET points were all better than 3%. The dose percentage difference for the ion chamber placed in the center of the phantom was only 0.2%.

#### III.B. Dose delivered for MVCBCT imaging

##### III.B.1. Prostate patient

Relative dose distributions per MU for MVCBCT and portal imaging on an average size pelvis patient are displayed in Fig. 3. Isodose lines are displayed on the axial, coronal, and sagittal planes crossing the treatment isocenter, which was located in the prostate. Two types of MVCBCT acquisitions were simulated. For MVCBCT using the current arc acquisition (left column), the dose formed a posterior-anterior gradient ranging from 0.4 to 1.2 cGy per MVCBCT MU. The DVHs analysis revealed that the dose received by the main pelvic structures for MVCBCT using the current arc acquisition ranges between 0.6 and 1.2 cGy per MVCBCT MU. In comparison to the MVCBCT dose using only arc 1, the MVCBCT dose per MU for the average of arc 1 and arc 2 in Fig. 3 (middle column) was more uniform, as expected. The DVH showed that by employing those two arcs for MVCBCT imaging, the pelvic structures would uniformly receive 0.8 cGy per MVCBCT MU. The maximum dose for MVCBCT imaging using the two arcs would also be reduced to 0.91 cGy per MVCBCT MU. The dose distribution per MU observed with portal imaging or film in Fig. 3 (right column) was similar to current MVCBCT imaging using only arc 1 (left column). Table I compares the absolute dose for a 9 MU MVCBCT to what is currently delivered to prostate patients at our institution for daily verification of

TABLE I. Dose delivered to a prostate patient for daily alignment verification. MVCBCT (9 MU) and portal imaging ( $2 \times 3$  MU = 6 MU).

	MVCBT (cGy)			Portal Imaging (cGy)		
	Min	Mean	Max	Min	Mean	Max
Prostate	6.4	<b>6.9</b>	7.6	4.1	<b>4.6</b>	5.0
Seminal vesicles	6.3	<b>6.4</b>	6.8	4.1	<b>4.4</b>	4.7
Nodes	5.2	<b>6.8</b>	10.1	3.3	<b>4.6</b>	7.5
Rectum	5.3	<b>5.9</b>	6.8	3.6	<b>4.1</b>	4.7
Bladder	6.7	<b>7.8</b>	9.5	4.4	<b>5.1</b>	6.2
Penile bulb	6.5	<b>6.9</b>	7.6	4.4	<b>4.7</b>	5.0
Left femoral	6.4	<b>7.8</b>	8.9	4.7	<b>6.2</b>	6.8
Small bowel	2.7	<b>8.3</b>	11.2	2.3	<b>5.4</b>	8.1
Spinal cord	0.9	<b>3.9</b>	5.2	0.6	<b>2.6</b>	3.8

setup using portal imaging. On average, the main pelvic structures receive 6.8 and 4.6 cGy for MVCBCT and portal imaging, respectively. The maximum doses to the rectum were 6.8 and 4.7 cGy for MVCBCT and portal imaging, respectively.

### III.B.2. Head and neck patient

Relative dose distributions per MU for MVCBCT and portal imaging on a head and neck patient are displayed in Fig. 4. Isodose lines are displayed on the axial, coronal, and sagittal planes crossing the isocenter, which was located in the upper neck area. For MVCBCT using the current arc

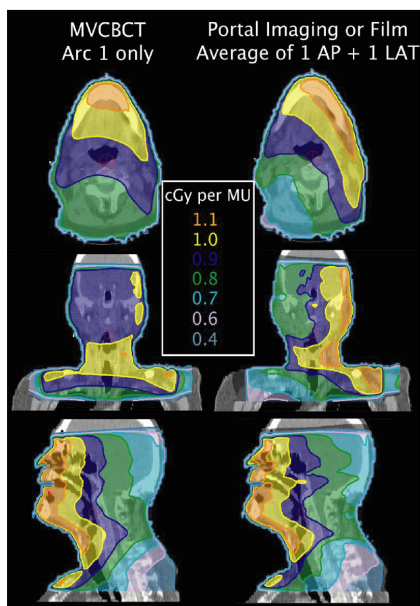


FIG. 4. Dose delivered per MU to a head and neck patient for MVCBCT and portal imaging. For the left column the current MVCBCT acquisition arc ( $270^\circ$  to  $110^\circ$ ) of 1 MU was simulated. The right column was the result of a 0.5 MU anterior-posterior portal image added to a 0.5 MU lateral portal image.

acquisition (left column), the dose formed a posterior-anterior gradient ranging from 0.4 to 1.1 cGy per MVCBCT MU. The dose distribution per MU observed with portal imaging (right column) was very similar to MVCBCT imaging. Table II compares the absolute dose delivered to a head and neck patient for a 5 MU MVCBCT with what is currently delivered at our institution for weekly verification of setup and anatomy using CR film and portal imaging. On average, the main head and neck structures received 4.8, 7.6, and 3.8 cGy for MVCBCT, CR film, and portal imaging, respectively. The maximum doses to the right lens were 5.5, 8.0, and 4.0 cGy for MVCBCT, CR film, and portal imaging, respectively. Methods to further reduce or eliminate the dose to critical structures with low radiation tolerance, such as the eyes, will be described in the Discussion.

### III.C. Compensating the plan to account for MVCBCT imaging dose

The compensation method described in this paper was applied on the plans of three patients.

#### III.C.1. Prostate patient treated with four-field box plus conformal boost

Figures 5 and 6 show dose distributions and DVHs for uncompensated and compensated plans for daily 9 MU MVCBCT imaging on a pelvis patient treated with a four-field box plus conformal boost. As seen with Fig. 5 (middle column) and Fig. 6 (top), simply adding daily 9 MU MVCBCT to the treatment dose results in a uniform dose increase of approximately 2.7 Gy ( $40$  fractions  $\times$  6.8 cGy). The volume of tissue receiving more than 77 Gy between the left and middle columns of Fig. 5 is clearly increased. The compensation factor of the first compensated plan using only arc 1 was 96%. As observed in Fig. 5 (right column), the compensation method reduces the dose in the high-dose region such that the amount of tissue receiving a high dose ( $\sim 50$  Gy or more) remained the same. Despite the compensation method, the volume of tissue receiving doses less than 50 Gy in the compensated plan was still slightly greater than with the treatment plan alone. The compensation factor of the second compensated plan using arc 1 and arc 2 for MVCBCT imaging was 96.4%. As observed with DVHs in Fig. 6, using two MVCBCT acquisition arcs (below) provided similar compensation results as using only the current MVCBCT arc acquisition (middle). The need for two MVCBCT arcs will be discussed in the next section.

#### III.C.2. Prostate patient treated with IMRT

Figure 7 presents DVHs of uncompensated and compensated plans for daily 9 MU MVCBCT imaging on a pelvis patient treated with IMRT. Similarly to the previous case, a uniform increase in dose was observed for all structures for the uncompensated plan (top). The mean increase in structure mean dose was 2.1 Gy ( $33$  fractions  $\times$  6.5 cGy). The compensation factor found using Eq. (1) was 96.8%. As ob-

TABLE II. Dose delivered to a typical head and neck patient for weekly verification of alignment and anatomy. MVCBCT (5 MU), CR film ( $2 \times 4$  MU = 8 MU) and portal imaging ( $2 \times 2$  MU = 4 MU)

	MVCBCT (cGy)			CR Film (cGy)			Portal Imaging (cGy)		
	Min	Mean	Max	Min	Mean	Max	Min	Mean	Max
GTV	4.8	<b>5.2</b>	5.8	6.6	<b>8.1</b>	9.5	2.4	<b>4.0</b>	4.8
CTV1	2.7	<b>5.0</b>	5.8	3.8	<b>7.8</b>	9.6	2.0	<b>3.8</b>	4.8
CTV2	4.5	<b>4.8</b>	5.1	6.6	<b>7.6</b>	8.6	3.2	<b>3.8</b>	4.2
Esophagus	3.9	<b>4.5</b>	5.0	6.1	<b>6.6</b>	7.1	3.0	<b>3.4</b>	3.6
Mandible	3.5	<b>5.4</b>	6.0	5.5	<b>8.6</b>	9.7	2.8	<b>4.2</b>	4.8
Spinal cord	3.3	<b>4.2</b>	4.8	5.1	<b>6.5</b>	7.5	2.6	<b>3.2</b>	3.8
Left parotid	2.4	<b>4.9</b>	5.3	4.2	<b>8.8</b>	9.4	2.0	<b>4.4</b>	4.8
Brain-stem	4.2	<b>4.4</b>	4.6	6.6	<b>7.2</b>	7.9	3.2	<b>3.6</b>	4.0
Brain	0.9	<b>4.1</b>	5.6	1.3	<b>6.5</b>	9.3	0.6	<b>3.2</b>	4.6
Skin	0.0	<b>4.4</b>	5.7	0.0	<b>7.0</b>	9.4	0.0	<b>3.6</b>	4.6
Left eye	1.6	<b>5.5</b>	5.8	2.5	<b>9.2</b>	9.8	1.2	<b>4.6</b>	5.0
Right lens	3.6	<b>5.1</b>	5.5	5.4	<b>7.5</b>	8.0	2.6	<b>3.8</b>	4.0

served in Fig. 7 (below), the compensated plan showed no increase in the high dose region and a small increase in the low dose region.

### III.C.3. Head and neck patient treated with IMRT

Figures 8 and Fig. 9 show dose distributions and DVHs of uncompensated and compensated plans for daily 5 MU MVCBCT imaging on a head and neck patient treated with IMRT. As seen with Fig. 8 (middle column) and Fig. 9 (top), simply adding daily 5 MU MVCBCT to the treatment dose results in a uniform dose increase of 1.8 Gy (33 fractions  $\times$  5.5 cGy). The volume of tissue receiving more than 74 Gy between the left and middle columns of Fig. 8 is slightly increased. The compensation factor of the compensated plan using only the current arc was 97.7%. As observed in Fig. 9

(below), the compensation method reduces the dose in the high-dose region such that the amount of tissue receiving a high dose ( $\sim 40$  Gy or more) remained the same. Despite the compensation method, the volume of tissue receiving less than 40 Gy in the compensated plan was still slightly greater than with the treatment plan alone. The mean difference in structure mean dose between the treatment alone and the compensated treatment plus imaging plan was 0.6 Gy. A simple method to completely eliminate the imaging dose delivered to the lenses will be presented in the Discussion.

## IV. DISCUSSION

In this article, we first validated the use of a commercial TPS to simulate the delivered dose from MVCBCT imaging. This is a beneficial feature of MVCBCT because complete imaging dose distributions can be obtained on patient images as opposed to only few points on the skin or in phantom with available detectors. In addition, simulating the MVCBCT dose on patients requires minimal work since most of the steps needed (CT imaging, image import, contouring) are already performed for regular treatment planning. MVCBCT is simply an arc treatment with a specific isocenter position, acquisition range, field size, and total number of MU. Monthly quality assurance is currently performed using a Farmer ion chamber to assure reproducibility in the beam output for MVCBCT imaging.

The MVCBCT dose delivered to a prostate and a head and neck patient was compared to what is currently used in our department for portal imaging and film. In general, MVCBCT delivers more dose than portal imaging but less than CR film. For similar or less dose than conventional films, MVCBCT provides a 3D image with soft tissue information to guide patient positioning and assess anatomical changes. Portal imaging is generally faster than MVCBCT but provides no soft tissue information. It has recently been shown that aligning simple objects such as seeds with portal imaging is just as accurate as with MVCBCT.<sup>11</sup> However, MVCBCT has a clear advantage to provide volumetric infor-

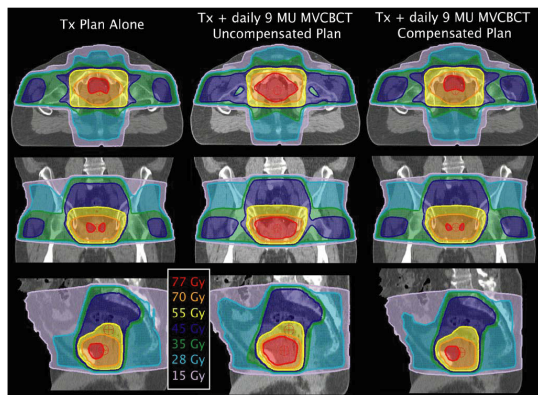


FIG. 5. Dose distributions calculated on a pelvis patient for different plans combining treatment and MVCBCT imaging dose. This prostate patient was treated with a four-field box (25 fractions) to the whole pelvis followed by two boosts; the first one including seminal vesicles and prostate (5 fractions) and the second including only the prostate (10 fractions). The treatment plan alone (treatment dose alone) (left) is compared with an uncompensated plan (treatment dose +  $40 \times 9$  MU MVCBCT) (middle) and a compensated plan (96% treatment dose +  $40 \times 9$  MU MVCBCT) (right).

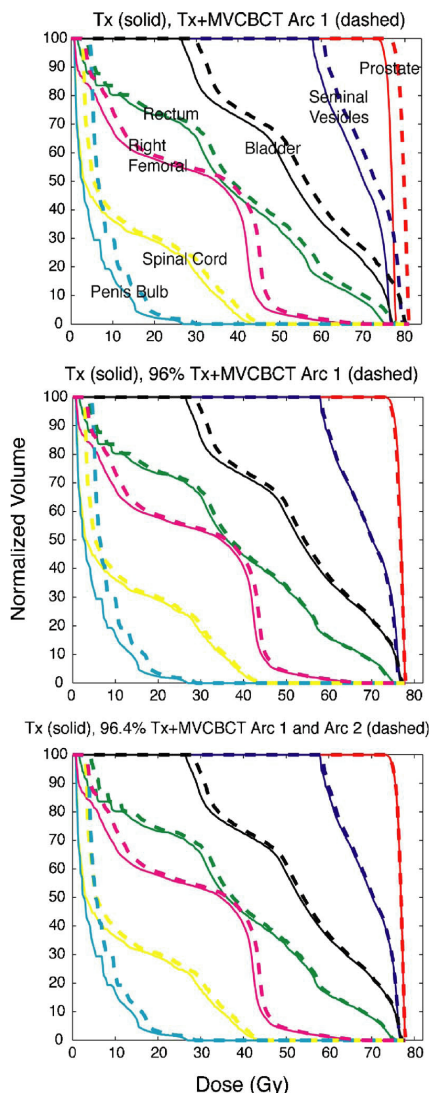


FIG. 6. DVHs for the prostate patient plans presented in Fig. 6. DVHs for the treatment dose alone (solid) were compared with different combinations of treatment and imaging dose (dashed). The treatment plan alone (treatment dose alone) was compared with (top) an uncompensated plan (treatment dose+40×9 MU MVCBCT), (middle) a compensated plan (96% treatment dose+40×9 MU MVCBCT), and (below) a compensated plan, alternating arc 1 (270° to 110°) and arc 2 (90° to 290°) (96.4% treatment dose+20×9 MU MVCBCT1+20×9 MU MVCBCT2).

mation, identify rotation, distortion, and anatomical changes. From our clinical experience with the current MVCBCT system, alignment based on soft tissue and bony anatomy can readily be performed with less than 12 and 6 cGy for the pelvic and head and neck patients, respectively. Preliminary results have also suggested that a given applied shift does not need to be verified with a second MVCBCT.

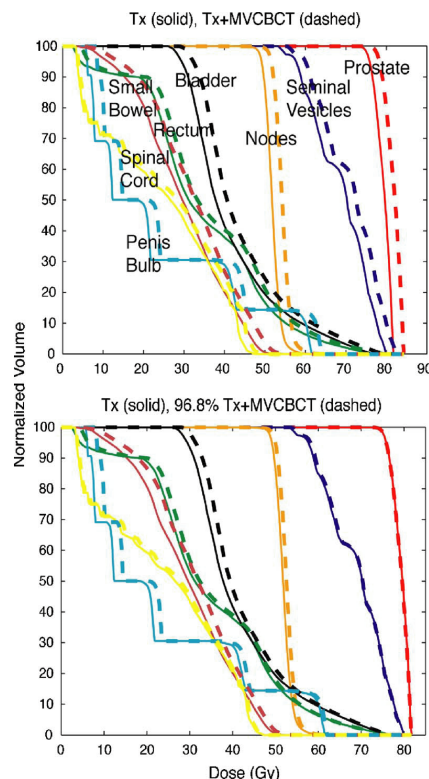


FIG. 7. DVHs for a prostate patient treated with IMRT. DVHs for the treatment dose alone (solid) were compared with (top) the treatment dose added to daily 9 MU MVCBCT (dashed) and (below) a compensated treatment dose added to daily 9 MU MVCBCT (dashed).

The MVCBCT dose obtained in this study can be compared to reported delivered dose by other IGRT technologies. The current in-room CT imaging systems deliver a maximum dose ranging between 1 and 16 cGy. Taking the RBE into account, one of the kVCBCT systems commercially available and MVCBCT delivered the most dose equivalent for imaging. While it is interesting to compare the delivered dose from the initial clinical product of the available in-room CT technologies, the systems likely differ in other important physical performance such as the image quality and the time required for imaging. Overall, studies on the dose delivered by IGRT technologies showed that the imaging dose for IGRT is small compared to the treatment dose (<4% of the prescription). However, higher dose to normal tissue may increase the risk of side effects and radiation induced cancer.<sup>25</sup> For this reason groups are studying ways to further reduce the imaging dose delivered by their system.<sup>26,27</sup>

In this article, our approach to minimize the dose delivered from routine MVCBCT imaging has been to incorporate the imaging and the treatment dose in a *composite* plan. This can be done because MVCBCT uses the same beam for treatment and imaging. Using the treatment and imaging plans simulated in the TPS, a compensation factor was introduced

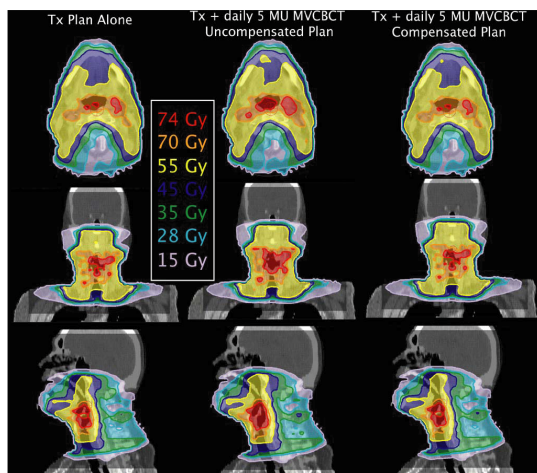


FIG. 8. Dose distributions simulated on a head and neck patient for different combinations of treatment and MVCBCT imaging dose. The patient was treated with IMRT. The treatment plan alone (treatment dose alone) (left) is compared with an uncompensated plan (treatment dose+33×5 MU MVCBCT) (middle) and a compensated plan (97.7% treatment dose+33×5 MU MVCBCT) (right).

to keep the target mean dose unchanged. This compensation factor can be obtained in less than 10 min for all patients. The method was tested on two prostate patients and one head and neck patient. All compensated plans compared to the initial plan without imaging showed no increase in the high dose region and small increases at low dose. For the cases examined, the additional dose in the low-dose region for the compensated plan is considered clinically insignificant. For the head and neck case presented, the maximum doses to the spinal cord for the treatment plan alone and the compensated plan were 44.0 and 44.4 Gy, respectively. However, the question whether the compensation method should be applied is still open. Most of our physicians feel no need to compensate for routine MVCBCT because the delivered dose is similar to portal imaging or film, neither of which have been compensated for in the past. However, given the ease of use of the method presented, the additional dose from IGRT could be greatly reduced or documented. The use of an opposed MVCBCT arc acquisition to reduce the imaging dose showed only a marginal additional reduction in dose when using the compensation method. The opposed arc could have its greatest benefit to image anterior sensitive structures, such as the eye lenses, while minimizing the dose delivered. Another direct method to reduce the dose to normal tissue, which has been used in our clinic, is to reduce the amount of tissue imaged in the cranio-caudal direction. All simulations performed in this paper were done using the maximum field size. Closing the Y jaw for imaging can be used to focus on a specific target, such as prostate, or to completely avoid dose to critical structures, such as the eyes. In addition, collimating the beam reduces the amount of scatter radiation reaching the detector, which improves the image quality. Finally, the most direct method to reduce the

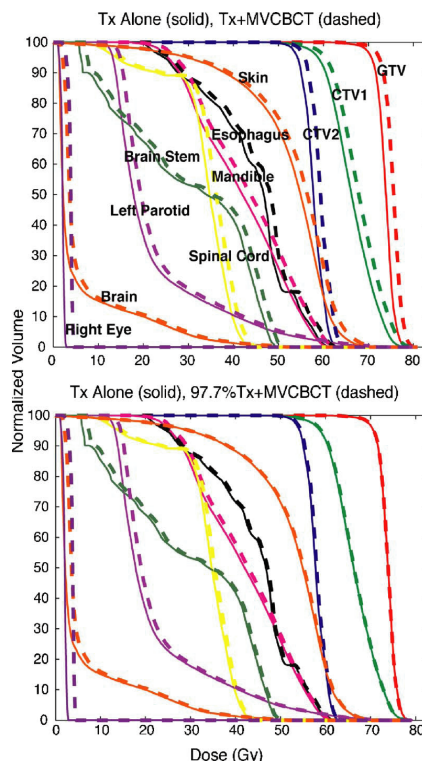


FIG. 9. Dose volume histograms (DVHs) for the head and neck patient plans presented in Fig. 8. DVHs for the treatment dose alone (solid) were compared with (top) the treatment dose added to daily 5 MU MVCBCT (dashed) and (below) a compensated treatment dose added to daily 5 MU MVCBCT (dashed).

MVCBCT dose is to use fewer MU per acquisition. This will become possible with the development of more sensitive detectors for MV imaging.<sup>28</sup> Preliminary investigations also suggest that an optimized beamline for MVCBCT imaging will provide a factor of 3.5 improvement in contrast-to-noise ratio, thus allowing a significant reduction of the exposure to obtain a given MVCBCT image quality.<sup>29</sup>

## V. CONCLUSION

A commercial TPS can be used to evaluate the dose delivered by MVCBCT. For a typical MVCBCT, the delivered dose forms a small anterior-posterior gradient roughly ranging from 0.6 to 1.2 cGy per MVCBCT MU. A MVCBCT acquisition of 9 MU in the pelvis area delivers slightly more dose than what is currently delivered by portal imaging in our department but renders some soft tissue information for positioning. A MVCBCT acquisition of 5 MU in the head and neck area delivers less dose than CR film. Overall, the additional dose from daily 9 MU MVCBCTs is small compared to the treatment dose (<4%). A simple and rapid plan compensation method for routine MVCBCT shows good results to reduce the total dose to critical structures for daily MVCBCT positioning. DVHs of compensated plans for pel-

vis and head and neck patients imaged daily with MVCBCT shows no additional dose to the target and small increases in low doses regions. Reducing the imaging volume in the cranio-caudal direction can further reduce the dose delivered for MVCBCT. This is a useful feature to eliminate the imaging dose to the eyes or to focus on a specific region of interest for alignment.

#### ACKNOWLEDGMENTS

The authors would like to acknowledge the following persons for their valuable contributions: Chris Malfatti for the CT acquisitions on phantoms, as well as Jeff Bellerose and Clayton Akazawa for the work done in the treatment planning system. This research was partly funded by Siemens Oncology Care Systems. Two of the authors (OM and JFA) wish to acknowledge a scholarship from the National Sciences and Engineering Research Council of Canada (NSERC).

- <sup>a1</sup>Address for correspondence: UCSF Comprehensive Cancer Center, Department of Radiation Oncology, 1600 Divisadero Street, Suite H1031, San Francisco, CA 94143. Electronic mail: morin@radonc17.ucsf.edu
- <sup>1</sup>R. de Crevoisier, S. L. Tucker, L. Dong, R. Mohan, R. Cheung, J. D. Cox, and D. A. Kuban, "Increased risk of biochemical and local failure in patients with distended rectum on the planning CT for prostate cancer radiotherapy," *Int. J. Radiat. Oncol., Biol., Phys.* **62**, 965–973 (2005).
- <sup>2</sup>A. Gillis, K. Bucci, M. Aubin, O. Morin, J. Chen, and J. Pouliot, "First clinical application of MV cone-beam CT: Patient positioning during radiation treatment [Abstract]," presented at the American Society for Therapeutic Radiology and Oncology, 47th Annual Meeting, Denver, CO (2005).
- <sup>3</sup>O. Morin, J. Chen, M. Aubin, A. Gillis, J.-F. Aubry, S. Bose, H. Chen, M. Descovich, P. Xia, and J. Pouliot, "Dose calculation using megavoltage cone-beam CT," *Int. J. Radiat. Oncol., Biol., Phys.* **67**, 1201–1210 (2007).
- <sup>4</sup>E. K. Hansen, M. K. Bucci, J. M. Quivey, V. Weinberg, and P. Xia, "Repeat CT imaging and replanning during the course of IMRT for head-and-neck cancer," *Int. J. Radiat. Oncol., Biol., Phys.* **64**, 355–362 (2006).
- <sup>5</sup>J. E. Marks, A. G. Haus, H. G. Sutton, and M. L. Griem, "The value of frequent treatment verification films in reducing localization error in the irradiation of complex fields," *Cancer* **37**, 2755–2761 (1976).
- <sup>6</sup>A. L. Boyer, L. Antonuk, A. Fenster, M. Van Herk, H. Meertens, P. Munro, L. E. Reinstein, and J. Wong, "A review of electronic portal imaging devices (EPIDs)," *Med. Phys.* **19**, 1–16 (1992).
- <sup>7</sup>M. Uematsu, M. Sonderegger, A. Shioda, K. Tahara, T. Fukui, Y. Hama, T. Kojima, J. R. Wong, and S. Kusano, "Daily positioning accuracy of frameless stereotactic radiation therapy with a fusion of computed tomography and linear accelerator (focal) unit: evaluation of z-axis with a z-marker," *Radiother. Oncol.* **50**, 337–339 (1999).
- <sup>8</sup>D. A. Jaffray, J. H. Siewerdsen, J. W. Wong, and A. A. Martinez, "Flat-panel cone-beam computed tomography for image-guided radiation therapy," *Int. J. Radiat. Oncol., Biol., Phys.* **53**, 1337–1349 (2002).
- <sup>9</sup>T. R. Mackie, J. Kapatoes, K. Ruchala, W. Lu, C. Wu, G. Olivera, L. Forrest, W. Tome, J. Welsh, R. Jeraj, P. Harari, P. Reckwerdt, B. Paliwal, M. Ritter, H. Keller, J. Fowler, and M. Mehta, "Image guidance for precise conformal radiotherapy," *Int. J. Radiat. Oncol., Biol., Phys.* **56**, 89–105 (2003).
- <sup>10</sup>K. J. Ruchala, G. H. Olivera, E. A. Schloesser, and T. R. Mackie, "Megavoltage CT on a tomotherapy system," *Phys. Med. Biol.* **44**, 2597–2621 (1999).
- <sup>11</sup>O. Morin, A. Gillis, J. Chen, M. Aubin, K. Bucci, and J. Pouliot, "Megavoltage cone-beam CT: system description and clinical applications,"

- Med. Dosim.* **31**, 51–61 (2006).
- <sup>12</sup>J. Pouliot, A. Bani-Hashemi, J. Chen, M. Svatos, F. Ghelmansarai, M. Mitschke, M. Aubin, P. Xia, O. Morin, K. Bucci, M. Roach, III, P. Hernandez, Z. Zheng, D. Hristov, and L. Verhey, "Low-dose megavoltage cone-beam CT for radiation therapy," *Int. J. Radiat. Oncol., Biol., Phys.* **61**, 552–560 (2005).
- <sup>13</sup>M. A. Hill, "The variation in biological effectiveness of x-rays and gamma rays with energy," *Radiat. Prot. Dosim.* **112**, 471–481 (2004).
- <sup>14</sup>W. R. Hendee and E. R. Ritenour, *Medical Imaging Physics*, 4th ed. (Wiley-Liss, New York, 2002).
- <sup>15</sup>B. J. Conway, J. L. McCrohan, R. G. Antonsen, F. G. Rueter, R. J. Slayton, and O. H. Suleiman, "Average radiation dose in standard CT examinations of the head: results of the 1990 NEXT survey," *Radiology* **184**, 135–140 (1992).
- <sup>16</sup>N. Wen, H. Guan, R. Hammoud, D. Pradhan, T. Nurushev, Q. Chen, S. Li, and B. Movsas, "TH-D-VaIB-02: Skin and body dose measurements for Varian cone-beam CT (CBCT) during IMRT for prostate cancer," *Med. Phys.* **33**, 2280 (2006).
- <sup>17</sup>M. K. Islam, T. G. Purdie, B. D. Norrlinger, H. Alasti, D. J. Moseley, M. B. Sharpe, J. H. Siewerdsen, and D. A. Jaffray, "Patient dose from kilovoltage cone beam computed tomography imaging in radiation therapy," *Med. Phys.* **33**, 1573 (2006).
- <sup>18</sup>S. L. Meeks, J. F. Harmon, Jr., K. M. Langen, T. R. Willoughby, T. H. Wagner, and P. A. Kupelian, "Performance characterization of megavoltage computed tomography imaging on a helical tomotherapy unit," *Med. Phys.* **32**, 2673–2681 (2005).
- <sup>19</sup>T. Li, E. Schreibmann, B. Thorndyke, G. Tillman, A. Boyer, A. Koong, K. Goodman, and L. Xing, "Radiation dose reduction in four-dimensional computed tomography," *Med. Phys.* **32**, 3650–3660 (2005).
- <sup>20</sup>J. Sillanpaa, J. Chang, G. Mageras, H. Riem, E. Ford, D. Todor, C. C. Ling, and H. Amols, "Developments in megavoltage cone beam CT with an amorphous silicon EPID: Reduction of exposure and synchronization with respiratory gating," *Med. Phys.* **32**, 819–829 (2005).
- <sup>21</sup>K. Sidhu, E. C. Ford, S. Spiro, E. Yorke, J. Chang, K. Mueller, D. Todor, K. Rosenzweig, G. Mageras, C. Chui, C. C. Ling, and H. Amols, "Optimization of conformal thoracic radiotherapy using cone-beam CT imaging for treatment verification," *Int. J. Radiat. Oncol., Biol., Phys.* **55**, 757–767 (2003).
- <sup>22</sup>O. Morin, J. Bellerose, M. Descovich, M. Aubin, J. Chen, J. Aubry, H. Chen, and J. Pouliot, "SU-FF-I-13: Dose delivered to patients for megavoltage cone-beam CT imaging [Abstract]," *Med. Phys.* **33**, 1999 (2006).
- <sup>23</sup>O. Gayou, D. S. Parda, M. Johnson, and M. Miften, "Patient dose and image quality from mega-voltage cone beam computed tomography imaging," *Med. Phys.* **34**, 499–506 (2007).
- <sup>24</sup>M. Aubin, O. Morin, J. Chen, A. Gillis, B. Pickett, J. F. Aubry, and J. Pouliot, "The use of megavoltage cone-beam CT to complement CT for target definition in pelvic radiotherapy in presence of hip replacement," *Br. J. Radiol.* **79**, 918–921 (2006).
- <sup>25</sup>K. Amemiya, H. Shibuya, R. Yoshimura, and N. Okada, "The risk of radiation-induced cancer in patients with squamous cell carcinoma of the head and neck and its results of treatment," *Br. J. Radiol.* **78**, 1028–1033 (2005).
- <sup>26</sup>P. Ravindran, M. Islam, and D. Jaffray, "TU-FF-A3-03: Investigation of dose reduction strategies for image guidance with KV-CBCT in radiation therapy [Abstract]," *Med. Phys.* **33**, 2221 (2006).
- <sup>27</sup>K. Sheng, R. Jeraj, R. Shaw, T. R. Mackie, and B. R. Paliwal, "Imaging dose management using multi-resolution in CT-guided radiation therapy," *Phys. Med. Biol.* **50**, 1205–1219 (2005).
- <sup>28</sup>A. Sawant, L. E. Antonuk, Y. El-Mohri, Z. Qihua, L. Yixin, S. Zhong, W. Yi, J. Yamamoto, D. Hong, I. Cunningham, M. Klugerman, and K. Shah, "Segmented crystalline scintillators: An initial investigation of high quantum efficiency detectors for megavoltage x-ray imaging," *Med. Phys.* **32**, 3067–3083 (2005).
- <sup>29</sup>B. Faddegon, F. Ghelmansarai, and A. Bani-Hashemi, "A low-Z target with no flattener and reduced energy for improved contrast in megavoltage cone-beam CT [Abstract]," *Med. Phys.* **33**, 2021 (2006).



## Dose-guided radiation therapy with megavoltage cone-beam CT

J CHEN, PhD, O MORIN, BSc, M AUBIN, Eng-MSc, M K BUCCI, MD, C F CHUANG, PhD and J POULIOT, PhD

UCSF Comprehensive Cancer Center, Department of Radiation Oncology, University of California San Francisco, 1600 Divisadero Street, Suite H1031, San Francisco, CA 94143, USA

**ABSTRACT.** Recent advances in fractionated external beam radiation therapy have increased our ability to deliver radiation doses that conform more tightly to the tumour volume. The steeper dose gradients delivered in these treatments make it increasingly important to set precisely the positions of the patient and the internal organs. For this reason, considerable research now focuses on methods using three-dimensional images of the patient on the treatment table to adapt either the patient position or the treatment plan, to account for variable organ locations. In this article, we briefly review the different adaptive methods being explored and discuss a proposed dose-guided radiation therapy strategy that adapts the treatment for future fractions to compensate for dosimetric errors from past fractions. The main component of this strategy is a procedure to reconstruct the dose delivered to the patient based on treatment-time portal images and pre-treatment megavoltage cone-beam computed tomography (MV CBCT) images of the patient. We describe the work to date performed to develop our dose reconstruction procedure, including the implementation of a MV CBCT system for clinical use, experiments performed to calibrate MV CBCT for electron density and to use the calibrated MV CBCT for dose calculations, and the dosimetric calibration of the portal imager. We also present an example of a reconstructed patient dose using a preliminary reconstruction program and discuss the technical challenges that remain to full implementation of dose reconstruction and dose-guided therapy.

Received 30 June 2005  
Revised 8 August 2005  
Accepted 7 September 2005

DOI: 10.1259/bjr/60612178

© 2006 The British Institute of Radiology

### The rationale for adaptive radiation therapy and dose-guided radiation therapy

Recent advances in fractionated external beam radiation therapy, such as three-dimensional conformal and intensity-modulated radiation therapy (IMRT), have increased our ability to deliver radiation doses that conform more tightly to the tumour volume. Clinical studies and simulations indicate that these more conformal, higher dose treatments can decrease both the spread of disease and normal tissue complications [1-5]. Increasing use of functional imaging will also motivate further complexity in radiation treatment plans to include concurrent boosts in regions of high cancerous growth [6, 7]. As these dose distributions conform more tightly to the patient anatomy, dose gradients necessarily become steeper inside the irradiated volume. Using IMRT, a dose gradient of 10%  $\text{m}^2$  can be achieved easily. Thus, it is increasingly important to set precisely the positions of the patient and the internal organs. Currently, external markers and patient immobilizing masks and casts are used to reproduce the skeletal position of the patient with about 3 mm accuracy over several weeks of treatment [8]. However, the effectiveness of these alignment and immobilization techniques are limited by changes in the internal organ locations relative to bony and external markers. For example, the prostate can shift up to 1 cm relative to the pelvic bones due to variations in rectal/bladder filling. During the course of head and neck cancer treatment, the tumour

can shrink and the patient can lose significant weight, resulting in dosimetric errors as large as 40% [9, 10]. For this reason, imaging tools in the treatment room and methods of adapting treatments to match the patient anatomy on the treatment table are the keys to realising the full benefit of conformal therapy.

For many decades, imaging inside the treatment room has played a role in verifying radiation therapy treatment. Portal images, projection images of the patient using the treatment aperture, are used to confirm the patient position and verify coverage of the tumour. The use of radiographic film for portal imaging has limited the frequency of this verification due to the required time and dose to the patient. However, recent implementation of electronic portal imaging devices (EPIDs) allows a digital image to be acquired in a few seconds with low doses. This has allowed the use of daily portal imaging to visualize and adjust the patient position before each treatment. For example, using implanted gold markers to locate the prostate, daily portal imaging has been used to position the prostate with 1-2 mm accuracy [11-13]. The use of portal imaging to adjust patient position before treatment is limited, however, because soft tissue cannot be visualized without implanted markers and the full three-dimensional (3D) geometry is obscured by the projection onto a two-dimensional (2D) plane. Therefore, considerable research now focuses on developing three-dimensional imaging of the patient on the treatment table. Several systems have been developed including (1) a "CT on rails" system, requiring an additional diagnostic CT machine in the treatment room [14]; (2) a kilovoltage cone-beam CT (kV CBCT) system, consisting

This research was supported by Siemens Oncology Care Systems.

of an additional kV X-ray source and detector attached to the treatment gantry [15,16] (these systems are described more fully in this issue in papers by Thieke et al and Moore et al, respectively); (3) a megavoltage cone-beam CT (MV CBCT) system using the pre-existing treatment machine and EPID for imaging [17–19]; (4) a MV CT system, using the pre-existing treatment machine with an attached arc of detectors [20]; and (5) a tomotherapy system, replacing the traditional treatment machine (beam) with a CT ring and a MV beam source [21–23]. These imaging systems continue to improve and recent results indicate that 1–2% soft-tissue contrast resolution is possible [15, 17, 18, 21] as well as accurate localization of various tumours [14, 16, 19, 20, 22, 23].

In the above examples of image-guided radiation therapy (IGRT), treatment room imaging modalities are used to translate and rotate the patient to better match the patient position used for treatment planning. Another potentially more powerful use of these images is to modify the delivered treatment fields to account for the variable patient position. This type of adaptive radiation therapy could adjust for the changing relative positions of the internal organs and the changing shape of the organs. This is particularly important for organs that move significantly during the course of treatment. For these sites, techniques under current development include gated treatments (halting irradiation when the target is out of a certain acceptable region) [24–27] or target tracking during irradiation using specially designed mobile linear accelerators [28, 29]. For some sites, however, the most important anatomical changes occur between treatment fractions. In this case, a pre-treatment image may be used to adjust the treatment fields immediately before irradiation [30, 31]. Another possibility is to determine patient-specific anatomical variation using images from the first week of treatment and to tailor the treatment plan for future fractions to account for the individual's variation [32–34]. Finally, if the dose that was delivered in previous fractions can be estimated, the treatment plan for future fractions may be re-optimized to compensate for dosimetric errors [35]. This dose-guided therapy could correct for both errors due to patient anatomical changes as well as machine delivery errors, thus providing the most accurate dose delivery. The various adaptive radiation therapy schemes are depicted in Figure 1.

## The development of dosimetric verification and reconstruction

Currently, few methods are used to track the dose delivered during treatment. Standard techniques involve measuring doses on the patient surface using diodes or thermoluminescent dosimeters. However, these techniques provide only point dose measurements, and the time and effort to place the dosimeters on the patient and process the data limit their clinical use. Consequently, few institutions use these methods regularly for treatment verification. A new implantable MOSFET dosimeter has also been developed [36]. This dosimeter directly measures the dose in critical internal structures, but again provides only a point measurement and is an invasive technique with limited application. What is needed to verify conformal therapies is an automated method to reconstruct the full 3D dose distribution.

Several researchers have suggested methods to reconstruct the delivered patient dose during treatment. Most methods propose using on-board EPIDs to quickly and easily acquire a two-dimensional array of digitized X-ray measurements in a precisely positioned plane in the treatment exit beam. A few formulae have been derived to estimate the dose to the exit surface, midplane, or centre point of the patient based solely on EPID measurements [37–40]. To find a 3D patient dose distribution, however, requires additional information about the patient position and attenuation of the beam. For breast treatments, a simple patient contour may give sufficient information [41]. However, in general, information on tissue inhomogeneity is also necessary. Several years ago, it was suggested that the planning CT could be used for this purpose [42, 43], but this method would fail to detect dosimetric errors produced by the variable patient and organ positions and shapes. The 3D imaging modalities that are being developed for IGRT provide an obvious opportunity to simultaneously obtain the patient geometry for reconstructing dose. Currently, there is active development of dose reconstruction procedures for tomotherapy systems, and 3% accuracy in low-gradient regions has been demonstrated [44]. A pilot study using MV CBCT on a traditional treatment machine also found good relative agreement with measurements, but a systematic absolute deviation [45].

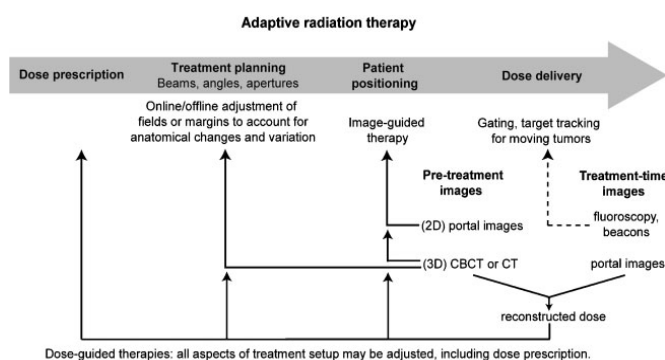


Figure 1. A general view of adaptive radiation therapy. The large grey arrow represents the conventional flow of treatment, and the small arrows indicate the possible points of feedback into the process.

## Dose-guided radiation therapy with MV CBCT

## Dose-guided radiation therapy using MV CBCT and treatment-time portal images

In 2003 [46], we began developing a procedure to reconstruct the dose delivered to the patient based on treatment-time portal images and pre-treatment MV CBCT. Our procedure follows the steps described below and depicted in Figure 2.

**Step 1A:** Prior to treatment, with the patient in the treatment setup position, acquire a MV CBCT image. This image can be used to align the patient as closely as possible to the planned position and also provides the photon attenuation information necessary to reconstruct the delivered dose.

**Step 1B:** Convert the MV CBCT to effective photon attenuation coefficient. Generally, this can be accomplished by calibrating the MV CBCT system using a calibration phantom composed of materials with known electron densities. However, imaging artefacts in the MV CBCT image may need to be corrected to improve the calibration accuracy.

**Step 2A:** During the treatment, acquire portal images of the treatment beam as it exits the patient. This portal image is acquired using the same EPID used for the CBCT imaging.

**Step 2B:** Convert the portal images to a 2D map of treatment beam energy fluence. The acquired portal image signal is a convolution of the energy fluence incident on the detector with the detector response to radiation. Moreover, the energy fluence consists of both the primary beam and radiation scattered from the patient. To use the portal image for dose calculations, the primary energy fluence must be derived from the portal image.

**Step 3:** Back-project the energy fluence measured at the detector plane through the CBCT of the patient, accounting for the  $1/r^2$  falloff of radiation from a point source and attenuation through the patient. This calculation is easily accomplished if the position of the detector plane relative to the patient and source is accurately known.

**Step 4:** Calculate the 3D dose distribution delivered to the patient using a dose calculation engine. This type of

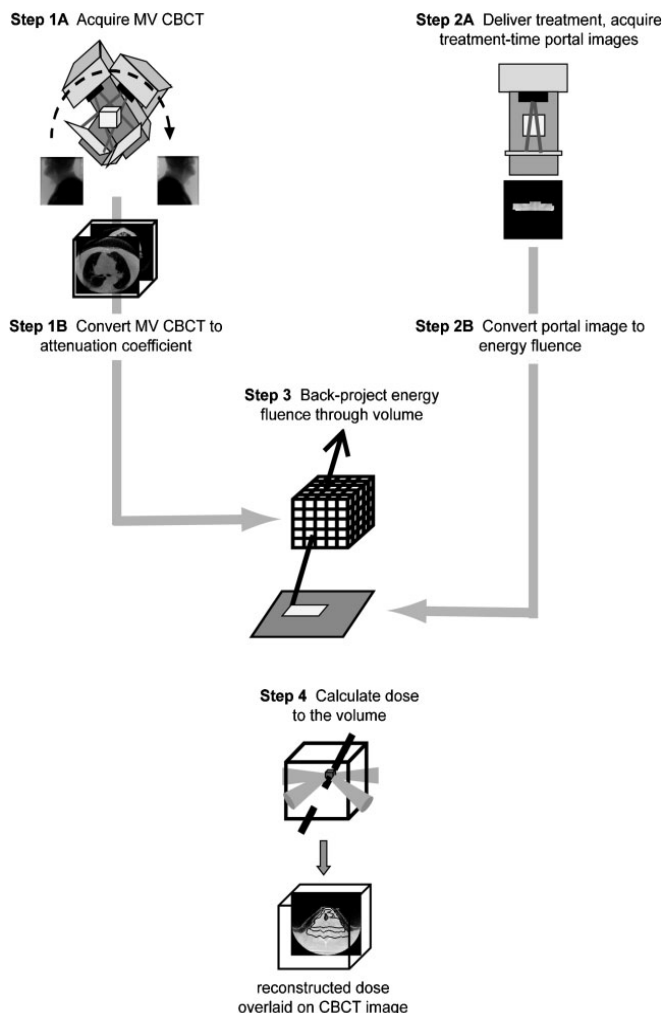


Figure 2. Overview of proposed dose reconstruction procedure using MV CBCT imaging and treatment-time portal imaging.

dose calculation is the same as that performed for treatment planning purposes, and all the techniques that have been developed for treatment planning may be used.

The reconstruction procedure described above provides an estimate of the 3D dose distribution deposited in the patient as represented by the MV CBCT. Several uses of the reconstructed dose distribution to guide future treatments can be envisaged. Scenario 1: The most basic use of the reconstructed dose is to provide a dosimetric verification that the treatment delivery generally provides the desired dose distribution and that no gross errors exist. This verification could be performed during the first treatment and repeated weekly throughout treatment. This simple approach would effectively reduce gross dosimetric errors, but would not otherwise increase the precision of the delivered dose. Scenario 2: If the patient dose is reconstructed for the first week of treatment, the variation in the delivered dose may also be evaluated. If the MV CBCT for each treatment is contoured to delineate the various important structures, the variation in dosimetric indices, such as the maximum dose to sensitive normal structures or the dose to 95% of the tumour volume, can be calculated. General systematic trends such as the under or over dosing of particular extremities of a structure may also be detected by examining the dose distributions over the first week. Based on this information, the treatment plan can be modified, for example, to increase or decrease margins of the tumour in particular directions. In this manner, the treatment plan can be tailored to each individual patient. Scenario 3: Finally, a complete dose-guided therapy system would be able to integrate the dose over previous fractions. This would require the ability to deform the daily MV CBCT images to map identical points in the patient before the integral dose is calculated [47]. The cumulative dose distribution can be used to adjust the treatment plan to compensate for deviations from the desired distribution, thus improving the accuracy and conformality of the overall treatment.

The dose reconstruction procedure and the dose-guided therapy described above continue to be developed and researched. This article summarizes the work to date and comments on the remaining challenges. First, we present a description of a MV CBCT system that has been implemented on a linear accelerator for clinical use. We then describe experiments performed to calibrate the MV CBCT for electron density and to use the calibrated MV CBCT for dose calculations. We also briefly describe the dosimetric calibration of an EPID for dose reconstruction. Finally, we present an example of a reconstructed patient dose using a preliminary reconstruction program and discuss the technical challenges that remain to full implementation of dose reconstruction and dose-guided therapy.

### MV cone-beam CT imaging

MV cone-beam CT imaging is a 3D reconstruction procedure similar to conventional CT. A series of projection measurements, in this case 2D portal images, are acquired at many angles around the patient. The image reconstructed is a 3D image without slice artefacts.

In the radiation oncology context, the imaging beam is produced by the conventional linear accelerator used for treatment, and the projection images are detected using on-board EPIDs. The imaging photons, therefore, are primarily in the mega-electron volt energy range. In this configuration, the patient can be positioned once on the treatment table and need not be repositioned between imaging and treatment.

As the linear accelerator gantry and the EPID rotate about the patient, the EPID and beam source positions will shift from their ideal isocentric locations due to sagging of the mechanical supports. To correct for this effect, we perform a geometric calibration of the system, illustrated in Figure 3 [48, 49]. This calibration provides a unique relationship between the position of a voxel in the reconstruction volume and a pixel on the detector plane for each angle. Because the EPID used for imaging is also used to detect the exit beam fluence, the same calibration information can be employed during the dose reconstruction procedure to back-project the energy

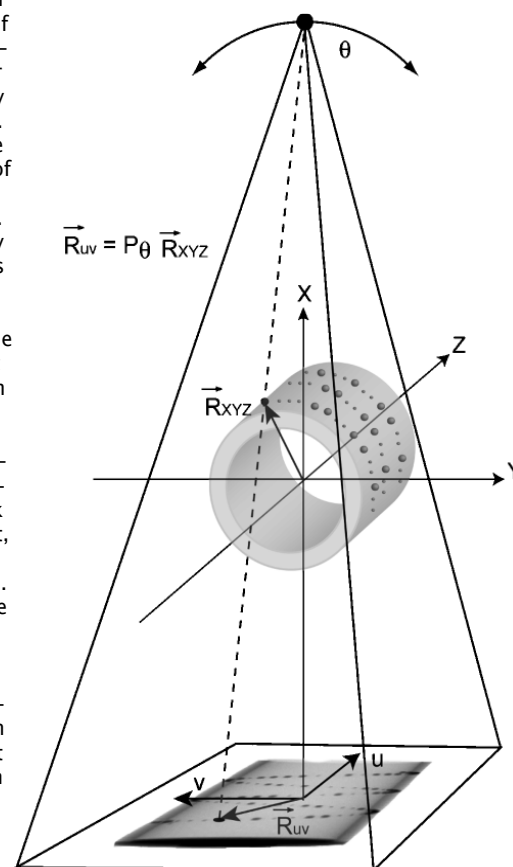


Figure 3. Depiction of the geometric calibration of the linear accelerator/electronic portal imaging device (EPID) system for cone beam CT (CBCT) imaging and for dose reconstruction. The result of the calibration is a set of projection matrices  $P$  that map a point in space  $R_{XYZ}$  to the projected point on the detector plane  $R_{uv}$ .

## Dose-guided radiation therapy with MV CBCT

fluence through the MV CBCT volume. This prevents any possibility of misregistration between the EPID measurements and the MV CBCT volume.

The MV CBCT system installed in our clinic has been previously described [19]. Briefly, it consists of an amorphous-silicon flat panel EPID integrated with a clinical linear accelerator. The total exposure of the CBCT acquisition can be varied from 1 to 60 monitor units. Upon patient selection, a reference CT is automatically loaded into the software. The linear accelerator gantry then rotates in a continuous 20° arc acquiring images at 1° increments. This acquisition procedure lasts about 45 s. The image reconstruction starts immediately after the acquisition of the first portal image, and a 256 × 256 reconstruction of the volume is completed in 110 s. The software automatically registers the MV CBCT with the reference CT and calculates table shifts for patient alignment.

To date, 38 patient MV CBCT images have been acquired in our clinic. All patients have given informed consent, and the patient image acquisitions are performed in accordance with the institutional review board's ethical standards. Depending on the frequency of the acquisitions, the dose used for MV CBCT ranges from approximately 1.5 cGy to 12 cGy delivered at the point of rotation (the isocentre). The dose at the entrance surface of the arc reaches about 160% of the isocentre dose for an imaged pelvis and 133% for the head and neck region. The dose at the exit surface falls to about 66% of the isocentre dose for a pelvis and 55% for the head and neck region. Figure 4 presents four MV CBCT images acquired weekly on the same patient to study tumour evolution. At each new acquisition, the dose was lowered. The last CBCT of the series was acquired with approximately 2.9 cGy delivered at the isocentre, still presenting enough soft-tissue information to assess the tumour size and perform patient alignment.

Three-dimensional imaging of the patient in the treatment position exposes the difficulties created by distortion of patient anatomy. Figure 5 displays the fusion of a MV CBCT image (grey) with the planning CT (colour). In this case, a physician has manually registered the two sets of images by aligning the base of the skull. A considerable shift, up to 6 mm, can be observed in the positions of the spinal cord between the two image sets. This misplacement of the spinal cord could not be corrected by translating or rotating the MV CBCT image relative to the CT as it was caused by an increase in the arching of the patient's neck. Although several fractions would be needed to assess if this misplacement occurs regularly, the new anatomy, as depicted by the MV CBCT image, could be used to study the dosimetric impact of the patient's anatomical distortion.

### MV CBCT calibration for dose calculation

To use the MV CBCT image in a dose reconstruction program, the signal from each voxel must be converted to effective photon attenuation coefficient for the beam spectrum (Step 1B of our dose reconstruction procedure). To perform this conversion, the MV CBCT system can be calibrated using a CT calibration phantom (CIRS Model 062, Norfolk, VA) with tissue-equivalent inserts, as is

currently done with kV CT. A table is formed mapping CT signal intensity to electron or physical density which can then be converted to photon attenuation coefficient for a known beam spectrum. Figure 6 shows the results of performing this simple calibration on our MV CBCT system using the following inserts of relative electron density with respect to water: lung inhale (0.190), lung exhale (0.489), adipose (0.952), breast (0.976), water (1), muscle (1.043), liver (1.052), trabecular bone (1.117) and dense bone (1.512). The relationship between MV CBCT signal and electron density is linear. These results are similar to previous work with MV fan-beam CT performed on a tomotherapy unit at 6 MV [50].

Although the above calibration works well for the narrow CT calibration phantom, the MV CBCT images of extended objects exhibit cupping artefacts due to the influence of scattered radiation reaching the EPID. Figure 7 illustrates this cupping effect on the MV CBCT of a large cylinder of water. If uncorrected, this cupping artefact will also appear in the image converted to photon attenuation coefficient, leading to errors in the calculated dose. However, a simulation study using the large cylinder of water pictured in Figure 7 indicates that the dosimetric errors in a homogeneous medium produced by such severe cupping artefacts remain relatively small, approximately 4% for a single open field [51]. This suggests that a crude correction of the cupping artefact in MV CBCT images may be sufficient to obtain acceptable dosimetric accuracy. To test this hypothesis, the MV CBCT of a water cylinder was used to model the spatial dependence of the cupping artefact. A spatially dependent correction function was derived from this cupping model. This correction function was then applied to the MV CBCT of an anthropomorphic head phantom as a rough correction for the cupping artefact in the image. After conversion to density using the MV CBCT calibration curve, this image was imported into a commercial treatment planning system (Philips Pinnacle, Bothell, WA). The dose calculated using the MV CBCT compared well with the dose calculated using a kV CT of the same phantom. Using a gamma index comparison with a 3% dose and 3 mm distance-to-agreement criterion, 98% of calculated dose points fell within the acceptance criteria.

The above example demonstrates the potential of using MV CBCT images for dose calculations. Besides using these images for dose reconstruction, using patient MV CBCT images in the treatment planning system, as performed on the head phantom described above, would also provide a useful verification. The MV CBCT provides a more accurate representation of the patient on the treatment table. Applying the treatment plan to the MV CBCT would provide a first estimate of the dose delivered to the patient during treatment. The effects of modified patient position or anatomy could be evaluated. However, the beam delivery itself could not be verified without a full dose reconstruction based on measurements of the treatment beam.

### Calibration of EPIDs for exit-plane dose

Besides the patient photon attenuation data, the other necessary piece of information for dose reconstruction is

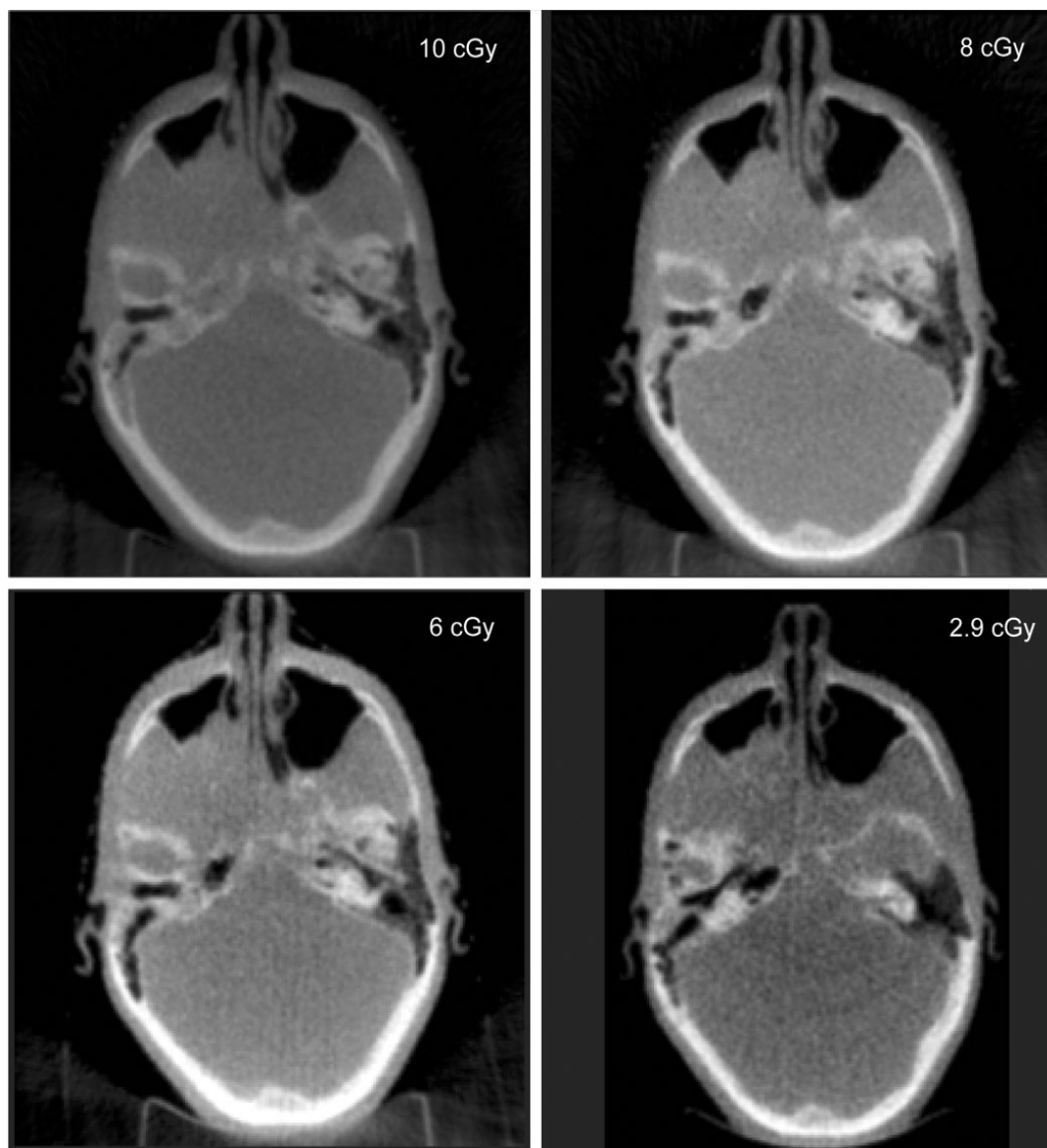


Figure 4. Examples of megavoltage cone beam CT (MV CBCT) images at different exposure levels, from 2.9 cGy to 10 cGy.

the treatment beam energy fluence derived from the be more easily converted to energy fluence due to the treatment-time portal images (Step 2 of our dose great number of water dose deposition models and reconstruction procedure). An intermediate step to algorithms that have already been developed. determining the energy fluence is to convert the EPID To translate the EPID signal to dose in water, we image to a measurable form of dose, in our case the dose employ convolution models of dose deposition. The in water measured in the detector plane and at a depth of lateral spread of the dose in the EPID and in the water is 1.5 cm [52]. The advantage of first calibrating the EPID described by empirically derived kernels. Because the against dose in water is that it can be accomplished by EPID consists of millions of individual pixels, the dose experiments since the dose in a water phantom is easily deposited in each pixel is also multiplied by a spatially measured. The calibration can then be validated by dependent sensitivity factor that accounts for inhomogeneity in the detector response. Finally, comparisons of measurements as well. Moreover, the dose in water can

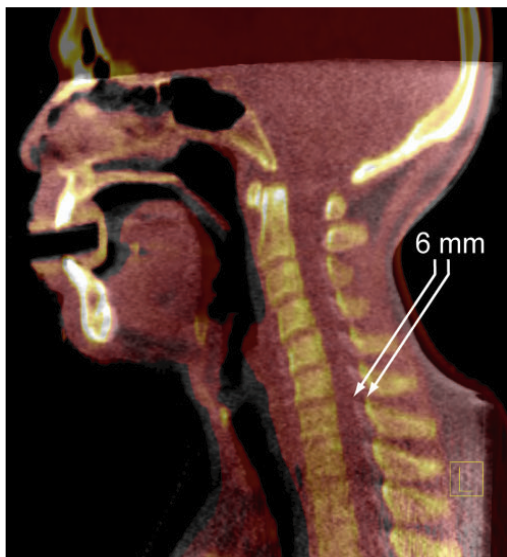


Figure 5. Registration of a patient megavoltage cone beam CT (MV CBCT) (grey) with the kV CT (colour) used for treatment planning. A large difference in the arching of the neck causes a considerable deviation in the spinal cord position.

EPID and ion chamber measurements are used to form conversion tables that translate between the EPID signal and dose in water.

To test the calibration procedure, EPID images of the exit beam were acquired through a Rando anthropomorphic head phantom (The Phantom Laboratory, Salem, NY). The calibrated EPID images were compared with the dose measured using an ion chamber (Scanditronix-Wellhofer CC13, Bartlett, TN) scanned in a water tank (Scanditronix-Wellhofer blue phantom,

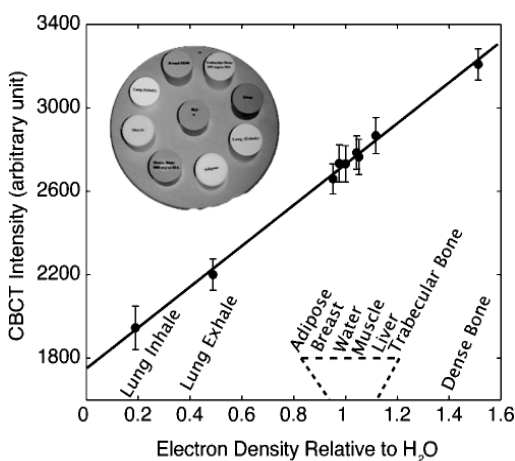


Figure 6. Megavoltage cone beam CT (MV CBCT) intensity as a function of electron density for tissue-equivalent inserts in a CT calibration phantom (pictured in above left).

Bartlett, TN). Figure 8 shows a comparison between the measured dose at a depth of 1.5 cm of water and the calibrated EPID signal for a 10 cm square open field. The EPID signal matches the measured dose to within 2% (2 standard deviations) for the in-field regions (excluding the penumbra).

#### A dose reconstruction program

Utilizing some of the work described above, we performed a preliminary version of the dose reconstruction procedure on the treatment of a head and neck patient in our clinic. A MV CBCT image was acquired of the patient set up on the table as for treatment (Step 1A). The same day, portal images were acquired (Step 2A) during the patient's normal course of treatment (6 MV beam, 2 opposed lateral wedged fields and an anterior-inferior oblique open field). To utilize the MV CBCT image in the dose reconstruction program, it must first be converted to effective photon attenuation coefficient (Step 1B). For this test case, the MV CBCT was converted to attenuation coefficient using a spatially dependent calibration that utilizes the kV CT patient image as a reference. This allowed us to reduce the effects of the MV CBCT calibration on the reconstructed dose, thus highlighting the dosimetric impact of the remaining steps of the procedure.

To convert the portal images to energy fluence (Step 2B), the portal images were first converted to equivalent dose in water using the calibration procedure described above. To infer the energy fluence at the detector plane from the equivalent dose in water, we used an in-house dose calculation program that predicts the dose at a depth of 1.5 cm of water given the energy fluence at the water surface. This energy fluence is then iteratively corrected until the predicted dose matches the measured dose. To calculate the dose in water, we used convolution kernels published in the literature [53], derived using Monte Carlo calculations and assuming a 6 MV spectrum. The energy fluence that is derived using this method is composed of both primary beam as well as radiation scattered from the patient. For this study, the contribution of the scattered radiation was neglected.

The two remaining steps to the dose reconstruction process are (Step 3) the back-projection of the energy fluence measured at the detector plane through the CBCT of the patient and (Step 4) the calculation of the 3D dose distribution delivered to the patient using a dose calculation engine. To perform the back-projection, we utilized the geometric information obtained during calibration of the MV CBCT imaging system (depicted in Figure 3). The geometric calibration of the system yields a set of projection matrices that map a point in space to a pixel in the detector plane. The projection matrix for each angle accurately accounts for all geometric factors such as sag in the detector or gantry, detector rotation, or variation in the detector to source distance. These projection matrices were used to back-project the energy fluence from the detector plane through the CBCT volume while correcting for  $\alpha^2$ /fall-off and the attenuation of each intersected voxel.

The final step of the reconstruction procedure is to calculate the dose deposited in the patient from the

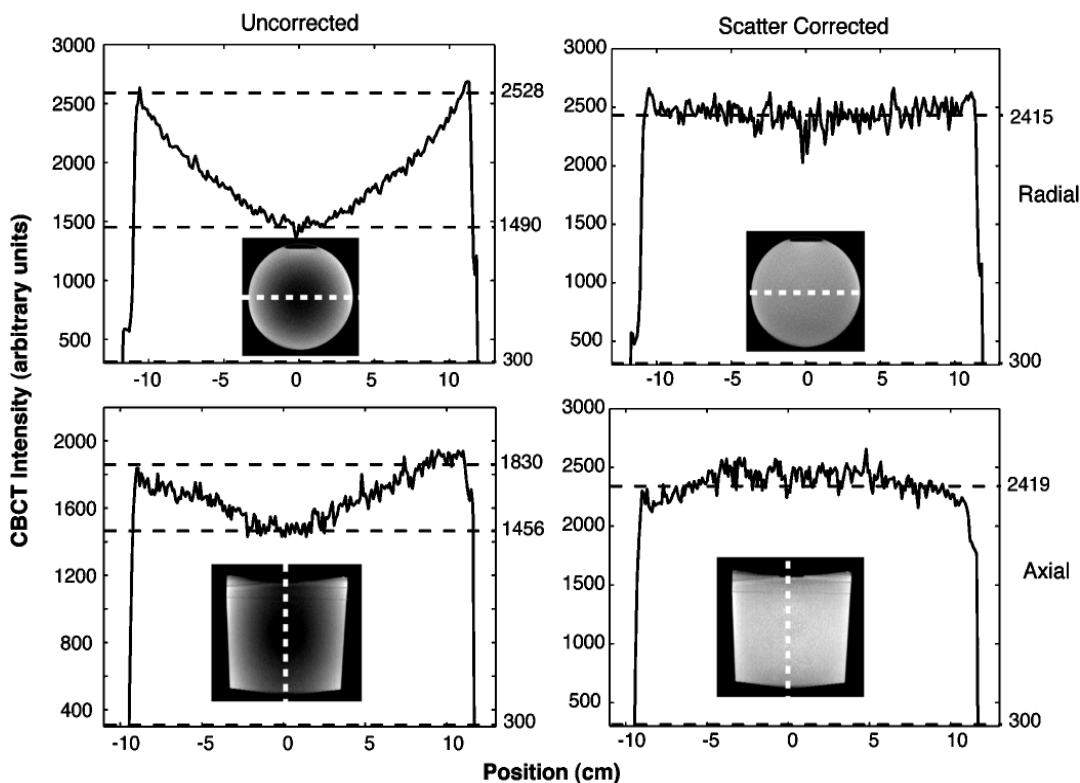


Figure 7. Radial (top row) and axial (bottom row) profiles through the megavoltage cone beam CT (MV CBCT) images of a large cylinder filled with water. The unmodified CBCT (left) exhibits a large cupping artefact as a result of scattered radiation reaching the electronic portal imaging device (EPID). Using a simple 3D cupping model effectively reduces the artefact (right). The radial and axial slices of the MV CBCT images (insets) are displayed using the same windowing level.

energy fluence and the attenuation coefficient for each fluence multiplied by the attenuation coefficient. The voxel. The total energy released in each voxel that spatial distribution of the deposited energy can then be interacts with the beam is proportional to the energy described using a kernel. The kernels we used for this

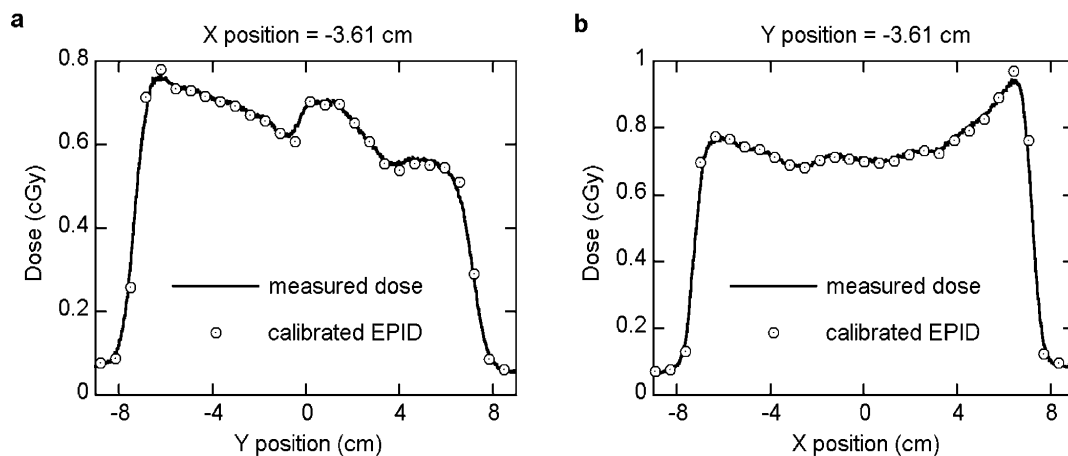


Figure 8. Comparisons of measured dose profiles (line) in water and calibrated electronic portal imaging device (EPID) profiles (circle with dot) for a 10 cm square field through a Rando head phantom.



## Dose-guided radiation therapy with MV CBCT

purpose were the same kernels used to determine the energy fluence at the detector plane from the equivalent alignment of the beams detected by the portal images. The doses from the treatment planning system suggest a slight gap between the opposed lateral fields and the anterior field. In contrast, the reconstructed dose distribution has a high dose band at the intersection of the fields. Without further verification, it is not clear whether this slight difference in field alignment was a real event detected using the treatment-time portal images. Other possible causes for the differences in the two dose distributions include differences in the dose calculation engines, differences in patient position or anatomy in the two images, as well as persistent cupping artefacts in the MV CBCT.

Figure 9 shows the comparison between the planned dose distribution found using the patient kV CT image and a commercial treatment planning system (Philips Pinnacle, Bothell, WA) and the reconstructed dose distributions found using the MV CBCT, the treatment-time portal images, and the in-house dose reconstruction program. There are some qualitative similarities, but also some marked differences. The reconstructed dose distribution appears to be approximately 10% higher than the dose predicted by the planning system. It is likely that this is in part due to an increase in the portal image signal from the scattered radiation that was not corrected in this preliminary version of the dose reconstruction.

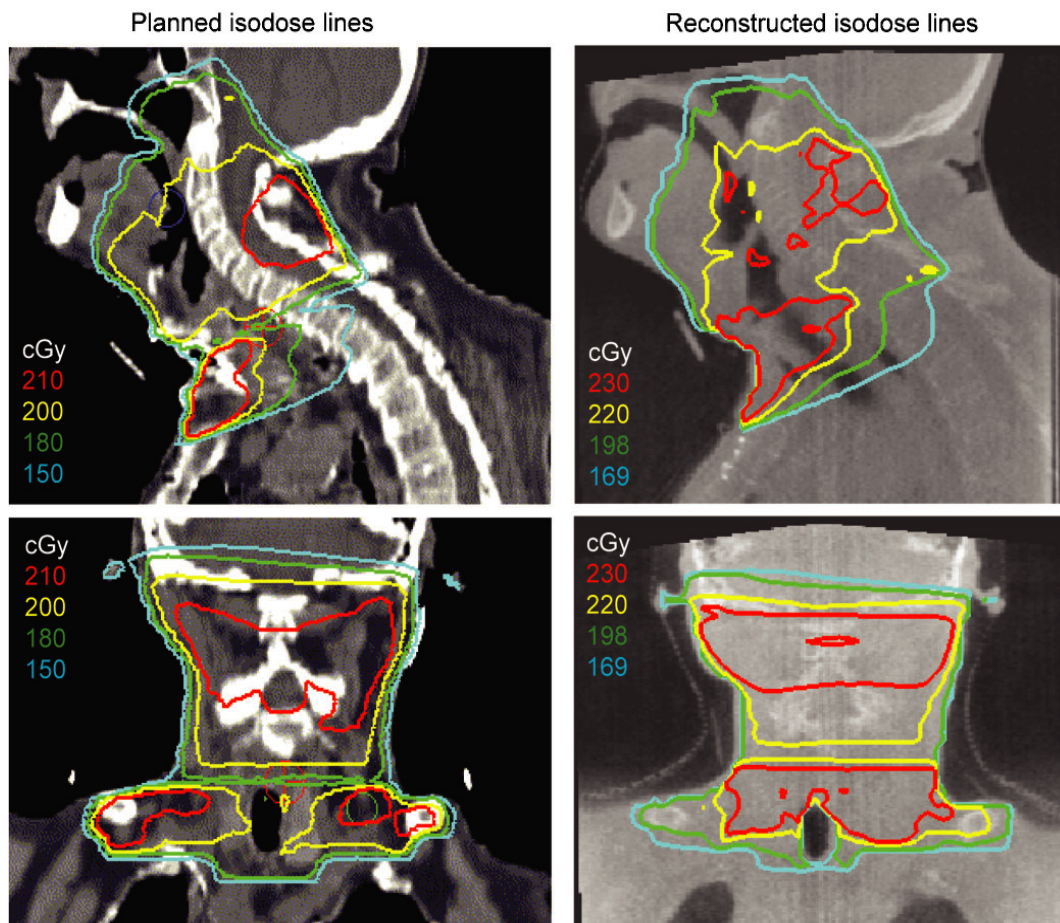


Figure 9. Comparisons between planned isodose contours calculated using the patient kV CT image and a commercial treatment planning system (left) and reconstructed isodose contours calculated using the megavoltage cone beam CT (MV CBCT), the treatment-time portal images, and an in-house dose reconstruction program (right).

calibration models described above and to improve the conversion of the EPID signal to primary energy fluence. One of the remaining challenges is to implement a correction for the scatter contribution in the portal images. Portal image scatter correction has been investigated by other researchers, and some good results have been reported using a scatter-to-primary ratio model and Monte Carlo-based scatter kernels [54–56]. Finally, once the individual steps of the dose reconstruction procedure have been optimized, the dosimetric accuracy of the full procedure will need to be determined using dose measurements in phantoms. As discussed below, the dosimetric accuracy achieved will affect the clinical application of the dose reconstruction procedure.

### Future directions in dose-guided therapy research

This article has summarized the work performed as well as the challenges remaining to develop a dose reconstruction procedure based on MV CBCT images of the patient on the treatment table and treatment-time portal images. As described earlier, the ability to reconstruct the delivered patient dose opens up the possibility of adapting the patient treatment plan to improve dose delivery. The accuracy of the dose reconstruction procedure and the availability of image processing tools will affect how treatment may be guided using this new dose information. Our initial goal is to achieve 5% accuracy for the reconstructed patient dose. With this level of accuracy, gross dosimetric errors, which have been demonstrated to be as high as 40% in cases of considerable patient weight loss [10], could be detected and corrected. Implementation of more complex dose-guidance strategies, such as scenarios 2 and 3 discussed earlier, will require increased dosimetric accuracy as well as the ability to precisely locate the dose distribution in terms of critical structures. It is here that the rapidly advancing field of 3D image processing will play a key role. Tools such as automated segmentation and 3D deformable registration increase our ability to determine under or over dosed regions as well as track the cumulative dose to various organs in the patient.

By focusing on the key parameter determining radiation treatment outcomes, dose verification and dose-guided therapy have the potential to considerably improve the treatment of cancer. Moreover, they offer the opportunity to increase our understanding of treatment effectiveness, improving our knowledge of the radiation doses and distributions that lead to the control of cancer or the injury of normal structures. Although this level of precision has long been a goal in radiation oncology, the continuing advances in imaging technology and in imaging processing may soon make this goal attainable.

### Acknowledgments

The authors would like to acknowledge the following persons for their valuable contributions, enlightening discussions and active participation on the acquisition of the clinical cone-beam images. At UCSF, Albert Chan,

Chris Malfatti, Amy Gillis, Ping Xia, Lynn Verhey. And at Siemens OCS, Ali Bani-Hashemi. This research was supported by Siemens Oncology Care Systems (OCS). One of the authors (OM) wishes to acknowledge a doctoral scholarship from NSERC-Canada.

### References

- Jacob R, Hanlon AL, Horwitz EM, Movsas B, Uzzo RG, Pollack A. The relationship of increasing radiotherapy dose to reduced distant metastases and mortality in men with prostate cancer. *Cancer* 2004;100:538–43.
- Lee N, Xia P, Fischbein NJ, Akazawa P, Akazawa C, Quivey JM. Intensity-modulated radiation therapy for head-and-neck cancer: the UCSF experience focusing on target volume delineation. *Int J Radiat Oncol Biol Phys* 2003;57:49–60.
- Kuban D, Pollack A, Huang E, Levy L, Dong L, Starkschall G, et al. Hazards of dose escalation in prostate cancer radiotherapy. *Int J Radiat Oncol Biol Phys* 2003;57:1260–8.
- Hurkmans CW, Cho BC, Damen E, Zijp L, Mijnheer BJ. Reduction of cardiac and lung complication probabilities after breast irradiation using conformal radiotherapy with or without intensity modulation. *Radiother Oncol* 2002;62:163–71.
- Tubiana M, Eschwege F. Conformal radiotherapy and intensity-modulated radiotherapy. *Acta Oncologica* 2000;39:555–67.
- Pouliot J, Kim Y, Lessard E, Hsu IC, Vigneron DB, Kurhanewicz J. Inverse planning for HDR prostate brachytherapy used to boost dominant intraprostatic lesions defined by magnetic resonance spectroscopy imaging. *Int J Radiat Oncol Biol Phys* 2004;59:1196–207.
- Wang JZ, Li XA. Impact of tumor repopulation on radiotherapy planning. *Int J Radiat Oncol Biol Phys* 2005;61:220–7.
- Verhey L. Patient immobilization for 3-D RTP and virtual simulation. In: Purdy JA, Starkschall G, editors. *A practical guide to 3-D planning and conformal radiation therapy*. Middleton, WI: Advanced Medical Publishing, Inc., 1999:151–74.
- Barker JL Jr, Garden AS, Ang KK, O'Daniel JC, Wang H, Court LE, et al. Quantification of volumetric and geometric changes occurring during fractionated radiotherapy for head-and-neck cancer using an integrated CT/linear accelerator system. *Int J Radiat Oncol Biol Phys* 2004;59:960–70.
- Hansen EK, Xia P, Quivey J, Weinberg V, Bucci MK. The roles of repeat CT imaging and re-planning during the course of IMRT for patients with head and neck cancer (abstract). *ASTRO 46th Annual Meeting; 2004 October 3–7; Atlanta, GA. Int J Radiat Oncol Biol Phys* 2004;60:S159.
- Millender LE, Aubin M, Pouliot J, Shinohara K, Roach M 3rd. Daily electronic portal imaging for morbidly obese men undergoing radiotherapy for localized prostate cancer. *Int J Radiat Oncol Biol Phys* 2004;59:6–10.
- Chung PW, Haycocks T, Brown T, Cambridge Z, Kelly V, Alasti H, et al. On-line aSi portal imaging of implanted fiducial markers for the reduction of interfraction error during conformal radiotherapy of prostate carcinoma. *Int J Radiat Oncol Biol Phys* 2004;60:329–34.
- Pouliot J, Aubin M, Langen KM, Liu YM, Pickett B, Shinohara K, et al. (Non)-migration of radio-opaque markers used for on-line localization of the prostate with an electronic portal imaging device. *Int J Radiat Oncol Biol Phys* 2003;56:862–6.
- Uematsu M, Sonderegger M, Shioda A, Tahara K, Fukui T, Hama Y, et al. Daily positioning accuracy of frameless stereotactic radiation therapy with a fusion of computed tomography and linear accelerator (focal) unit: evaluation of z-axis with a z-marker. *Radiother Oncol* 1999;50:337–9.

## Dose-guided radiation therapy with MV CBCT

15. Jaffray DA, Siewerdsen JH, Wong JW, Martinez AA. Flat-panel cone-beam computed tomography for image-guided radiation therapy. *Int J Radiat Oncol Biol Phys* 2002;53:1337-49.
16. Létourneau D, Martinez AA, Lockman D, Yan D, Vargas C, Ivaldi G, et al. Assessment of residual error for online cone-beam CT-guided treatment of prostate cancer patients. *Int J Radiat Oncol Biol Phys* 2005;62:1239-46.
17. Seppi EJ, Munro P, Johnsen SW, Shapiro EG, Tognina C, Jones D, et al. Megavoltage cone-beam computed tomography using a high-efficiency image receptor. *Int J Radiat Oncol Biol Phys* 2003;55:793-803.
18. Ghelmansarai FA, Bani-Hashemi A, Pouliot J, Calderon E, Hernandez P, Mitschke M, et al. Soft tissue visualization using a highly efficient megavoltage cone beam CT imaging system. In: Flynn MJ, editor. *Medical imaging 2005: physics of medical imaging*. Proceedings of SPIE Medical Imaging: Physics of Medical Imaging; 2005 February 13-15; San Diego, CA. Bellingham, WA: SPIE Press, 2005:159-70.
19. Pouliot J, Bani-Hashemi A, Chen J, Svatos M, Ghelmansarai F, Mitschke M, et al. Low-dose megavoltage cone-beam CT for radiation therapy. *Int J Radiat Oncol Biol Phys* 2005;61:552-60.
20. Nakagawa K, Aoki Y, Tago M, Ohtomo K. MV CT assisted stereotactic radiosurgery for thoracic tumors. *Int J Radiat Oncol Biol Phys* 2000;48:449-57.
21. Ruchala KJ, Olivera GH, Schloesser EA, Mackie TR. Megavoltage CT on a tomotherapy system. *Phys Med Biol* 1999;44:2597-621.
22. Mackie TR, Kapatoes J, Ruchala K, Lu W, Wu C, Olivera G, et al. Image guidance for precise conformal radiotherapy. *Int J Radiat Oncol Biol Phys* 2003;56:89-105.
23. Langen KM, Zhang Y, Andrews RD, Hurley ME, Meeks SL, Poole DO, et al. Initial experience with megavoltage (MV) CT guidance for daily prostate alignments. *Int J Radiat Oncol Biol Phys* 2005;62:1517-24.
24. Mageras GS, Yorke E. Deep inspiration breath hold and respiratory gating strategies for reducing organ motion in radiation treatment. *Semin Radiat Oncol* 2004;14:65-75.
25. Berson AM, Emery R, Rodriguez L, Richards GM, Ng T, Sanghavi S, et al. Clinical experience using respiratory gated radiation therapy: comparison of free-breathing and breath-hold techniques. *Int J Radiat Oncol Biol Phys* 2004;60:419-26.
26. Petersch B, Bogner J, Dieckmann K, Potter R, Georg D. Automatic real-time surveillance of eye position and gating for stereotactic radiotherapy of uveal melanoma. *Med Phys* 2004;31:3521-7.
27. Shirato H, Shimizu S, Kitamura K, Nishioka T, Kagei K, Hashimoto S, et al. Four-dimensional treatment planning and fluoroscopic real-time tumor tracking radiotherapy for moving tumor. *Int J Radiat Oncol Biol Phys* 2000;48:435-42.
28. Murphy MJ. Tracking moving organs in real time. *Semin Radiat Oncol* 2004;14:91-100.
29. Schweikard A, Shiomi H, Adler J. Respiration tracking in radiosurgery. *Med Phys* 2004;31:2738-41.
30. Court LE, Dong L, Lee AK, Cheung R, Bonnen MD, O'Daniel J, et al. An automatic CT-guided adaptive radiation therapy technique by online modification of multileaf collimator leaf positions for prostate cancer. *Int J Radiat Oncol Biol Phys* 2005;62:154-63.
31. Wu C, Jeraj R, Lu W, Mackie TR. Fast treatment plan modification with an over-relaxed Cimmino algorithm. *Med Phys* 2004;31:191-200.
32. Brabbins D, Martinez A, Yan D, Lockman D, Wallace M, Gustafson G, et al. A dose-escalation trial with the adaptive radiotherapy process as a delivery system in localized prostate cancer: analysis of chronic toxicity. *Int J Radiat Oncol Biol Phys* 2005;61:400-8.
33. Rehbinder H, Forsgren C, Lof J. Adaptive radiation therapy for compensation of errors in patient setup and treatment delivery. *Med Phys* 2004;31:3363-71.
34. van Herk M. Errors and margins in radiotherapy. *Semin Radiat Oncol* 2004;14:52-64.
35. Wu C, Jeraj R, Olivera GH, Mackie TR. Re-optimization in adaptive radiotherapy. *Phys Med Biol* 2002;47:3181-95.
36. Scarantino CW, Ruslander DM, Rini CJ, Mann GG, Nagle HT, Black RD. An implantable radiation dosimeter for use in external beam radiation therapy. *Med Phys* 2004;31:2658-71.
37. Kirby MC, Williams PC. The use of an electronic portal imaging device for exit dosimetry and quality control measurements. *Int J Radiat Oncol Biol Phys* 1995;31:593-603.
38. Boellaard R, van Herk M, Uiterwaal H, Mijnheer B. Two-dimensional exit dosimetry using a liquid-filled electronic portal imaging device and a convolution model. *Radiation Oncol* 1997;44:149-57.
39. Boellaard R, Essers M, van Herk M, Mijnheer BJ. New method to obtain the midplane dose using portal vivo dosimetry. *Int J Radiat Oncol Biol Phys* 1998;41:465-74.
40. Chang J, Mageras GS, Chui CS, Ling CC, Lutz W. Relative profile and dose verification of intensity-modulated radiation therapy. *Int J Radiat Oncol Biol Phys* 2000;47:231-40.
41. Louwe RJW, Damen EMF, van Herk M, Minken AWH, Torzsok O, Mijnheer BJ. Three-dimensional dose reconstruction of breast cancer treatment using portal imaging. *Med Phys* 2003;30:2376-89.
42. McNutt TR, Mackie TR, Reckwerdt P, Paliwal BR. Modeling dose distributions from portal dose images using the convolution/superposition method. *Med Phys* 1996;23:1381-92.
43. Hansen VN, Evans PM, Swindell W. The application of transit dosimetry to precision radiotherapy. *Med Phys* 1996;23:713-21.
44. Kapatoes JM, Olivera GH, Balog JP, Keller H, Reckwerdt PJ, Mackie TR. On the accuracy and effectiveness of dose reconstruction for tomotherapy. *Phys Med Biol* 2001;46:943-66.
45. Partridge M, Ebert M, Hesse B-M. IMRT verification by three-dimensional dose reconstruction from portal beam measurements. *Med Phys* 2002;29:1847-58.
46. Pouliot J, Xia P, Aubin M, Verhey L, Bani-Hashemi A, Ghelmansarai F, et al. Low-dose megavoltage cone-beam CT for dose-guided radiation therapy (abstract). *ASTRO 45th Annual Meeting*; 2003 October 19-23; Salt Lake City, UT. *Int J Radiat Oncol Biol Phys* 2003;57:5183-4.
47. Schaly B, Kempe JA, Bauman GS, Battista JJ, van Dyk J. Tracking the dose distribution in radiation therapy by accounting for variable anatomy. *Phys Med Biol* 2004;49:791-805.
48. Wiesent K, Barth K, Navab N, Durlak P, Brunner T, Schutz O, et al. Enhanced 3-D reconstruction algorithm for C-arm systems suitable for interventional procedures. *IEEE Trans Med Imaging* 2000;19:391-403.
49. Morin O, Chen J, Aubin M, Pouliot J. Evaluation of the mechanical stability of a megavoltage imaging system using a new flat panel positioner. In: Flynn MJ, editor. *Medical Imaging 2005: Physics of Medical Imaging*. Proceedings of SPIE Medical Imaging: Physics of Medical Imaging; 2005 February 13-15; San Diego, CA. Bellingham, WA: SPIE Press, 2005:704-10.
50. Ruchala KJ, Olivera GH, Schloesser EA, Hinderer R, Mackie TR. Calibration of a tomotherapeutic MVCT system. *Phys Med Biol* 2000;45:N27-36.
51. Chen J, Morin O, Chen H, Aubin M, Pouliot J. The effect of MV cone-beam CT cupping artifacts on dose calculation accuracy (abstract). *AAPM 47th Annual Meeting*; 2005 July 24-28; Seattle, WA. *Med Phys* 2005;32:1936.

52. Chen J, Chuang C, Morin O, Aubin M, Pouliot J. Calibration of an amorphous-silicon flat panel detector for absolute dosimetry (abstract). AAPM 46th Annual Meeting; 2004 July 25-29; Pittsburgh, PA. *Med Phys* 2004;31:1831 and 1832.
53. Ahnesjö A. Collapsed cone convolution of radiant energy for photon dose calculation in heterogeneous media. *Med Phys* 1989;16:577-92.
54. Hansen VN, Swindell W, Evans PM. Extraction of primary signal from EPIDs using only forward convolution. *Med Phys* 1997;24:1477-84.
55. Partridge M, Evans PM. The practical implementation of a scatter model for portal imaging at 10 MV. *Phys Med Biol* 1998;43:2685-93.
56. Spies L, Partridge M, Groh BA, Bortfeld T. An iterative algorithm for reconstructing incident beam distributions from transmission measurements using electronic portal imaging. *Phys Med Biol* 2001;46:N203-11.

## SHORT COMMUNICATION

# The use of megavoltage cone-beam CT to complement CT for target definition in pelvic radiotherapy in the presence of hip replacement

M AUBIN, MSc, O MORIN, BSc, J CHEN, PhD, A GILLIS, MD, B PICKETT, MSc, J F AUBRY, MSc, C AKAZAWA, CMD, J SPEIGHT, MD, M ROACH III, MD and J POULIOT, PhD

Department of Radiation Oncology, University of California San Francisco, Comprehensive Cancer Center, San Francisco, CA-94143, USA

**ABSTRACT.** In Europe and the USA combined, over half a million people had a hip joint replaced in 2005, contributing to the increasing number of radiotherapy patients with metallic hip prostheses. The treatment plan for external beam radiation therapy is based on the delineation of the anatomy in the planning CT scan. When implanted objects of high atomic number (Z) material are present, however, severe image artefacts are generated in conventional CT, strongly hindering the ability to delineate some organs. This is particularly the case for the planning of prostate patients with hip prostheses. This short communication presents the use of a new imaging modality, megavoltage cone-beam CT, to complement the regular CT for target definition of prostate cancer treatment of patients with hip replacements.

Received 20 January 2006  
 Revised 22 June 2006  
 Accepted 4 July 2006

DOI: 10.1259/bjr/19559792

© 2006 The British Institute of Radiology

Treatment planning for external beam radiation therapy is based on the delineation of the anatomy visualized in the planning CT scan. However, image artefacts caused by the presence of a hip replacement often render CT images useless for prostate delineation (Figure 1, left), and preclude precise dose calculation.

It was recently suggested that CT-MR image registration could facilitate target definition for a prostate patient with hip replacements [1]. Effectively, MR images provide an accurate definition of the clinical target volume (CTV) and better visualization of normal structures. A number of factors, however, were found to affect image quality and/or accuracy of target definition. The standard MR couch, different from a CT or linac treatment couch, might result in different patient position, and the presence of the metallic implants may create significant distortion. Finally, in the presence of a hip replacement, neither the regular CT nor the MR can provide accurate electron density information for heterogeneous dose calculation. Promising artefact reduction techniques on regular CT are being developed to minimize the impact of streaking artefacts [2]. At that time, they may require manual image post-processing and most CT scanners available in radiation oncology departments are not equipped with these features.

We report on the use of megavoltage cone-beam CT (MV CBCT) to complement the conventional CT for

target organ definition in seven patients treated for prostate cancer with external beam radiation therapy. In this study, we exploited the predominantly Compton scattering of high-energy photons delivered in MV CBCT systems to obtain 3D images of the anatomy in the presence of unilateral or bilateral hip replacements and complement the planning CT during the target delineation process.

## Method

A cone-beam CT image is reconstructed from a large set of projection images acquired at various angles around a patient in a process similar to that of conventional CT. In cone-beam CT, a two-dimensional (2D) array of detectors, in our case a portal imager attached to the linear accelerator (linac), is used to reconstruct a three-dimensional (3D) image. For MV CBCT, the 6 MV treatment beam of the accelerator, containing photons primarily in the MeV range, is used for the imaging.

A MV CBCT system [3, 4] integrated onto an ONCOR clinical Linac (Siemens Oncology Care Systems, Concord, CA) was used to acquire 3D images in treatment position for seven prostate patients with unilateral or bilateral hip prostheses. MV CBCT acquisitions were performed by rotating the linac in a continuous 200 arc (270° to 110° clockwise) acquiring one portal image for each degree. Because MV CBCT uses the treatment beam, the treatment planning system (Pinnacle, Phillips, Best, The Netherlands) was used to evaluate the dose delivered during an MV CBCT

Address correspondence to: Dr Jean Pouliot, Department of Radiation Oncology, University of California San Francisco, 1600 Divisadero Street, Suite H1031, San Francisco, CA 94941-1708, USA. E-mail: pouliot@radonc17.ucsf.edu.  
 This research was supported by Siemens Oncology Care Systems.

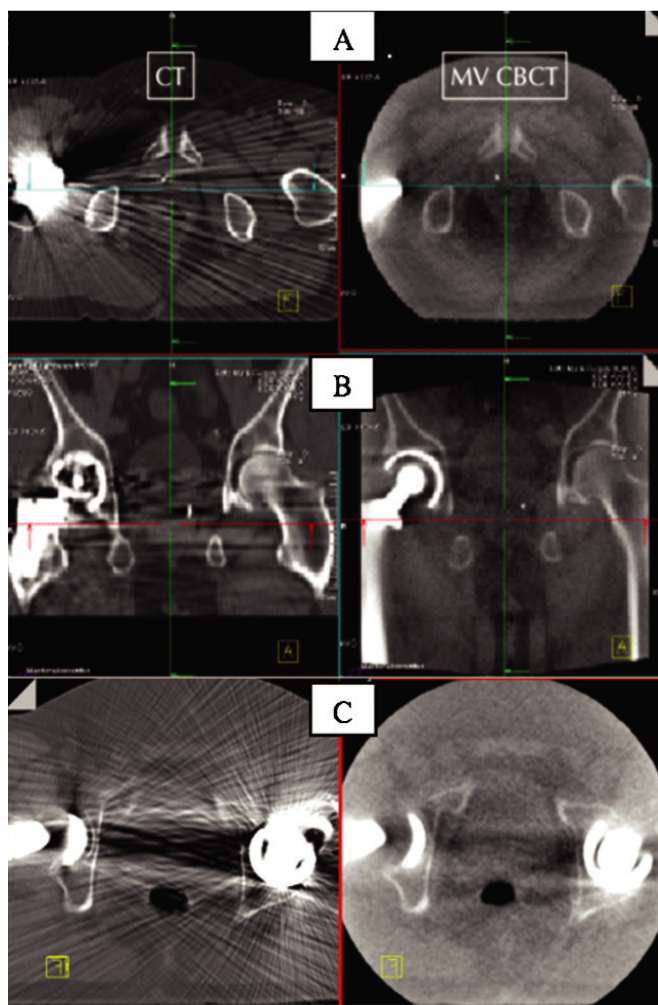


Figure 1. Comparison of a conventional CT (left) and megavoltage cone beam CT (MV CBCT) (right). (A) Axial and (B) coronal views are shown for a unilateral hip replacement. (C) Axial view for a bilateral hip replacement.

acquisition. For a typical acquisition procedure, the dose at the isocentre was 0.05 Gy and the acquisition lasted 45 s. The reconstructed image, a typical volume (27.4 cm × 27.4 cm × 27.4 cm), was available less than 2 min after the acquisition of the first portal image. A first order scatter correction was applied to facilitate the adjustment of window/levels. For each patient, the MV CBCT images were imported into the treatment planning system and registered with the original planning CT using bony anatomy contoured on each image set. The target volumes and organs at risk for prostate treatment were contoured using both the CT and the MV CBCT for single hip replacement, and using only the MV CBCT for bi-lateral hip prostheses.

## Results

The MV CBCT images could be used to visualize clearly the hip prosthesis and bony anatomy and provide sufficient soft-tissue contrast to help delineate the

prostate, bladder and rectum. The artefacts on the tube anterior wall of the rectum (Figure 1A, left) and the interface between the prostate base and the bladder neck (Figure 1B, left). The MV CBCT images were particularly useful to help delineate these structures as well as the lateral extension of the prostate in the axial plane, the seminal vesicles and the lymph nodes. Also, normal anatomy such as pelvic bones, penile bulb, bladder, femoral heads, rectum and small bowel can be delineated with higher accuracy as well.

An example of organ segmentation is presented in Figure 2. The change of shape of the prostate (red), bladder (green) and rectum (blue) between the CT (left) and the MV CBCT (right) can be easily observed. In this study, the time intervals between the CT and the MV CBCT ranged from a few hours to 1 week. By itself, this can explain the change in rectum and bladder volumes due to different fillings. For the six patients with a single hip replacement, the posterior limit of the prostate was found to be more anterior, and therefore the prostate

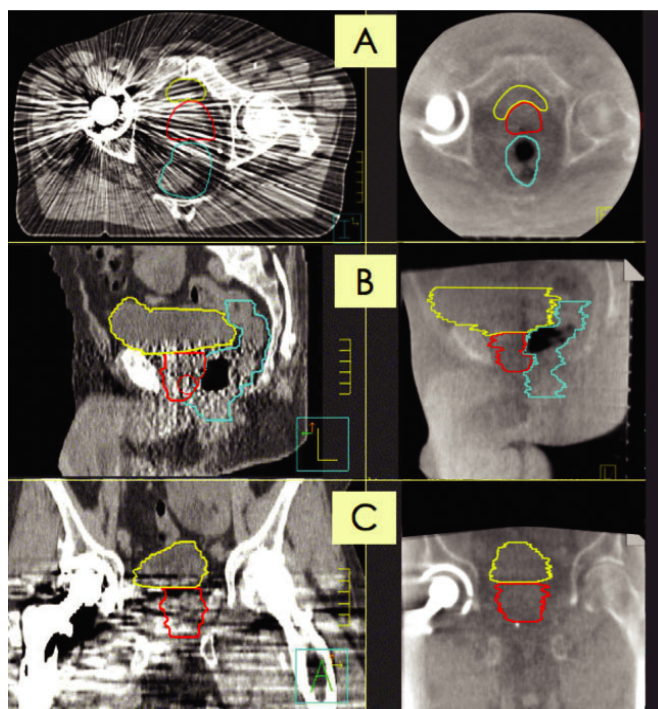


Figure 2. Segmentation of the bladder, prostate and rectum using the conventional CT (left) and the megavoltage cone beam CT (MV CBCT) (right) shown on the (A) axial, (B) sagittal and (C) coronal views.

volumes contoured with the help of MV CBCT were generally smaller than the volumes that would have been estimated using only the regular CT containing severe artefacts. These smaller prostate volumes may prevent overdosage of the rectum. Target delineation for the patient with bilateral hip prostheses was entirely performed using the MV CBCT, since the relevant organs were totally obscured due to the severity of the artefacts on the conventional CT.

## Discussion

Image artefacts (Figures 1 and 2, left) caused by the presence of hip replacements render regular CT images difficult to use for prostate delineation. In contrast, the presence of high-Z material has relatively little impact on the image quality of MV CBCT.

Tests performed on phantoms [5] showed that the presence of a metallic object strongly impacts on Hounsfield numbers (up to 70% error) of a conventional CT image and therefore disturbs the electron density even far away from the object, making CT inaccurate for dose calculation. For this reason, CT treatment plans of patients with hip replacements are generally produced without density correction. Similar tests performed with MV CBCT on a phantom with and without a metallic object demonstrated that Hounsfield numbers remain unchanged (within 3%) in the presence of metallic objects, allowing for significantly more accurate dose calculation. Thus, the next step after using MV CBCT for image segmentation will be to use MV CBCT for dose calculation. Research to develop calibration procedures

to use MV CBCT for dose calculations is being performed. There is also ongoing technical development to increase the field of view of the current version of MV CBCT (27 cm x 27 cm) to encompass the entire pelvic region.

The possibility of considering dose escalation protocols depends on the ability to identify the prostate volume and critical structures for treatment planning, and the accuracy of the dose calculation. Because of degradation of image quality in the presence of high-Z material, treatment planning and dose calculations are limited in these settings. Consequently, patients with hip prostheses may not be candidates for advanced treatment planning like intensity-modulated radiotherapy (IMRT). With the advance capability of using MV CBCT in the treatment planning software, it is now possible to deliver accurately higher doses of radiation to the prostate in patients with hip prosthesis. While MV CBCT acquisition dose is two to three times higher than a conventional CT, it represents only a very small fraction (0.1%) of the treatment dose. With dose escalation these patients may benefit from a decreased risk of treatment failure.

MV CBCT in the presence of high-Z material may improve treatment planning, allowing patients with pelvic malignancies and hip prostheses the most advanced form of radiation therapy.

## Conclusion

MV CBCT provides 3D anatomical information of the patient in the treatment position, even in the presence of

“CT non-compatible” objects. MV CBCT registered with the planning CT can complement missing information and facilitate segmentation for planning purposes when hip prostheses are present.

## References

1. Charnley N, Morgan A, Thomas E, Wilson S, Bacon S, Wilson D, et al. The use of CT-MR image registration to define target volumes in pelvic radiotherapy in the presence of bilateral hip replacements. *Br J Radiol* 2005;78:634-6.
2. Yazdia M, Gingras L, Beaulieu L. An adaptive approach to metal artifact reduction in helical computed tomography for radiation therapy treatment planning: experimental and clinical studies. *Int J Radiat Oncol Biol Phys* 2005;62:1224-31.
3. Pouliot J, Bani-Hashemi A, Chen J, et al., Low-dose megavoltage cone-beam CT for radiation therapy. *Int J Radiat Oncol Biol Phys* 2005;61:238-46.
4. Morin O, Gillis A, Chen J, Aubin M, Bucci MK, Pouliot J. Megavoltage cone-beam CT: system description and IGRT clinical applications. Special issue on image-guided radiation therapy (IGRT). *Med Dosim* 2006;31:51-61.
5. Aubin M, Morin O, Bucci K, Chan A, Chen J, Ghelmsarai F, et al. Megavoltage conebeam CT to complement prostate planning CT in presence of hip prosthesis. ESTRO Annual Meeting (abstract), Lisbon, 2005.





## RAPID COMMUNICATION

## IMAGE-GUIDED RADIOTHERAPY USING MEGAVOLTAGE CONE-BEAM COMPUTED TOMOGRAPHY FOR TREATMENT OF PARASPINOUS TUMORS IN THE PRESENCE OF ORTHOPEDIC HARDWARE

ERIC K. HANSEN, M.D., DAVID A. LARSON, M.D., PH.D., MICHELE AUBIN, M.Sc.E.E.,  
 JOSEPHINE CHEN, PH.D., MARTINA DESCOVICH, PH.D., AMY M. GILLIS, M.D., OLIVIER MORIN, B.Sc.,  
 PING XIA, PH.D., AND JEAN POULIOT, PH.D.

Department of Radiation Oncology, University of California San Francisco, San Francisco, CA

**Purpose:** This report describes a new image-guided radiotherapy (IGRT) technique using megavoltage cone-beam computed tomography (MV-CBCT) to treat paraspinous tumors in the presence of orthopedic hardware.

**Methods and Materials:** A patient with a resected paraspinous high-grade sarcoma was treated to 59.4 Gy with an IMRT plan. Daily MV-CBCT imaging was used to ensure accurate positioning. The displacement between MV-CBCT and planning CT images were determined daily and applied remotely to the treatment couch. The dose–volume histograms of the original and a hypothetical IMRT plan (shifted by the average daily setup errors) were compared to estimate the impact on dosimetry.

**Results:** The mean setup corrections in the lateral, longitudinal, and vertical directions were 3.6 mm (95% CI, 2.6–4.6 mm), 4.1 mm (95% CI, 3.2–5.0 mm), and 1.0 mm (95% CI, 0.6–1.3 mm), respectively. Without corrected positioning, the dose to 0.1 cc of the spinal cord increased by 9.4 Gy, and the doses to 95% of clinical target volumes 1 and 2 were reduced by 4 Gy and 4.8 Gy, respectively.

**Conclusions:** Megavoltage-CBCT provides a new alternative image-guided radiotherapy approach for treatment of paraspinous tumors in the presence of orthopedic hardware by providing 3D anatomic information in the treatment position, with clear imaging of metallic objects and without compromising soft-tissue information. © 2006 Elsevier Inc.

**Image-guided radiotherapy, Megavoltage cone-beam computed tomography, Intensity-modulated radiotherapy, Primary spine tumor, Metastatic spine tumor.**

### INTRODUCTION

Each year in the United States, approximately 25,000 individuals develop metastatic spinal cord compression and an additional 400 persons develop primary bone/soft tissue spine sarcomas (1, 2). Surgery plays a primary management role and permanent metallic hardware is often required (3). For “radioresistant” histologies and for retreatment of paraspinous tumors, spinal cord tolerance limits radiotherapy doses (4–6).

IMRT provides conformal treatments that spare normal tissues, but sharp dose gradients require accurate delineation of hardware and anatomy and accurate daily setup. Unfortunately, postoperative hardware artifact on standard computed tomography or magnetic resonance imaging may make image fusion or dosimetry problematic during treatment planning. A 5% to 10% dose reduction to tissues in regions behind stabilization rods has been noted (7). With-

out special techniques that allow highly accurate setup and dose escalation (8–11), some patients who might benefit from radiotherapy may remain untreated or may be treated with doses unlikely to provide long-term local control.

Megavoltage cone-beam computed tomography (MV-CBCT) is a new imaging technique used in image-guided radiotherapy (IGRT) to correct patient setup immediately before treatment (12, 13). MV-CBCT allows rapid acquisition of 3D images that can be registered with the planning CT with millimeter precision. The artifact and image degradation associated with kilovoltage (kV) CT imaging in the presence of high atomic number material is greatly reduced with MV-CBCT.

We provide the first clinical report on the use of MV-CBCT to aid in treatment of a patient with implanted hardware after surgery for a paraspinous high-grade sarcoma.

Reprint requests to: Jean Pouliot, Ph.D., University of California San Francisco, 1600 Divisadero Street, Suite H-1031, San Francisco, CA 94115. Tel: (415) 353-7175; Fax: (415) 353-9883; E-mail: pouliot@radonc17.ucsf.edu

This work was supported by Siemens OCS.  
 Received April 21, 2006, and in revised form May 4, 2006.  
 Accepted for publication May 16, 2006.

## METHODS AND MATERIALS

### Case report

A 62-year-old woman developed progressive mid-back pain and lower extremity weakness. MRI revealed a T3 pathologic compression fracture secondary to a 3.3-cm mass involving the T3 vertebral body with posterolateral extension, resulting in spinal stenosis and spinal cord edema (Fig. 1a). CT of the chest, abdomen, and pelvis revealed no metastases. The patient underwent urgent posterior T2 to T4 laminectomy, T3 posterior corpectomy, T1 to T6 posterior spinal fusion and instrumentation, and strut graft with T2 to T4 humeral ring allograft placement. The tumor involved the T3 vertebra with invasion of adjacent musculature. All gross tumor was removed in fragments. Pathology revealed a high-grade undifferentiated sarcoma. Postoperative MRI revealed no obvious residual tumor, but hardware artifact limited interpretation (Fig. 1b). Postoperative IMRT was recommended to reduce risk of local recurrence.

### Treatment planning

The patient underwent spiral CT simulation with 3-mm spacing with head and shoulder thermoplastic mask immobilization. Target volumes and normal structures were contoured by physicians. MV-CBCT imaging was later obtained and fused with the planning CT to confirm accurate delineation of hardware, normal tissues, and target volumes. Clinical target volume 1 (CTV1) represented areas at highest risk for residual/recurrent disease based on intraoperative findings and postoperative imaging. Clinical target volume 2 (CTV2) represented tissues thought to harbor moderate risk of microscopic disease, and extended 1 to 2 cm in axial dimensions and 2 to 4 cm in craniocaudal directions beyond CTV1. Planning volume expansions were used on the spinal cord (3 mm) and esophagus (2 mm). The IMRT plan (Fig. 1c) was generated using 9 axial beam angles using inverse planning (Corvus, Nomos Corporation, Cranberry Township, PA). Electron density corrections were performed after overriding areas of artifact on the planning CT that were distinct from the hardware on optimally windowed planning CT images; this was later confirmed with fused MV-CBCT images. A dose of 58 Gy was prescribed to the 72% isodose line in 29 fractions. (The total dose was 59.4 Gy, however, as the patient received an additional 1.4 Gy over the treatment course related to the verification and daily MV-CBCT and flat-panel imaging with 6 MV photons: [31 acquisitions (1 verification MV-CBCT & 30 pre-treatment MVBCTs, including two on the day of significant rotational setup error)  $\times$  (4.5 MU/MV-CBCT acquisition + 2 MU/pair of flat panel images)  $\times$  0.7 cGy/MU = 1.4 Gy]). The spinal cord volume receiving  $>50.4$  Gy was limited to 1 cc, and that receiving  $\geq 51.5$  Gy was limited to 0.1 cc.

### MV-CBCT imaging

Daily MV-CBCT images were obtained with the 6-MV beam of a clinical Siemens Primus accelerator (Siemens AG, Munich, Germany) by rotating the gantry in a continuous 200° arc as previously described (12). Each acquisition procedure (including image reconstruction) lasted  $<2$  min and required 4.5 MU. Daily MV-CBCT images were automatically registered with the planning CT using a maximization of mutual information algorithm, and fine adjustments were manually performed by physicians to align anatomic landmarks based on anatomy in axial, coronal, and sagittal planes in both regions with and without artifact (Fig. 2). The required table shift to correct patient position was remotely applied. A significant rotational setup error was identified once, after which the patient was immediately repositioned and MV-CBCT image registration repeated. Because MV-CBCT had not

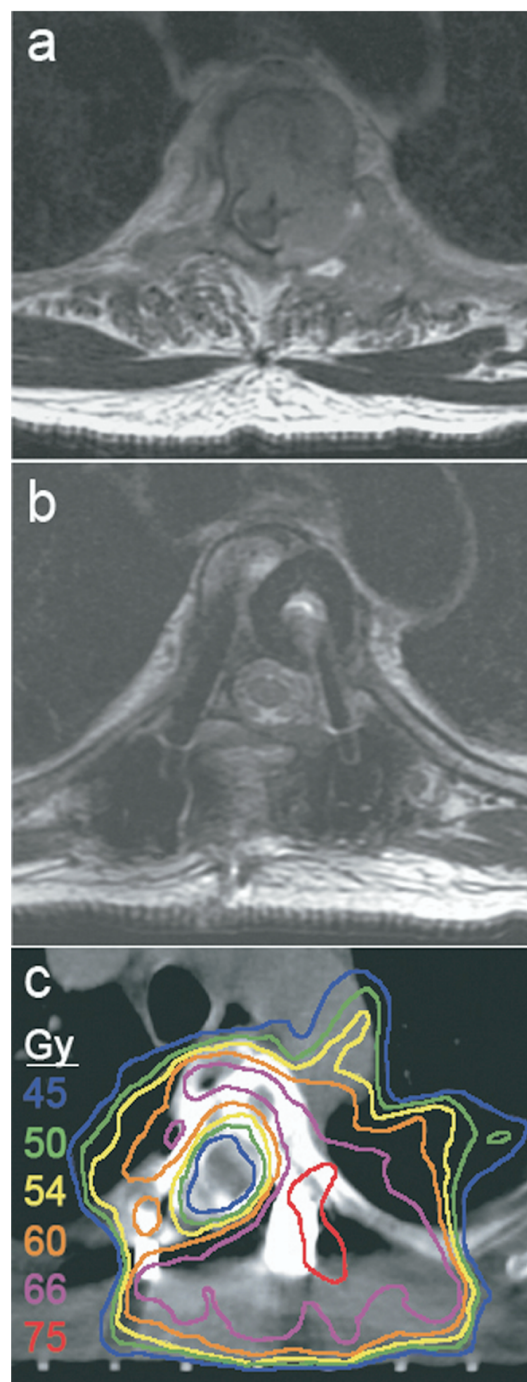


Fig. 1. (a) Preoperative axial T2 fat spin-echo magnetic resonance image (MRI) of T3 high-grade sarcoma. (b) Postoperative axial pure T2 MRI with hardware artifact. (c) Intensity-modulated radiotherapy (IMRT) plan.

previously been used in this setting, daily orthogonal flat-panel images were obtained after the table shifts to confirm position of the isocenter using the traditional 2D approach. During the first

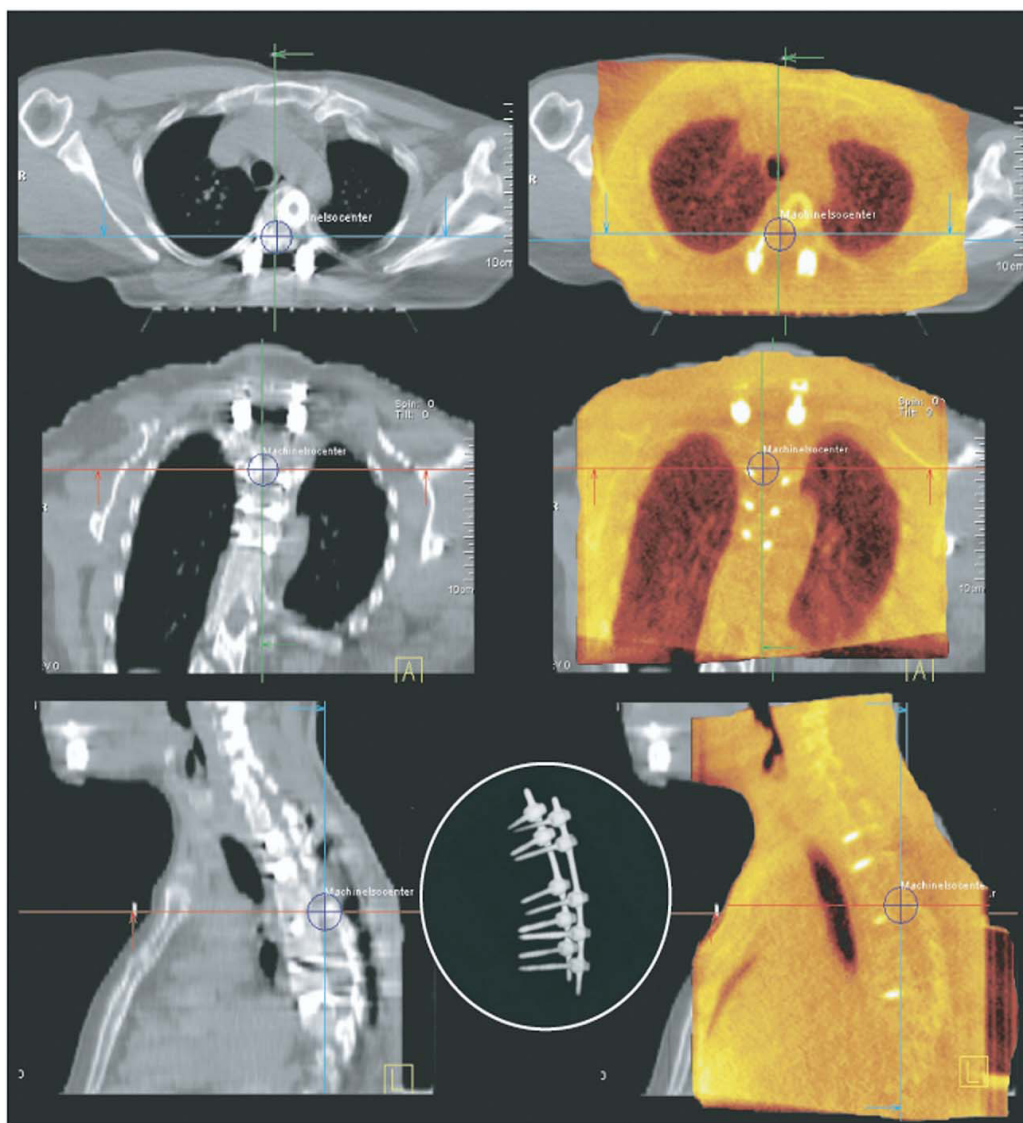


Fig. 2. Three-dimensional (3D) image registration of megavoltage cone-beam computed tomography (MV-CBCT) (orange) with planning CT (grayscale) in all 3 planes. Inset demonstrates 3D MV-CBCT reconstruction of hardware without typical artifact.

week, orthogonal flat panel images were acquired at the end of treatment to confirm that the patient did not move during dose delivery (range, 0–2.2 mm).

### RESULTS

The entire pretreatment daily setup procedure was performed in 6–8 min. The range of required daily table shifts in the right(–)/left(+), inferior(–)/superior(+), and posterior(–)/anterior(+) directions were –9.4 to 9.4 mm, –9.5 to 4.0 mm, and –3.5 to 1.0 mm, respectively. The mean magnitude of setup corrections obtained from the daily

MV-CBCT imaging in the lateral, longitudinal, and vertical directions were 3.6 mm (95% CI = 2.6–4.6 mm), 4.1 mm (95% CI = 3.2–5.0 mm), and 1.0 mm (95% CI = 0.6–1.3 mm), respectively.

To estimate the impact of the daily MV-CBCT shifts on dosimetry, the inverse planning system was used to create a hypothetical IMRT plan by applying the beam configurations of the original IMRT plan to the same planning CT with the isocenter shifted by the mean shifts listed above. The dose-volume histograms of the original and hypothetical IMRT plans were then compared. Had daily shifts not been detected

Table 1. Dosimetric comparisons

Location	Original IMRT Plan (achieved with daily MV-CBCT setup corrections)	Hypothetical IMRT Plan (without correcting mean setup errors obtained via daily MV-CBCT)
Spinal cord		
D <sub>1cc</sub>	50.3 Gy	58.9 Gy
D <sub>0.1cc</sub>	51.5 Gy	60.9 Gy
CTV1		
D <sub>99</sub>	47.9 Gy	42.3 Gy
D <sub>95</sub>	51.6 Gy	47.6 Gy
V <sub>93</sub>	88.5%	81.7%
CTV2		
D <sub>99</sub>	44.7 Gy	38.3 Gy
D <sub>95</sub>	49.5 Gy	44.7 Gy
V <sub>93</sub>	87.0%	80.0%

**Abbreviations:** CTV = clinical target volume 1; CTV2 = clinical target volume 2; D<sub>1cc</sub> = dose to 1 cc of the volume; D<sub>0.1cc</sub> = dose to 0.1 cc of the volume; D<sub>95</sub> = dose to 95% of the volume; D<sub>99</sub> = dose to 99% of the volume; IMRT = intensity-modulated radiotherapy; MV-CBCT = megavoltage cone beam computed tomography; V<sub>93</sub> = percentage of volume receiving  $\geq 93\%$  of the prescribed dose.

and corrected, spinal cord dose would have increased, and target volume coverage would have decreased (Table 1).

The patient developed no acute side effects during treatment, and her lower extremity strength and ambulation remains stable.

## DISCUSSION

There are several obstacles to treating patients with paraspinal tumors with orthopedic hardware using other techniques.

Metallic implants create image distortion with standard kV CT and MRI, which can impede image fusion and accurate delineation of hardware and anatomy, thereby limiting subsequent electron density corrections and dose calculations. Hardware artifact in standard digitally reconstructed radiographs may also preclude accurate identification of landmarks during image registration, although the use of digitally composited radiographs is an innovative solution (8). Traditional 2D port films or flat panel images do not show out-of-plane rotation, which is easily visualized with MV-CBCT. In the setting of extensive hardware, implanted fiducial markers and/or small screws or pins used for tracking with the CyberKnife system (Accuray Inc., Sunnyvale, CA) (9, 10) sometimes cannot be adequately imaged. Even with the excellent dose distributions of protons, without accurate daily setup, spinal cord tolerance could be at risk.

This rapid communication demonstrates that MV-CBCT provides a new alternative IGRT approach for the treatment of paraspinal tumors in the presence of orthopedic hardware. The speed of the MV-CBCT procedure demonstrates that clinically useful MV-CBCT can be performed on a daily basis. Ongoing studies will define the role of MV-CBCT in aiding contouring and improving dose calculations (12–15). Future investigations will compare MV-CBCT techniques with other reported methods for treatment of these patients.

## CONCLUSION

Megavoltage-CBCT provides a new alternative IGRT approach for treatment of paraspinal tumors in the presence of orthopedic hardware by providing 3D anatomic information in the treatment position, with clear imaging of metallic objects and without compromising soft-tissue information.

## REFERENCES

- Khan SN, Donthineni R. Surgical management of metastatic spine tumors. *Orthop Clin N Am* 2006;37:99–104.
- Schiff D. Spinal cord compression. *Neurol Clin North Am* 2003;21:67–86.
- Fisher CG, Keynan O, Boyd MC, and Dvorak MF. The surgical management of primary tumors of the spine. *Spine* 2005;30:1899–1908.
- Emami B, Lyman J, Brown A, et al. Tolerance of normal tissue to therapeutic irradiation. *Int J Radiat Oncol Biol Phys* 1991;21:109–122.
- Marcus RB Jr, Million RR. The incidence of myelitis after irradiation of the cervical spinal cord. *Int J Radiat Oncol Biol Phys* 1990;19:3–8.
- Bilsky MH, Yamada Y, Yenice KM, et al. Intensity-modulated stereotactic radiotherapy of paraspinal tumors: a preliminary report. *Neurosurgery* 2004;54:823–830.
- Liebross RH, Starkschall G, Wong P, et al. The effect of titanium stabilization rods on spinal radiation dose. *Med Dosim* 2002;27:21–24.
- Lovelock DM, Hua C, Wang P, et al. Accurate setup of paraspinal patients using a noninvasive patient immobilization cradle and portal imaging. *Med Phys* 2005;32:2606–2614.
- Ryu SI, Chang SD, Kim DH, et al. Image-guided hypofractionated stereotactic radiosurgery to spinal lesions. *Neurosurgery* 2001;49:838–846.
- Gerszten PC, Ozhasoglu C, Burton SA, et al. CyberKnife frameless stereotactic radiosurgery for spinal lesions: clinical experience in 125 cases. *Neurosurgery* 2004;55:89–98.
- Medin PM, Solberg TD, De Salles AAF, et al. Investigations of a minimally invasive method for treatment of spinal malignancies with linac stereotactic radiation therapy: accuracy and animal studies. *Int J Radiat Oncol Biol Phys* 2002;52:1111–1122.
- Pouliot J, Bani-Hashemi A, Chen J, et al. Low-dose megavoltage cone-beam CT for radiation therapy. *Int J Radiat Oncol Biol Phys* 2005;61:552–560.
- Aubin M, Morin O, Chen J, et al. The use of megavoltage cone-beam CT to complement CT for target definition in pelvic radiotherapy in the presence of hip replacement. *Br J Radiol* 2006; in press.
- Martinez AA, Di Y, Lockman D, et al. Improvement in dose escalation using the process of adaptive radiotherapy combined with three-dimensional conformal or intensity-modulated beams for prostate cancer. *Int J Radiat Oncol Biol Phys* 2000;50:1226–1234.
- Morin O, Gillis A, Chen J, et al. Megavoltage cone-beam CT: system description and clinical applications. *Med Dosim* 2006; 31:51–61.

# Bibliography

- [1] American cancer society website. [www.cancer.org](http://www.cancer.org), 2007.
- [2] S.A. Leibel and T.L. Phillips. *Textbook of Radiation Oncology*. Elsevier, Philadelphia, 2004.
- [3] K. Colvett. The history of radiation oncology. *Southern Medical Journal*, 99(10):1155(2), 2006.
- [4] H.A. Shih, S.B. Jiang, K.M. Aljarrah, K.P. Doppke, and N.C. Choi. Internal target volume determined with expansion margins beyond composite gross tumor volume in three-dimensional conformal radiotherapy for lung cancer. *International Journal of Radiation Oncology, Biology, Physics*, 60(2):613–622, 2004.
- [5] M.W. Lometti, O. Morin, M. Aubin, A.R. Gottschalk, B. Pickett, M. Roach III, and J. Pouliot. Intra-fraction prostate motion using MV fluoroscopy [abstract]. *International Journal of Radiation Oncology, Biology, Physics*, 63:S195, 2005.
- [6] R. de Crevoisier, S.L. Tucker, L. Dong, R. Mohan, R. Cheung, J. D. Cox, and

- D.A. Kuban. Increased risk of biochemical and local failure in patients with distended rectum on the planning CT for prostate cancer radiotherapy. *International Journal of Radiation Oncology, Biology, Physics*, 62(4):965–973, 2005.
- [7] E.K. Hansen, M.K. Bucci, J.M. Quivey, V. Weinberg, and P. Xia. Repeat CT imaging and replanning during the course of IMRT for head-and-neck cancer. *International Journal of Radiation Oncology, Biology, Physics*, 64(2):355–362, 2006.
- [8] J.L. Barker Jr., A.S. Garden, K.K. Ang, J.C. O’Daniel, H. Wang, L.E. Court, W.H. Morrison, D.I. Rosenthal, S.C. Chao, S.L. Tucker, R. Mohan, and L. Dong. Quantification of volumetric and geometric changes occurring during fractionated radiotherapy for head-and-neck cancer using an integrated CT/linear accelerator system. *International Journal of Radiation Oncology, Biology, Physics*, 59(4):960–970, 2004.
- [9] R. Jacob, A.L. Hanlon, E.M. Horwitz, B. Movsas, R.G. Uzzo, and A. Pollack. The relationship of increasing radiotherapy dose to reduced distant metastases and mortality in men with prostate cancer. *Cancer*, 100:538–43, 2004.
- [10] N. Lee, P. Xia, N.J. Fischbein, P. Akazawa, C. Akazawa, and J.M. Quivey. Intensity-modulated radiation therapy for head-and-neck cancer: The UCSF experience focusing on target volume delineation. *International Journal of Radiation Oncology, Biology, Physics*, 57(1):49–60, 2003.

- [11] D. Kuban, A. Pollack, E. Huang, L. Levy, L. Dong, G. Starkschall, and I. Rosen. Hazards of dose escalation in prostate cancer radiotherapy. *International Journal of Radiation Oncology, Biology, Physics*, 57(5):1260–1268, 2003.
- [12] C.W. Hurkmans, B.C. Cho, E. Damen, L. Zijp, and B.J. Mijnheer. Reduction of cardiac and lung complication probabilities after breast irradiation using conformal radiotherapy with or without intensity modulation. *Radiotherapy & Oncology*, 62(2):163–171, 2002.
- [13] M. Tubiana and F. Eschwege. Conformal radiotherapy and intensity-modulated radiotherapy: Clinical data. *Acta Oncologica*, 39(5):555–567, 2000.
- [14] C.-M. Ma and K. Paskalev. In-room CT techniques for image-guided radiation therapy. *Medical Dosimetry*, 31:30–39, 2006.
- [15] J.R. Wong, C.W. Cheng, L. Grimm, and M. Uematsu. Clinical implementation of the world’s first Primatom, a combination of CT scanner and linear accelerator, for precise tumor targeting and treatment [abstract]. *Medica Physica*, 17:271–276, 2001.
- [16] D.A. Jaffray, J.H. Siewerdsen, J.W. Wong, and A.A. Martinez. Flat-panel cone-beam computed tomography for image-guided radiation therapy. *International Journal of Radiation Oncology, Biology, Physics*, 53(5):1337–49, 2002.
- [17] U. Oelfke, T. Tucking, S. Nill, A. Seebert, B. Hesse, P. Huber, and C. Thilmann.

- Linac-integrated kV cone-beam CT: technical features and first applications. *Medical Dosimetry*, 31:62–70, 2006.
- [18] S.P. Sorensen, E. Chow, S. Kriminski, P.M. Medin, and T.D. Solberg. Image guided radiotherapy using a mobile kilovoltage x-ray device. *Medical Dosimetry*, 31:40–50, 2006.
- [19] J. Pouliot, A. Bani-Hashemi, J. Chen, M. Svatos, F. Ghelmansarai, M. Mitschke, M. Aubin, P. Xia, O. Morin, K. Bucci, M. Roach III, P. Hernandez, Z. Zheng, D. Hristov, and L. Verhey. Low-dose megavoltage cone-beam CT for radiation therapy. *International Journal of Radiation Oncology, Biology, Physics*, 61(2):552–560, 2005.
- [20] J. Sillanpaa, J. Chang, G. Mageras, H. Riem, E. Ford, D. Todor, C.C. Ling, and H. Amols. Developments in megavoltage cone beam CT with an amorphous silicon EPID: reduction of exposure and synchronization with respiratory gating. *Medical Physics*, 32(3):819–29, 2005.
- [21] J. Gildersleve, D.P. Dearnaley, P.M. Evans, M. Law, C. Rawlings, and W. Swindell. A randomised trial of patient repositioning during radiotherapy using a megavoltage imaging system. *Radiotherapy & Oncology*, 31(2):161–168, 1994.
- [22] P.M. Evans, J.Q. Gildersleve, C. Rawlings, and W. Swindell. Technical note: The implementation of patient position correction using a megavoltage imaging



- device on a linear accelerator. *British Journal of Radiology*, 66(789):833–838, 1993.
- [23] T.R. Mackie, J. Kapatoes, K. Ruchala, W. Lu, C. Wu, G. Olivera, L. Forrest, W. Tome, J. Welsh, R. Jeraj, P. Harari, P. Reckwerdt, B. Paliwal, M. Ritter, H. Keller, J. Fowler, and M. Mehta. Image guidance for precise conformal radiotherapy. *International Journal of Radiation Oncology, Biology, Physics*, 56(1):89–105, 2003.
- [24] W. Swindell, E.J. Morton, P.M. Evans, and D.G. Lewis. The design of megavoltage projection imaging systems: some theoretical aspects. *Medical Physics*, 18(5):855–66, 1991.
- [25] K. Nakagawa, A. Akanuma, Y. Aoki, K. Karasawa, A. Terahara, Y. Onogi, N. Muta, Y. Sasaki, K. Kawakami, and K. Hanakawa. A quantitative patient set-up and verification system using megavoltage CT scanning. *International Journal of Radiation Oncology, Biology, Physics*, 21(SUPPL. 1):228, 1991.
- [26] M.A. Mosleh-Shirazi, P.M. Evans, W. Swindell, S. Webb, and M. Partridge. A cone-beam megavoltage CT scanner for treatment verification in conformal radiotherapy. *Radiotherapy & Oncology*, 48(3):319–28, 1998.
- [27] S. Midgley, R. M. Millar, and J. Dudson. A feasibility study for megavoltage cone beam CT using a commercial EPID. *Physics in Medicine & Biology*, 43(1):155–69, 1998.

- [28] L. Spies, M. Ebert, B.A. Groh, B.M. Hesse, and T. Bortfeld. Correction of scatter in megavoltage cone-beam CT. *Physics in Medicine & Biology*, 46(3):821–33, 2001.
- [29] E.C. Ford, J. Chang, K. Mueller, K. Sidhu, D. Todor, G. Mageras, E. Yorke, C.C. Ling, and H. Amols. Cone-beam CT with megavoltage beams and an amorphous silicon electronic portal imaging device: potential for verification of radiotherapy of lung cancer. *Medical Physics*, 29(12):2913–24, 2002.
- [30] B.A. Groh, J.H. Siewerdsen, D.G. Drake, J.W. Wong, and D.A. Jaffray. A performance comparison of flat-panel imager-based MV and kV cone-beam CT. *Medical Physics*, 29(6):967–75, 2002.
- [31] E.J. Seppi, P. Munro, S.W. Johnsen, E.G. Shapiro, C. Tognina, D. Jones, J.M. Pavkovich, C. Webb, I. Mollov, L.D. Partain, and R.E. Colbeth. Megavoltage cone-beam computed tomography using a high-efficiency image receptor. *International Journal of Radiation Oncology, Biology, Physics*, 55(3):793–803, 2003.
- [32] F. Ghelmansarai, A. Bani-Hashemi, J. Pouliot, E. Calderon, P. Hernandez, M. Mitschke, M. Aubin, and K. Bucci. Soft tissue visualization using a highly efficient megavoltage cone-beam CT imaging system [abstract]. *SPIE-Int. Soc. Opt. Eng. Proceedings of Spie - the International Society for Optical Engineering. Medical Imaging*, 5745:159–170, 2005.
- [33] K. Sidhu, E.C. Ford, S. Spirou, E. Yorke, J. Chang, K. Mueller, D. Todor,

- K. Rosenzweig, G. Mageras, C. Chui, C.C. Ling, and H. Amols. Optimization of conformal thoracic radiotherapy using cone-beam CT imaging for treatment verification. *International Journal of Radiation Oncology, Biology, Physics*, 55(3):757–767, 2003.
- [34] M.A. Anastasio, S. Daxin, P. Xiaochuan, C. Pelizzari, and P. Munro. A preliminary investigation of local tomography for megavoltage CT imaging. *Medical Physics*, 30(11):2969–80, 2003.
- [35] J. Pouliot, M. Aubin, L. Verhey, A. Bani-Hashemi, M. Mitschke, P. Hernandez, and J. Hughes. Low dose megavoltage cone beam CT reconstruction for patient alignment [abstract]. *7th International Workshop on Electronic Portal Imaging*, 2002.
- [36] A.C. Kak and M. Slaney. *Principles of computerized tomographic imaging*. IEEE Transactions on Medical Imaging. 1988.
- [37] H. Turbell. *Cone-Beam reconstruction using filtered backprojection*. PhD thesis, 2001.
- [38] L.A. Feldkamp, L.C. Davis, and J.W. Kress. Practical cone-beam algorithm. *Journal of the Optical Society of America A-Optics & Image Science*, 1(6):612–19, 1984.
- [39] J. Monteil and A. Beghdadi. New adaptive nonlinear anisotropic diffusion for

- noise smoothing. *IEEE International Conference on Image Processing*, 3:254, 1998.
- [40] K. Wiesent, K. Barth, N. Navab, P. Durlak, T. Brunner, O. Schuetz, and W. Seissler. Enhanced 3D-reconstruction algorithm for C-arm systems suitable for interventional procedures. *IEEE Transactions on Medical Imaging*, 19(5):391–403, 2000.
- [41] J.T. Bushberg, J.A. Seibert, E.M. Leidholdt, and J.M. Boone. *The essential physics of medical imaging*. Lippincott Williams & Wilkins, Philadelphia, second edition edition, 2002.
- [42] A. Sawant, L.E. Antonuk, Y. El-Mohri, Z. Qihua, L. Yixin, S. Zhong, W. Yi, J. Yamamoto, D. Hong, I. Cunningham, M. Klugerman, and K. Shah. Segmented crystalline scintillators: an initial investigation of high quantum efficiency detectors for megavoltage x-ray imaging. *Medical Physics*, 32(10):3067–83, 2005.
- [43] M.H.P. Smitsmans, J. De Bois, J.-J. Sonke, A. Betgen, L.J. Zijp, D.A. Jaffray, J.V. Lebesque, and M. Van Herk. Automatic prostate localization on cone-beam CT scans for high precision image-guided radiotherapy. *International Journal of Radiation Oncology, Biology, Physics*, 63(4):975–984, 2005.
- [44] O. Morin, S. Bose, J. Chen, M. Aubin, and J. Pouliot. The impact of portal imager shifts and the assumption of rigid isocentricity on megavoltage cone-beam CT images [abstract]. *Medical Physics*, 32:1916, 2005.

- [45] O. Morin, J. Chen, M. Aubin, and J. Pouliot. Evaluation of the mechanical stability of megavoltage imaging system using a new flat panel positioner [abstract]. *SPIE-Int. Soc. Opt. Eng. Proceedings of Spie - the International Society for Optical Engineering. Medical Imaging*, 5745:704–710, 2005.
- [46] D.A. Jaffray, J.J. Battista, A. Fenster, and P. Munro. X-ray scatter in megavoltage transmission radiography: physical characteristics and influence on image quality. *Medical Physics*, 21(1):45–60, 1994.
- [47] W.J.C. van Elmpt, S. Nijsten, B.J. Mijnheer, and A.W.H. Minken. Experimental verification of a portal dose prediction model. *Medical Physics*, 32(9):2805–18, 2005.
- [48] J. Maltz, B. Gangadharan, D. Hristov, and A. Bani-Hashemi. Site-specific image-gain calibration for MV CBCT (SU-FF-I-11) [abstract]. *Medical Physics*, 33(6):1999, 2006.
- [49] R.T. Droege and R.L. Morin. A practical method to measure the MTF of CT scanners. *Medical Physics*, 9(5):758–60, 1982.
- [50] E.L. Nickoloff. Measurement of the PSF for a CT scanner: appropriate wire diameter and pixel size. *Physics in Medicine and Biology*, 33:149, 1988.
- [51] J.M. Boone and J.A. Seibert. An analytical edge spread function model for

- computer fitting and subsequent calculation of the LSF and MTF. *Medical Physics*, 21(10):1541, 1994.
- [52] Z. Chen and R. Ning. Three-dimensional point spread function measurement of cone-beam computed tomography system by iterative edge-blurring algorithm. *Physics in Medicine & Biology*, 49(10):1865–80, 2004.
- [53] K.M. Langen, S.L. Meeks, D.O. Poole, T.H. Wagner, T.R. Willoughby, P.A. Kupelian, K.J. Ruchala, J. Haimerl, and G.H. Olivera. The use of megavoltage CT (MVCT) images for dose recomputations. *Physics in Medicine & Biology*, 50(18):4259–76, 2005.
- [54] O. Morin, A. Gillis, M. Descovich, J. Chen, M. Aubin, J.-F. Aubry, H. Chen, A.R. Gottschalk, P. Xia, and J. Pouliot. Patient dose considerations for routine megavoltage cone-beam CT imaging. *Medical Physics*, 34(5):1819, 2007.
- [55] B. Faddegon, F. Ghelmansarai, and A. Bani-Hashemi. A low-z target with no flattener and reduced energy for improved contrast in megavoltage cone-beam CT [abstract]. *Medical Physics*, 33(6):2021, 2006.
- [56] G.C. Bentel. *Patient positioning and immobilization in radiation oncology*. McGraw-Hill Professional Publishing, New York, 1st ed edition edition, 1999.
- [57] J.M. Balter, K.L. Lam, H.M. Sandler, J.F. Littles, R.L. Bree, and R.K. Ten Haken. Automated localization of the prostate at the time of treatment

- using implanted radiopaque markers: technical feasibility. *International Journal of Radiation Oncology Biology Physics*, 33(5):1281–1286, 1995.
- [58] E. Vigneault, J. Pouliot, J. Laverdiere, J. Roy, and M. Dorion. Electronic portal imaging device detection of radioopaque markers for the evaluation of prostate position during megavoltage irradiation: a clinical study. *International Journal of Radiation Oncology, Biology, Physics*, 37(1):205–212, 1997.
- [59] J.M. Balter, L.A. Dawson, S. Kazanjian, C. McGinn, K.K. Brock, T. Lawrence, and R.T. Haken. Determination of ventilatory liver movement via radiographic evaluation of diaphragm position. *International Journal of Radiation Oncology Biology Physics*, 51(1):267–70, 2001.
- [60] Y. Seppenwoolde, H. Shirato, K. Kitamura, S. Shimizu, M. van Herk, J.V. Lebesque, and K. Miyasaka. Precise and real-time measurement of 3D tumor motion in lung due to breathing and heartbeat, measured during radiotherapy. *International Journal of Radiation Oncology Biology Physics*, 53(4):822–34, 2002.
- [61] J. Pouliot, M. Aubin, K.M. Langen, Y.-M. Liu, B. Pickett, K. Shinohara, and M. Roach III. (Non)-migration of radiopaque markers used for on-line localization of the prostate with an electronic portal imaging device. *International Journal of Radiation Oncology, Biology, Physics*, 56(3):862–866, 2003.
- [62] P.W.M. Chung, T. Haycocks, T. Brown, Z. Cambridge, V. Kelly, D.A. Alasti, H. and Jaffray, and C.N. Catton. On-line aSi portal imaging of implanted fiducial

- markers for the reduction of interfraction error during conformal radiotherapy of prostate carcinoma. *International Journal of Radiation Oncology, Biology, Physics*, 60(1):329–334, 2004.
- [63] L.E. Millender, M. Aubin, J. Pouliot, K. Shinohara, and M. Roach III. Daily electronic portal imaging for morbidly obese men undergoing radiotherapy for localized prostate cancer. *International Journal of Radiation Oncology, Biology, Physics*, 59(1):6, 2004.
- [64] K.M. Langen and D.T.L. Jones. Organ motion and its management. *International Journal of Radiation Oncology Biology Physics*, 50(1):265–78, 2001.
- [65] M.E.S. Beaver, K.E. Matheny, D.B. Roberts, and J.N. Myers. Predictors of weight loss during radiation therapy. *Otolaryngology - Head and Neck Surgery*, 125(6):645–648, 2001.
- [66] O. Morin, J. Chen, M. Aubin, A. Gillis, J.-F. Aubry, S. Bose, H. Chen, M. Descovich, P. Xia, and J. Pouliot. Dose calculation using megavoltage cone-beam CT. *International Journal of Radiation Oncology Biology Physics*, 67(4):1201–1210, 2007.
- [67] S.J. Thomas. Relative electron density calibration of CT scanners for radiotherapy treatment planning. *British Journal of Radiology*, 72(860):781–6, 1999.



- [68] D.A. Low, W.B. Harms, S. Mutic, and J.A. Purdy. A technique for the quantitative evaluation of dose distributions. *Medical Physics*, 25(5):656–61, 1998.
- [69] J. Seco and P.M. Evans. Assessing the effect of electron density in photon dose calculations. *Medical Physics*, 33(2):540–52, 2006.
- [70] J. Chen, O. Morin, H. Chen, M. Aubin, and J. Pouliot. The effect of MV cone-beam CT cupping artifacts on dose calculation accuracy (SU-FF-J-72) [abstract]. *Medical Physics*, 32(6):1936, 2005.
- [71] M. Aubin, O. Morin, J. Chen, A. Gillis, B. Pickett, J.F. Aubry, and J. Pouliot. The use of megavoltage cone-beam CT to complement CT for target definition in pelvic radiotherapy in presence of hip replacement. *British Journal of Radiology*, 79:918–921, 2006.
- [72] A.H. Mahnken, R. Raupach, J.E. Wildberger, B. Jung, N. Heussen, T.G. Flohr, R.W. Guenther, and S. Schaller. A new algorithm for metal artifact reduction in computed tomography: In vitro and in vivo evaluation after total hip replacement. *Investigative Radiology*, 38(12):769–775, 2003.
- [73] M. Descovich, O. Morin, J. Aubry, M. Aubin, J. Chen, A. Bani-Hashemi, and J. Pouliot. Characteristics of megavoltage cone-beam digital tomosynthesis. *Medical Physics*, In review, 2007.
- [74] O. Morin, A. Gillis, J. Chen, M. Aubin, K. Bucci, and J. Pouliot. Megavoltage

- cone-beam CT: system description and clinical applications. *Medical Dosimetry*, 31(1), 2006.
- [75] O. Morin, M. Aubin, J.F. Aubry, S. Bose, J. Chen, M. Descovich, L. Verhey, and J. Pouliot. Physical performance and image quality of megavoltage cone-beam CT (TU-FF-A4-5) [abstract]. *Medical Physics*, 34(6), 2007.
- [76] O. Morin, M. Aubin, J.F. Aubry, J. Chen, M. Descovich, and J. Pouliot. Quality assurance of megavoltage cone-beam CT (TH-D-L100J-5) [abstract]. *Medical Physics*, 34(6), 2007.
- [77] J. Pouliot, P. Xia, M. Aubin, L. Verhey, K. Langen, A. Bani-Hashemi, M. Svatos, F. Ghelmansarai, and M. Mitchke. Dose-guided radiation therapy using low-dose megavoltage cone-beam CT (SU-EE-PDS-11) [abstract]. *Medical Physics*, 30(6):1337, 2003.
- [78] J. Chen, C.F. Chuang, O. Morin, M. Aubin, and J. Pouliot. Calibration of an amorphous-silicon flat panel portal imager for exit-beam dosimetry. *Medical Physics*, 33(3):584–94, 2006.
- [79] J. Chen, O. Morin, M. Aubin, C. Chuang, and J. Pouliot. Dose-guided radiation therapy using megavoltage cone-beam CT. *British Journal of Radiology*, 79:S87–S98, 2006.

### **Publishing Agreement**

*It is the policy of the University to encourage the distribution of all theses and dissertations. Copies of all UCSF these and dissertations will be routed to the library via the Graduate Division. The library will make all theses and dissertations accessible to the public and will preserve these to the best of their abilities, in perpetuity.*

### **Please sign the following statement:**

*I hereby grant permission to the graduate Division of the University of California, San Francisco to release copies of my thesis or dissertation to the Campus Library to provide access and preservation, in whole or in part, in perpetuity.*

Oliver Morin

Author Signature

08/10/07

Date